SENSITIVE VOLUME MODELS FOR SINGLE EVENT UPSET ANALYSIS AND RATE PREDICTION FOR SPACE, ATMOSPHERIC, AND TERRESTRIAL RADIATION ENVIRONMENTS

By

Kevin M. Warren

Dissertation

Submitted to the Faculty of the

Graduate School of Vanderbilt University

in partial fulfillment of the requirements

for the degree of

DOCTOR OF PHILOSOPHY

in

Electrical Engineering

August, 2010

Nashville, Tennessee

Approved:

Robert A. Weller

Ron D. Schrimpf

Robert A. Reed

Lloyd W. Massengill

Charles M. Lukehart

© Copyright by Kevin M. Warren 2010

All Rights Reserved

ACKNOWLEDGEMENTS

I would like to thank Dr. Robert Weller, for his support as my advisor and his tireless work on development of the MRED code as well as the rest of my committee for their time and effort applied to the completion of this degree. I would like to acknowledge my ISDE coworkers Brian Sierawski and Dr. Andrew Sternberg for their input and suggestions during the course of this work, as well as their assistance in software development and application.

I would like to acknowledge the support of Lew Cohn of the Naval Research Laboratories (formerly with the Defense Threat Reduction Agency), and Ken LaBel of the National Aeronautics and Space Administration at the Goddard Space Flight Center as well as Jeffrey Wilkinson and Mark Porter of Medtronic, Inc. for their enthusiastic participation in the development of the applications related to this work, as well as the continuous stream of experimental data they supplied.

I would like to thank my wife, Tessa, and our son, Rafe for their support and patience during the course of this degree. Tessa's encouragement has been invaluable in motivating me during the final months of this effort.

Finally, I would like to thank my Parents, Jon and Nina, for instilling a sense of curiosity and independent thought in me as well as supporting my education for so many years. It is to them that I owe all that I have been able to become.

TABLE OF CONTENTS

Page

ACKNOWLEDGEMENTS iii

LIST OF TABLES vii

LIST OF FIGURES viii

Chapter

I. INTRODUCTION 1

Basic Mechanisms 2
Stopping Power and Linear Energy Transfer 2
Predicting SEU Rates by Particle Type 6
Heavy Ion Charged Particles 6
High Energy Protons and Neutrons 14
Thermal Neutrons 19
Alpha Particles 20
Factors Affecting Charge Collection and Circuit Response 22
Intra- and Inter-cell Variations 22
Single-particle Multiple Node Effects 24
Single-particle Multiple Bit Effects 25
Circuit Effects 27
Conclusions 28

II. THE MULTIPLE SENSITIVE VOLUME MODEL 30

Introduction and Problem Statement 30
Proposed Solution: The Multiple Sensitive Volume Model 32
Nested Sensitive Volumes 34
Multiple Sensitive Volume Groups 39
Simulation Analysis of the Multiple Sensitive Volume Model 41
Software Tools and Technology Benchmark 41
Single Node Charge Collection 43
Multiple-Node Charge Collection 57
Application of Multiple Sensitive Volume Model 67
Histograms and Probabilities 67
SEU Cross-section Curves 69
Conclusions 71

III. PHYSICS BASED TRANSPORT AND THE MULTIPLE SENSITIVE VOLUME MODEL 74

Introduction 74

Device and Circuit Analysis 75
TCAD: Transistor-level Charge Collection 75
TCAD: Full-cell SRAM Simulations 76
SPICE: Circuit Simulation 79
MRED Base-line Models and Configuration 82
SRAM Solid Model 82
Sensitive Volume Model 83
Experimental: Heavy ion SEU Measurement 83
Sensitive Volume Calibration 84
High-Energy Protons 89
Testing and Simulation 89
High-Energy Neutrons 92
High-Energy Neutron Error Rate Calculation 93
Thermal Neutron Error Rate Calculation 97
Simulating Alpha Sources 98
Americium Foil Source 101
Thorium Thick Source 104
Conclusions 107

IV. SENSITIVE VOLUME GROUPS AND MULTI-NODE SEU MECHANISMS 108

Introduction 108
Latch Design 108
Experimental 108
SEU Analysis 111
SPICE: Circuit Simulation 111
TCAD: Transistor and Cell Simulation 111
MRED Base-Line Models and Configuration 114
DICE Latch Solid Model 114
MRED SEU Conditions 114
Sensitive Volume Model 116
Sensitive Volume Calibration 117
Heavy Ion Space Environment Rate Prediction 119
Conclusions 122

V. INTEGRATION OF MONTE CARLO RADIATION TRANSPORT AND CIRCUIT LEVEL SIMULATORS 124

Introduction 124
The SPICE Interface 125
Current Pulse Calculation 125
Python Interface 129
General Device Description and Test Conditions 131
DICE Version 1 133
MRED Model and Calibration 133
SEU Rate 136
Analysis 139
Sources of Uncertainty and Systematic Error 141
DICE Version 2 143

MRED Model and Calibration . . . 144
SEU Rate . . . 146
Analysis . . . 147
Conclusions . . . 152

VI. SOURCES OF UNCERTAINTY . . . 155

VII. CONCLUSIONS . . . 162

Appendix

A. POISSON PROCESSES . . . 165

The Poisson Distribution . . . 165
Sum of Poisson Distributed Random Variables . . . 166
Estimation . . . 169

B. MONTE CARLO CALCULATIONS OF SEU CROSS SECTIONS AND ERROR RATES . . . 172

SEU Cross Section and Rate Prediction . . . 172
Monte Carlo Integration . . . 174
Randomization Methods . . . 176
Linear Sampling and Transformation of Variables . . . 176
Logarithmic Sampling . . . 178
Picking Points on a the Interior of a Disk . . . 179
Picking Points on the Surface of a Sphere . . . 180
Monte Carlo Ray Tracing (MRT) Simulator . . . 181
Introduction . . . 181
Construction . . . 183
Analysis Techniques . . . 186
The Histogram: A Measure of the Event Probability . . . 186
Run-Time Analysis . . . 191

REFERENCES . . . 193

LIST OF TABLES

Table Page

1. TCAD derived SEU cross sections. 78

2. Parameters used for double exponential current source to simulate heavy ion strikes on NMOS 81

3. Parameters used for double exponential current source to simulate heavy ion strikes on PMOS 81

4. Heavy Ion Species. 84

5. Sensitive Volume Parameters for the SRAM at 1.4 V 88

6. Physics Models 91

7. ^{241}Am Simulation Parameters 104

8. Latch Sensitive Node Pairs and Critical Charge. 112

9. Default Current Pulse Parameters. 128

10. The error rate on the V1 flip-flop for three types of multi-node events. 141

11. The baseline SEU rate and the effect of limiting the omnidirectional LET. . . 144

12. Randomization Terms. 184

LIST OF FIGURES

Figure		Page
1.	Cartoon of the relationship between an ion strike, ionization of the device, and the junction within that device that affect charge collection.	5
2.	Simplified drawing of a SRAM cell showing ionization near the NMOS pull-down device (left). The resultant state-change that defines a single event upset (right).	5
3.	The sensitive volume model as it relates to energy deposition and charge generation in a device.	7
4.	Differential probability of chord lengths in an RPP volume of dimensions 2x2x1 μm^3.	8
5.	Differential partial flux over the combined set of species (Z) and the corresponding integral flux as a function of linear energy transfer for the geosynchronous environment during solar minimum conditions calculated using CREME96.	9
6.	Hypothetical heavy ion SEU cross section curve illustrating the effect of irradiance angle for each species, including a Weibull fit to the data points.	10
7.	Calculation of the energy deposition profile of 523 MeV neon ions in a cuboidal volume of silicon with overlayers containing tungsten.	13
8.	Effects of nuclear reactions on the macroscopic cross-section curve.	13
9.	Fragmentation of 25 MeV/u ^{20}Ne on tungsten in silicon.	14
10.	Los Alamos WNR/ICE House neutron spectrum compared to atmospheric rate (40,000 feet), scaled by a factor of 1.5×10^5.	17
11.	The directional dependence of the proton beam relative to the device surface and the measured cross section curve in the low energy ranges.	18
12.	An illustration of the charge collection profile as a function of strike location on a body-tied SOI NMOS transistor (left) and the resulting SEU cross-section curve (right).	23
13.	Illustration of the multi-node SEU process (left). SEU Cross section curve for a radiation hardened DICE latch (right).	25
14.	Three dimensional simulation of charge collection over a singly diffused device surface as a function of strike location at normal incidence.	31
15.	Example SEU cross section curves at normal incidence for a 0.20 x 0.20 x 0.75 μm^3 sensitive volume as a function of LET and critical charge.	32
16.	Conceptual illustration of the nested configuration of sensitive volumes.	36

17. Conceptual illustration of the nested configuration of sensitive volumes. . . . 38

18. Graphic of the nested configuration of sensitive volumes where x, y and z extents differ for a fixed s and m. The outermost volumes extend to $\pm 4.0\ \mu m$ in $\pm x$, but are not shown as the cumulative collection efficiency is < 0.01 %. . . 40

19. 3-Dimensional TCAD model of the single n-diffusion device with the (x,z) cut-plane shown for reference. 44

20. Illustration of the location, sizes, and efficiencies of the multiple sensitive volume parameters applied to the single diffusion TCAD model with one active silicon region volume and 30 nested substrate volumes. 45

21. TCAD (open markers) and nested sensitive volume (SV, lines) predictions at normal incidence for single node at multiple LET. 46

22. TCAD (open markers) and sensitive volume predictions (solid lines) over strike positions for 45° over the surface, and 90° over the depth. 47

23. TCAD model of the single NMOS device. 48

24. TCAD generated spatial distribution of the collected charge as a function of strike location for the single node NMOS device at 0.1 $pC/\mu m$ (top down view). 50

25. Selected NMOS TCAD and extracted SV charge collection profiles for an LET of 0.1 $pC/\mu m$. 51

26. TCAD structure of single-node p^+ diffusion in an n-type well. 52

27. TCAD (open markers) and sensitive volume predictions (solid lines) of charge collected by a p+ diffusion over strike positions for 0°, 45° over the surface, and 90° over the depth. For 90° strike angles, TCAD simulations predicted an abrupt drop in collected charge between 18.6 and 19.0 μm. 53

28. TCAD model of the single pmos device. 54

29. Spatial distribution of the collected charge as a function of strike location for the single node PMOS device at 0.1 $pC/\mu m$ (top down view). 55

30. Selected PMOS TCAD and extracted SV charge collection profiles for an LET of 0.1 $pC/\mu m$. 56

31. TCAD model of 3-node NMOS structure containing relevant cut planes. . . . 58

32. TCAD and nested sensitive volume predictions for three nodes. 59

33. TCAD model of the three-transistor NMOS device. 60

34. Division of the active silicon sensitive volumes in a single NMOS for the 3-NMOS model. 60

35. Charge collection profile along x-axis at y=-1.0 for three NMOS devices as predicted by TCAD and fit using MRT. 61

36. Charge collection profile along y-axis at x=0.0 for three NMOS devices as predicted by TCAD and fit using MRT. 62

37. TCAD model of 3 PMOS transistors. 62

38. Charge collection profile for three PMOS devices as predicted by TCAD and fit using MRT. 63

39. Top down view of the single NMOS structure illustrating the location of the additional sensitive volumes used to capture secondary charge collection mechanisms. 64

40. Subset of cut-planes comparing the nested sensitive volume predictions and the TCAD results which include the additional volumes used to capture secondary charge collection mechanisms. 65

41. TCAD model of the three-transistor NMOS device along the y-axis at x=0.0. Additional volumes have been placed between $0.0 \leq y \leq 2.0$ μm to account for coupling to the N-well. 66

42. Progression from raw counts distribution to cross-section calculations using the singly diffused NMOS volumes. 68

43. Cross section curves for a series of collected charges using MRT and the calibrated sensitive volume models. 70

44. Coincident node SEU cross sections for the 3-n+ diffusion model with $Q_{crit} = 5\ fC$. 71

45. Collected charge vs. LET for NMOS transistor. 77

46. Collected charge vs. LET for PMOS transistor. 77

47. 3D SRAM cell. Dark blue regions indicate p-type dopant, red regions indicate n-type dopant. Trenched areas reflect the omitted STI and raised areas are polysilicon gates. 78

48. Regions sensitive to SEU (red) of the SRAM for 1, 2, and 6 $MeVcm^2/mg$ at V_{DD} =2.0 V. 79

49. Schematic of the 0.25 μm TSMC SRAM circuit used for SEU simulations. . . 80

50. TCAD current profile and the corresponding SPICE double exponential fit for an LET of 2.0 $MeVcm^2/mg$ on the NMOS transistor. 80

51. SPICE and experimental SEU results for the SRAM circuit. 82

52. SEM cross section(left) and CAD models (right) of SRAM. 83

53. Heavy ion SEU cross sections at a supply voltage of 1.4 V. 85

54. Heavy ion SEU cross sections at a supply voltage of 1.5 V. 85

55. Heavy ion SEU cross sections at a supply voltage of 2.0 V. 86

56. SEU cross sections as a function of logic pattern. 86

57. Active silicon region and substrate (pink) and sensitive regions (green) determined from TCAD and microbeam results. 87

58. Positioning of sensitive volumes in the active silicon region for the NMOS and PMOS transistors. 88

59. Experimental heavy ion cross sections and calibrated MRED model at normal incidence, V_{DD}=1.4 V. 90

60. Simulated and measured proton SEU cross sections at 1.4 V. 92

61. Comparison of simulated proton and neutron SEU cross sections at $\mathrm{V_{DD}}$ = 1.4 V. 93

62. Comparison of simulated proton and neutron cross sections near threshold. . 94

63. Full NYC neutron spectrum (Goldhagen) with *high-energy range* illustrated. . 95

64. A comparison of the neutron flux at sea level and the ICE House neutron spectrum. 96

65. Calculated neutron FIT rates from experiment and simulation.. 96

66. Thermal neutron cross section as a function of critical charge for the naturally occurring and purified compositions of $^{10}B/^{11}B$. 99

67. Predicted soft error rate as a function of Q_{crit}. The rates for 95% and 99% purified ^{11}B in BPSG are also shown. 100

68. Side and Top Views of the SRAM solid model and emission locations as simulated in MRED (^{241}Am foil). 101

69. Series containing the simulation of ^{241}Am activity as a function of energy for a range of source depths and the actual source used in measurement. 102

70. Graphical representation of the maximum emission angle (left) and capture efficiency calculations (right) for the MRED ^{241}Am alpha model. 104

71. Soft error rate as a function of air gap thickness for the 300 nCi Am source on the 4 Mbit SRAM. Each series is for a given atmospheric pressure (in units of torr). 105

72. Simulated ^{232}Th source activity in secular equilibrium. The gold passivation is intended to capture degradation due to source or detector passivation materials. Peaks of the various ^{232}Th decay products are shown. 106

73. MRED simulated and experimentally measured alpha SEU cross-section as a function of polyimide film degrader film thickness on the SRAM. The source activity was calibrated to the vendors ^{232}Th thick source. 107

74. Schematic and Layout of DICE Latch. 109

75. Orientation of the ion beam with respect to the DUT surface and related nomenclature. 110

76. Compilation of heavy ion data from irradiation of the latch shown in the classical effective LET manner. 110

77. Depiction of the TCAD model containing the N0 and N2 transistors separated by the n-well (left). Charge diffusion from the track to both N0 and N2 causes upset (right). 113

78. TCAD simulation showing electrostatic potential in the vicinity of the N0-P1 transistor pair before a heavy ion strike (left) and the N-well potential collapse after the strike (right). 114

79. Solid model of a single latch. The oxide and interlayer-dielectric material has been made transparent to illustrate the metallization layers. 115

80. Conceptual 2-dimensional cross sectional drawing of two (multi-)sensitive volume groups. 116

81. Final placement of the sensitive volume set for each transistor with respect to the circuit layout. The dashed lines represent the outer boundary of the sensitive volume set for a transistor. 117

82. SEU cross sections for the 10 MeV/u xenon (58.7 $MeV cm^2/mg$) beam at 75° tilt as a function of roll angle. 118

83. SEU cross sections for the 10 MeV/u argon (9.7 $MeV cm^2/mg$) beam at 75° tilt as a function of roll angle. 118

84. SEU cross sections for the 10 MeV/u xenon (58.7 $MeV cm^2/mg$) beam at 40° tilt as a function of roll angle. 119

85. SEU cross sections for the 10 MeV/u krypton (31.2 $MeV cm^2/mg$) beam at 40° tilt as a function of roll angle. No SEU were recorded in MRED between 60° and 120°. 119

86. SEU cross sections for the 10 MeV/u krypton (31.2 $MeV cm^2/mg$) beam at 75° tilt as a function of roll angle. 120

87. SEU cross sections for the 10 MeV/u krypton (31.2 $MeV cm^2/mg$) beam at 65° tilt as a function of roll angle. 120

88. SEU cross sections for the 10 MeV/u xenon (58.7 $MeV cm^2/mg$) beam at 65° tilt as a function of roll angle. 121

89. SEU cross sections for the 10 MeV/u argon (9.7 $MeV cm^2/mg$) beam at 65° tilt as a function of roll angle. 121

90. SEU rate of the latch for each species in the space environment. 122

91. Double exponential current pulse for a series of Q_{coll}. 129

92. Pulse width and peak current as a function of Q_{coll}. 129

93. Diagram of the current pulse injection and upset monitoring sequence of the flip-flop circuit. 131

94. Block level drawing of DICE flip-flop. 132

95. Schematic of the DICE flip-flop chains used during heavy ion irradiation. . . 133

96. Orientation of heavy ion irradiation and simulation angles with respect to the devices' surface. 133

97. Solid model of the V1 flip-flop. 134

98. Experimental and simulated cross sections at normal incidence for the V1 flip-flop. 135

99. Experimental and simulated cross sections at 60° tilt and 0° roll for the V1 flip-flop. 136

100. Experimental and simulated cross sections at 60° tilt and 90° roll for the V1 flip-flop. 137

101. The integral LET spectrum for the Adams 90% environment (open squares) and the equivalent response plot of the V1 DICE flip-flop (solid line). 138

102. Solid-angle normalized error rate as a function of the ions tilt component from the on-orbit SEU rate calculation (open triangles) of the V1 flip-flop integrated over all roll angles 139

103. Solid-angle normalized error rate as a function of the ions roll component of the directional vector from the on-orbit SEU rate calculation of the V1 flip-flop integrated over all tilt angles 140

104. Schematic and layout views illustrating charge sharing between NMOS devices in the V1 flip-flop. 142

105. Layout view of the V1 flip-flop with the NMOS pair and PMOS pair sensitive regions circled. 142

106. Selected layers from the solid model of the Version 2 DICE flip-flop. 144

107. Neon at 80° tilt, plotted over roll. 145

108. Experimental and simulated copper (16 $MeVcm^2/mg$) SEU cross-sections as a function of roll at a tilt angle of 80° at 100 kHz. 146

109. Experimental and simulated copper (16 $MeVcm^2/mg$) SEU cross-sections as a function of tilt at a roll angle of 60° (right) at 100 kHz. 146

110. The relative error rate as a function of tilt for the flip-flop in the Adams 90% space environment at 100 kHz. 147

111. The relative error rate as a function of roll for the flip-flop in the Adams 90% space environment at 100 kHz. 148

112. Locations of the dominant SEU rate directions and struck transistors in the Version 2 flip-flop. 148

113. Experimental (100 kHz) SEU cross sections over tilt angle versus MRED predictions for Argon at 60° roll. 149

114. Percentage of errors from charge collection on a single transistor relative to the overall error rate as a function of frequency. 149

115. Scatter plot of the relative contribution of tilt angles to the SEU rate prediction at 1000 MHz, integrated over all roll conditions. 150

116. Simulated heavy ion relative SEU cross-section curves. 151

117. Relative error rates as a function of frequency for MRED simulations and CREME96 Weibull parameters, normalized to the static SEU rate estimate from the 80/60 data. 153

118. Example of the progression of the estimated rate with increasing samples in a Monte Carlo simulation. 158

119. Concept of the world volumes (left) and parameters in the general rate equation (right). 172

120. Design of the Monte Carlo Ray Tracing Program 184

121. Continuous and Monte Carlo sampled energy probability distributions in an RPP of 5 x 10 x 15 μm^3. 190

122. Continuous and Monte Carlo sampled reverse integrated probabilities. 191

CHAPTER I

INTRODUCTION

Few, if any, environments are devoid of particle radiation. The nature of the radiation, in terms of energy and composition, is a function of both the immediate local environment (e.g., surrounding sourcing and shielding materials), position with the solar system and/or universe (e.g., terrestrial, earth orbit, interplanetary, or beyond the heliopause), and time (e.g., solar cycle variations) [1] [2] [3]. Man-made radiation may exist in addition to the natural radiation background, such as in medical diagnostic environments [4], nuclear power and weapons [5], and radioisotope thermoelectric power generation [6]. Alpha emissions also occur from within electronic devices or their packaging due to the decay of radioactive isotopes that are present as part of the manufacturing and packaging process [7].

A single particle of radiation passing through an electronic device, under the right conditions, can have catastrophic consequences for an entire chip, system, or even spacecraft, if proper test and design protocols are not followed. Failures from single particles, generally classified as single event effects or SEE, were first theorized to cause data corruption in J-K flip-flops operating in the space environment as early as 1975 [8]. Atmospheric neutrons were recognized as a potential source of failures in integrated circuits by Ziegler and Lanford [2]. Alpha-emitting contaminants in packaging material were identified by May and Woods in 1979 as a reliability concern for dynamic random access memories (DRAM) and charged coupled devices (CCD) [7]. It is from these early works that the field of radiation effects developed and in the aforementioned references, many key terms relevant to the work presented in this paper were introduced.

SEE encapsulate a broad category of radiation effects on electronics devices (and potentially systems) and can be subdivided into non-destructive and destructive types, where the line between the two is blurred depending on the degree of intervention required to recover

to normal operation, if possible [9]. The focus of this dissertation is on the area of single event upsets, in which ionization of the semiconductor in and around electric junctions, from a single particle, corrupts the logic state of a storage element. Common SEU-susceptible elements include, but are not limited to static random access memories (SRAM), dynamic random access memories (DRAM), and latches or flip-flops (FF). SEUs are generally considered non-destructive or soft [10]. The term single event upset is used interchangeably with soft error, where the former is predominantly used in the space effects community and the latter in commercial terrestrial electronics.

Basic Mechanisms

Stopping Power and Linear Energy Transfer

The rate at which energy is lost by radiation, per unit path length in matter, is defined as the stopping power. The study of the stopping and energy loss of ions in matter ions dates back to 1909 to work by Geiger and somewhat simultaneously by J.J. Thomson. Details of the history as well as detailed information on calculating stopping power have been gathered by Zielger [11]. Linear energy transfer (LET) is related to the stopping power by (1), where $\frac{dE}{dx}$ is the stopping power and ρ is the material density [10].

$$LET = \frac{-1}{\rho}\frac{dE}{dX} \tag{1}$$

Stopping power and LET are often used interchangeably in the field of radiation effects with the implicit assumption that the rate of energy loss has been appropriately scaled by ρ (1). LET is a function of all the parameters of the radiation (i.e., type, atomic number, and energy) as well as the material through which it passes (i.e., elemental composition, density, and even lattice orientation). LET is often expressed in units of energy per areal density or charge generated per unit path length for the material.

Energy loss by the ion, and the processes of energy absorption in a semiconductor result

in a nearly continuous path of free electron-hole pairs (ehp). The energy required to generate a free ehp, E_{ehp}, is approximated by (2), where E_g is the band-gap in electron volts (eV) [12]. For silicon, this translates into approximately 3.6 eV per thermalized ehp.

$$E_{ehp} = 2.73E_g + .55\ eV \tag{2}$$

For small path lengths, s, the generated charge, Q_{gen}, is given by (3), where ρ is the material's density and E_{ehp} is the energy required to generate a single ehp [13]. The small path length assumption is a requirement, as the LET is a function of the ion's energy, which decreases, as energy is lost to the surrounding material.

$$Q_{gen} = \frac{LET \cdot \rho \cdot s}{E_{ehp}} \tag{3}$$

Charge Collection and Single Event Upset

Once carriers are created by an ionizing radiation event, they are subject to drift and diffusion per the semiconductor current equations for holes and electrons shown in (4) and (5) [14]. The total current density for electrons and holes (J_n and J_p, respectively) is a result of the combined drift and diffusion components. Carrier drift results from the force exerted by the local electric field, E, on that charge, and is proportional to the product of the unit charge (q), the mobility of the carriers (μ), and the carrier concentration (n or p). The diffusion component is also proportional to the charge, the diffusion coefficient, D, and the gradient of the carrier concentration, $\frac{dn}{dx}$ or $\frac{dp}{dx}$, shown for the one-dimensional case.

$$J_n = q\mu_n n E_x + qD_n \frac{dn}{dx} \tag{4}$$

$$J_p = q\mu_p p E_x - qD_p \frac{dp}{dx} \tag{5}$$

Figure 1 contains a conceptual drawing of the ionization and charge collection process for a single device node. In this example, the *node* is a physical contact to a low resistance, highly doped region. The *bulk region* is doped with impurities in such a manner as to allow for the formation of a metallurgical junction at the dopant interface (i.e., n-p junction). The node represents the electrical point of contact to other devices (e.g., transistors) within the circuit. If ionization occurs in or near the electric field from the reversed bias junction (or the built in junction fields), charge collection can be enhanced by distortion of the potential field lines into the substrate (or funnel) from which an increased quantity of carriers are drawn [15]. The ion-generated carriers move rapidly from the influence of the electric field from around the junction areas and may diffuse to the field regions due to concentration gradients that are created from ionization and the motion of charge [16]. Detailed examinations of the process of charge transport from single events have been published using technology computer aided design (TCAD) electrical device simulators, which solve the current equations (4), (5) and the continuity equation for models of semiconductor devices [17], [18], [19], [20].

Charge arising from an ionizing event may reach a critical circuit node. The rate at which the charge is collected at the node is a current. The induced current may sufficiently alter the voltage at that node to cause a single event upset (SEU). A simple example is shown for the case of a static random access memory (SRAM) in Figure 2. The left-hand side of the figure shows an ion passage near the n-channel metal oxide semiconductor (NMOS) transistor. The flow of current at the NMOS node affects the node potentials of the circuit. If the radiation induced current exceeds the ability of the PMOS transistor to restore the potential at the V_{BL} line an SEU occurs. SEU in this structure is a function of the charge generated, the restorative ability of the pull-up PMOS transistor, and the feedback time of the second leg of the circuit. The details of SEU in SRAM devices have been studied extensively. Specific examples of the time evolution of the circuit potentials from radiation events, as determined by simulation, can be found in [21] and [22].

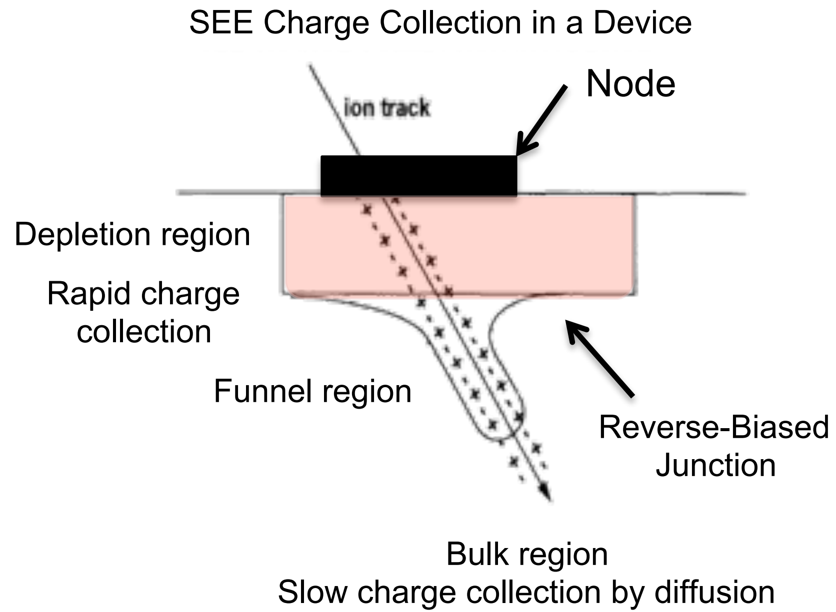

Figure 1: Cartoon of the relationship between an ion strike, ionization of the device, and the junction within that device that affect charge collection.

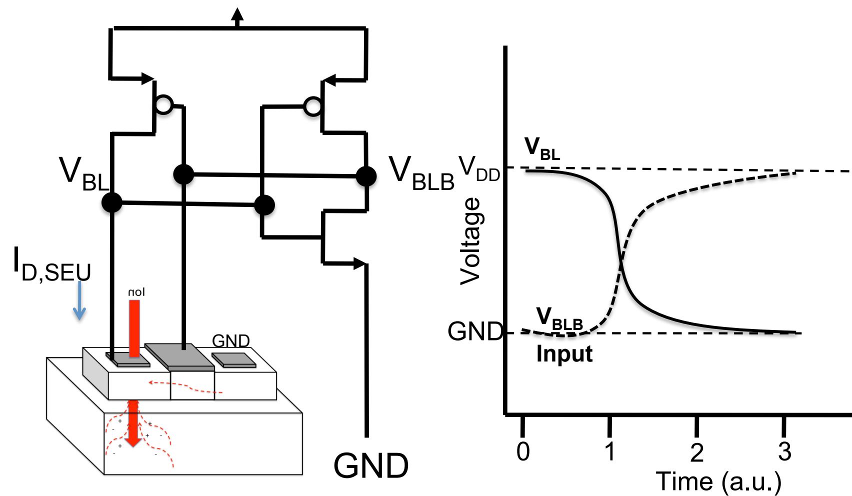

Figure 2: Simplified drawing of a SRAM cell showing ionization near the NMOS pull-down device (left). The resultant state-change that defines a single event upset (right).

Predicting SEU Rates by Particle Type

Heavy Ion Charged Particles

For the remainder of this work, direct ionization will refer to ionization of the semiconductor by the primary radiation species originating from the external or internal environment. An indirectly ionizing event is one for which a nuclear scattering process produces a secondary particle, or particles, which lead to ionization in sufficient quantity to cause SEU. For example, protons are weakly ionizing particles with relatively small LET. However, they may react with silicon or other nuclei within the die, generating a shower of recoils with substantially higher stopping power [23]. SEUs by protons (in most cases) are therefore the result of indirect ionization by the primary particle.

The rectangular parallelepiped (RPP) or chord-length model is most commonly used for predicting SEU from direct ionization by heavy ions (Z¿1) in space environments [24],[25],[26]. In the RPP model it is assumed that there is a bounded region within a device called the sensitive volume (SV) having the shape of a rectangular parallelepiped, such that if sufficient charge is generated within it, by the ion, a SEU will occur. The ion's stopping power is assumed to be constant over the path within the SV so that generated charge is the product of the LET and the chord length through the SV (3). In essence, the RPP is the dosimeter defined within the region of the circuit or device that is sensitive to ionization.

The RPP has dimensions length, L, width, W, and depth, D (Figure 3). In Figure 3, the collection of charge at the drain node of a single transistor illustrates a plausible SV location, although from an experimental perspective, it need not be limited to transistor nodes or even distinct electrically active devices. Experimental measurements of SEU cross section are used to determine the parameters of the SV, but one need not verify the specific location or mechanism to use the model for SEU rate predictions. Naturally, if one observes a discrepancy between what is physically justifiable and the parametric representation determined by experiment, the validity of the model must be questioned.

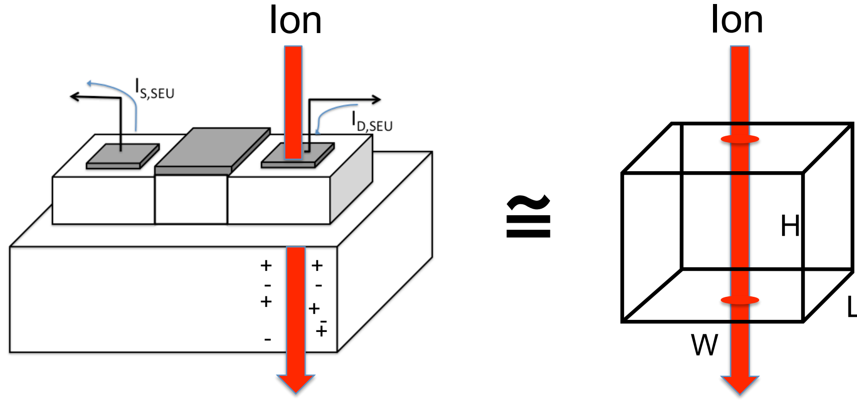

Figure 3: The sensitive volume model as it relates to energy deposition and charge generation in a device.

Keeping with (3), for any ionizing species traversing the sensitive volume, the total charge generated in the volume is the product of the LET and the chord length through it. It is assumed that the LET of the ion or ions is known at the boundaries of the volume and that the LET is constant over the length of the chord within the volume. An error condition occurs If Q_{gen} exceeds Q_{crit}. Q_{crit} can be extracted from experimental measurements [27] or circuit simulation methods. Q_{crit} is largely a function of node capacitance and restorative drive capability of the circuit for the sensitive nodes [28].

The frequency with which Q_{crit} is exceeded in the environment is the SEU rate, and is calculated using (6) where l_{max} and l_{min} represent the maximum chord length and minimum chord length capable of causing SEU, respectively. F is the integral flux of particles as a function of LET at the point of the quotient of Q_{crit} and l. p_c is the probability for the chord length for a given l, and A is the surface area of the RPP [29].

$$R = \frac{A}{4} \int_{l_{min}}^{l_{max}} F \left(\frac{Q_c}{l} \right) p_c \left(l \right) dl \qquad (6)$$

Derivation of the chord length distributions in a RPP, $p_c(l)$, for an isotropic environment is not trivial and the first known error-free equations were published by Bendel [30]. An example plot of the differential chord length probability calculated from [30] for the specific

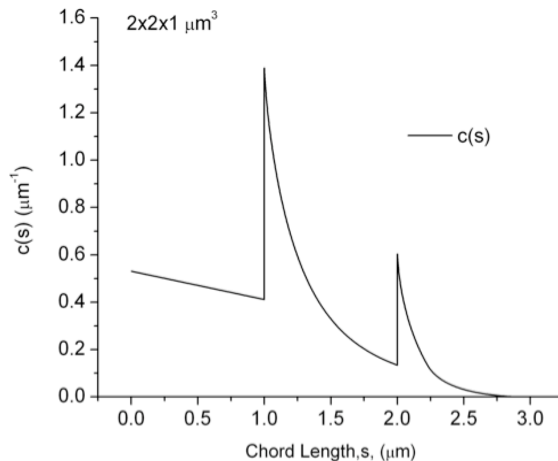

Figure 4: Differential probability of chord lengths in an RPP volume of dimensions 2x2x1 μm^3.

case of a 2x2x1 μm volume is shown in Figure 4.

The particle flux as a function of LET must be determined for the target environment. An illustration of the relationship between the flux-energy spectra over z and the combined LET spectrum (Heinrich Curve) is shown in Figure 5. The natural, known environment has been converted into the equivalent (integral) stopping power curve using CREME96 [31]. Note that the RPP model assumes, by definition, that the environmental contribution to the rate is solely determined by the LET of the ions.

RPP parameters are determined by heavy ion broad beam, testing. Various facilities exist that are suitable for performing SEU tests (e.g., Brookhaven National Laboratories [32], the Texas A&M cyclotron [33], etc.), each of which provides the tester with a high-energy collimated beam of quasi-uniform particle distribution. SEU cross sections, σ_{seu}, are measured over a range of LET. The effective cross section, is calculated according to (7) [34] where N is the number of recorded errors, Φ is the beam flux per unit area normal to the beam direction, θ is the angle formed between the DUT surface normal vector and the ion beam direction, n is an optional normalization to the number of bits (e.g., the size

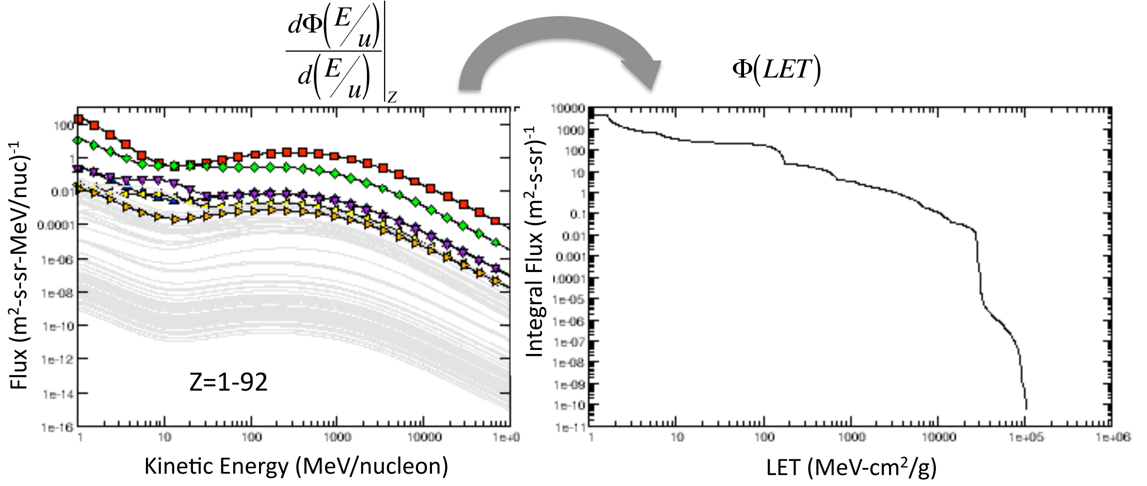

Figure 5: Differential partial flux over the combined set of species (Z) and the corresponding integral flux as a function of linear energy transfer for the geosynchronous environment during solar minimum conditions calculated using CREME96.

of a memory), and t is the exposure time. LET_{eff} is also a function of the tilt angle (θ), motivated by the increased path length ion associated with off-normal passage through the RPP. The relationship between the intrinsic LET (LET_o) of the particle and the tilt angle are shown in (8).

$$\sigma_{SEU,LET_{eff}} = \frac{N}{\Phi \cdot t \cdot cos\left(\theta\right)} \tag{7}$$

$$LET_{eff} = \frac{LET_o}{cos\left(\theta\right)} \tag{8}$$

Figure 6 contains a plot of the SEU cross section as a function of LET_{eff} for a hypothetical device. The shape of the curve is characteristic of a majority of components, especially older CMOS electronics [24]. The Weibull function is commonly used to describe the measured SEU cross section curve and is shown in (9) [34], where σ_{sat} is the saturation cross-section, L_o is SEU onset in units of LET, and w and s are more empirically based fitting parameters. An example plot of the Weibull function is shown in Figure 6.

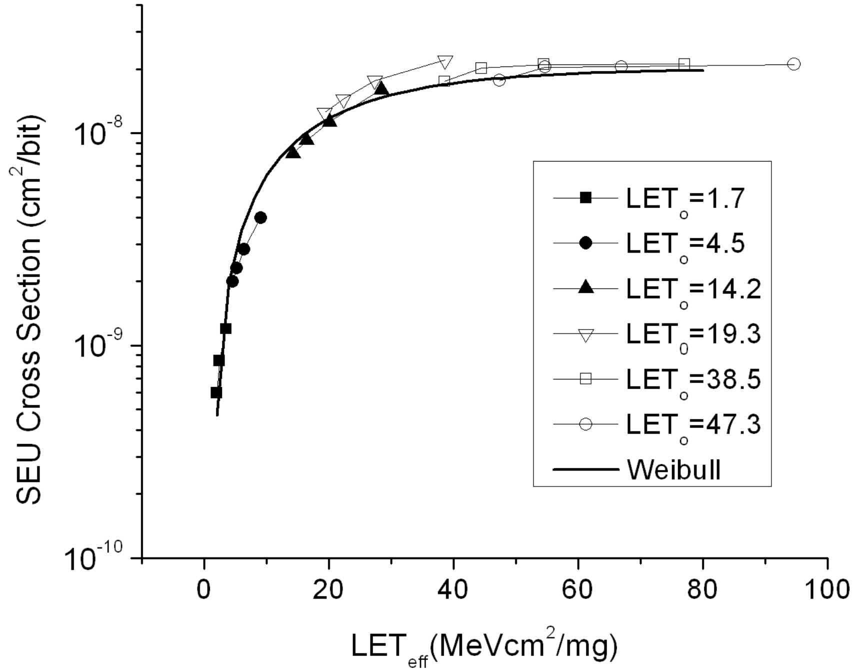

Figure 6: Hypothetical heavy ion SEU cross section curve illustrating the effect of irradiance angle for each species, including a Weibull fit to the data points.

$$\sigma_{seu}\left(LET;\sigma_{sat},L_o,s,W\right)=\begin{cases}\sigma_{sat}\left(1-\left[e^{\frac{L_o-LET}{W}}\right]^s\right) & LET\geq L_o\\ 0 & LET<L_o\end{cases}\tag{9}$$

The SEU cross sectional dependence on LET is often inconsistent with the assumptions of the RPP model (e.g., Figure 6 and data in [34]). For a fixed depth, D, and Q_{crit} the RPP model predicts a step function at the point that $D \cdot LET = Q_{crit}$ (where LET has been transformed into charge generated per path length). The non-step response of SEU cross section with LET complicates the choice of LET_o and consequently the determination of Q_{crit}.

A major refinement to the RPP model is the Integral-Rectangular Parallepiped model (IRPP). It retains all the assumptions of the RPP model except that the constraint of a unique Q_{crit} is relaxed [34]. The cross section curve is assumed to represent the cumulative distribution of the microscopic cross-sections for all individual circuits (or cells) of the

irradiated device whose variability is in Q_{crit}, although each sensitive volume is geometrically equivalent. The IRPP model is the de-facto standard for SEU rate prediction.

Distortion of the equipotential field lines along the direction of the ionization track results in enhanced carrier transport to the circuit node [15], [35]. The re-orientation of the equipotential lines resembles a funnel. Methods of transforming both effective LET [36] and the measured SEU cross section into an effective cross section [25] have been proposed. For example, (10) contains the transformation described in [36], where h is the sensitive volume depth, θ is the angle between the surface normal and the beam, L is the inherent LET of the particle, and S_f is the funneling depth (the funnel effect is shown in Figure 1. Conceptually, the funnel increases the apparent charge collection depth.

$$L_{eff} = \left[\frac{h + cos\left(\theta\right) s_f}{h + s_f}\right] \frac{L}{cos\left(\theta\right)} \tag{10}$$

Track geometry was hypothesized early in the study of SEU to contribute to differences observed between different ions and energies but of equal LET [37]. Higher energy and ionization states of the ion result in greater kinetic energy transfer to secondary electrons, which in turn increases their radial range, relative to the ions direction, before thermalizing. While the net ionization per unit path length of two ions determines LET, LET does not itself contain information about the radial distribution of how that energy is deposited. Experimental attempts at modeling the effect of track structure [38], [39], estimating the radial distribution of thermalized carriers [40], and placing the estimate within context of the sensitive volume construct [37] have been extensive and have found some integration into accepted rate prediction and modeling techniques [27], [41]. It is important to recognize that the correction terms applied to the RPP model are used to transform the experimental data, $\sigma_{eff}(LET_{eff}(\theta), \theta)$, in such a way as to make them consistent with the fundamental single-volume RPP assumption. The models do not directly alter the fundamental properties of the charge collection region.

As previously discussed, the basic RPP model has been expanded to include more detailed mechanisms such as charge funneling and the effects of ion track structure, and as will be seen, variations in individual circuit sensitivities over the entire die. Numerous comparisons between RPP-like calculations and measured on-orbit error rates support the validity of the assumptions that have been made and the fidelity of the otherwise simple model [9], [41], [42], [43], [44], [45]. However the RPP model has also been known, or has been recently shown, to have deficiencies that call its fidelity into question for certain devices and SEU mechanisms, especially at the small Q_{crit} and packing densities of modern manufacturing processes.

Linear energy transfer has been the metric against which SEU cross sections are measured. Researchers have speculated that factors beyond LET need to be considered for certain devices [39], [46], [38], [47]. Because energy loss processes include not only electronic stopping, but also electron/nuclear coulombic and nuclear reactions (elastic/inelastic processes) [29], indirect ionization can lead to SEU. An example of this effect is illustrated in Figure 7 for 523 MeV Neon ions [48], normally incident to the target surface. In the classic stopping power approximation, each particle generates roughly 35 fC of charge over the path length within the sensitive volume, however a certain fraction of the primary particles interact in such a way as to generate charge that exceeds the expected average LET-chord length product by over an order of magnitude. The production probability is small relative to the direct ionization processes, but for circuit critical charges beyond the bulk LET induced charge, they determine the SEU probability (Figure 8) and rate. The process is depicted in Figure 9 [49]. In effect, the standard RPP model, which only utilizes the point-LET value, predicts no errors beyond a critical charge of approximately 35 fC, however SEU were measured for a part known to have a critical charge in excess of 1 pC.

The RPP model assumes that a single sensitive volume is sufficient to describe the macroscopic SEU response (experiment) and the charge generated within it defines the circuit response through the Q_{crit} relationship. It has been shown through laser studies

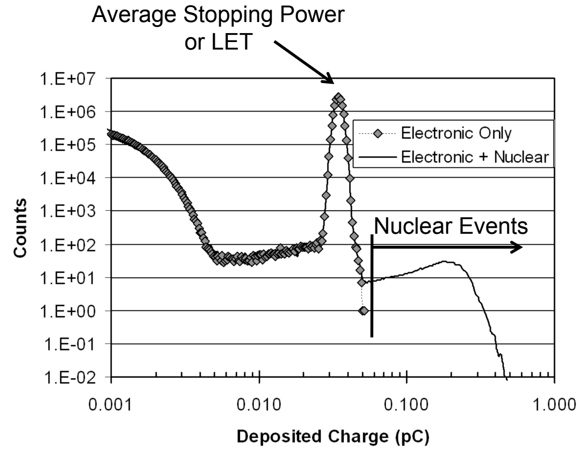

Figure 7: Calculation of the energy deposition profile of 523 MeV neon ions in a cuboidal volume of silicon with overlayers containing tungsten.

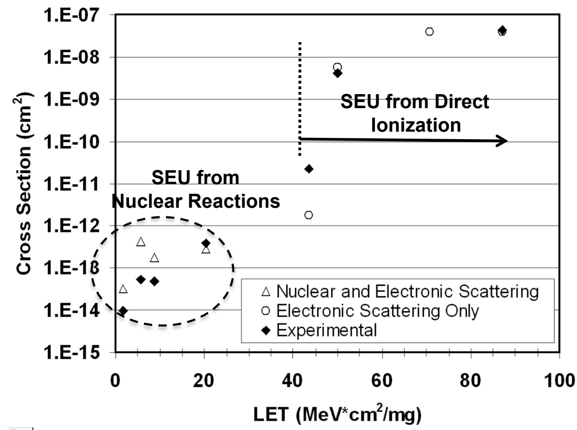

Figure 8: Effects of nuclear reactions on the macroscopic cross-section curve.

and micro-beam analyses that the amount of charge that is collected at any given node is a function of strike location with respect to that node [4], [50], [51], [52]. Further, if a circuit error can only occur by energy deposition in the vicinity of multiple transistors, or charge diffusion from a single location to multiple devices, the RPP model is not physically valid [53], [54]. In such cases as that reported in [54], the SEU cross section over angle does not follow that of (7) and (8).

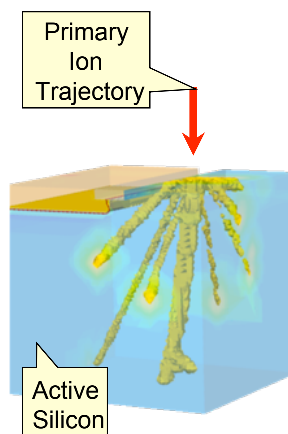

Figure 9: Fragmentation of 25 MeV/u ^{20}Ne on tungsten in silicon.

High Energy Protons and Neutrons

Protons have smaller peak and average stopping powers over energy relative to higher Z particles. However, in low earth orbit (LEO), trapping in the earth's magnetosphere produces a high flux of particles, which can dominate the SEU rate despite the relatively low probability of SEU through indirect ionization processes (e.g., nuclear reactions) [55]. Time-dependent increases in the proton flux may also be observed from increased solar activity [1], [55]. Within the earth's atmosphere, the high-energy proton flux is attenuated, but neutrons are present in relatively high abundance [3]. The high-energy proton to neutron ratio is approximately 10-1%, depending on energy and altitude [56]. Neutrons do not directly ionize the target material, but may displace ions or undergo nuclear reactions in a manner similar to high-energy protons.

Two approaches to modeling proton SEU in space exist: 1) perform a purely empirical calculation based upon a convolution of the proton cross section over energy, and the proton spectrum of the desired environment [23],[57] or 2) reduce the proton secondary spectrum to a combined stopping power curve as is done in the space environment [58], [59] and apply a model of charge generation and upset similar to the RPP model.

In the purely empirical method, proton cross sections are measured and calculated in

a manner similar to heavy ions, albeit at discrete energies rather than LET (11). Cross-Sections are typically fit to the one or two-parameter Bendel equations. The two-parameter function is shown in (12) and (13). Aside from loose physical justification for the two-parameter model in [57], it is not based upon a physical representation of the device or circuit. The fitted function, $\sigma_p(E)$, is combined with the energy spectrum of the proton environment to calculate the SEU per (14). The proton error rate is determined by integration over all flux directions, Ω, and energies, E, from the threshold energy, E_o to the maximum energy in the environment, E_{max}, for differential particle flux, $\frac{\mathrm{d}\Phi}{\mathrm{dE}}$ [3].

$$\sigma_{p,SEU}\left(E_i\right) = \frac{N}{\Phi\left(E_i\right) \cdot t \cdot n} \tag{11}$$

$$\sigma_{p,SEU}\left(E\right) = \left(\frac{B}{A}\right)^{14} \left\{1 - e^{-0.18Y^{0.5}}\right\}^{4} \tag{12}$$

$$Y = \left(\frac{18}{A}\right)^{0.5} \left(E - A\right) \tag{13}$$

$$Rate = \int_{\Omega} d\Omega \int_{E_o}^{E_{max}} \sigma_p\left(E\right) \frac{\Phi_p\left(E\right)}{dE} dE \tag{14}$$

Alternatively, physics-based transport codes such as CUPID [60], [61] and GEANT4 [62], have been used to generate LET spectra of the secondary species. Once a suitable transformation is calculated, the error calculation proceeds in a manner similar to the RPP model. The usual RPP limitations apply, and the recoil products from the reaction are assumed to be isotropic.

Cosmic ray neutrons, in the energy range of approximately a few MeV to many GeV, cause SEUs through indirect ionization processes similar to that of protons [10]. They originate from the interaction of GCRs with elements in the earths atmosphere [63]. The heritage of atmospheric and terrestrial neutron SEU begins in the late 1980s, with Boeing and IBM who performed a joint study demonstrating neutron SEU in-flight from dedicated avionics

test bests [11]. The measurement of neutron induced SEU is part of commercial parts qualification when reliability levels must be guaranteed [64]. Three approaches to cosmic ray neutron SER prediction have gained acceptance in the community: the burst generation rate method, mono-energetic proton testing, and white-spectrum neutron testing; with the last two called tests because they are entirely empirical in nature.

The burst generation rate (BGR) method for estimating SER rates in avionics and ground-based systems was first introduced by Ziegler and Lanford [2], and refined by Normand [3]. The BGR method provides an estimate to the rate at which Q_{crit} is exceeded within a RPP-like volume from the burst production of particles from a neutron (or proton)-Si reaction. The BGR Rate calculation is shown in (15), where C is the charge collection efficiency, t is the sensitive volume thickness, $\Delta\sigma$ is the difference between the cross section of the ith and $(i-1)^{th}$ heavy ion cross section, LET is the recoil particle LET at the point of evaluation (i), and J is the particle flux. The integration is performed over all particle energies, E, in the spectrum. The BGR function in the integrand is the rate at which a proton or neutron of energy, E, exceeds the critical charge (given by $0.23t \cdot LET$). The BGR method is an early proposal for correlating direct ionization cross-sections and circuit response with secondary particle production driven mechanisms.

$$Rate_{BGR} = C \sum_i t\Delta\sigma_i \int BGR\left(E, 0.23t \cdot LET_i\right) \left(\frac{dJ}{dE}\right) dE \qquad (15)$$

Terrestrial and atmospheric neutron rates can be determined by the measurement of mono-energetic proton SEU cross sections [64]. Mono-energetic protons are easier to generate than neutrons because they are charged and can be focused (e.g., bending magnets). It is assumed that the neutron and proton SEU cross sections are equal at the same energy due to the similarity of the means by which they interact with the nuclei of the target material. Data are fit to a suitable function (e.g. Weibull or Bendel) the calculation proceeds in a manner similar to that of (14).

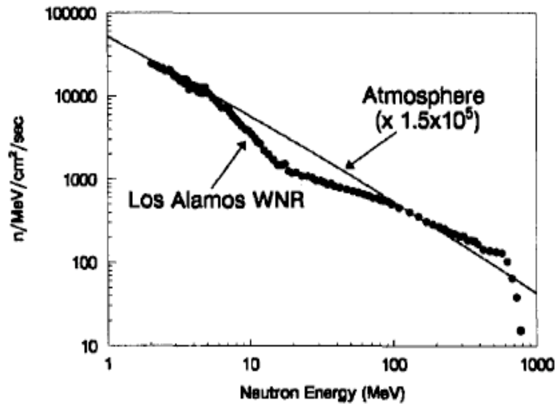

Figure 10: Los Alamos WNR/ICE House neutron spectrum compared to atmospheric rate (40,000 feet), scaled by a factor of 1.5×10^5.

An alternative empirical method for predicting cosmic ray neutron rates is by direct measurement of the rate at a white neutron source, such as that at the ICE House facility of Los Alamos National Laboratories [65]. Irradiation of a tungsten target by high-energy protons produces a distribution of neutrons whose relative energy spectrum is similar to that found in the earth's atmosphere. A comparison of the accelerated flux over energy for the beam, and the scaled atmospheric flux, are shown in Figure 10. The benefits of this approach over the mono-energetic proton testing are that it does not require any limiting assumptions about the equivalency of neutron and proton recoil distributions and the calculation of the atmospheric rate is related to test rate by a scale factor (e.g., 1.5×10^5 at 40,000 feet). Researchers have shown this approach to be in good agreement with rate predictions made using the mono-energetic proton method [66] and by direct comparison to measured ground-level SEU rates [67].

The purely empirical methods of predicting proton and neutron SEU rates assume, to first order, that the distribution of recoil products is isotropic and independent of energy. Thus, the relationship between the trajectory of the proton or neutron and the device is irrelevant. This is implicit in the application of the one- and two-parameter Bendel fitting models and the method most familiar to the space community for proton testing. The

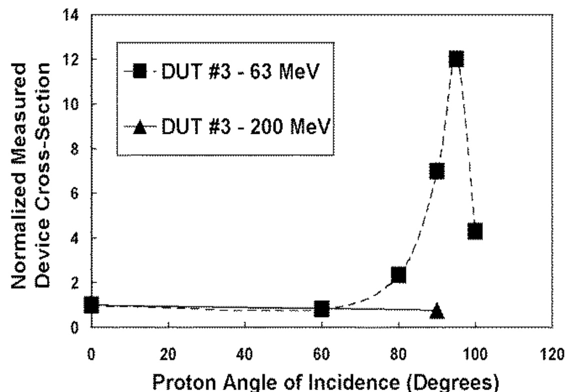

Figure 11: The directional dependence of the proton beam relative to the device surface and the measured cross section curve in the low energy ranges.

assumptions of isotropic SEU response are technically incorrect [68] and proton testing has shown strong angular dependency as a function of proton energy for some technologies, such as the work performed by Reed, et al. on silicon on insulator (SOI) and silicon on sapphire (SOS) memories, shown in Figure 11 [61]. In such cases, the experimentalist may either select the worst-case unidirectional SEU cross section and use it in the Bendel calculation for a conservative estimate, or attempt to generate a differential SEU cross section (over a range of solid angles) which can be used to calculate the rate against the environmental spectrum. In either case, the experimentalist cannot quantify the isotropic response, or have any reasonable expectation of it, without measurement. Mono-energetic proton and neutron rate prediction methods do not account for potential angular effects.

For predicting the cosmic ray neutron SEU rate from mono-energetic proton testing, one must assume that proton and neutrons interact in a similar manner with nuclei of the target device. For devices with pSEU thresholds above 20 MeV this approximation is reported to be satisfactory. Lambert, et al. [69] have recently compared proton and neutron cross sections for a variety of bulk CMOS devices and found that after proper correction of the neutron tail (an artifact of the neutron production process), cross sections were in good agreement between the two down to 20 MeV for parts having Q_{crit} in the 3-70 fC range

($0.18 - 0.5\ \mu m$ technologies), although it is not clear that the neutron or proton threshold was determined for both species.

In the low energy regime the assumption of proton-neutron equivalency is not valid. A simple calculation of the coulombic forces, per (16), shows that it takes approximately 5 MeV for protons to overcome the repulsive force associated with a proton incident on a silicon nucleus. In this regime, proton and neutrons on silicon clearly do not interact in an identical manner. The overall effect the difference has on predicting SEU rates from mono-energetic proton testing is still being considered [70].

For components with very low critical charges, Coulomb scattering and energy loss by the incident proton at any energy can lead to SEU by direct ionization, and the equivalency model can potentially fail over a much broader range of energies. Research in this area is ongoing and presents technical challenge to experimentalists and to the process of SEU rate prediction in space environments. To date, direct ionization by protons has been observed in sequential logic with very small $Q_{crit}(\sim 1\ fC)$ [71].

$$E \simeq 1.1\ MeV \cdot \frac{Z_1 Z_2}{A_1^{\frac{1}{3}} + A_2^{\frac{1}{3}}} = \frac{1.1\ MeV \cdot 14}{1 + 28^{\frac{1}{3}}} = 5\ MeV \tag{16}$$

Thermal Neutrons

Thermal neutrons ($\sim$ 26 meV) are abundant at ground level and can be found near moderating materials (concrete, water, or the earth itself). They can also cause SEU through neutron capture by elements in the semiconductor, which subsequently decay. The effect is most prevalent in processes containing boron where neutron capture reactions by ^{10}B produce energetic alpha and lithium recoils, $^{10}B(n, \alpha)^{7}Li$. The reaction is both relatively high in cross-section and both the lithium ($\sim$ 0.84 MeV) and alpha particle ($\sim$ 1.47 MeV), emitted at 180°, can cause SEU over several microns from the point of the reaction [72]. ^{10}B is a naturally occurring isotope of boron and has a natural abundance relative to all Boron isotopes of approximately 20%.

Boron is used in the formation of borophosphosilicate glass (BPSG), a historically common material used in reflow/planarization in semiconductor processing and is in close physical proximity to the active semiconductor regions. The maximum possible charge generated in silicon by the lithium and alpha particles from the $^{10}B(n,\alpha)^{7}Li$ reaction is approximately 37 fC and 65 fC, respectively. Consequently, thermal neutron SEU became an increasing concern through the 1990s, as circuit critical charges became smaller. The increasing reliability concern has motivated many manufacturers to move away from the use of BPSG.

Boron is also used as a p-type dopant and may be found in concentrations of approximately 10^{21} cm^{-3} in source/drain implant regions, in which its concentration is comparable to that of BPSG [73]. Recent studies have demonstrated that implantation involving ^{10}B and the possibility of SEU from thermal neutron capture is a viable reliability threat [74].

Thermal neutron SEU rates are determined by measurement at a suitable thermal neutron source (e.g., National Institute of Standards and Technology). The experimentally measured rate is scaled by the expected abundance of thermal neutrons in the operating environment relative to the thermal neutron beam flux. The test method is straightforward and allows one to directly calculate the SEU rate. Like other purely empirical methods, it does not provide insight into the mechanism of SEU and measurements made at thermal neutron facilities cannot be used to deduce error rates from other radiation sources.

Alpha Particles

Alpha particle-induced SEU from the decay of contaminant elements (or isotopes of non-contaminants) have long been recognized as a reliability concern by the commercial industry, dating back to the pioneering work of May and Woods [7]. Alpha particles are emitted either from the die encapsulate (or die package)[75], from solder [76], or from the basic constituents of the die manufacturing process [77]. Common contaminants include uranium, thorium, and lead. Recent advances in packaging methods utilize extensive solder bonding in and around active silicon structures due to the need for a large number of signal

paths into and out of the die where proximity of the solder bonds to active devices increases the susceptibility of those structures to SEU [78].

Standard practices for testing electronics against alpha sources are outlined in the JEDEC standard JESD89A [64]. Direct exposure of the die by a thin or thick alpha emitting source, commonly ^{241}Am, ^{232}Th, or ^{238}U is used to determine the error rate as a function of the test source activity. This rate is then scaled by the activity of the package material.

A general expression for the overall error rate from alpha particles on a chip is given by (17) [7] where A is the area of the unit cell (e.g., DRAM), N is the number of cells in the device, Φ_{oa} is the flux of alpha particles emitted from the source's surface, and S is the sensitivity factor. S is the average cross section calculated by (18). In this early work, A_{stor} was assumed to be the overall drain/source diffusion node area. The integral for the computation of S is performed over the normalized energy spectrum, $N(E)$, and the cross section at that energy, σ_a. The difficulty in the calculation is with the determination of $\sigma_a(E;Q_c)$. May and Woods used an early form of Monte Carlo simulation to estimate $\sigma_a(E;Q_c)$.

$$Rate_{\alpha} = A_{cell} N_{cell} \Phi_{oa} S \tag{17}$$

$$S \equiv \left(\frac{A_{stor}}{A_{cell}}\right) \int_0^{\infty} \sigma_a\left(E;Q_c\right) N\left(E\right) dE \tag{18}$$

Other analytic models have been published that provide a more detailed treatment of charge transport [79], [80], including field funning and drift. Both models employ concepts from the May and Woods manuscript, as well as attributes of the modified RPP models (e.g., funnel length).

Alpha emission is inherently isotropic, and common contaminants or their decay products can emit alpha particles between approximately 1 and 10 MeV [81]. While the higher energy alpha particles may have ranges as high as 70 μm in silicon, the most abundant

emissions fall at approximately 5 MeV with a range of less than 30 μm. The presence of air, passivation, and back-end-of-line (BEOL) materials can dramatically alter the stopping power of the alpha particle in and around the active regions of the circuit. Assumptions of infinite range and constant stopping power are not valid, especially when taken into consideration with the particles being emitted isotropically. The thickness of the emission source can also produce an energy-spreading upon leaving the surface of the source.

A significant problem with relating experimental measurements to operational SEU rates is the process correlating the activity rate and alpha energy spectrum of the test source with that of the package and other manufacturing contaminants. Modern package activity levels can be very low (0.001 $cm^{-2}hr^{-1}$) [82], making it not only difficult to quantify the materials activity level, but also economically unfeasible to estimate the energy spectrum. While lowering the activity level through purification of the packaging materials, by a choice of alternative solder materials [83], or by the use of encapsulants [75], reduces the error rate for a given technology, the trends of decreasing Q_{crit} and increased packaging density make any level of alpha emitting contaminate a reliability concern [84]. Efforts are on going to establish a suitable relationship between test conditions, package activity levels, and energy spectrum of the source contaminants.

Factors Affecting Charge Collection and Circuit Response

Intra- and Inter-cell Variations

Multiple researchers have contemplated the mechanisms leading to the fine structure of the heavy ion cross-section curve. Petersen, et al. [34] enumerate three candidates of device (transistor, cell, or chip-level) response, which are still appropriate today: 1) variations of critical charge, 2) variations of collected charge and 3) variations of sensitive area. A detailed treatment of all the published mechanisms and their appropriate taxonomy within the three items enumerated above stands alone an entire body of work. However, examples

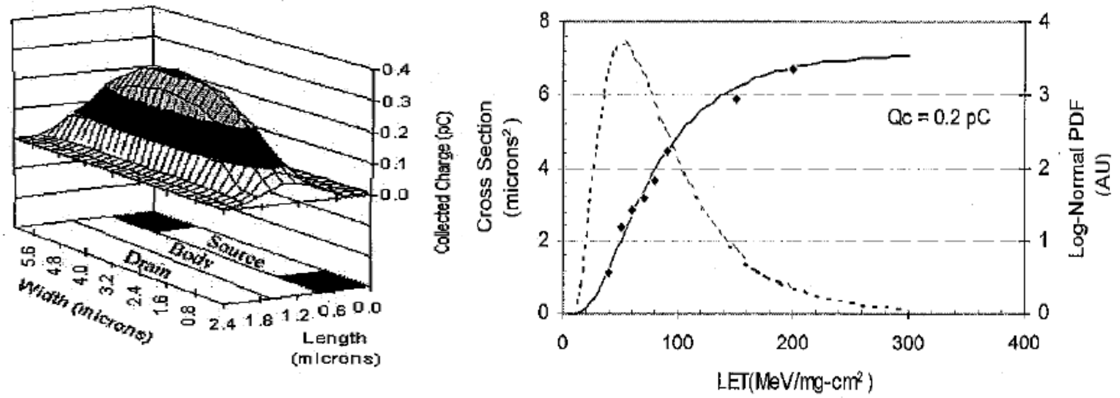

Figure 12: An illustration of the charge collection profile as a function of strike location on a body-tied SOI NMOS transistor (left) and the resulting SEU cross-section curve (right).

of each will be briefly presented within the context of the structure of the heavy ion SEU cross section curve and SEU rate predictions. Inter- and intra-cell variability can be loosely defined as any microscopic variability within a unit cell (e.g., SRAM bit) or between unit cells (array of bits) that affects the macroscopic SEU cross-section.

Intra-cell variability arises from localized differences in SEU sensitivity over a single unit cell, be it from charge collection by multiple transistors within the unit cell or variations in sensitivity over the surface of a single transistor, such as that arising from parasitic bipolar gain in SOI structures [85]. The functional dependence of strike location on charge collection in a single SOI transistor is shown in Figure 12 (left) and the effect it has on the predicted cross section curve (right) [86]. Charge diffusion affects the efficiency with which charge is collected at circuit nodes, recognizing by intuition that strikes farther from the node responsible for charge collection will result in less collected charge (ignoring drift effects and possible parasitic mechanisms) [8]. The IRPP model cannot account for the variations in charge collection efficiency over the surface of an individual cell. Extensive experimental studies have shown that circuit sensitivity is a function of the strike location [4], [50], [52], [87], [88].

Inter-cell variability is from differences in SEU sensitivity between two otherwise identically designed cells that occurs from normal process variations over the die surface [89]. Assuming that the shape of the heavy ion cross section curve arises from inter-cell variations alone is particularly convenient for SEU rate calculations in which one can consider distributions of critical charges for sensitive volumes of equal dimensions. For example, the IRPP model indirectly accounts for inter-cell variability by assuming that the Weibull (or log-normal) distribution function fit to the SEU cross section data represents the cumulative density function of critical charges [25]. It retains only one geometrical entity, the sensitive volume, whose dimensions do not vary between cells. The chord length distribution need not be recalculated at each point in the distribution.

Single-particle Multiple Node Effects

A single primary particle (and possibly recoil products) may affect multiple transistors via the sharing of charge (e.g., via diffusion) or from localized ionization in multiple regions. This is a requirement for SEU in certain circuits, especially those that are designed to be immune to single event upset. An early, if not the first, conclusive example of charge sharing as a mechanism of SEU in hardened circuitry (dual-interlocked cell or DICE design) was presented by Velazco, et al. [53], where the authors demonstrate that large amounts of charge injection can cause multiple nodes to be perturbed from a single ionizing event. A conceptual drawing of a multi-node SEU mechanism is illustrated in the left-hand side of Figure 13. In this hypothetical case, the condition of the Data line is perturbed only if both OUTA and OUTB are driven into a logic zero condition, which can only be achieved if a single particle passes near A and B transistors. The result is a highly directional SEU response over 4π, which peaks in the direction of the line segment that passes closest to the two sensitive nodes. The heavy ion SEU cross section curve for a part with this type of mechanism is shown in the right-hand side of Figure 13 [54]. The effective LET does not uniquely define the cross-section and the potential bounds over which one might perform a

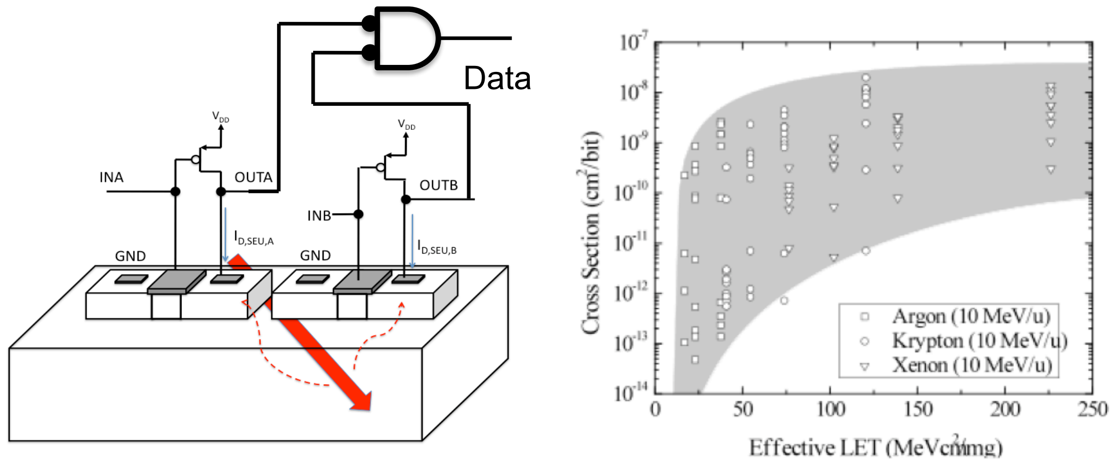

Figure 13: Illustration of the multi-node SEU process (left). SEU Cross section curve for a radiation hardened DICE latch (right).

Weibull-fit (using the IRPP method), and consequently the single volume methods cannot be used. Similar mechanisms have been observed by the activation of parasitic conduction paths by charge deposition in the n-well of multiple PMOS transistors, which also serves to increase the probability of N-PMOS charge sharing [19],[90],[91].

Edmunds has proposed an analytic multi-volume solution for modeling the heavy ion response of DICE circuits, although it is limited to two-node groups [92]. Likewise, Fulkerson, et al. have used a form of the multiple volume concept to derive analytic solutions to the on-orbit SEU rates for SOI devices [93]. Warren, et al., have demonstrated the necessity of allowing coupling between multiple combinations of transistors in DICE circuitry to accurately model the heavy ion response for which there are multiple combinations of Q_{crit} [54].

Single-particle Multiple Bit Effects

Multiple Bit upsets or MBU, are a concern in both terrestrial and space environments. They occur when a single quantum of radiation alters the state of multiple bits (e.g., SRAM,

DRAM, etc.). If primary or secondary particles have sufficient range, they can pass in proximity to active regions of multiple bits or cells. The decrease in feature size, and increase in packing density that arise from technological advancements in lithography and manufacturing increase the probability of MBU, both from a geometrical and charge transport perspective. MBU warrant special concern because of the difficulty in measurement [94], modeling and rate prediction [95] as well as mitigation in high reliability systems [96]. MBU have been reported in experimental measurements for all types of ionization radiation (neutrons [97], protons and heavy ions [98], alpha [64]), as well as being observed in spacecraft [99].

Single-bit errors, through the use of error detection and correction (EDAC) methods or degenerate signal paths (triple modular redundancy or TMR [100]), can either be detected and/or corrected. MBU, however, are more difficult to detect when they occur within a single word in a multi-bit array. For this reason, they are problematic at not only the device and circuit level, but at the chip level. Although EDAC circuitry can be made to correct two-bit (or more) errors within a single word, it introduces substantial overhead in terms of die area, access times, or scrubbing rates. Note that thirteen errors from a single primary event have been reported in advanced CMOS devices [96]. MBU sensitivity is often orientation dependent with respect to the incoming particle [99], [101], complicating both the test campaign and the MBU rate prediction itself.

Analytical methods for estimating multiple-bit SEU rates have been derived by Martin, et al. [102], and by Edmunds [103], where the former considers the ion track radii for normally incident ion induced two-bit upset, and the latter provides a general mathematical framework for two arbitrarily distributed RPP without track structure effects. Neither model can be generalized to an arbitrary number of cells, which is clearly required given the complexity of the spatial pattern, particle-device orientation dependence, and frequency of multiple bit errors reported in [99], [96], [101].

Circuit Effects

The concept of critical charge is ubiquitous throughout the models for both space and terrestrial rate predictions, although its usage is problematic for two reasons: 1) Like charge transport, the physical response of any circuit is time dependent to some degree and 2) Circuits are composed of multiple transistors and hence there are many circuit nodes, which may or may not be sensitive to charge collection depending on the state of the circuit at the time of the event. Measured SEU cross sections are the average of the response of all processes occurring and attempting to understand and quantify the SEU response can be complicated by the dynamics of the circuit. Furthermore, recognizing when an SEU has occurred can be an extreme challenge for the experimenter in larger designs such as microprocessors and gate-array devices, complicating the design process if improved SEU performance is required by the manufacturer.

To enhance the analysis of SEU beyond the simple one- and two-transistor charge collection models presented through this text, researchers have used circuit and logic-level simulation. Circuit level simulation (e.g., Spice) is analog in nature and can be used to follow the propagation of transient signals, such as those introduced by single events, and identify the circuit-level mechanisms of SEU. Circuit level simulation is often used when the complexity of the SEU response goes beyond that of a single-particle/single-bit flip and the details of the signal propagation (such as in combinational logic) are of particular importance [52], [104]. Hybrid methods, which combine critical circuit-level attributes (e.g., capacitance) with high-level logic-level descriptions of fault injection have also been proposed for combinatorial logic [105], [106], [107]. Fault injection techniques for analyzing SEU propagation in both combinational and sequential logic for large field-programmable gate arrays (FPGA) [108] and microprocessors [109] have been reported. Circuit, hybrid, or logic-level only simulators are not immediately practical for direct SEU rate computations, as they do not directly contain information about the probability of the internal fault being generated, aside from rough calculations of node areas based on the technology being

evaluated.

Conclusions

The RPP model establishes the concept of a single fixed dosimetry region that determines the amount of charge that is generated in silicon from an ion strike. RPP dimensions are determined by experiment measurements of SEU cross section over ion beam angle (with respect to the device) and LET. The IRPP model is based upon the single sensitive volume concept, but includes a probability distribution function that defines the probability of Q_{crit} over an array of otherwise geometrically identical cells. The probability distribution is also determined during the course of heavy ion broadbeam experiments. The RPP model does not capture inter-cell or inter-transistor level dependencies of ion strike location on SEU cross section that have been observed and reported in the literature. For SEU rate calculations, the RPP and IRPP model are dependent on the analytical chord length probability functions in a single rectangular volume, where the chord length represents an ion's path through the volume, and assumes a constant LET over that path.

The RPP model and its variants are not applicable to predicting SEU rates for circuits that require simultaneous charge generation and collection on multiple transistors to upset. Mechanisms of this type will be shown to produce heavy ion SEU cross section data that exhibit strong angular dependence on beam direction. Coincidence requires two physically separate regions be struck, which naturally suggests that more than one dosimetry region is required.

SEU rate prediction and modeling in environments other than the inter-planetary space require measurement of the response of the device being tested in that environment, or a subset of it. Examples include high energy protons for the trapped proton environments in the earth's magnetosphere, and neutrons and alpha particles in terrestrial environments. The approaches (e.g., Bendel/Mono-energetic proton testing and JESD89A) are purely empirical and are disjoint between particle types. High-energy proton testing is subject to

the limitations of the accelerator facility, and for predicting high-energy neutron SER, an approximation that breaks down in the sub-25 MeV range. Consequently, models that are capable of investigating and quantifying discrepancies between accelerated test environments and operational environments are warranted.

CHAPTER II

THE MULTIPLE SENSITIVE VOLUME MODEL

Introduction and Problem Statement

Within the RPP model, it is assumed that the relationship between the energy deposited by an ion, the charge collected at the circuit node, and the SEU cross section are described in terms of a single dosimetric region. It does not capture intra-cell variations in charge collection efficiency. For example, Figure 14 contains the collected charge as a function of strike location for a simple n^+ diffused region in an active silicon island above a silicon substrate, as determined by TCAD analyses for an ion with an LET of 0.10 $pC/\mu m$[1]. The doped regions forms a junction that is tied to a contact through which charge is monitored and integrated over time. Each TCAD solution represents the total collected charge for an ion at that position at normal incidence to the surface of the TCAD structure.

If it is assumed that the RPP reflects the extent of the charge collection region, one potential choice of RPP parameters has a single collection region centered about the collecting node, extending to a depth, in this example, of 0.75 μm. The corresponding σ_{SEU} for all possible $Q_{crit} \geq 80\ fC$ is approximately 0.04 μm^2 at LET $\approx 10\ MeV cm^2/mg$ or 0.10 $pC/\mu m$.

However, for $Q_{crit} < 10\ fC$, at normal incidence and the same LET, the RPP still predicts a SEU cross section of 0.04 μm^2, whereas the actual SEU cross section would increase as more physical area becomes sensitive. Naturally, one could approximate the response in this region by increasing the lateral RPP dimensions, but this would over-predict the cross section at lower values of LET. While an acceptable single point solution for a fixed LET can be achieved, the single volume RPP model cannot be made to accurately capture

[1] For the remainder of this document, when LET is expressed units of $pc/\mu m$, it is understood to be in silicon. The calculation is shown in Chapter I, Equation 3

the functional dependence of the collection volume dimensions (i.e., SEU cross section) on particle LET.

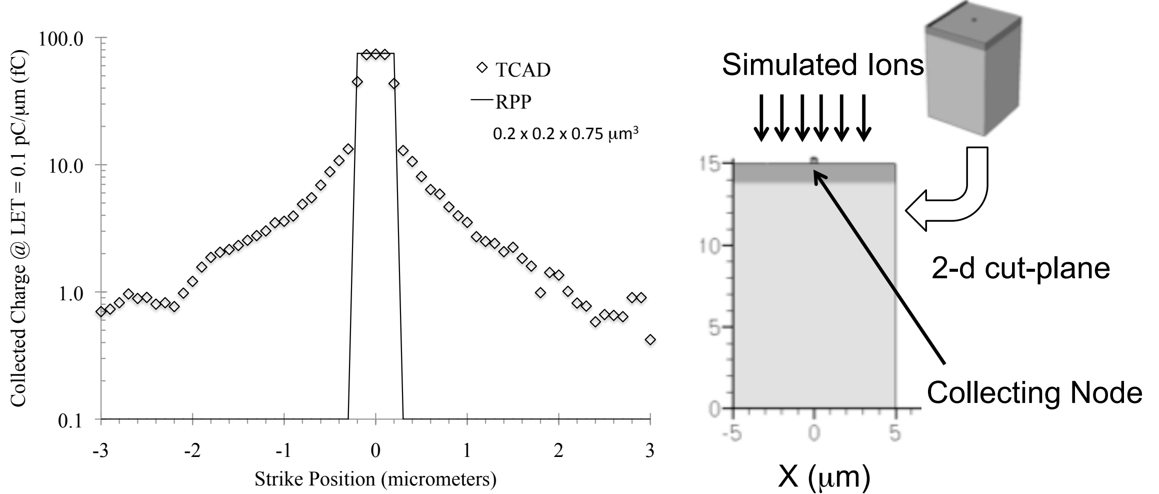

Figure 14: Three dimensional simulation of charge collection over a singly diffused device surface as a function of strike location at normal incidence.

To further illustrate the problem, the SEU cross section curve arising from Figure 14, assuming a 0.2 x 0.2 x 0.75 μm^3 RPP, for a range of Q_{crit} is shown in Figure 15. Note that the singular RPP model predicts an abrupt rise in σ_{SEU} at the point at which $Q_{coll} \geq Q_{crit}$, but σ_{SEU} has no functional dependence on LET aside from the point at which the Q_{crit} condition is met. This is inconsistent with common experimental observations, which show that σ_{SEU} changes in a continuous, usually monotonically increasing, manner with LET.

Previous works (e.g., [13]) have demonstrated that this is due to an increase in the area of the device or circuit that is sensitive to SEU with ions of progressively larger stopping powers (e.g., [85]). It will be shown that there is approximately a linear increase in collected charge with deposited charge over the device surface, which accounts for the increase in SEU cross section, or σ_{SEU}. More precisely, the change in collected charge with LET is approximately linear at a given LET.

An improved model, which approximates the process of charge generation, transport,

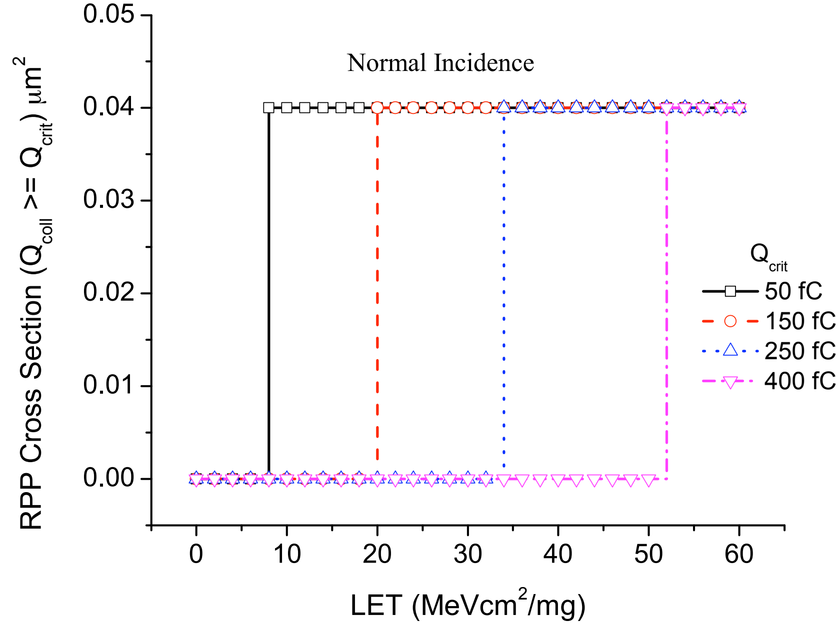

Figure 15: Example SEU cross section curves at normal incidence for a 0.20 x 0.20 x 0.75 μm^3 sensitive volume as a function of LET and critical charge.

and collection is required to better represent the physical mechanism by which ionization leads to SEU. The model must not only include spatial variations in charge collection efficiency with respect to the surface normal (as shown in Figure 14), but also include the proper response over all ion trajectories and positions with respect to the collecting node. Further, the model must reflect the functional dependence of collected charge on the ion's stopping power.

Proposed Solution: The Multiple Sensitive Volume Model

The RPP model represents a single dosimetric region that maps deposited energy (equivalent to generated charge) to collected charge, but it cannot capture the spatial variation in charge collection efficiency as a function of the location of ionization with respect to a transistor (or multiple transistor) node. The proposed solution to this problem is to incorporate additional RPP with individually assigned collection efficiencies, placed at suitable relative

locations, to approximate the total collected charge by an individual transistor. Spatial aspects are reflected in the relative placement and size of the volumes, and the magnitude of collected charge with respect to the generated charge is determined by their individual efficiencies. The problem of determining computational solutions to (correlated) chord length distributions in the multiple sensitive volume model is overcome by approximation using Monte Carlo methods (Appendix B).

$$Q_{coll} = \sum_{i=1}^{N} \alpha_i Q_{gen,i} + \sum_{i=1}^{N} \sum_{j=1}^{N} \gamma_{ij} Q_{gen,i} Q_{gen,j} + ... \tag{19}$$

The mathematical description of the multiple sensitive volume model is shown in (19), where Q_{coll} is the collected charge for a single ion event, and $Q_{gen,i}$ is the charge generated in the ith volume. The first and second order efficiency parameters are α and γ, respectively. The summation is taken over the total number of volumes, N, that describe the transistor or device node. Higher order efficiency terms are possible but are not shown. Each value of Q_{gen} is a function of the stopping power of the ion or ions that enter the individual volume, the size of the volume, and the position and direction of the ion as it enters and passes through (or stops) within the volume. Recognize that Q_{coll} is for a *single event* but multiple particles may contribute to the total collected charge. This statement is not contradictory in that a single particle may arrive at the device, but undergo some form of interaction with the material, and produce multiple secondary particles. Thus, the *event* refers to the single particle originating from a pre-defined environment, which may or may not produce multiple secondary ionizing species.

For the remainder of this work, only first order contributions to (19) are considered, and the multiple sensitive volume concept is treated as a linear summation of the weighted energy deposited within the volume set, shown in (20). Nonlinear terms may have applications in cases where coupling between adjacent junctions, such as single event latchup (SEL), is required to produce the measured effect, or in the case of simple charge collection, to

account for nonlinearity in the relationship between Q_{coll} and Q_{gen} or LET.

$$Q_{coll} = \sum_{i=1}^{N} \alpha_i Q_{dep,i} \tag{20}$$

The traditional RPP model is the simplest case of (20), in which there is a sensitive rectangular volume having an efficiency, α_1, equal to unity. The charge generated by the ion within the volume (in the form of the chord length-LET product) translates directly into collected charge and is shown in (21).

$$Q_{coll} = \alpha_1 Q_{dep,1} = Q_{dep} \tag{21}$$

Equation (19) allows for a highly flexible model of describing the relationship between energy loss by an ion and charge collected at a transistor node. The added flexibility introduces additional degrees of freedom that scale with the number of volumes and complicate the process of determining the sensitive volume parameters. For example, each volume can can described by minimum and maximum vertices and a respective alpha, for 7 total degrees of freedom per volume. It is beneficial to use what is known in terms of charge transport in semiconductors as a function of charge generation and the location of collecting nodes to constrain the sensitive volume parameters. The remainder of this work will emphasize the *nested* physical arrangement to describe the process of charge collection from the substrate combined with physically separate volumes for terminal junction regions.

Nested Sensitive Volumes

Nested sensitive volumes are a unique configuration in which each volume is sized and positioned to be contained entirely within the next larger volume. They are not required to be arranged in a concentric fashion, and may share faces and edges. The nested configuration is particularly useful in that it is a convenient way to approximate the process of charge diffusion in the silicon substrate to a collecting node, which is generally at a single point or

geometrical face, such as the plane of a source/drain junction boundary.

The configuration is intuitively appealing in that it describes the charge collection efficiency as a function of distance to the collecting node where points further from the node are less efficient relative to those in closer proximity. A graphical illustration of the effect of nesting sensitive volumes is shown in Figure 16. Because the charges within individual volumes are combined in a linear fashion and each are independent by definition, Q_{coll} is equivalent to the summation of weighted chord lengths (ultimately multiplied by LET), where the weight is the charge collection efficiency parameter, α. The result is the composite image illustrated on the left of Figure 16. The β term is a description of the net efficiency in the specific region of space that results from the combination of all sensitive volumes in that region. It is important to stress that the β is the actual efficiency of charge collection at the point (or region) in the semiconductor. The use of β arises from the geometrical constraint of the sensitive volumes being solid cuboidal entities, rather than cuboidal shells. Figure 16 is an illustration of the case when the ion does not stop, change direction, or its LET does not vary appreciably as it passes through the volume set. This is not an inherent limitation of the model, but only of the as-drawn illustration.

Another example of a nested volumes sharing *top* and *bottom* planes (z) is shown in Figure 17. The innermost region, V_1, extends, in the two-dimensional projection, between $-x$ and $+x$ and is entirely contained within V_2 through V_4. In this figure, α does not increase monotonically with decreasing distance relative to the center of mass of the nested volume set. However, the net or cumulative collection efficiency, β, increases at a rate determined by the composite of all α. In this manner, the result of the summation is largest for charge segments generated near the center of the sensitive volume groups, and conversely, smallest for charge generated distal to the node.

The nested sensitive volume arrangement provides a general constraint for the placement and sizes of sensitive volumes. However, at this level alone, it does not technically provide any reduction in the number of degrees of freedom in the model.

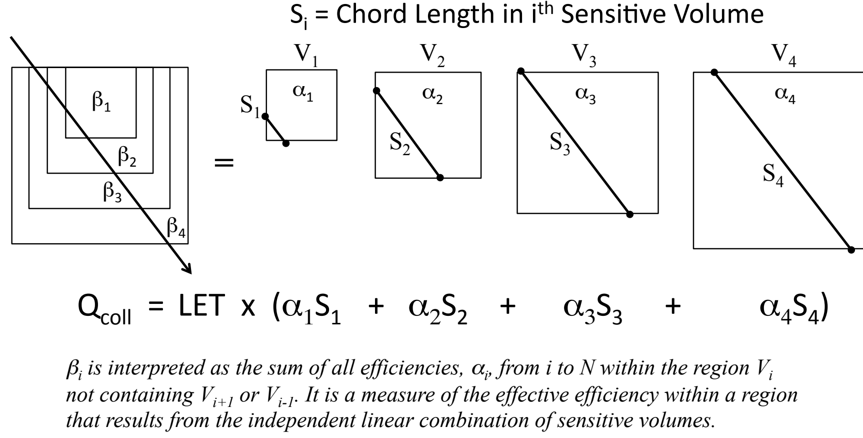

Figure 16: Conceptual illustration of the nested configuration of sensitive volumes.

Parameterization of Nested Sensitive Volumes

In certain instances, it is desirable to parameterize the nested volume group; that is, to define a functional relationship between the parameters of each volume within the multiple-volume group. A parameterized approach reduces the overall parameter space required in the calibration phase, though it may introduce unacceptable limitations depending on the application and geometry of the structure being analyzed.

An example function that is used throughout the remainder of this chapter to parameterize nested sensitive volume models is given by (22), where β_o is the peak cumulative collection efficiency of the innermost volume, which decreases with increasing distance (x) from the node center, which is assumed to be at 0 for simplicity, and s and m are fitting parameters. β_o occurs within the region defined by the inner-most volume because it is the region that is shared by all volumes.

$$\beta(x) = \beta_o e^{-\left(\frac{x}{m}\right)^s} \tag{22}$$

Because each sensitive volume represents discrete regions in space (and a unique α) rather than a continuum solution, (22) must also be divided into discretely defined regions. The extents in x, y, or z of each volume can be described by a linear or logarithmic gridding

function such as those shown in (23) or (24), respectively. It is assumed, in these equations, that the volumes are centered about the (0,0,0) point. An example is shown in Figure 17, where the nested volume group is labeled *Substrate collection volumes*. Each volume, i, has a width, given by $\Delta x(i)$, which is the difference between the positive and negative extents of that volume, per (25). The innermost and outmost volume $\pm$ extents relative to the center position are given by x_{min} and x_{max}, respectively. The cumulative collection efficiency, $\beta(i)$ in the discrete form is then calculated by (26), from which the individual volume efficiencies, α_i, are calculated by (27).

$$^{\pm}x(i) = \pm 1 \cdot \left[x_{min} + (i-1)\left(\frac{x_{max} - x_{min}}{n-1}\right)\right] \{i = 1, 2, ..., n\} \tag{23}$$

$$^{\pm}x(i) = \pm x_{min}\left(\sqrt[n-1]{\frac{x_{max}}{x_{min}}}\right)^{i-1} \{i = 1, 2, ..., n\} \tag{24}$$

$$\Delta x(i) =^{+} x(i) -^{-} x(i) \{i = 1, 2, ..., n\} \tag{25}$$

$$\beta\left(i\right) = \beta_o e^{-\left(\frac{\Delta x_i - \Delta x_1}{2m}\right)^s} \tag{26}$$

$$\alpha_i = \begin{cases} \beta_i - \beta_{i+1} & x \geq x_o \\ \beta_i - \beta_{i-1} & x < x_o \end{cases} \tag{27}$$

Figure 17 also contains an example plot of α and β for a hypothetical sensitive volume group (parameters shown in plot). Note that the plot is shown for only positive values of x, but the actual volumes extend equally in the negative x direction. The efficiency within the bounds of V_0, shown as x_o or x_{min}, is unity and begins to decrease beyond x_{min}. The spacing of the volumes is shown for both linear and logarithmic gridding. The number of volumes, n, only increases the resolution of the continuous efficiency function and does not alter the rate of decrease in β with increasing x. Note that the last volume, located

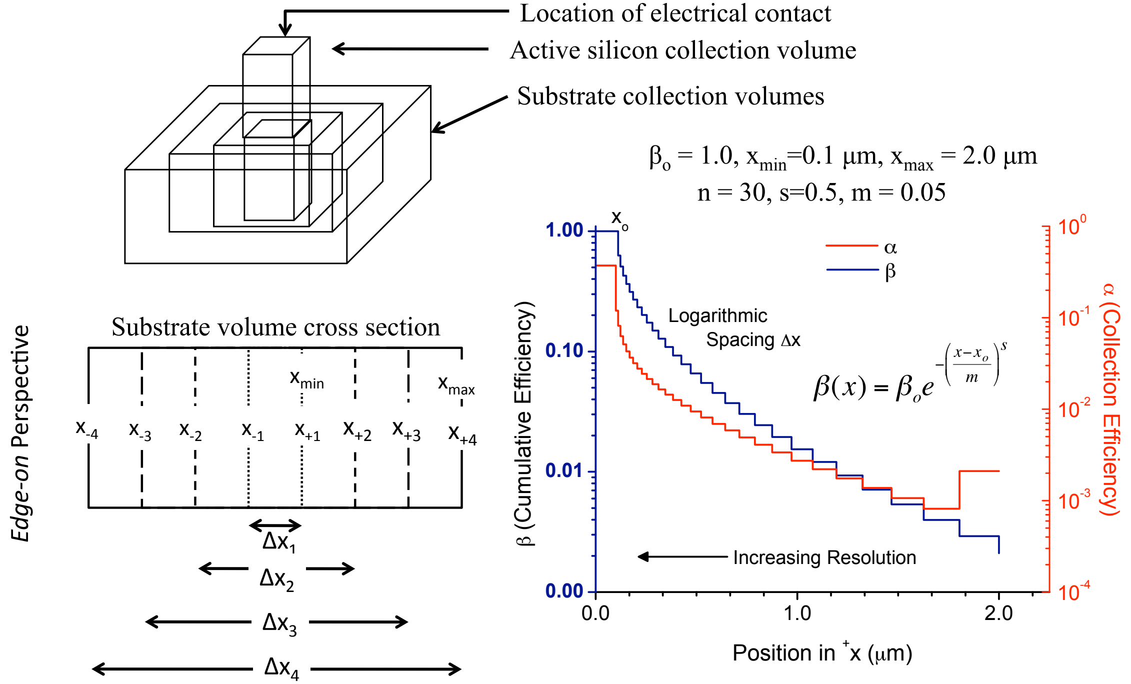

Figure 17: Conceptual illustration of the nested configuration of sensitive volumes.

at $\approx 2.0\mu m$, has a marked increase in α because the outermost volume α is defined to be equivalent to β (there are no overlapping volumes in that region).

Also shown in Figure 17 is the *active silicon collection volume.* This is the region of silicon above the level of the substrate, contained within an isolation oxide. It is the region that contains the implant regions, which define the transistor or the collecting node. The *active silicon collection volume* may be further divided into its own nested group if required (e.g., in the case of modeling parasitic bipolar condition in NMOS). Efficiencies within the *active silicon collection volume* are generally higher than in the substrate as the volume is in closest proximity to the charge collecting junction or transistor node. All subsequent analyses in this research utilize at least one *active silicon collection volume* for each transistor as all fabrication processes are on bulk CMOS. In the case of SOI, one would use only *active silicon collection volumes.*

Equations (22) and (26) are shown for one dimension only. In three dimensions, m and

s cannot be varied independently in the nested volume configuration. However, one may choose different extents in x and y by virtue of changing the values the the min and max values. This has the effect of compressing or extending the efficiencies in those directions relative to x. An example case of choosing an alternative z configuration is shown in Figure 18. In addition, the substrate volumes have been translated in the $+z$ direction so that they are coplanar at their uppermost surface. This is the typical arrangement used in this work as the top-most plane represents the interface to the active silicon region and ultimately the charge collecting node. The entire volume group can be translated in any manner that is desired, depending on the application.

In configurations where no volumes overlap in space, unique values of s and m may be given for each dimension (e.g., x, y, z) and $\beta = \alpha$ for each volume. Naturally, adding these degrees of freedom complicates the fitting process, though a higher degree of fidelity with respect to TCAD simulation or experimental measurements is achievable.

The nested sensitive volume concept is used to illustrate the utility of the multiple sensitive volume model, especially as it applies to charge collection from the substrate. It will serve as the basic construct during proof of concept in this chapter where it is demonstrated that there exists a nested configuration of sensitive volumes that can, within acceptable degrees of accuracy, relate the charge generation by an ionizing particle to the charge collected at a device node for typical N and PMOS devices. It is not the intent of this chapter to demonstrate that the concept of critical charge is valid in defining the circuit level (or higher) single event upset properties. This is addressed in subsequent chapters for specific types of circuits.

Multiple Sensitive Volume Groups

For the purpose of definition, a sensitive volume group is the aggregate of all sensitive volumes that define the collected charge at a given device node. It generally includes both the substrate and active silicon volumes. Multiple sensitive volume groups are an array

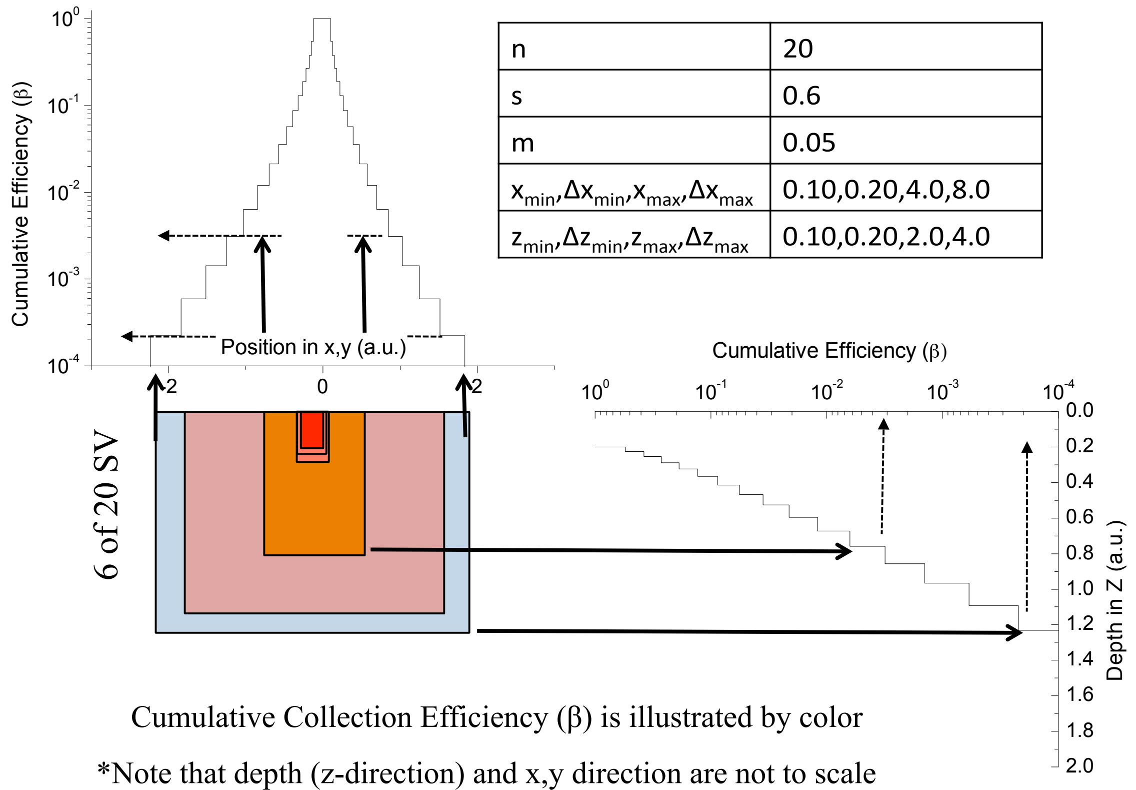

n	20
s	0.6
m	0.05
x_{min},Δx_{min},x_{max},Δx_{max}	0.10,0.20,4.0,8.0
z_{min},Δz_{min},z_{max},Δz_{max}	0.10,0.20,2.0,4.0

Figure 18: Graphic of the nested configuration of sensitive volumes where x, y and z extents differ for a fixed s and m. The outermost volumes extend to $\pm 4.0\ \mu m$ in $\pm x$, but are not shown as the cumulative collection efficiency is < 0.01 %.

(of arbitrary number and location) of sensitive volume groups. Whether multiple sensitive volumes are described in a nested configuration, in the limiting case of a single RPP, or some other suitable problem-specific description, the set describing collection at a single node cannot physically represent circuit level effects that arise from simultaneous charge collection on multiple collecting nodes. Such effects are significant for the SEU modeling and rate prediction of hardened circuitry [53], [20] and will become more significant with the continued decrease in feature size and packing density associated with the advancements of semiconductor manufacturing [91].

The proposed solution to the modeling of devices and circuitry for which multiple-node charge collection contributes significantly to the SEU rate is to assign sensitive volume

groups to each transistor node within the circuit being investigated. SEU response is then described in terms of the relationship between collected charge from the groups. This conceptually simple solution has not been previously implemented due to the difficulty of deriving generalizable analytic solutions to the probability distribution of chord-lengths (and coincidence criteria) for multiple node mechanisms.

Simulation Analysis of the Multiple Sensitive Volume Model

Software Tools and Technology Benchmark

Throughout this chapter, analyses of charge generation and transport are conducted using technology-assisted computer aided design (TCAD). As discussed in the introductory chapter, TCAD provides a mechanism for solving electron/hole continuity and current transport equations as well as Poisson's equation. A variety of models, including carrier recombination, generation, mobility, lattice heating, and numerous others can be selected by the user depending on the problem under investigation. The solutions are generated using finite-element analysis at points within arbitrarily complex geometrical and material entities specified by the user. Analytic approximations to doping processes are assigned to material regions to control donor and acceptor concentrations. Voltage and current characteristics, either static or transient, of the specified electrical contact faces provide a simple mechanism by which to track the impact of charge generation from heavy ions in semiconductor materials.

Electrical and single event simulations were performed using *Synopsys, Inc. Sentaurus Device v. A2007-12*. Solid model construction and meshing operations were performed using *Synopsys SDE and Mesh* tools of the same version release. Field dependent, including the normal field component, doping dependent, and high-field saturation, mobility models were used. Shockley-Read-Hall, Auger, and doping dependent recombination models were used. Single event simulations were performed using a Gaussian charge profile normal to

the track path with a characteristic radius of 50 nm. Collected charge, Q_{coll}, was calculated by integration of transient current generated by the single event simulation prior to the event time to a point where the node current or currents returned to pre-strike levels.

For the remainder of this chapter, TCAD charge collection predictions are based upon a process description approximating that of a known 90 nm bulk CMOS technology. P-type substrate doping is $1 \times 10^{16}\ cm^{-3}$ with a latchup-mitigating deep implant of $1 \times 10^{18}\ cm^{-3}$ at a depth of approximately 1.2 μm. n-well, and p-well peak doping levels are $2 \times 10^{17}\ cm^{-3}$ approximately 0.5 μm below the active silicon surface. Shallow trench isolation (STI) was used with a thickness of 0.35 μm. Lightly doped drain (LDD) implantation and threshold voltage, V_t, implantations were applied in such a way as to calibrate N and PMOS transistors to known current-voltage characteristics.

The Monte Carlo ray tracing (MRT) tool is used to calculate the distribution of chord lengths in the sensitive volume configurations that are examined in this chapter. The chord lengths are used to calculate the collected charge and SEU cross-sections of the proposed sensitive volume models. A comprehensive description of the simulator construction and operation is given in Appendix B and specific details are provided in the remaining text of this chapter, as needed.

The remainder of this chapter is dedicated to demonstrating that a set of sensitive volumes can be constructed that describe the relationship between energy deposited by an ion and the charge collected at device nodes for a range of physical device configurations through the use of TCAD simulation and the MRT ray tracing tool. The parameterization described by (22) through (27) is used. The multiple sensitive volume model is applied to simple diffused n and p regions as well as N and PMOS transistors over LET, ion angle, and strike location.

Because MRT is a ray tracing tool, it does not capture the radial extent of charge generation (track is a 2-dimensional line segment), and thus any line segment that does not intersect sensitive volume will result in zero charge generation within that volume, regardless

of its efficiency. TCAD, however, will generate charge at an amount that is proportional to the radial distance from the segment that describes the track trajectory, regardless of the presence or absence of material at the center of the track. Although not specifically discussed in the results, the difference between the two introduces error when making direct comparisons between MRT and TCAD simulation output.

Single Node Charge Collection

Single node charge collection refers to the charge collected at a single device or circuit node from the passage of an ion. It warrants individual treatment, relative to *multiple node charge collection*, in that it assumes that the properties of the transport process are independent of adjacent devices, which may also collect charge. The RPP model, for example, assumes a single charge-collecting node represents the response seen at heavy ion broadbeam testing, and that the collected charge by a single node is sufficient to upset the circuit. Subsequent chapters demonstrate that this assumption is not always valid.

Single Node - n^+ in p-type well

A TCAD model of a single 0.40 μm x 0.40 μm active silicon region on the standard, doped silicon substrate of the 90 nm process (previously described) containing a n^+ implant (1×10^{20} cm^{-3}, junction depth of 40 nm) was constructed to examine the simple and symmetric case of charge collection from an ion strike at an n^+ node. Although not an accurate representation of an active device typically involved in the SEU process, it provides a simplest example against which to test the multiple sensitive volume model. Aside from the p-type well contact at the extreme boundary of the device, there are no adjacent structures or junctions to introduce asymmetry (with respect to strike location) in the charge collection process. Boundary conditions in TCAD simulation were reflective, but the effects were minimized by creating a structure with large physical dimensions relative to the collecting node.

The substrate of the model is the same as that described in the introductory section of this chapter (including the p-type well and latchup mitigation implants). The 3-dimensional structure and cut-plane alone the center of the active region is shown in Figure 19. The n-diffusion region was biased at 1.2 V relative to the p-well and substrate nodes. TCAD simulations were performed for the 3-dimensional device in the plane defined by bisecting the active silicon region in the direction perpendicular to the z-plane (that is the x, z plane at y=0). SEU strikes were simulated at normal incidence, ±45°, and 90° relative to the surface of the TCAD structure.

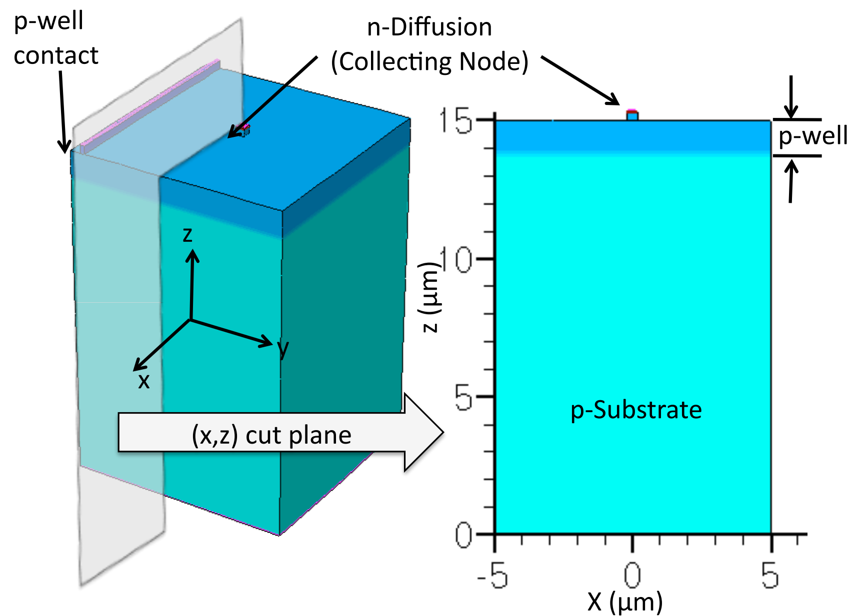

Figure 19: 3-Dimensional TCAD model of the single n-diffusion device with the (x,z) cut-plane shown for reference.

A multiple sensitive volume model containing 30 nested volumes (n = 30) was constructed symmetrically about the center of the diffusion region (x,y = 0,0), with the top surfaces coplanar with the TCAD surface (z=15.0 μm). An additional, non-nested volume enclosing the active silicon region was included with an $\alpha = 1.0$. Unless otherwise stated, the active silicon region (sitting above the substrate) is assumed to have a collection efficiency of

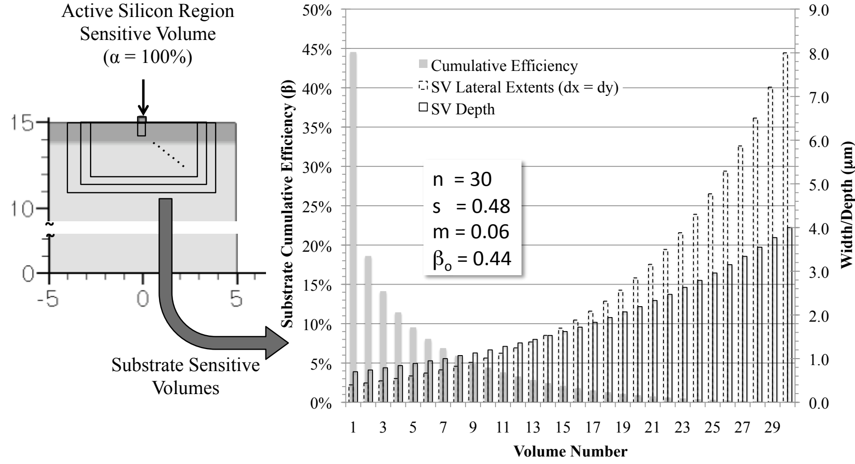

Figure 20: Illustration of the location, sizes, and efficiencies of the multiple sensitive volume parameters applied to the single diffusion TCAD model with one active silicon region volume and 30 nested substrate volumes.

unity. The nested substrate volumes were parameterized according to (22). Because of the symmetry of the structure, the sensitive volume widths were equal in x and y dimensions (surface plane). The maximum vertical depth (z), that of the outermost volume, was fixed at 4.0 μm. A linear spacing was chosen for the sensitive volume boundaries over the range.

MRT was used to randomly search over s, m, and β_0 space until a minimum relative error between the TCAD results and the MRT prediction was found. In this application, MRT calculated the segment lengths of the ion ray within the specific instance of the multiple sensitive volume model whose s, m, and β_o parameters were generated randomly. The ray position, direction, and LET for each simulation conducted in MRT was determined from the database containing the TCAD results. MRT, for each TCAD simulation result, determined the weighted sum of the chord lengths and determined the collected charge for the SV configuration. The relative error between Q_{coll} by TCAD and Q_{coll} for each ion position, direction, and LET was accumulated until a minimum error condition was satisfied. The minimum error was defined at the point for which no better solution was found in 10,000 subsequent trials. Thus, MRT assumes that best-fit results are a reasonable

minimum, but does not track and identify the number or quantity of local minima identified during extraction and one should not assume that the reported minimum represents a global minimum, or that the result is unique.

For this structure, the fitting parameters m and s were found to be 0.06 and 0.48, respectively. The peak cumulative substrate efficiency, β_o was 0.44. The sizes and efficiencies of the sensitive volumes are shown in Figure 20. Note that although good agreement with respect to the TCAD model was achieved with the specified maximum SV depths of 4.0 μm, the optimizer has dropped the collection efficiency by two orders of magnitude within 2.5 μm of the substrate surface (volume #23). 90% of charge collection takes place in the top 1.0 μm of the substrate (volume #8), corresponding to approximately the p-implant depth.

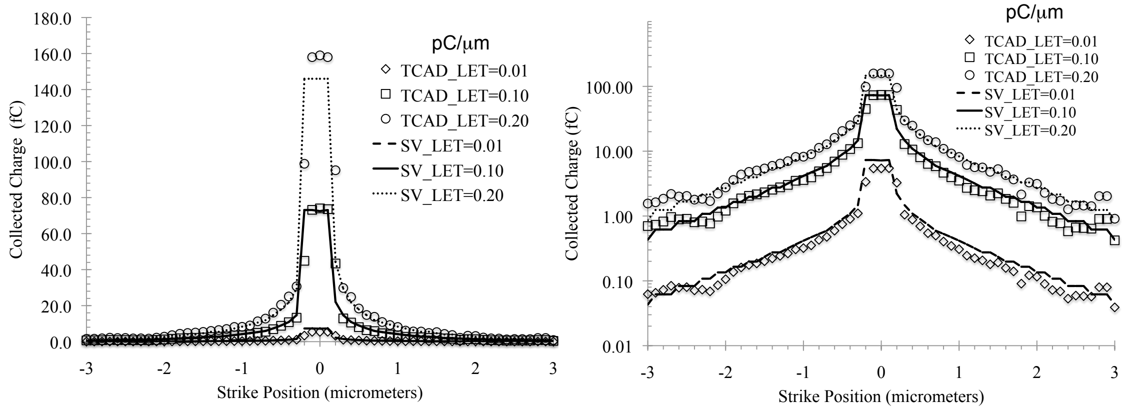

Figure 21: TCAD (open markers) and nested sensitive volume (SV, lines) predictions at normal incidence for single node at multiple LET.

The results of the minimization routine and the TCAD simulations are shown in Figure 21 for the normally incident ions for LET of 0.01, 0.10, and 0.20 $pC/\mu m$. Note that the quantity of collected charge is approximately linear over the range of LET at each strike location. The fitting routine was able to fit the model parameters in such a way as to agree with the electrical simulations over location and LET.

Figure (22) contains TCAD and MRT results for 45° strikes and grazing incidence strikes (90°) over a range of depths into the substrate. The angular simulations are asymmetric

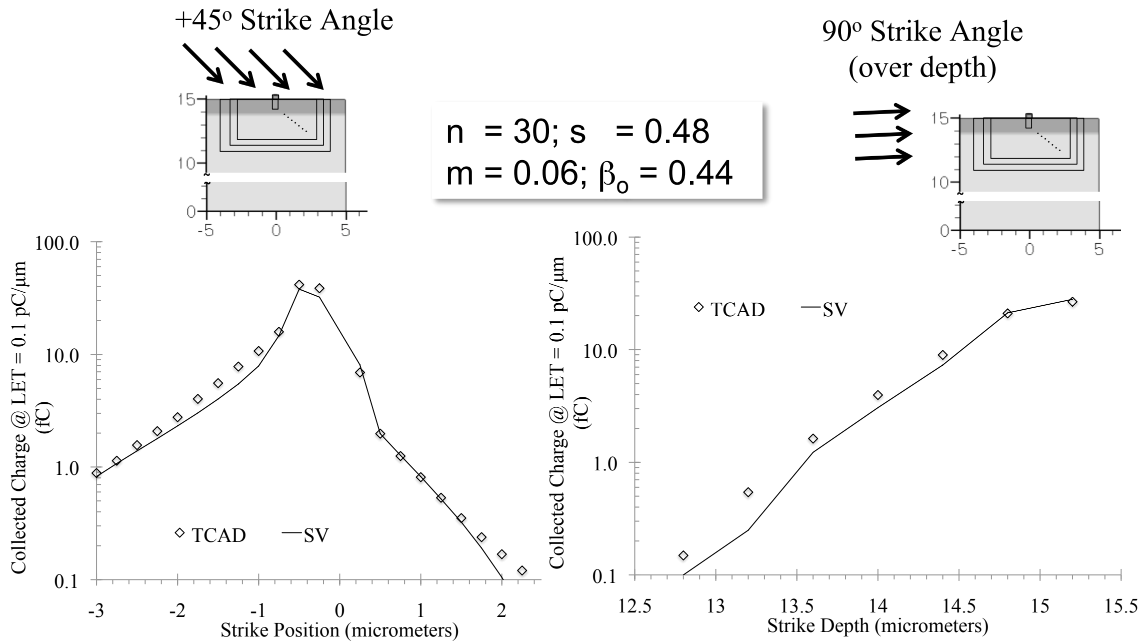

Figure 22: TCAD (open markers) and sensitive volume predictions (solid lines) over strike positions for 45° over the surface, and 90° over the depth.

with respect to the device node and offset from the zero position. The offset arises because the particles are launched from a z-position above the device surface and travel laterally before intersecting the sensitive volumes.

In the case of the single diffusion region, the parameterized implementation of the nested multiple sensitive volume model is suitable as a transfer function between Q_{dep} and Q_{coll} over a range of strike locations, angles and LET. Note that the nested sensitive volume model, including a separate volume representing collection in the active silicon area, is suitable for structures in which the collected charge is symmetric about a single point (or plane).

NMOS Transistor

The previous section demonstrated that the multiple sensitive volume model could be constructed in such a way as to represent an accurate transfer function between the charge

generated from an ion strike and that collected at the circuit node associated with the volume group. In this section, a similar analysis is conducted for an NMOS device, fabricated in the same technology.

The TCAD device of the NMOS transistor used in this section is shown in Figure 23. The length and width of the device were 80 nm and 200 nm, respectively. The structure also contains a region representing an adjacent n-well. The n-well is added to investigate the possible impact of coupling between it and the NMOS device. In all simulations the n-well contact and the NMOS drain were biased at 1.2 V with respect to the NMOS source, p-well, substrate contacts.

Charge collection was calculated by integration of the drain current over the duration of the single event induced current transient in the usual manner, and used to build the strike direction, location, LET and collected charge database utilized by MRT. The database consisted of 825 TCAD simulations over normal incidence (relative to device surface), grazing incidence (90°), and at ±45° along both the x and y axes. Sensitive volume extractions utilized all strike locations. The planes shown in subsequent plots of the collected charge as a function of strike location are labeled in Figure 23 (e.g., $(y, z)_{norm}$, $(y, z)_n$, $(y, z)_g$, etc.).

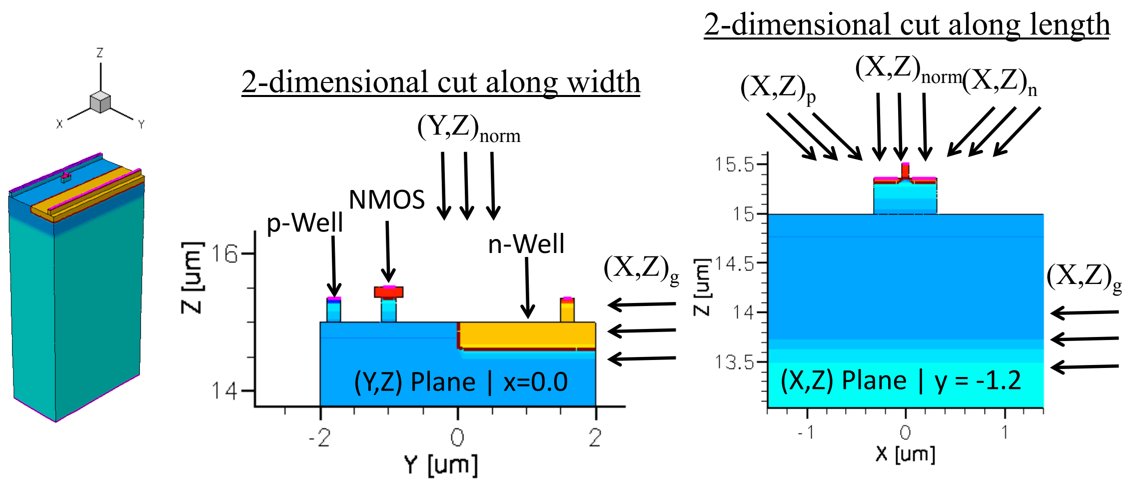

Figure 23: TCAD model of the single NMOS device.

A substrate nested sensitive volume group containing 30 linearly spaced (nested) volumes and a single volume of unity efficiency within the active silicon centered on the drain node was specified in a manner similar to the n^+ single-node case. Because of the asymmetry of the TCAD structure, the extent of the volumes in the y direction (toward the n-well boundary) were allowed to vary independently of the extents in the x direction during the process of determining the best SV configuration. The range of the volumes in z was also allowed to vary between the fixed innermost depth, 0.10 μm and a randomly evaluated maximum. The MRT extraction routine was used to determine an optimal parameterization for the substrate volumes.

An example plot of Q_{coll} as a function of strike location normal to the TCAD model surface and a subset of the sensitive volumes is shown in Figure 24. Note that the most intense region of charge collection is for strikes in the drain node of the NMOS. There is some asymmetry in charge collection with respect to the p-well contact strip direction. This is due to coupling between the adjacent n-well boundary (not shown, running parallel to the p-well contact strip at $y = 0.0$) as well as between the p-well contact. The charge collection profiles in the region of the NMOS drain are consistent with those reported in [13]. The maximum vertical extent, relative to the active silicon/substrate interface was 1.98 μm for the s and m parameters determined during error minimization. It is important to recognize that this does not imply that significant charge collection occurs from the maximum depth, as MRT *drives* the outermost volume's α to the values determined by the *roll-off* parameters, s and m in the x direction. The value of α in the z direction is therefore indirectly determined by the number of volumes placed between z_{min} and z_{max}.

Figure 25 contains a summary of the MRT calibrated nested sensitive volume configuration and the TCAD results for a select set of cut-planes through the NMOS device (orientations and planes are labeled in Figure 23. The effect of charge coupling between the NMOS drain node and the n-well is evident in the plot of the $(y, z)_{norm}$ and $(y, z)_g$. The simple nested sensitive volume group, centered about the drain node, is not sufficient to

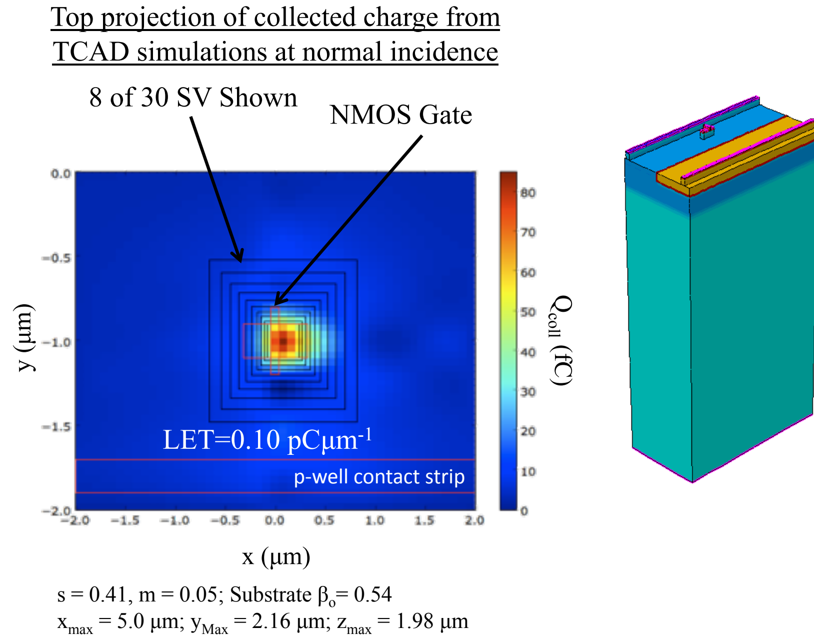

Figure 24: TCAD generated spatial distribution of the collected charge as a function of strike location for the single node NMOS device at 0.1 $pC/\mu m$ (top down view).

capture this effect. In such instances that coupling is deemed crucial to the SEU response of the circuit, additional volumes should be placed in the region where the effect is observed. A discussion of the process is presented in a subsequent section within this chapter.

Figure 25 and the extracted sensitive volume sets used to generate the plots within it were based upon a minimization of the relative error between the TCAD and the MRT calculations. It is worthwhile to note that minimization against the absolute error will provide a weighting in favor of the values of highest Q_{coll}. Given that the nested sensitive volume model is an approximation of the outcome of the charge collection process, one may choose to increase the model's fidelity in the most sensitive regions (e.g., NMOS drain) at the expense of fidelity in the relatively inefficient regions, if the threshold of SEU is more vital in the ultimate rate calculation. As in any model construction, determination of the best approach depends on the nature of the problem being addressed.

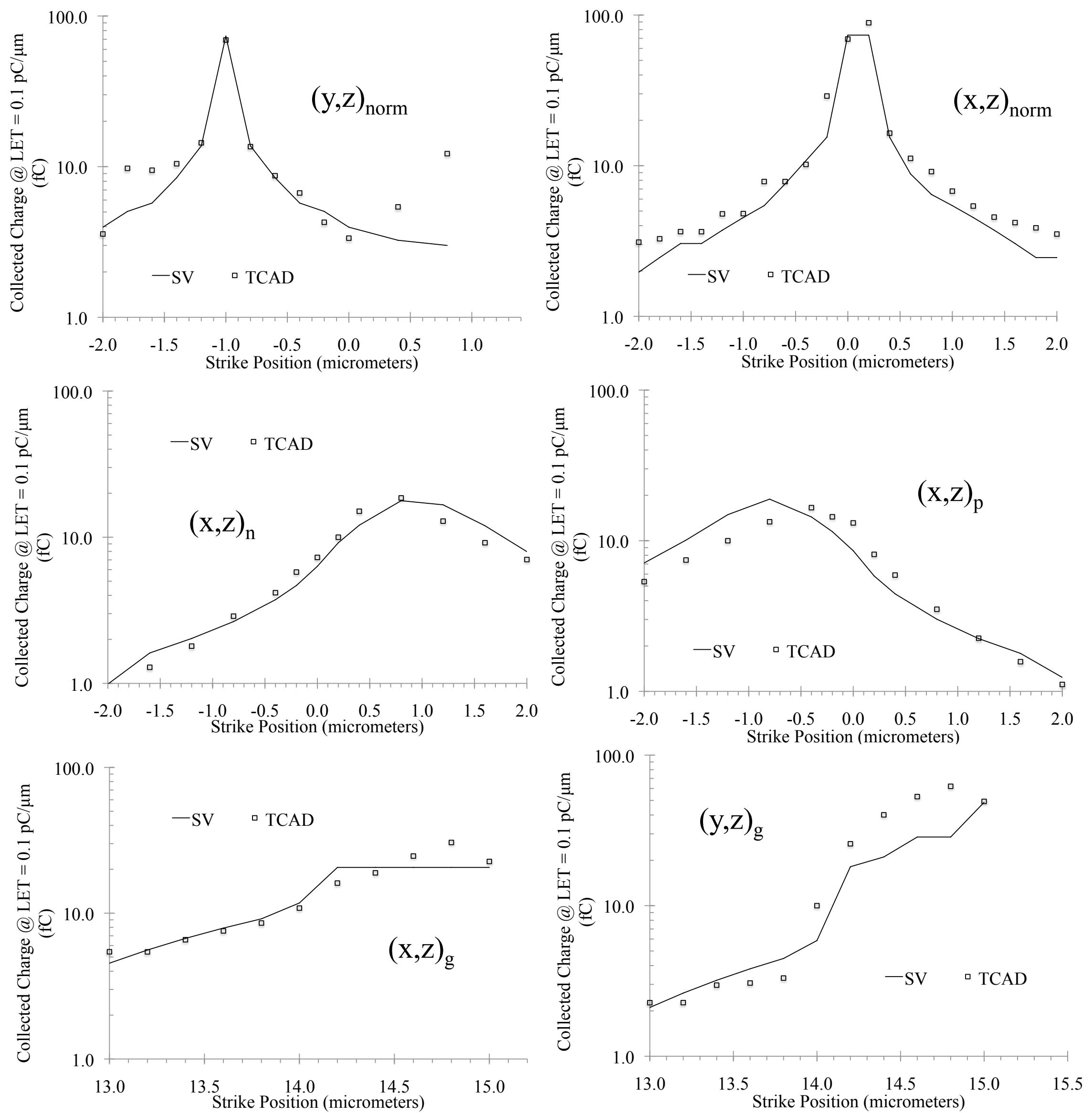

Figure 25: Selected NMOS TCAD and extracted SV charge collection profiles for an LET of 0.1 $pC/\mu m$.

Single Node - p^+ in n-type well

A TCAD model of a single 0.40 μm x 0.40 μm active silicon region, on the 90 nm process substrate, containing a p^+ implant (1×10^{20} cm^{-3}, junction depth of 40 nm) was constructed to examine the simple and symmetric case of charge collection from an ion strike at an p^+ node contained within an n-well. The simulation configuration is the analog

of the n^+ diffusion previously discussed.

The substrate of the model is the same as that described in the introductory section of this chapter (including the p-well and latchup mitigation implants), but also included an n-well implant and contact region. The 3-dimensional structure and cut-plane alone the center of the active region is shown in Figure 26. The p^+ contact and the n-type well region were biased at 1.2 V relative to the p-well and substrate nodes. Note that this bias configuration is different than the typical *off-state* mode commonly considered in PMOS analysis. The bias conditions were chosen to mimic the n^+ diffusion case for comparative purposes. An *off-state* analysis of a PMOS transistor is presented in a subsequent subsection.

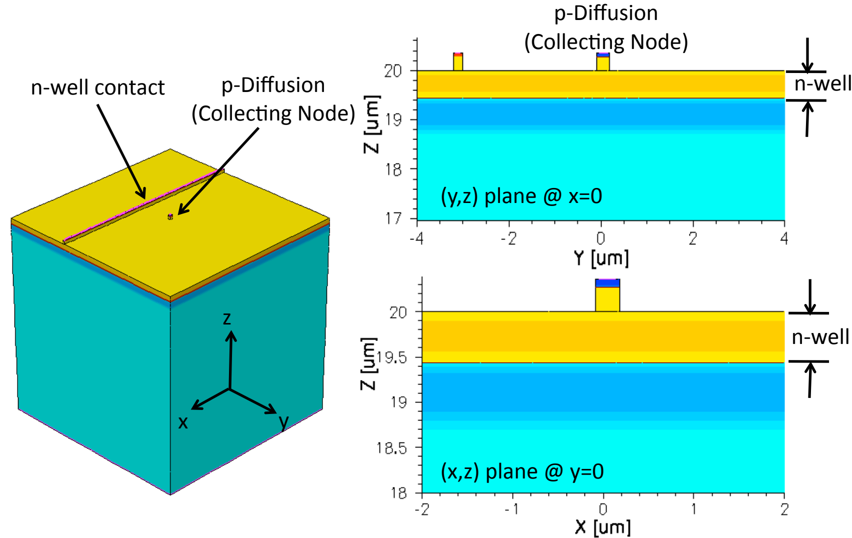

Figure 26: TCAD structure of single-node p^+ diffusion in an n-type well.

TCAD simulations were performed for the 3-dimensional device in the plane defined by bisecting the active silicon region in the direction perpendicular to the z-plane (that is the x, z plane at y=0). SEU strikes were simulated at normal incidence and over angle, including grazing angles. MRT optimizations were performed in a manner identical to that described in the previous n^+ diffusion section. An LET of 0.10 $pC/\mu m$ was used in all simulations.

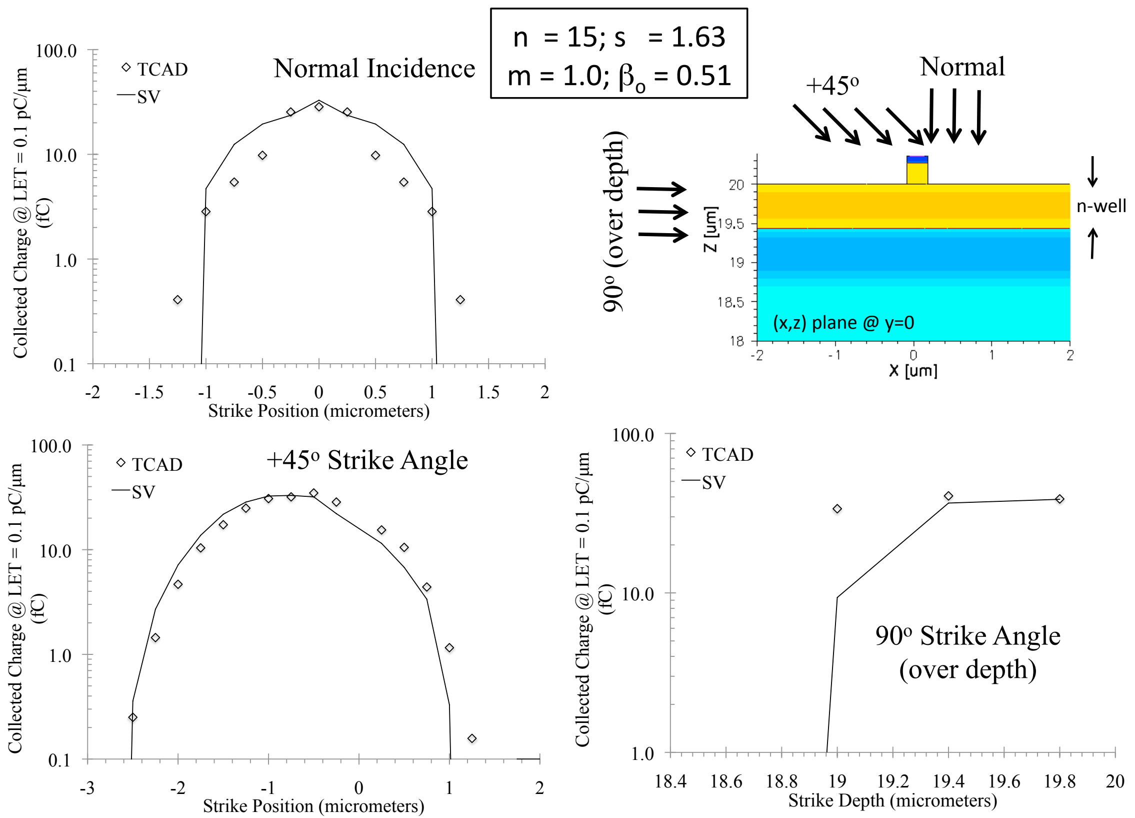

Figure 27: TCAD (open markers) and sensitive volume predictions (solid lines) of charge collected by a p+ diffusion over strike positions for 0°, 45° over the surface, and 90° over the depth. For 90° strike angles, TCAD simulations predicted an abrupt drop in collected charge between 18.6 and 19.0 μm.

The characteristics of the charge collection efficiency as a function of strike location for the p^+ contact is shown in Figure 27. The results indicate a significantly shorter range of interaction than the n^+ example. At normal and grazing incidence, the shape of the curve defined by (22) is not in agreement with the TCAD simulations. However, the peak collected charge in all instances is in good agreement with the TCAD simulations and any error introduced by the fit at normal and grazing incidences will result in an error in cross section (at the given LET) and not the threshold LET. An alternative parameterization (or visual best-fit) may be chosen to improve fidelity. Solutions involving this approach are presented in subsequent chapters and involve selections of α for the sensitive volumes that

are not strictly coupled, as they are in (22). It is worthwhile to note that this is a simulation of the collected charge on a p^+ node biased to the supply voltage; a condition that differs from the commonly encountered case of the *off-state* PMOS transistor, which is examined in the following section.

PMOS Transistor

The TCAD device of the PMOS transistor used in this section is shown in Figure 28. The active silicon region is 0.92 μm by 0.40 μm. The drawn channel lengths and widths of the device are 80 nm and 400 nm, respectively. The structure contains a region representing an adjacent p-type well. The p-type type well is added to investigate the possible impact of coupling between it and the PMOS device. In all simulations the n-type well contact and the PMOS source are biased at 1.2 V with respect to the PMOS drain, p-type well, substrate contacts ($V_{SD} = 1.2\ V$).

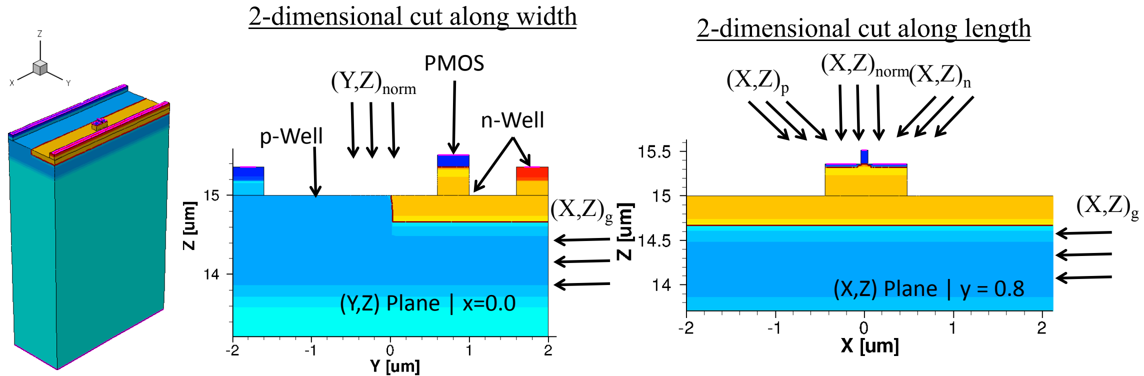

Figure 28: TCAD model of the single pmos device.

Ion strikes were simulated at normal, ±45°, and grazing incidence as shown in Figure 28 for an LET of 0.10 $pC/\mu m$. Normal and 45° strikes were simulated over the entire surface of the device at 0.40 μm increments. Grazing incidence simulations were preformed from the active silicon surface (15.36 μm) to 2 μm below the active silicon-substrate interface (13.0 μm) at 0.20 μm increments.

Charge collection was calculated by integration of the drain current over the duration of the single event induced current transient in the usual manner, and used to build the strike direction, location, LET and collected charge database utilized by MRT. Integrated current for the PMOS was negative (opposite direction relative to NMOS). Reported Q_{coll} values are shown as being positive (for ease of visualization) in all plots.

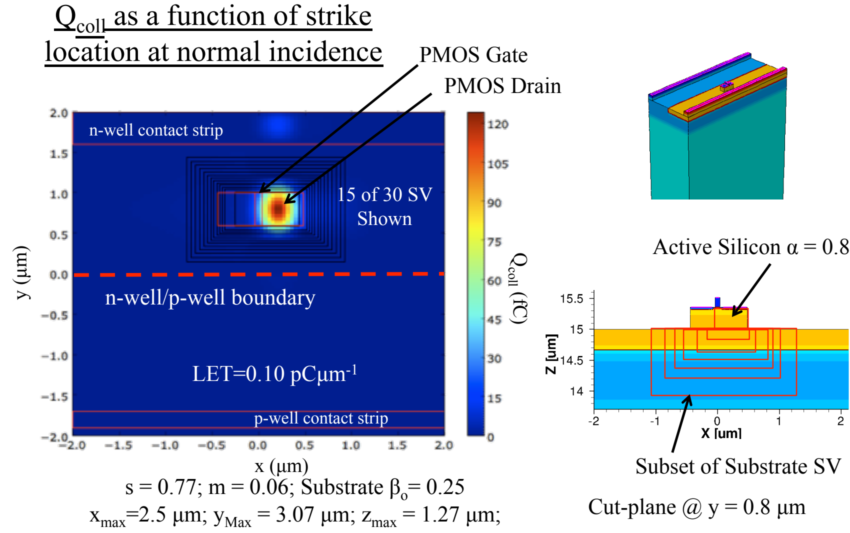

Figure 29: Spatial distribution of the collected charge as a function of strike location for the single node PMOS device at 0.1 $pC/\mu m$ (top down view).

Figure 29 shows the charge collected as a function of strike location at normal incidence for the PMOS device in addition to the location of the sensitive volumes relative to the transistor placement. The largest values of collected charge (and charge collection efficiency) are those proximal to the PMOS drain.

Figure 30 contains plots of the collected charge along cut planes corresponding to those shown in 28. The normally incident and 45 ° values predicted by MRT (shown by the series label SV) are asymmetric because of the relative placement of the active silicon region and the center of the substrate collection volumes (Figure 29). In other words, the inner-most substrate follows the outline of the active silicon-substrate interface, whereas the active silicon volume is contained with the drain region.

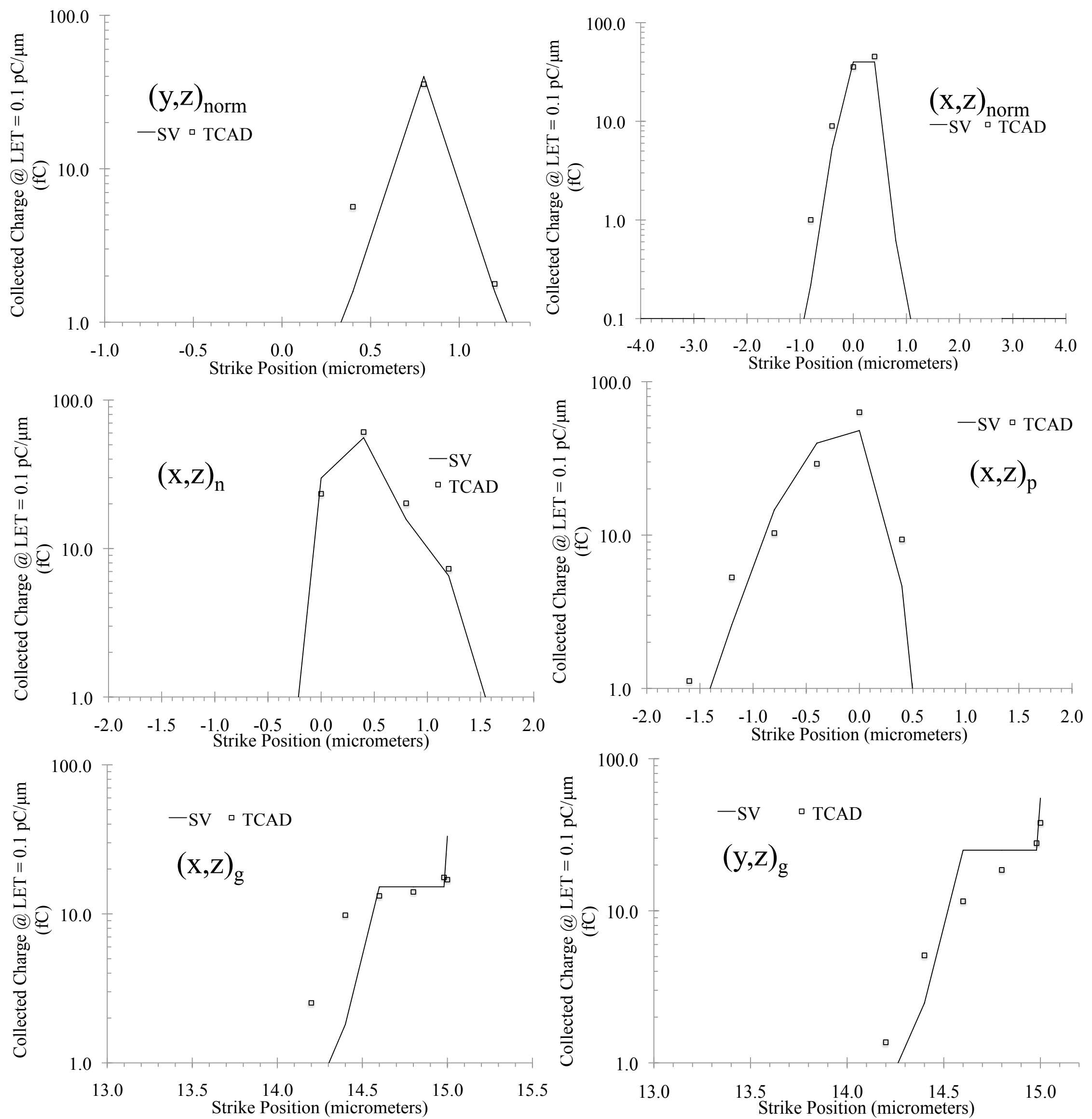

Figure 30: Selected PMOS TCAD and extracted SV charge collection profiles for an LET of 0.1 $pC/\mu m$.

Qualitatively, the trends for the PMOS model with the chosen parameterization function are in better agreement at normal incidence than that of the single p^+ diffusion. The functional fit is less accurate for grazing incidence, predicting a premature drop in the collected charge at or around the n-well boundary. The coupling of the vertical rate of roll-off with the lateral rate is clearly a limitation of the nested volume approach. Vertical

(grazing incidence) accuracy is sacrificed at the expense of achieving greater accuracy in the normal and $\pm 45^{\circ}$ fit. Limitations of the chord approximation used by MRT (no track structure) further introduce error near interfaces because the TCAD simulated ion track has radial dimension which *smooths* the energy loss by the ion in the radial direction relative to the ion's trajectory.

Multiple-Node Charge Collection

As discussed in [91], [19], charge coupling (or *charge sharing*) between neighboring transistors is a mechanism by which multiple nodes simultaneously collect charge from a single ion strike as a result of their relative proximity. As packing density increases with reduced feature size, the problem is anticipated to become more pronounced in the context of SEU modeling and rate prediction. In this section, multiple node charge collection from single ion strikes will be invested in TCAD using the same 90 nm process previously investigated. The sensitive volume sets used in the single transistor examples will be applied to arrays of three n^+ diffusions, three NMOS transistors, and 3 PMOS transistors in separate analyses.

Multiple n^+ Diffused Contacts

The multiple sensitive volume model is used to approximate the collected charge for three n^+ diffusions regions. The TCAD model, shown in Figure 31, is constructed in an identical manner to the singly diffused device. However, two additional diffusion regions are added, as shown in the figure. The size of the diffusions are 0.40 x 0.40 μm^2 and are separated by 0.40 μm of oxide.

A sensitive volume group was assigned to each transistor node. That is, there were three distinct groups of multiple sensitive volumes. Each volume group contained 31 volumes (30 substrate + 1 active silicon) where the collected charge was approximated by the linear sum of the weighted generated charge. However, the charge is not summed over all volume groups, rather it is tracked separately for each group and thus a separate collected charge

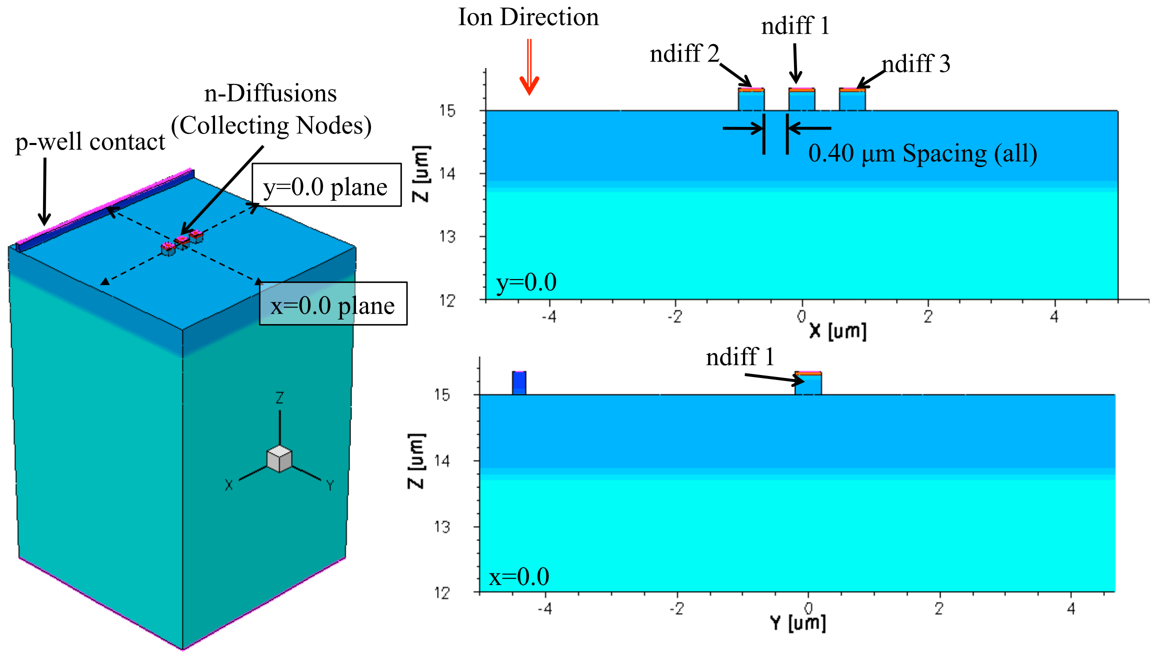

Figure 31: TCAD model of 3-node NMOS structure containing relevant cut planes.

is calculated for each transistor node for a single ion strike.

The parameters described by (22) through (27) were used with each volume group constrained by the same values of m, s, and $\Delta\vec{x}$ as in the single n^+ case. A single LET of 0.10 $pC/\mu m$ was examined. The results are shown in Figure 32.

Figure 32 suggests that *charge sharing* is a misnomer for the charge collection process in this example. This conclusion is supported the observation that the 3-node diffusion model agrees equally well (by visual inspection) with the 1-node example for the same set of sensitive volume parameters (each group has the same parameter set as the single node example). *Charge sharing* implies that an arbitrary quantity of generated charge within a given volume element (not sensitive volume) is divided between two or more nodes. However, it is likely more reasonable that in this example the relatively low efficiency of the outer-volumes indicates there is little interaction between adjacent structures. This may not necessarily be true in all cases, especially at larger values of LET or where parasitic

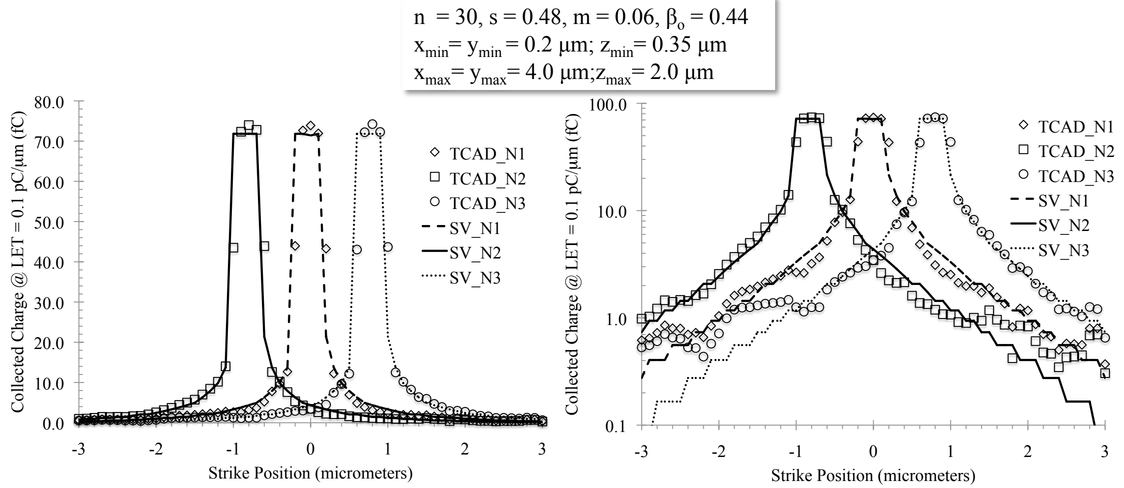

Figure 32: TCAD and nested sensitive volume predictions for three nodes.

mechanisms enhance node-to-node coupling, as in [91].

Multiple NMOS Transistors

A TCAD model of three NMOS transistors, each having the same dimensions as the single NMOS example, was constructed to examine charge collection on multiple NMOS devices from single ion strikes. The TCAD model is shown in Figure 33. In the single NMOS example, the stepping resolution, 0.40 μm did not resolve possible variations in charge collection efficiency over the active silicon region. In this study, TCAD simulations were performed for ions at normal incidence at a stepping resolution of 0.20 μm in the x and y directions at an LET of 0.10 $\frac{pC}{\mu m}$. The finer stepping size guaranteed multiple strikes would be simulated along the direction of the transistor lengths (x).

Two sensitive volumes were used in the active silicon region of each NMOS transistor as shown in Figure 34 and the center of the substrate sensitive volumes were offset in the direction of the drain node. The sensitive volume efficiency beneath the source contact was chosen as a free parameter as well as the substrate s and m in the error minimization calculation. A subset of the the parameters taken from the single NMOS parameters were

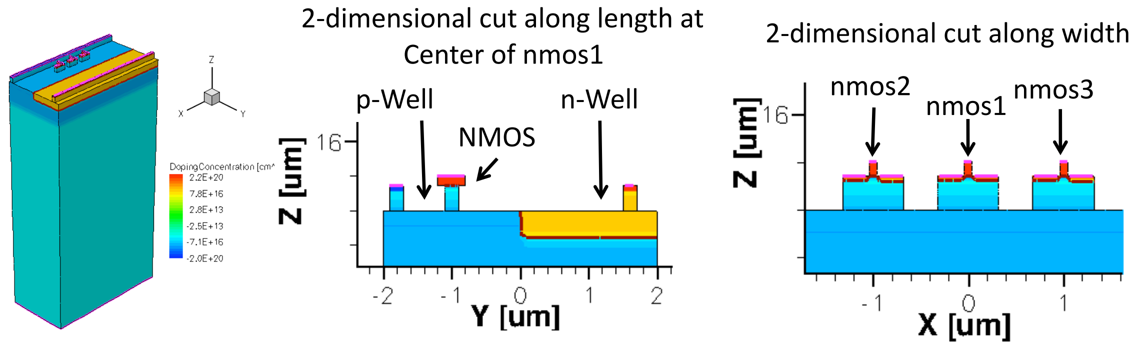

Figure 33: TCAD model of the three-transistor NMOS device.

fixed and used in this example; specifically, $z_{max} = 1.98\ \mu m$, $y_{max} = 2.16\ \mu m$ and substrate β_o= 0.54.

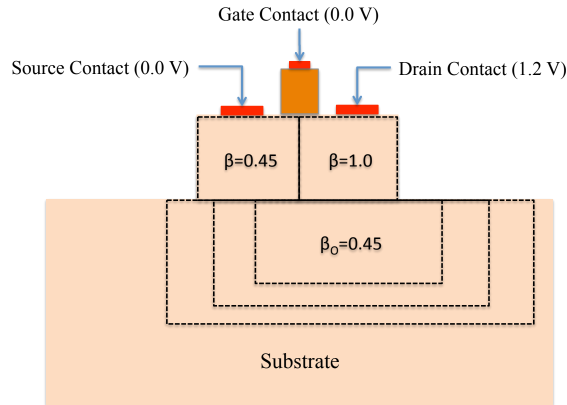

Figure 34: Division of the active silicon sensitive volumes in a single NMOS for the 3-NMOS model.

The best fits for s and m were 0.36 and 0.03, respectively. The source active silicon volume β was 0.54. The results for the TCAD simulations and the sensitive volumes are shown in Figures 35 and 36. The asymmetry in the collected charge along the transistors' channel length (x direction) with respect to the center of the gate is illustrated in Figure 35, where the centers are located at 0.0, -1.0, and +1.0 μm for N1, N2, and N3, respectively. Dividing the active silicon volume into two separate regions allows one to capture the effects

observed in simulation and improves the accuracy of the model in the region of high charge collection efficiency.

As in the case of the single NMOS device, the error between the nested volume model and the TCAD results are most pronounced for strikes in the n-type well, shown in Figure 36. In the both NMOS studies, the accuracy of the centric (diffusion only) nested volume model and the chosen equation to describe the efficiency roll-off with distance from the collection node is insufficient to model coupling to the n-type well. The limitations and proposed solutions are discussed in greater detail in the *Parasitic Mechanisms* subsection of this chapter.

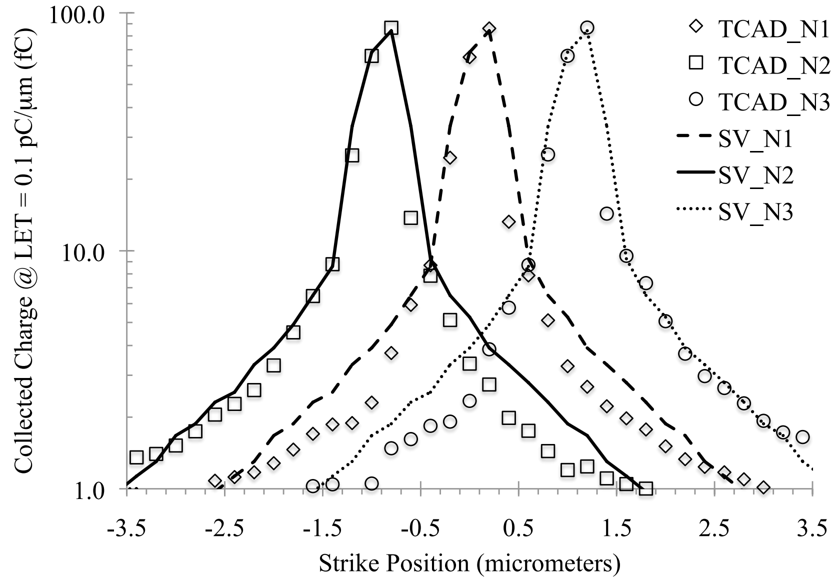

Figure 35: Charge collection profile along x-axis at y=-1.0 for three NMOS devices as predicted by TCAD and fit using MRT.

Multiple PMOS Transistors

The same parameters used in the single PMOSFET example were used in the three-transistor case where s = 0.77, m = 0.06, z_{max} = 1.27 μm, y_{max} = 3.07 μm, Substrate β_o= 0.25. The results of the 30 volume set compared with the TCAD predictions in Figure

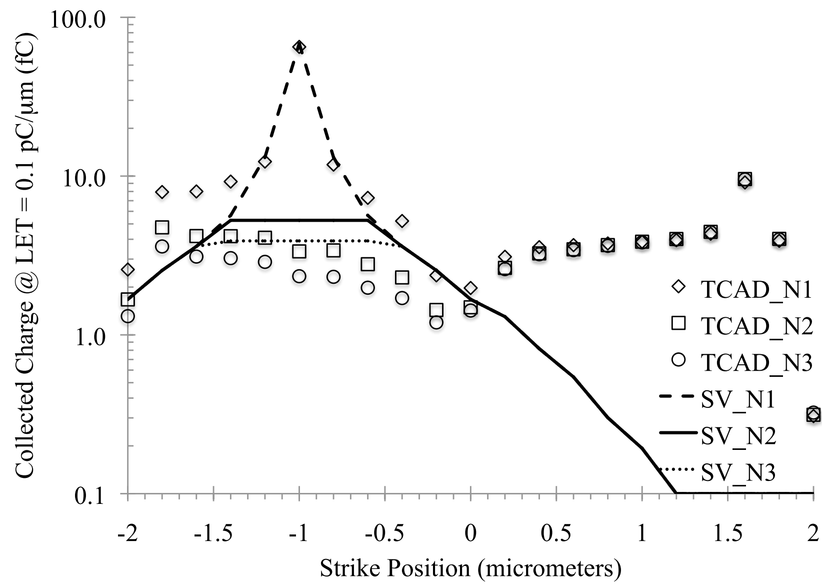

Figure 36: Charge collection profile along y-axis at x=0.0 for three NMOS devices as predicted by TCAD and fit using MRT.

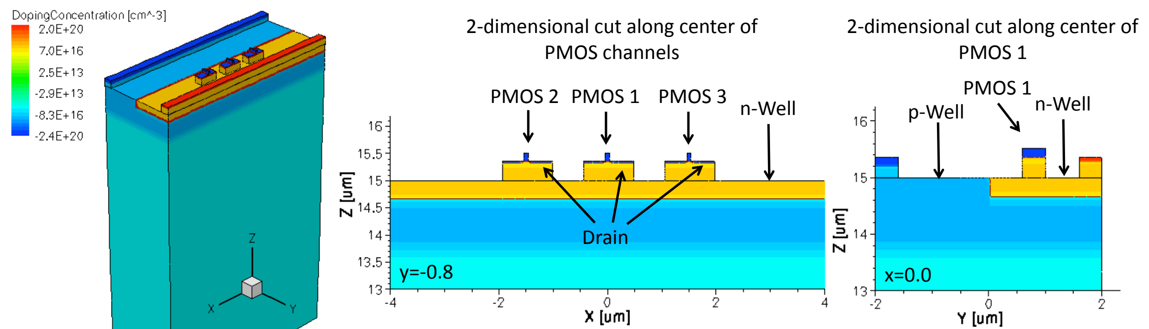

Figure 37: TCAD model of 3 PMOS transistors.

38. Note that the sensitive volume group was not adjusted to account for leakage current and thus under-predicts the collected charge over the integration interval. Since this is a non-radiation related phenomenon, adjustments for leakage are not necessarily pertinent. Capturing second order effects is mentioned in the *Parasitic Mechanisms* section of this chapter.

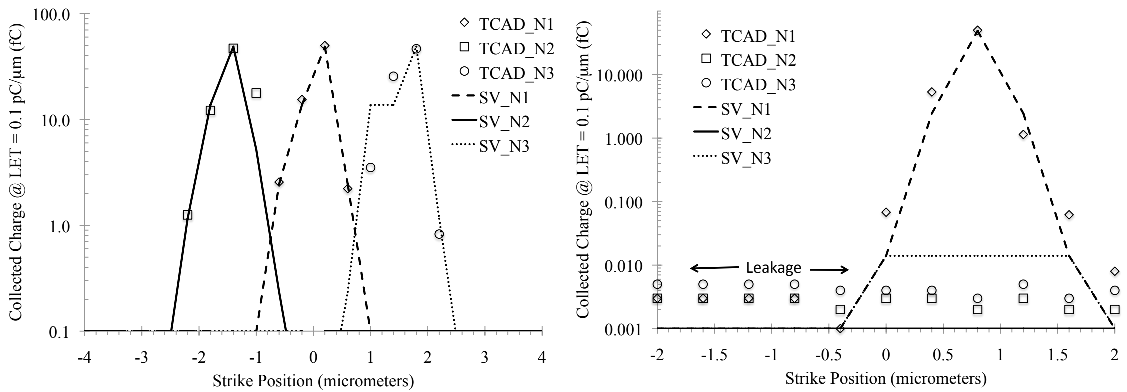

Figure 38: Charge collection profile for three PMOS devices as predicted by TCAD and fit using MRT.

Parasitic Mechanisms

In the case of the single and multiple NMOS transistor examples, the accuracy of the substrate nested volume model deviates significantly from the TCAD predictions for ion strikes within the n-type well. In applications where it has been determined that the TCAD model is physically reasonable (it is an accurate physical representation of the true charge transport and collection process), additional sensitive volumes are required.

Detailed analyses of the NMOS TCAD results indicated that in the $-y$ direction, (referring to Figure 23), the reflective boundary conditions imposed in TCAD, produced a likely non-physical increase in the total collected charge at the drain node. In the $+y$ direction (toward the n-well), the substrate and p-well potential increased due to coupling with the n-well. This was verified by examining the source and drain currents for those simulations, which indicated that the collected charge on the NMOS drain was approximately equal to current sourced by the NMOS source (source to drain conduction). For the sake of illustration, the objective of the refined sensitive volume model will be to capture the effects predicted by TCAD, but not justify that the TCAD results themselves are physically realistic. Verification of the TCAD results would require experimental measurements and test structures, an effort that is outside of the scope of this work.

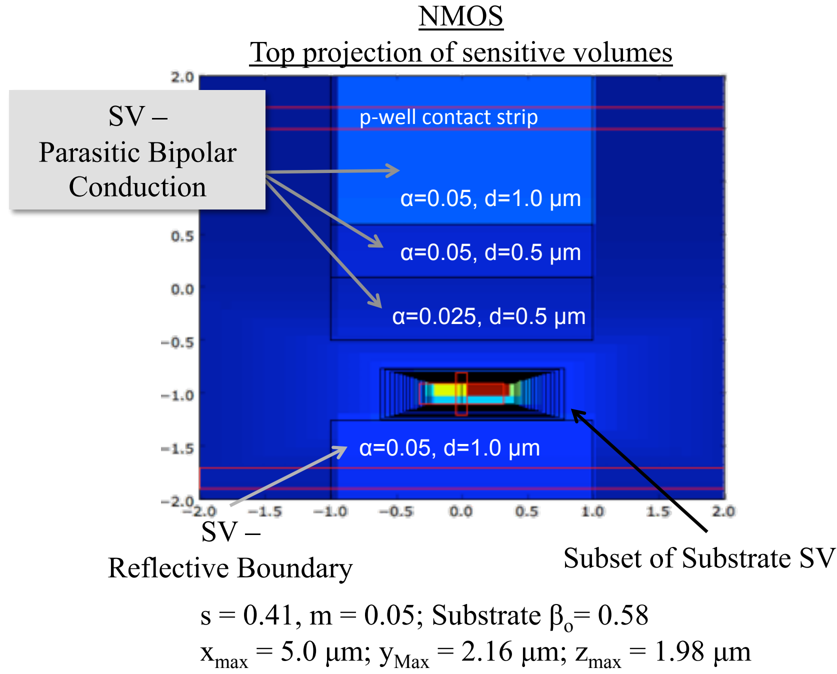

Figure 39: Top down view of the single NMOS structure illustrating the location of the additional sensitive volumes used to capture secondary charge collection mechanisms.

Additional sensitive volumes were placed on either side ($\pm y$) of the NMOS device according to Figure 39. The precise placement location, size, and depths were based upon inspection of the TCAD results. The baseline parameters of the substrate volume of the original NMOS case were used as initial *guesses* for the sensitive volume relative error minimization algorithm, and allowed to vary by 10% of those values to account for the newly introduced volumes. The total volume count, n, was increased to 30, which affects only the resolution of the predictions in x, y, and z.

The efficiency of the additional volumes was allowed to vary unconstrained to produce the best possible fit to the TCAD results. The results of the simulation are shown in Figure 40, with the same plane references (e.g., $(x, y)_g$) used in Figure 23. The modified NMOS model produces results that are in better visual agreement with the TCAD predictions, especially for those strikes in the n-well ($y > 0.0$) and near the structure boundary ($y < -0.5$). A greater relative error is observed immediately near the NMOS device in the

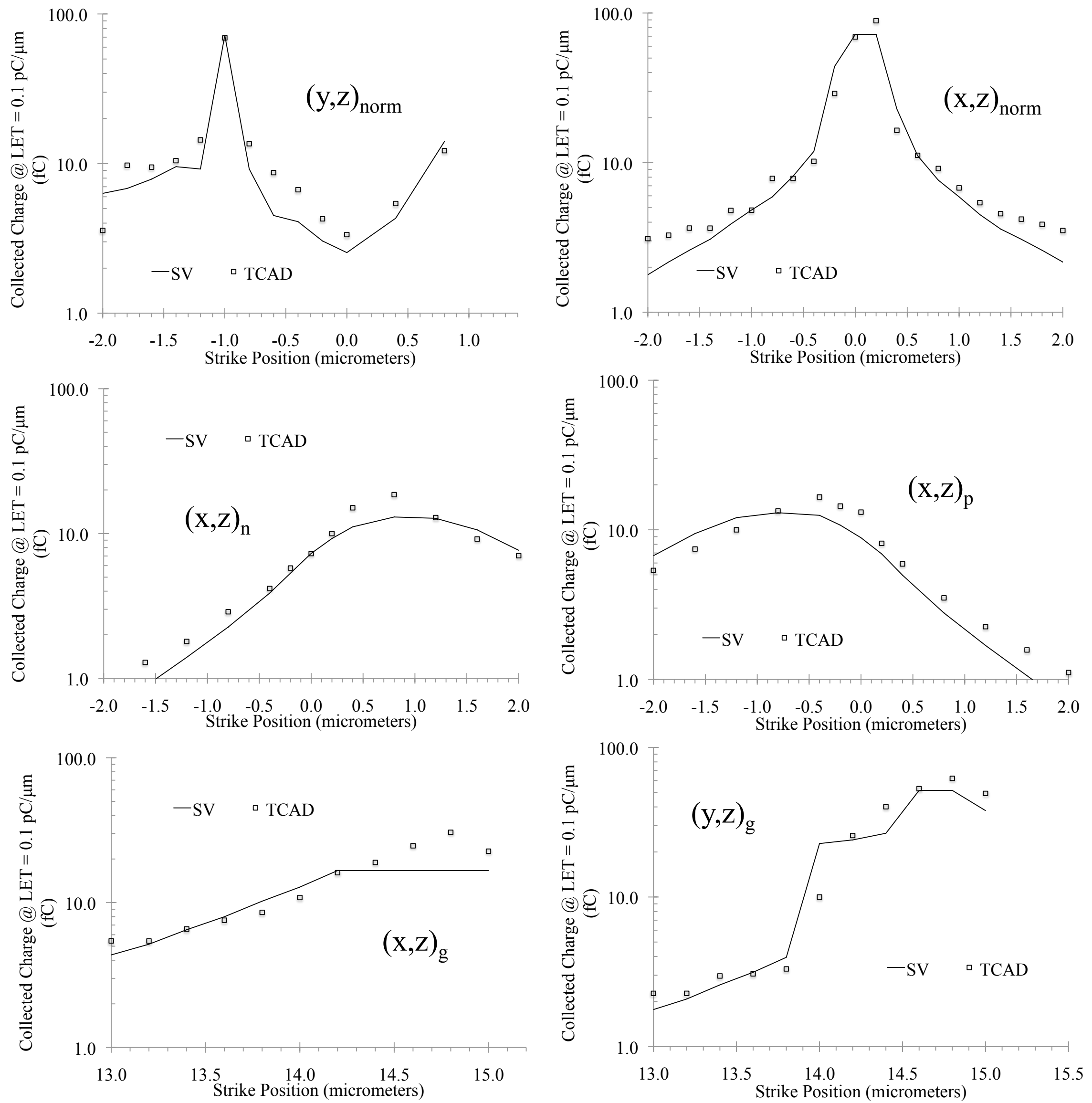

Figure 40: Subset of cut-planes comparing the nested sensitive volume predictions and the TCAD results which include the additional volumes used to capture secondary charge collection mechanisms.

$(y, z)_{norm}$, $y \approx -0.5\ \mu m$.

Likewise, the 3-transistor NMOS structure was modified to include the additional substrate volumes (identical to the single transistor NMOS). A subset of the pertinent results shown in Figure 41 indicating the reduction in error between the TCAD and extracted SV model when parasitic mechanisms are included. Note that Figure 41 shows the charge

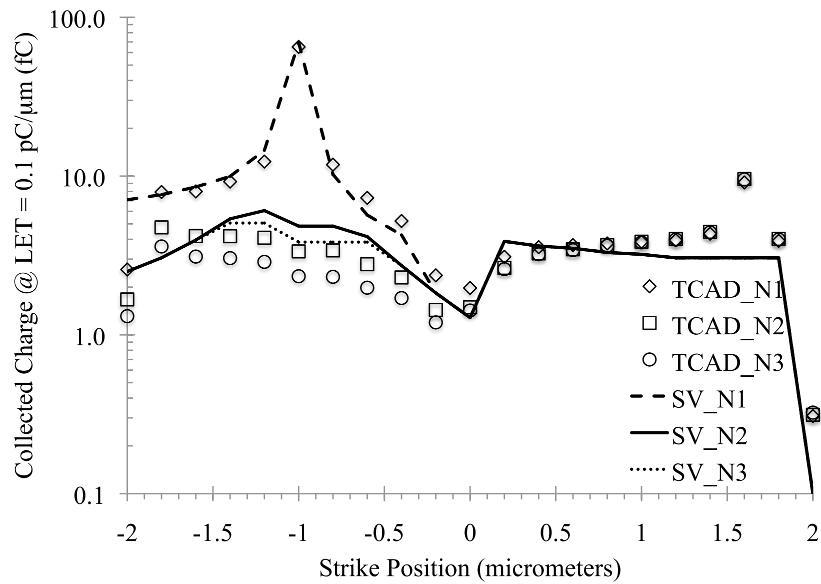

Figure 41: TCAD model of the three-transistor NMOS device along the y-axis at x=0.0. Additional volumes have been placed between $0.0 \leq y \leq 2.0\ \mu m$ to account for coupling to the N-well.

collected at each of the three NMOS devices for strikes along the center of $N1$. This is why the $N2$ and $N3$ collected charges are approximately equal along the cut-plane.

In ideal cases of a purely symmetric layout and for devices distant (as determined by TCAD) to n/p-well boundaries, a simple substrate collection model is adequate. However, the simple nested substrate volume model may not accurately reflect the total sensitive area of the transistor(s) for a given value of collected charge if parasitic mechanisms are identified by TCAD analyses. Clearly, the need to include additional un-nested substrate volumes must be carefully assessed based on the objectives of the simulation (e.g., SEU cross-section calculations and error rate predictions).

Application of Multiple Sensitive Volume Model

Histograms and Probabilities

The previous sections of this chapter demonstrate the level of fidelity achievable by use of the multiple sensitive volume model for a set of specific example devices and configurations, where the measure of fidelity is based upon the sensitive volume model's ability to capture the positional and directional dependence of the ion strike parameters on the devices' collected charge.

The purpose of the multiple sensitive volume model is to relate the probability of an outcome (e.g., collected charge) to a given set of environmental conditions. Probability may be measured in units of cross-section, or in terms of an error rate, depending on the objectives of the work. The random variable or variables are the environmental parameters, such as the position of the emission point of the ion only (e.g., broadbeam simulation), or the position and direction (isotropic environment). For physics-based simulations, the interaction processes themselves are random, such as the occurrence of a nuclear reaction or scattering between the ion and the nuclei of the target material.

In Appendix B, the concept of the histogram is introduced and the procedure for calculating cross sections from frequency distributions is formally presented. The following paragraphs provide a summary of the process for a specific example.

The histogram, in the context of this work, is a measure of the frequency of occurrence of an event based upon an event criterion. When properly normalized, the histogram becomes the probability density function of the desired independent variable, such as the collected charge, Q_{coll}. An example of the progression of the calculation is shown in Figure 42 for a broadbeam exposure simulation at normal incidence to the single n^+ diffusion using MRT. The independent variable is collected charge, calculated from the sensitive volume model and the ion parameters for 500,000 events. The randomized parameter in this example is the position of the emitted particle in the plane normal to the device surface.

Normalization of the frequency distribution to the histogram's bin width (in units of charge) and total event count (500,000), yields the probability density function. Five series are shown for a range of ion LET from 50 to 100 $fC/\mu m$. This distribution is the multiple sensitive volume model equivalent of the path length probability distribution function described in chapter one, but scaled to charge rather than chord length. Note that there is an outlier in each series that corresponds to the relatively small probability of an ion strike to the active silicon volume. The continuous distributions at lower relative values of collected charge represent the substrate nested volumes.

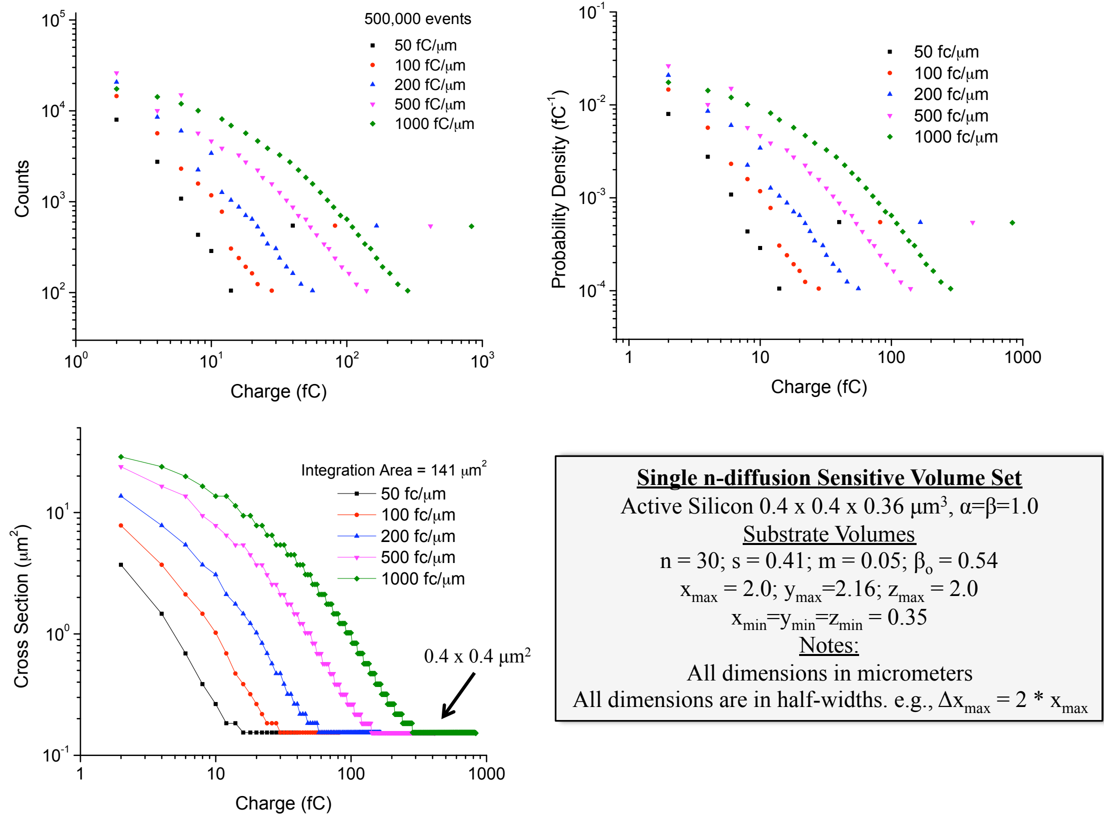

Figure 42: Progression from raw counts distribution to cross-section calculations using the singly diffused NMOS volumes.

The histogram, when reverse integrated and scaled to the integration area, produces the cumulative probability of an event having a collected charge equal to, or greater than

the collected charge at that point. The reverse-integration procedure is useful in that it is applicable to the simple SEU requirement of $Q_{coll} \geq Q_{crit}$. Specifically, one is interested in the probability of all events exceeding the critical charge. The integration area is the total area of the circle that results from the projection of the sphere inscribing the target geometry onto a plane in the direction of the ion's path. Note that the minimum cross section in each series corresponds to the total surface-normal area of the active silicon sensitive volume (0.16 μm^2). Thus, for a given Q_{crit}, a suitable sensitive volume model, and the proper randomization algorithms the SEU cross section curve can be calculated.

SEU Cross-section Curves

The previous section described the process of generating histograms and cross-sections as a function of collected charge based on a given sensitive volume model and randomization procedures. In practical applications, it is useful to determine the cross section (in this case of a given collected charge) as a function of the ion's LET. The procedure follows naturally from the analysis shown in Figure 42, where the trend is now taken over LET for a series of Q_{coll}. The result of the operation is shown in Figure 43 (for the n^+ diffusion).

If one interprets Q_{coll} as Q_{crit}, it's clear that this method may be used to generate the heavy ion broad beam cross section curves described in Chapter I. Naturally, the fidelity of the prediction depends on an accurate knowledge of Q_{crit}, that Q_{crit} itself is an adequate measure of the SEU response, and that the constructed sensitive volume model adequately approximates the underlying charge transport process. Qualitatively, the shape of the cross section curve predicted in this manner bears a strong resemblance to those measured experimentally. Furthermore, that shape is a function of the spatial relationship between the generated and collected charge, which is a form of intra-cell variation in SEU response, described in Chapter I.

In certain instances, the generation of histograms as an intermediate path to calculating SEU cross sections is not practical (or required). Such is the case when multiple transistors

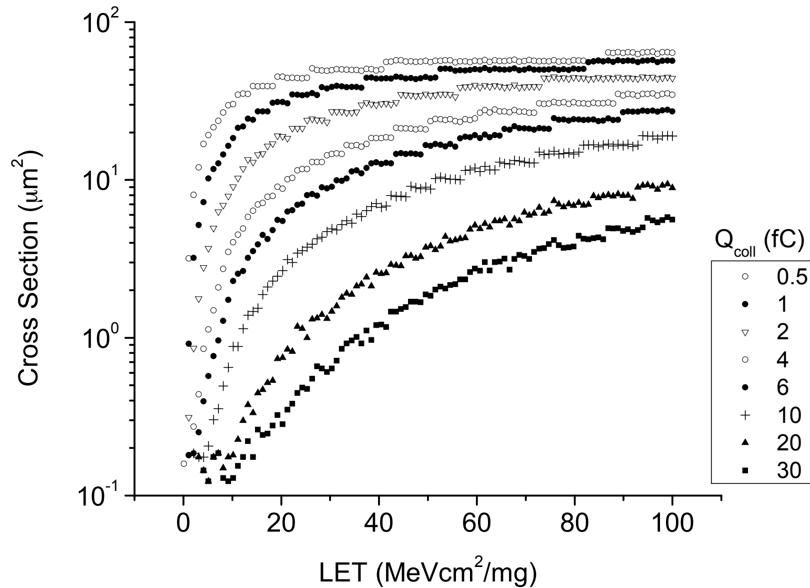

Figure 43: Cross section curves for a series of collected charges using MRT and the calibrated sensitive volume models.

must simultaneously collect charge to cause an SEU. Considering the 3 n^+ diffusion model previously described, if coincidence is required between any two or all of the nodes to satisfy an SEU condition, then tracking that correlation on an event-by-event basis with histograms is computationally difficult, and reduction of the data in that form into meaningful cross section curves is unnecessarily cumbersome.

The alternative approach is to pre-define the Q_{coll} and logical requirements that lead to a valid event. An example is shown in Figure 44. The figure legend contains three hypothetical conditions: The first is that any one of the three nodes collects more than 5 fC, an SEU occurs. The second logical requirement is that at least two nodes selected from the three collect more than 5 fC, and the final requirement is that all three must simultaneously collect 5 fC to cause a valid event.

During simulation, and on an event-by-event and LET-by-LET basis, the simulator (MRT in this example) determines the collected charge on each node, and applies the necessary logic for a valid SEU conditions. The valid events are accumulated for each LET.

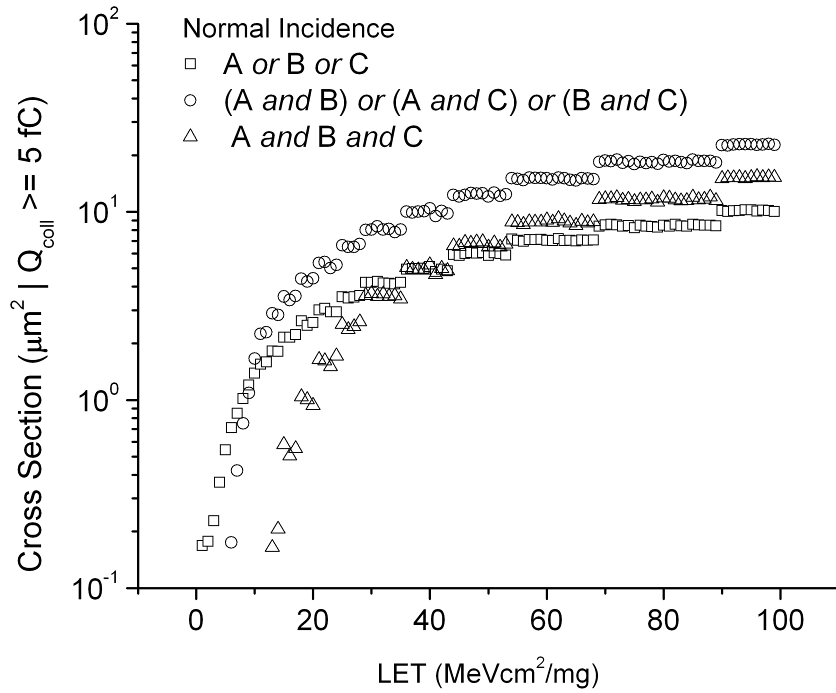

Figure 44: Coincident node SEU cross sections for the 3-n+ diffusion model with $Q_{crit} = 5\ fC$.

The final cross section at each LET is calculated by the quotient of the number of valid events and the total particle count. In effect, the reverse-integration procedure is performed in simulation. The drawback of this approach is that details of the variability in cross section with Q_{crit} are lost. While the concept of chord-length distribution is retained in the single group multiple sensitive volume model, it has little meaning in calculating cross sections and error rates for coincident node mechanisms.

Conclusions

A novel sensitive volume model, described by the linear combination of weighted sensitive volumes (20), has been shown effective for approximating the relationship between the charge generated by an ion strike and the total charge collected at transistor nodes. A concentric or nested volume configuration, parameterized according to (23) through (27),

provides good agreement with TCAD predictions for charge collection from the silicon substrate. The placement of additional volumes around regions of enhanced collection can be used when the concentric set is inadequate, as in the case of enhanced charge collection from the adjacent n-type well of the NMOS models.

The multiple sensitive volume model can be used to capture intra-cell variations in charge collection efficiency at a level of fidelity that was previously impossible with the single cuboidal volume (required by the RPP model). Furthermore, the use of multiple sensitive volume groups allows one to concurrently track collected charge for any number of transistors. In this manner, the circuit response is directly tied to the charge collected at any and all transistor nodes in the circuit, and as such it can be mapped directly to circuit level simulators (SPICE). SPICE simulation is used in all subsequent chapters to establish SEU criteria.

The increased flexibility the model and solution method provide will be used to explore SEU cross section and error rate prediction methods in a manner previously impossible with the limitations imposed by the RPP model. Two categories of SEU mechanisms will be specifically addressed in the remainder of this dissertation:

1. A circuit contains multiple transistors, some number of which are sensitive to an ion strike, and a valid SEU condition requires a minimum of Q_{crit} be collected on a single circuit node. A unique value of Q_{crit} is possible for each transistor. Static random access memories are a classic example, where charge collection on the off-state NMOS or PMOS device causes SEU. This case is examined in Chapter III.
2. A circuit contains multiple transistors and a valid SEU conditions requires that a minimum of two transistors simultaneously collect charge at an amount equal to or greater than the coincident critical charge [53]. The dual interlocked storage cell (DICE), used in latches and flip-flops, is a classic example. Multiple sensitive volume groups will be used in Chapters IV and V to investigate the angular dependence of the SEU cross-section associated with this class of circuitry, as well as analyze and predict an on-orbit SEU rate.

Radiation loses energy as it passes through material at a rate that depends on the species of the ion and the composition of the material. In ray tracing methods (e..g, MRT) a constant stopping power and infinite path length (relative to the dimensions of the volumes) is

assumed. In some environments the approximation is reasonable (e.g., interplanetary space and the GCR environment). However, as discussed in Chapter I, terrestrial SEU largely result from neutrons and alpha particles. The former undergo nuclear reactions with the semiconductor material and the secondary charged species ionize the silicon. The secondary particles, as well as the latter case of alpha particles, may have ranges comparable to the dimensions of the sensitive volumes. In other words, they are not accurately represented by single chords of constant LET and infinite range. This is primarily why separate models and methods for SEU rate prediction as a function of radiation type exist. Physics-based transport codes, which are capable of capturing the detailed mechanisms of particle transport and energy loss, are used Chapter III in conjunction with the multiple sensitive volume model to unify error rate predictions across radiation species.

CHAPTER III

PHYSICS BASED TRANSPORT AND THE MULTIPLE SENSITIVE VOLUME MODEL

Introduction

In this chapter, the application of the multiple sensitive volume model to physics based transport using the Monte Carlo Radiative Energy Deposition (MRED) simulator is examined for a static random access memory. Unlike the MRT simulations in Chapter II, MRED incorporates physics based models which capture the detailed mechanisms of energy loss by energetic particles in materials [29], [110]. MRED allows one to abandon the limitations of the chord length and constant LET assumptions and focus on all possible mechanisms (that are specified by the user) that lead to energy loss and charge generation. The spatial resolution and translation of the energy loss to charge collected at one or more circuit nodes is captured by the multiple sensitive volume model.

In Chapter II, TCAD simulations were used to derive and define the parameters of the multiple sensitive volume model for individual transistors. In this chapter, TCAD analyses are performed on the SRAM structure to approximately identify the location and extents of the sensitive volumes. Unlike Chapter II, the precise efficiencies (α) and extents of each volume within the set are estimated by inspection of SEU cross section measurements and minimization of the error of the predicted cross sections with the experimental data. The TCAD analyses, in conjunction with circuit level simulation using SPICE, serve as the basis for the sensitive volume configuration and the definition of valid error conditions within MRED.

Furthermore, it is demonstrated that a sensitive volume model, a calibrated set of valid SEU criteria, and accurate radiation transport physics can be used to predict the single event upset response of the SRAM circuit over all species commonly encountered in the terrestrial

radiation environment. This unified approach deviates from the traditional, independent methods discussed in Chapter I.

Device and Circuit Analysis

The device analyzed is a 4 Mbit, 6-transistor SRAM fabricated on a 0.25 μm bulk CMOS process. In order to develop a suitable multiple sensitive volume model for the SRAM circuit, a detailed investigation of the charge collection dynamics of the as-built device was performed at the circuit and device level using SPICE and TCAD, respectively. The analyses provided a measure of the spatial sensitivity (intra-cell variations) of the circuit as well as the sensitivity to ions of a range of LET.

TCAD: Transistor-level Charge Collection

Technology computer aided design (TCAD) was used to perform silicon-level electrical simulations of individual transistors in the SRAM. TCAD studies were performed by Brian Sierawski[1]. Discrete (individual transistor) two and three-dimensional models of relevant 0.25 μm devices were constructed for the purposes of identifying, both spatially and electrically, the single event upset response. Doping profiles for the substrate, n-well, and p-well were supplied by the vendor. Three-dimensional transistor models were constructed from a simple layout using the obtained doping profiles. The p-well doping reaches a peak concentration at 0.4 μm from the surface shallow trench isolation (STI). The n-well reaches a peak concentration of 0.5 μm from the STI surface. The STI, and thus, the active silicon thickness was modeled with a depth of 0.3 μm. The gate oxide was 5 nm thick, and the gate polysilicon was 100 nm thick. Models for both n-MOSFET and p-MOSFET devices were constructed with gate lengths of 0.25 μm and widths of 20 μm. All devices were simulated with the Synopsys Dessis TCAD solver.

The single event simulations were performed with the devices in an off state. V_{DD}

[1] At the Institute for Space and Defense Electronics at Vanderbilt University.

was assumed to be 2.0 V. In all simulations, the normal incident particle struck the drain body junction as a worst case on strike location. Incident particles had LET of 0.5, 1, 2, and 3 $MeVcm^2/mg$. To assess the current limiting impact of a complementary transistor attached to the drain, a separate simulation with a resistive load was performed. The load was an estimate of the channel resistance based on the transfer characteristics obtained with the SPICE models. The NMOS assumed a load of 67 $k\Omega$. The PMOS assumed a load of 33 $k\Omega$.

Figures 45 and 46 contain the response of the respective SEE simulation in terms of drain current over the four values of incident particle LET. As expected, each transistor responses differently under loaded and unloaded conditions. The resistive load in both cases limits the peak drain current and increases the width of the transient pulse. Based on the 2.0 V heavy ion test results (Figure 55) and an approximate LET$_{TH}$ (@ 10% σ_{sat}) of $1.5 - 2.0$ $MeVcm^2/mg$, the $Q_{crit,n}$ and $Q_{crit,p}$ from the discrete transistor models is approximately 10 and 15 fC, respectively. The reduced supply voltage case of 1.4 and 1.5 V results in a decrease in the estimated $Q_{crit,n}$ and $Q_{crit,p}$ to approximately 5 and 7 fC, respectively.

TCAD: Full-cell SRAM Simulations

To identify the sensitive areas of the SRAM cell, and to a lesser extent, verify the experimentally determined LET$_{TH}$, detailed simulations of the entire SRAM cell were performed in TCAD. The results were used to guide the geometrical placement and size of the sensitive volume model used in subsequent simulations.

The SRAM cell was constructed using the GDSII layout provided by the vendor. A 3-Dimensional image of the SRAM cell, including access transistors is shown in Figure 47. To ease the computational burden of the device simulation, the local interconnect and large portions of polysilicon were replaced with SPICE-level components. Initial conditions were generated by biasing the appropriate nodes (e.g. V_{DD}) prior to single event simulations.

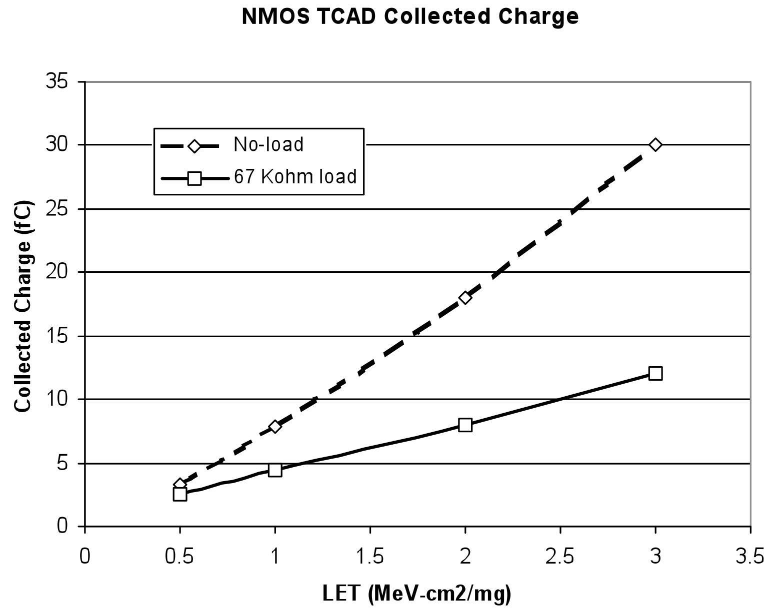

Figure 45: Collected charge vs. LET for NMOS transistor.

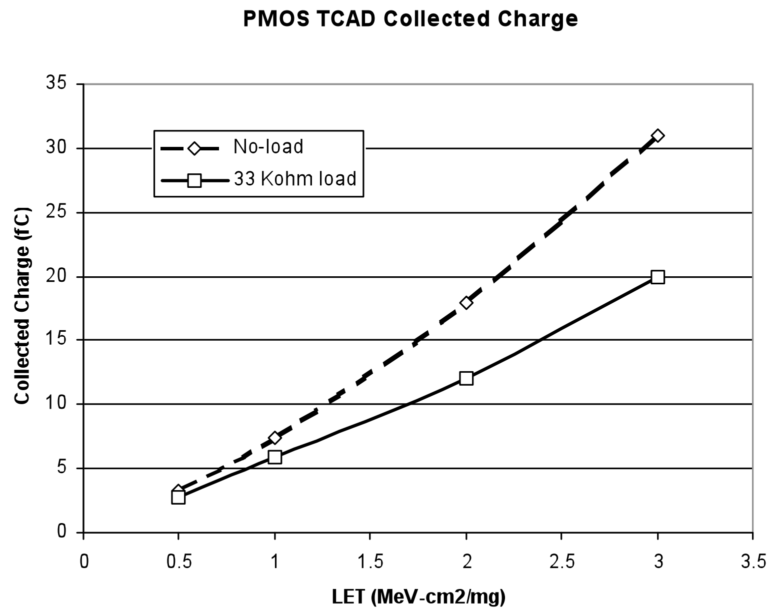

Figure 46: Collected charge vs. LET for PMOS transistor.

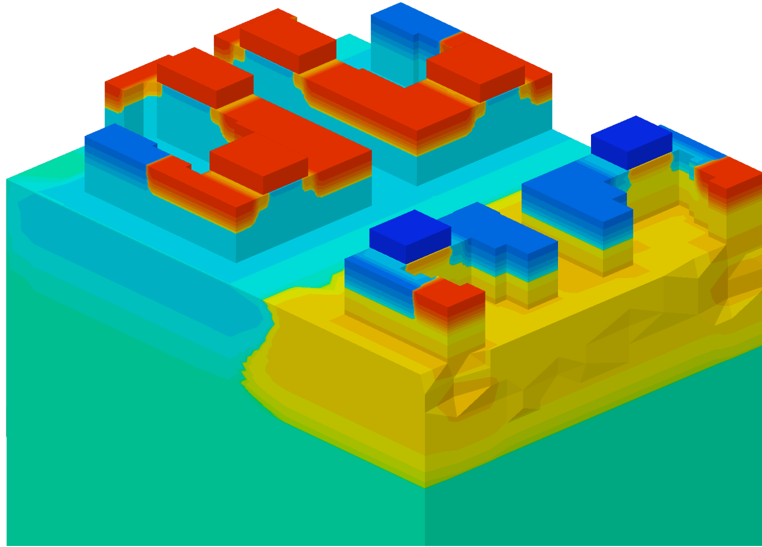

Figure 47: 3D SRAM cell. Dark blue regions indicate p-type dopant, red regions indicate n-type dopant. Trenched areas reflect the omitted STI and raised areas are polysilicon gates.

Table 1: TCAD derived SEU cross sections.

Supply Voltage (V)	LET ($MeV cm^2/mg$)	σ_{SEU} (μm^2)
2.0	1.0	0.00
2.0	2.0	0.75
1.4	6.0	1.63

The SEU simulations were performed by rastering a particle strike over the entire surface of the cell at normal incidence. The steps were 0.25 μm in both the x and y dimensions for a total of 88 strike locations. Each raster set was repeated for LET over a range of 1.0 to 6.0 $MeV cm^2/mg$. A valid error condition occurred when the final voltage state on the bit-line resulted in a state opposite that of the initial condition following the ionizing event. A summary of the net sensitive area under the three conditions shown in Figure 48 are summarized in Table 1.

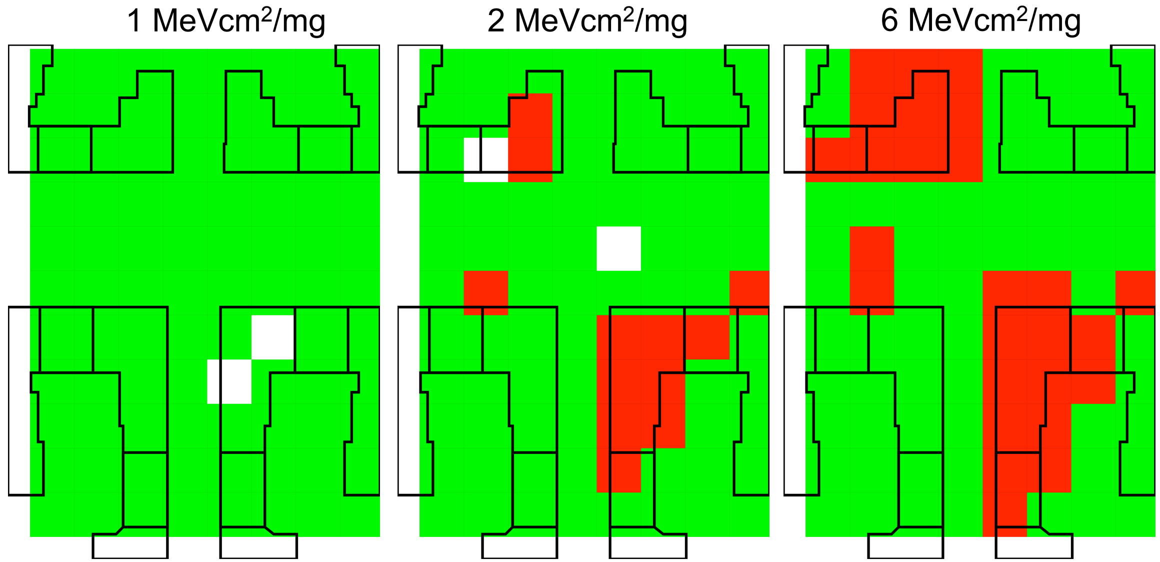

Figure 48: Regions sensitive to SEU (red) of the SRAM for 1, 2, and 6 $MeVcm^2/mg$ at V_{DD} =2.0 V.

SPICE: Circuit Simulation

Nominal SPICE models, provided by the vendor, were used for the PMOS and NMOS, respectively, within the inverters. The circuit schematic is shown in Figure 49. Heavy ion strikes were simulated using current pulses taken from the TCAD simulations. The current profiles were fit to a double exponential current pulse as shown for the example case of an LET of 2.0 $MeVcm^2/mg$ in Figure 50. The parameters for the double-exponential source for N- and P-MOS devices are shown in Table 2 and Table 3, respectively. Current profiles for the loaded transistors were used in all simulations and the net collected charge was verified to be within 1% of the TCAD results in each case. NMOS SEU first occur at an LET of 2.0 $MeVcm^2/mg$ and PMOS SEU first occurs at 3.0 $MeVcm^2/mg$. This is in good agreement with the experimental results where the LET_{th} is approximately $1.5 - 2.0$ $MeVcm^2/mg$, depending on which approach for determining threshold is used.

Comparison of SPICE results to SEU data from broad-beam experiments was performed by assuming the transistor sensitive regions were equivalent to the gate and drain diffusion

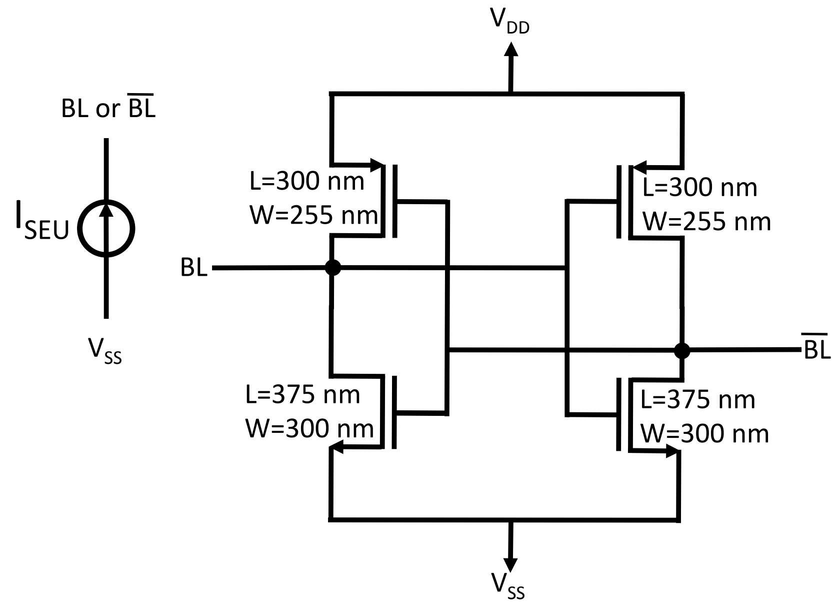

Figure 49: Schematic of the 0.25 μm TSMC SRAM circuit used for SEU simulations.

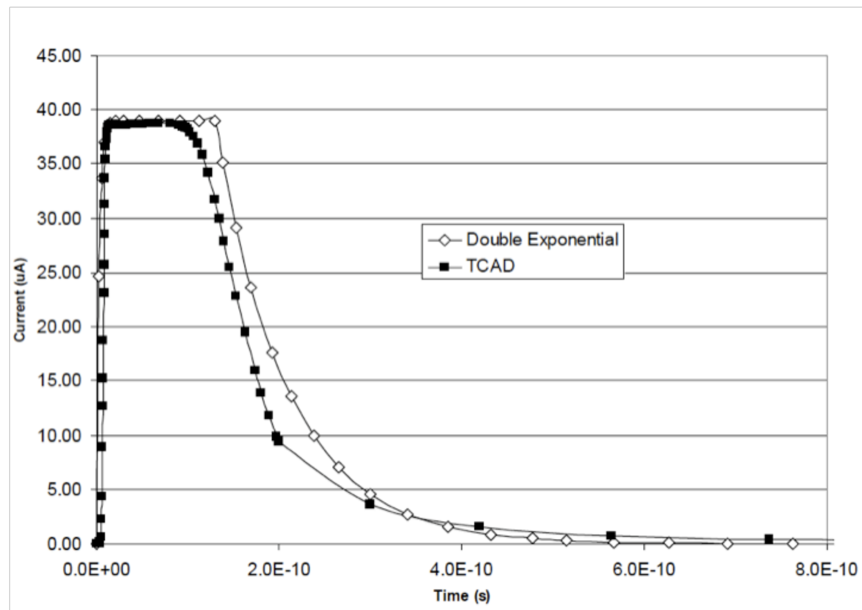

Figure 50: TCAD current profile and the corresponding SPICE double exponential fit for an LET of 2.0 $MeV cm^2/mg$ on the NMOS transistor.

Table 2: Parameters used for double exponential current source to simulate heavy ion strikes on NMOS

LET ($MeVcm^2/mg$)	Peak Current (μA)	Rise Time (pS)	Hold Time (pS)	Fall Time (pS)	SEU ? (Y/N)
0.5	37.0	3.0	30.0	40.0	N
1.0	38.0	3.0	75.0	50.0	N
2.0	39.0	3.0	130.0	79.0	Y
3.0	39.5	3.0	170.0	138.0	Y

Table 3: Parameters used for double exponential current source to simulate heavy ion strikes on PMOS

LET ($MeVcm^2/mg$)	Peak Current (μA)	Rise Time (pS)	Hold Time (pS)	Fall Time (pS)	SEU ? (Y/N)
0.5	55.0	5.0	10.0	46.0	N
1.0	55.0	5.0	45.0	67.0	N
2.0	55.0	5.0	100.0	124.0	N
3.0	55.0	5.0	180.0	190.0	Y

areas. In the case of the SRAM, the total NMOS and PMOS sensitive areas were estimated to be 0.36 and 0.28 μm^2, respectively. As was previously shown, NMOS and PMOS strikes produce SEU at different LET. Therefore, at an LET of 2.0 $MeVcm^2/mg$, only the NMOS sensitive region produces an upset, whereas at LET equal to, or greater than, 3.0 $MeVcm^2/mg$ the sensitive region is the sum of both areas. This is consistent with the observation that the PMOS and NMOS transistors collect different quantities of charge for ions having the same LET.

A comparison between experimental heavy ion SEU cross section curve and circuit simulation results is shown in Figure 51, where it is assumed that for the circuit simulations the physical area of the active silicon for the N- and PMOS transistors corresponds to the SEU cross-section. The cross sections are in relatively good agreement near threshold. Deviations below threshold ($2-3$ $MeVcm^2/mg$) are likely due, in part, to intracell variations in charge collection efficiency, inter-cell variations in critical charge, and possibly nuclear

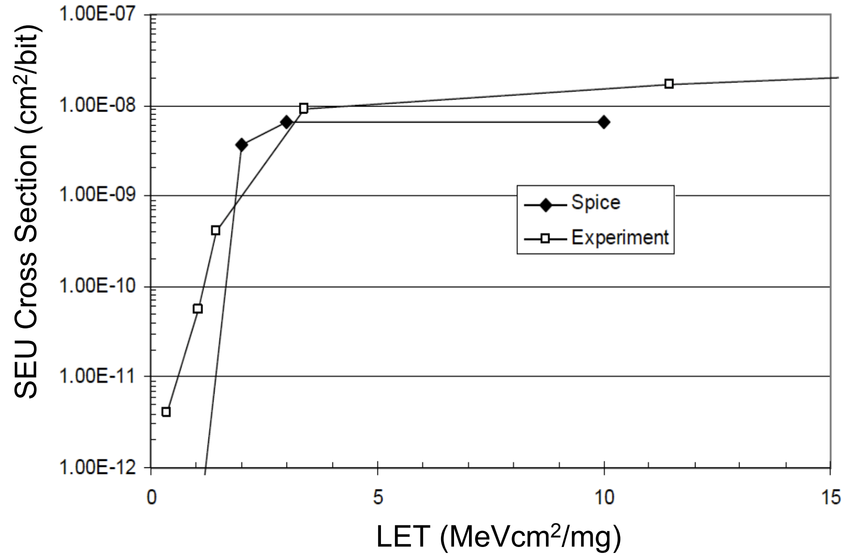

Figure 51: SPICE and experimental SEU results for the SRAM circuit.

reactions at the lowest LET. At σ_{sat}, the assumption of the diffusion and gate areas being a strictly bounded limit for the cross section is inaccurate due to charge collection by diffusion in the substrate. In general, the TCAD/SPICE analysis is in good agreement with the experimental data given the number of assumptions made in the analysis.

MRED Base-line Models and Configuration

SRAM Solid Model

In order for the SV to be used to tabulate energy deposition and approximate charge collection, a material or model in which to place the SV was required. For the SRAM, a complete 3-dimensional solid model was generated from layout information and scanning electron microscope (SEM) cross-sections (Figure 52). Each material within the real process was represented accurately, both from a spatial and compositional standpoint. While such target fidelity is not inherently necessary for heavy ion simulation, it is required for extensibility of the model to more complex environments such as high-energy neutrons and

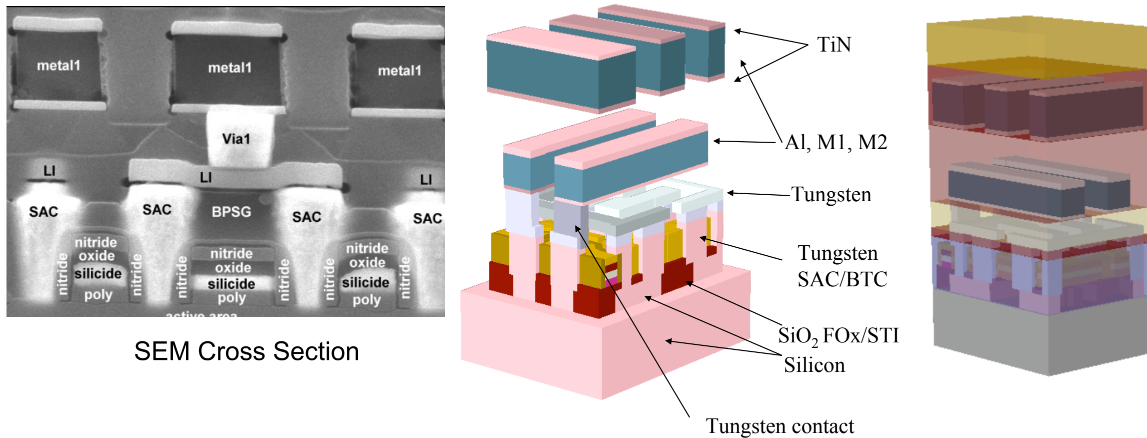

Figure 52: SEM cross section(left) and CAD models (right) of SRAM.

low-energy alpha particles.

Sensitive Volume Model

For the analysis described herein, a semi-empirical method of calibrating the sensitive volume efficiencies (α) to heavy ion SEU experimental measurements was used. Physical placement of the sensitive volumes was constrained by features of the solid model (oxide isolation, junction depths, etc.) and the charge collection efficiencies were adjusted to produce simulated SEU cross sections in agreement with the experimental measurements. MRED Version 8.23 was used to emulate the heavy ion broadbeam conditions from experiment with only the *Standard Screened* physics module invoked [29].

Experimental: Heavy ion SEU Measurement

Heavy ion testing was performed as a collaborative effort at the Brookhaven National Laboratory Tandem Van de Graaff facility with components, test fixtures, and evaluation software supplied by Jeffrey Wilkinson[1]. Upset cross sections were measured for the particle

[1]At Medtronic, Inc.

Table 4: Heavy Ion Species.

Ion	Energy (MeV)	LET ($MeV cm^2/mg$)
^{7}Li	56	0.375
^{11}B	84	1.07
^{12}C	99	1.44
^{7}F	140	3.38
^{35}Cl	210	11.4
^{58}Ni	265	26.6

species and energies shown in Table 4. The die surfaces were exposed for testing by removal of the package cover. Parts were irradiated in a static clock configuration to a user specified beam fluence after which point the state of the individual bits were downloaded to the evaluation software. Irradiations were performed for checkerboard, all zero, and all one logic configurations. The beam fluence was adjusted to guarantee that a maximum of 1% of total SRAM bits were upset in a given exposure frame. Irradiation angles, with respect to the beam direction and device surface, were 0°, 45°, and 60°.

SEU cross sections for supply voltages of 1.4, 1.5, and 2.0 V are shown in Figure 53, Figure 54, Figure 55, respectively. The most notable effects of supply voltage on SEU performance is a decrease in the threshold LET with decreasing voltage. Figure 56 contains the SEU cross sections as a function of the logic pattern stored in the SRAM. No change in SEU cross sections were observed as a function of logic state.

Sensitive Volume Calibration

A nested sensitive volume configuration was used to track energy loss in the substrate. Separate volumes were placed within the active silicon regions. for the SRAM. The locations of the sensitive regions were determined by examination of the layout and process, as well as TCAD simulation results. Charge collection, and thus energy loss, was only monitored in silicon regions. Insulating boundaries (e.g., STI, gate oxide), junction boundaries

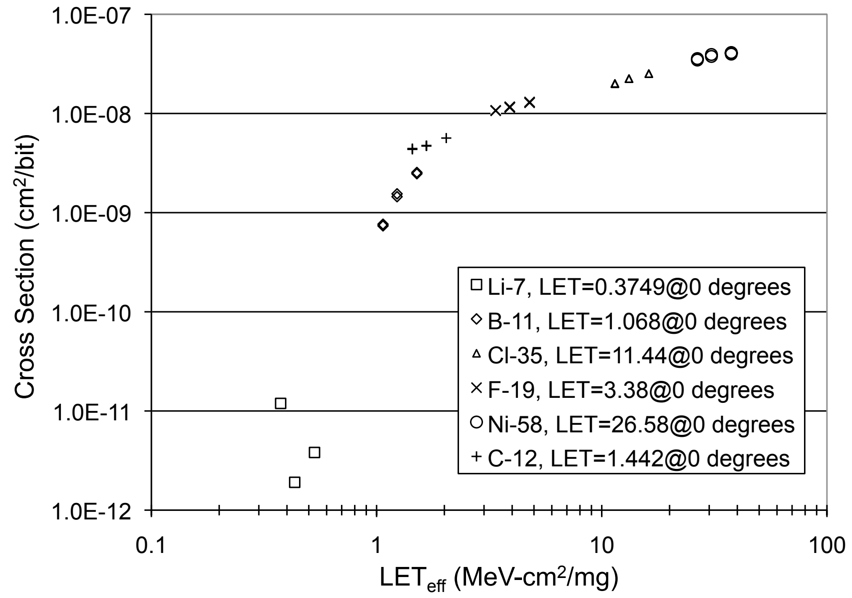

Figure 53: Heavy ion SEU cross sections at a supply voltage of 1.4 V.

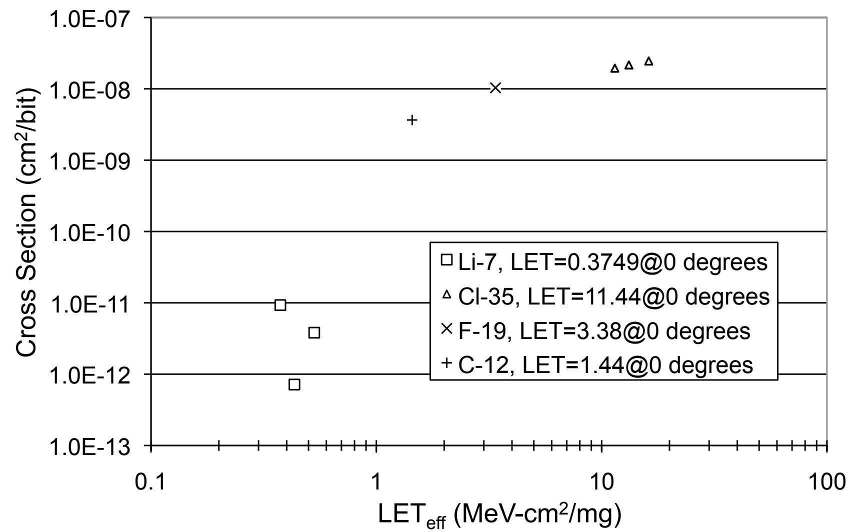

Figure 54: Heavy ion SEU cross sections at a supply voltage of 1.5 V.

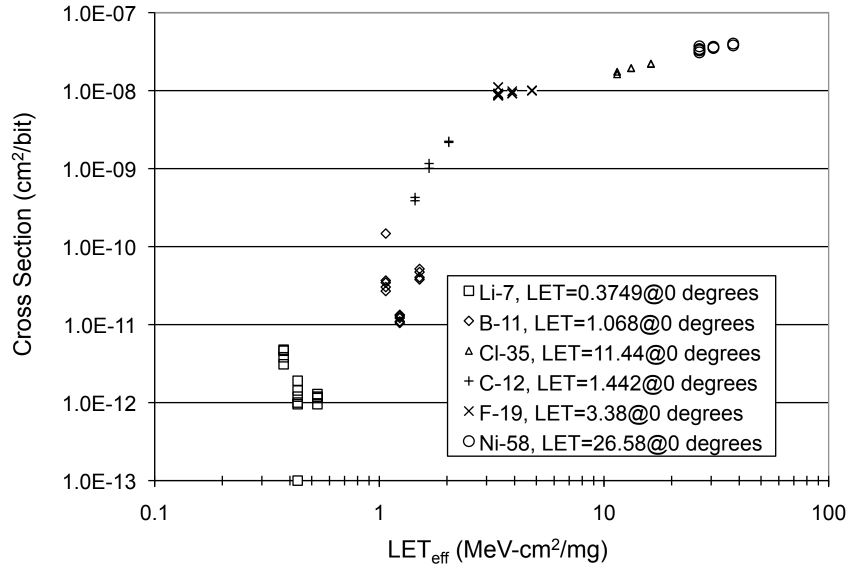

Figure 55: Heavy ion SEU cross sections at a supply voltage of 2.0 V.

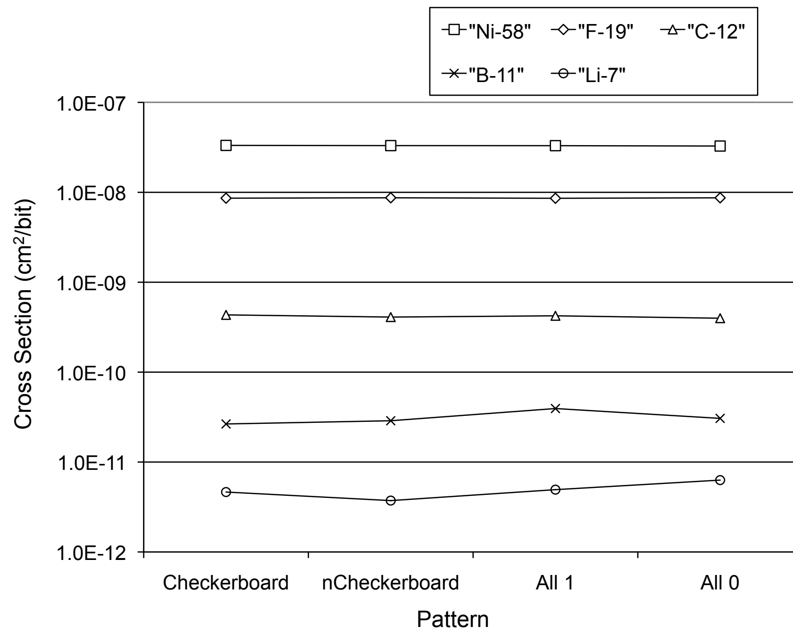

Figure 56: SEU cross sections as a function of logic pattern.

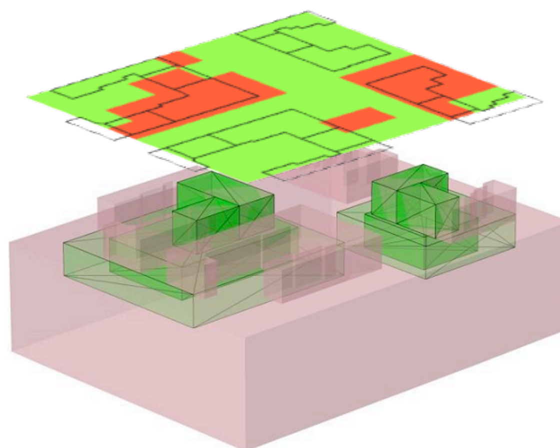

Figure 57: Active silicon region and substrate (pink) and sensitive regions (green) determined from TCAD and microbeam results.

(e.g., source-gate or drain-gate or well implant) established the lateral and vertical extents. Substrate sensitive volumes were centered beneath the center of the active silicon volumes extended laterally as needed to match the heavy ion cross sections.

Twelve volumes (Figure 57) were used to describe the sensitive regions of the circuit in a given logic configuration. The substrate volumes extended 0.2 μm beneath the STI. By inspection of the TCAD results, the highest values of α were found to be in the active silicon region of the off-state transistors drains. Efficiencies were substantially less for regions beneath the STI and far from the transistor drains. An example parameter set for the SRAM at $V_{DD} = 1.4$ V is shown in Table 5. The substrate volume sizes and efficiencies were adjusted as appropriate for the 1.5 V and 2.0 V data to reflect the differences in the experimental heavy ion SEU data (not shown).

The critical charges Q_{crit} @ $V_{DD} = 1.4$ V for the NMOS and PMOS transistors were determined to be 4.7 fC and 6.9 fC, respectively. For generating combined-cell energy deposition histograms, the efficiency of the PMOS transistor was lowered in such a way as to produce an effective Q_{crit} for PMOS strikes of 4.7 fC ($\frac{4.7}{6.9} \approx 0.68$). In other words, an SEU condition occurred when the total collected charge from the summation of all weighted

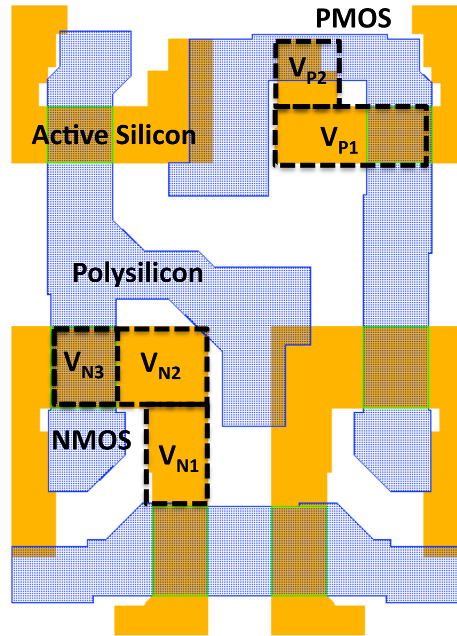

Figure 58: Positioning of sensitive volumes in the active silicon region for the NMOS and PMOS transistors.

Table 5: Sensitive Volume Parameters for the SRAM at 1.4 V

SV	α	Area μm^2	Depth μm	Transistor	Description
V_{N1}	0.75	0.12	0.30	NMOS	Active Silicon
V_{N2}	0.75	0.27	0.30	NMOS	Active Silicon
V_{N3}	0.15	0.11	0.30	NMOS	Active Silicon (under gate)
V_{NS1}	0.50	0.72	0.20	NMOS	Substrate
V_{NS2}	0.10	1.03	0.20	NMOS	Substrate
V_{NS3}	0.20	1.73	0.20	NMOS	Substrate
V_{P1}	1.00	0.15	0.30	PMOS	Active Silicon
V_{P2}	1.00	0.11	0.30	PMOS	Active Silicon
V_{PS1}	0.15	0.52	0.20	PMOS	Substrate
V_{PS2}	0.10	0.70	0.20	PMOS	Substrate
V_{PS3}	0.10	0.86	0.20	PMOS	Substrate
V_{PS3}	0.20	1.25	0.20	PMOS	Substrate

energy loss exceeded 4.7 fC.

When not producing energy deposition histograms the weighted collected charge for the NMOS and PMOS devices was evaluated separately against the 4.7 fC and 6.9 fC Q_{crit}, respectively. Histogram analysis is particularly relevant for examining the effects of reduced Q_{crit}, or the uncertainty in Q_{crit}, on the cross section or error rate. Otherwise treating NMOS and PMOS devices separately for each particle event is acceptable. For simple devices, such as an SRAM, the approach is valid. As will be shown in subsequent chapters, for devices containing more complex SEU mechanisms and higher transistor counts, determining cross sections and errors from histograms is unnecessarily burdensome, if not computationally impossible.

In this study, no difference was observed in using the histogramming method (Appendix B) and determining valid SEU events on an individual basis by direct comparion to $Q_{crit,p}$ and $Q_{crit,n}$. The validity of the multiple sensitive volume model, the parameters describing them, and the virtualization process is evidenced by the comparison of simulation to experiment as shown in Figure 59. Note that the particle species chosen for the SRAM analysis and calibration were those of the heavy ion experiments performed on the SRAM (Table 4).

High-Energy Protons

Testing and Simulation

Mono-energetic, high-energy proton testing of the SRAM was performed at the Northeast Proton Therapy Center (NPTC) associated with Massachusetts General Hospital [111] by Jeffrey Wilkinson. The primary beam at the center is 230 MeV and was degraded incrementally to a minimum energy of 27 MeV for SEU testing. The SRAM devices were configured in a checkerboard (alternating 1s and 0s) pattern and irradiated in a continuous read back mode of operation.

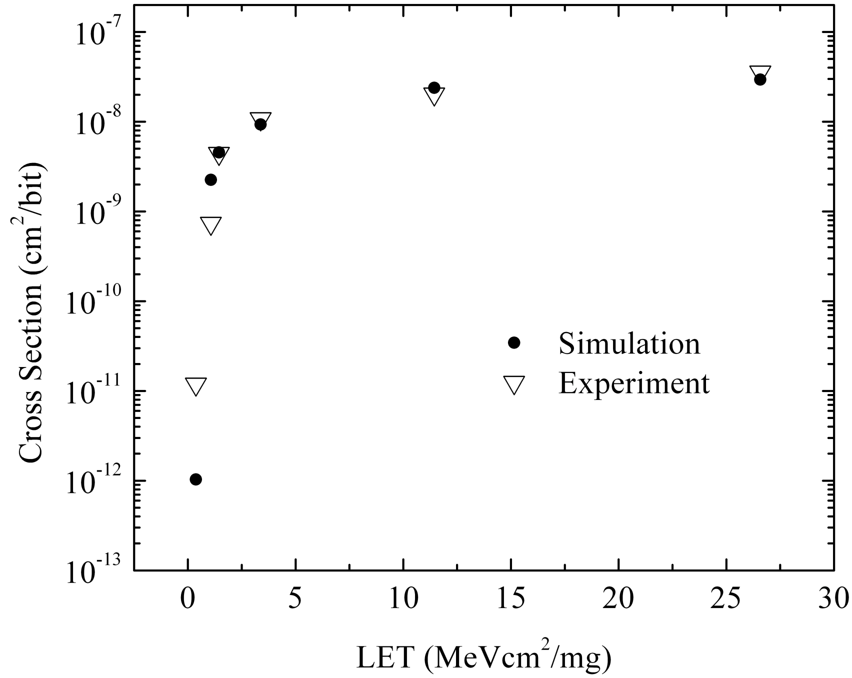

Figure 59: Experimental heavy ion cross sections and calibrated MRED model at normal incidence, V_{DD}=1.4 V.

Simulated cross sections were determined by using the calibrated heavy ion sensitive volume model. Identical sensitive volume parameters and critical charge requirements from the heavy ion calibration were used. It is important to recognize that while heavy ion simulations are not generally sensitive to process details, proper simulation of proton and neutron SEU requires capturing the material and geometrical details of the process front-end-of-line (FEOL) and back-end-of-line (BEOL). As is shown in Figure 52, the CAD model contains this level of detail.

The size of the solid model was extended to capture 4 SRAM cells simultaneously, and the 4-bit array replicated into a 16x16-bit array (using replication features contained within MRED). In addition, 4 dummy cells (those not containing sensitive volumes, and not included in the per-bit normalization of σ_{SEU}) were added at each boundary to allow for secondary particle creation outside of the monitored region and to reduce potential edge

Table 6: Physics Models

Name	Comments
Standard Screened	Electronic stopping and screened coulomb scattering
NucleonInelasticA	Binary Cascade, High-precision neutron ($< 20\ MeV$)
Hadron Elastic	Nuclear Elastic
Hadron Inelastic	Nuclear Inelastic
IonInelastic	Ion-ion nuclear reactions ($Z > 1$)
PiK Inelastic	Pion and kaon production

effects. The physics model selection for the proton and neutron simulations is shown in Table 6. MRED Version 8.23 was used in all simulations.

The predicted and measured proton induced SEU cross section are shown in Figure 60 for a supply voltage of 1.4 V. The simulated energy range was decreased below the experimental minimum of 27 MeV to 5 MeV, which is the highest energy at which no SEUs were predicted. The excellent agreement between experimental and simulation results demonstrates the validity of using physics based simulation and a single model to capture the SEU response of the SRAM circuit.

The measured device cross section is a function of four prominent factors: The total elastic and inelastic cross section for the incident species, the angular distribution and type of secondary species resulting from inelastic collisions, the stopping power and range of the resultant species with respect to the reactions and sensitive volume placement, and the circuit response. It's important to recognize at this point that the heavy ion and proton response and the models used to predict them are unified into one simulation construct.

Of note in the cross-sections of Figure 60 is the peak shown in the simulated σ_{pSEU} at approximately 25 MeV. A rise in σ_{pSEU} is suggested by the measured data but not resolved due to test limitations. Such peaking has previously been reported by [112]. The total $^{28}Si(p, X)$ cross sections indicates a peak at approximately the same proton energy [113].

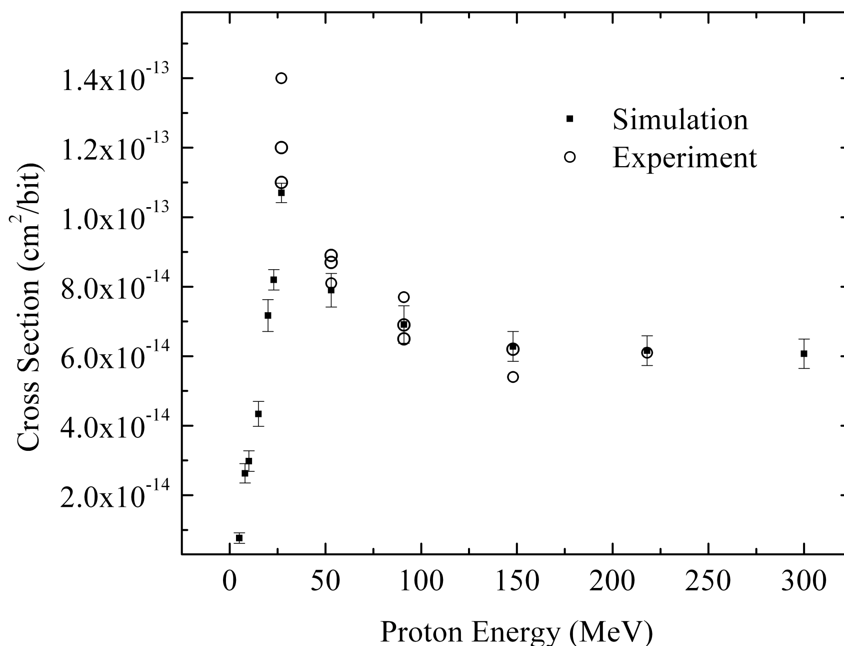

Figure 60: Simulated and measured proton SEU cross sections at 1.4 V.

High-Energy Neutrons

As in the case of protons, simulated neutron cross sections were determined by using the calibrated heavy ion model. However, no mono-energetic neutron data were available against which to compare the simulated results. A comparison of the simulated neutron and proton cross sections over the same energy range is shown in Figure 61. Systematically, the neutron cross sections are higher by approximately 10%. The prediction is consistent with analyses performed by Lambert, et al. [112], where the ratio of production cross sections for protons to neutrons in silicon producing events which exceed 10 fC was also approximately 10%, although his dosimetry configuration is not equivalent to the one presented here for the SRAM.

A comparison of the low energy range of the neutron and proton cross sections is shown in Figure 62. The energy threshold for neutron SEU is lower than that of protons, which is consistent with nuclear Coulombic effects associated with protons. This will also contribute

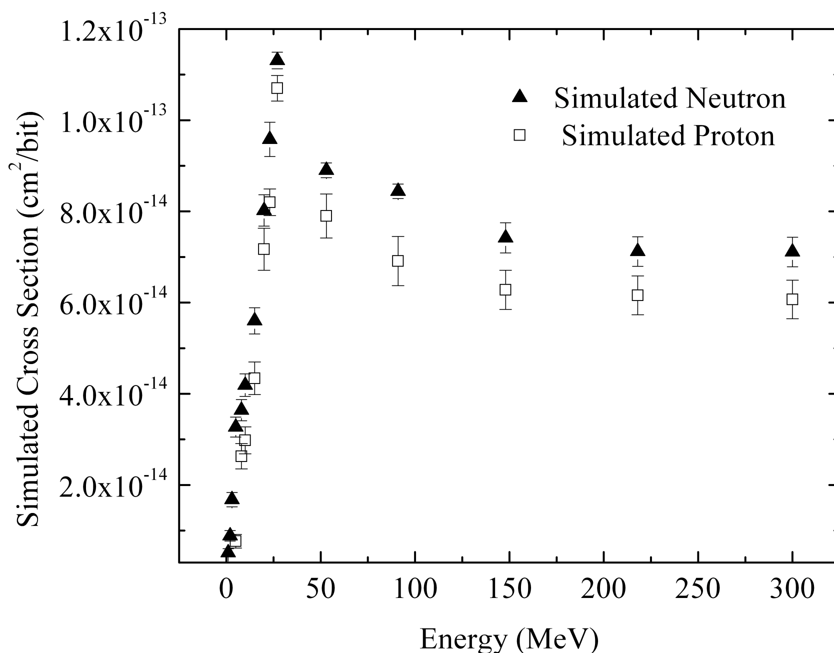

Figure 61: Comparison of simulated proton and neutron SEU cross sections at $V_{DD} = 1.4$ V.

to under-prediction of the soft error rate using proton data alone per the methods described in JESD89A [64].

High-Energy Neutron Error Rate Calculation

The soft error rate was calculated using the methods outlined in JESD89A for the New York City high-energy neutron environment (Figure 63). The calculation was discussed in the introductory chapter and the equation is reintroduced here in (28) where R is the rate in errors per bit-second, Φ is the neutron flux $(cm^{-2}s^{-1}MeV^{-1})$ in the ith bin of the discrete spectrum, and $\sigma(E_i)$ is cross section (cm^2/bit) at that energy. ΔE is the width of the bin in units of energy (MeV). The summation is taken over the total number of energy bins, n, in the environmental spectrum. For this calculation, an interpolated cross section between energy points was used. For energies beyond those measured, the cross section was assumed to saturate at the last data point (therefore, the cross section does not drop to zero at high

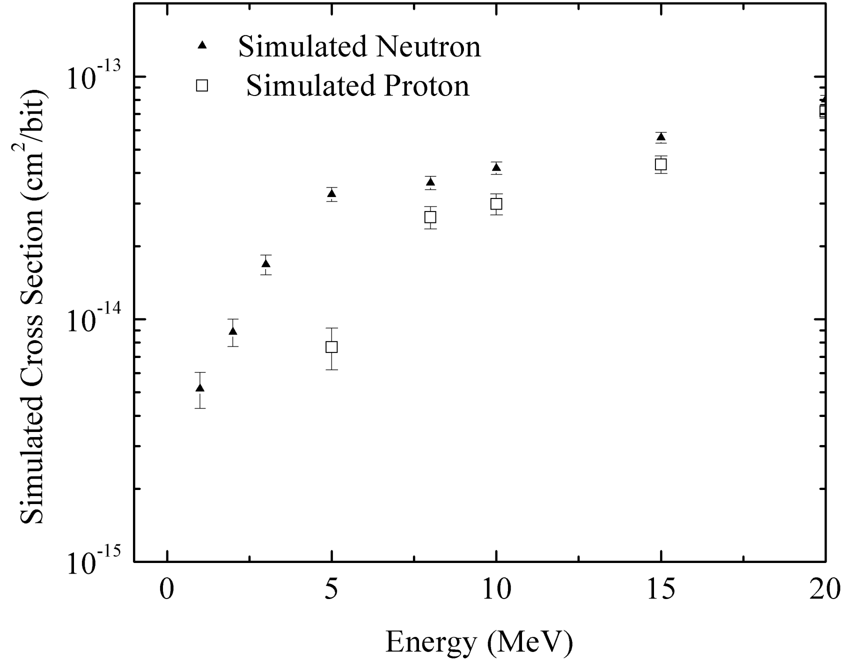

Figure 62: Comparison of simulated proton and neutron cross sections near threshold.

energies).

$$R = 3.8 \times 10^{18} \frac{FIT}{MBIT \cdot s} \left(\sum_{i=0}^{n} \Phi\left(E_i\right) \sigma\left(E_i\right) \Delta E \right) \tag{28}$$

The neutron error rate for New York City was calculated to be 800 and 910 FIT/MBIT based on the experimental and simulated proton cross sections, respectively using (28), where Φ is the neutron flux in $cm^{-2}s^{-1}MeV^{-1}$, σ is the neutron cross section in cm^2, and E is the energy in MeV. The mean 12% difference is predominantly due to the absence of low energy cross section experimental data (27 MeV minimum); thus, the error rate derived from the simulated cross section over the full energy range is believed to be more accurate.

An alternate approach to calculating the soft error rate is to test at the ICE House neutron facility and is discussed in JESD89A. The neutron spectrum of ICE house mimics that of the natural environment at a substantially higher flux (Figure 64). Simulation allows one to evaluate the validity of both the predicted error rate from the discrete proton cross

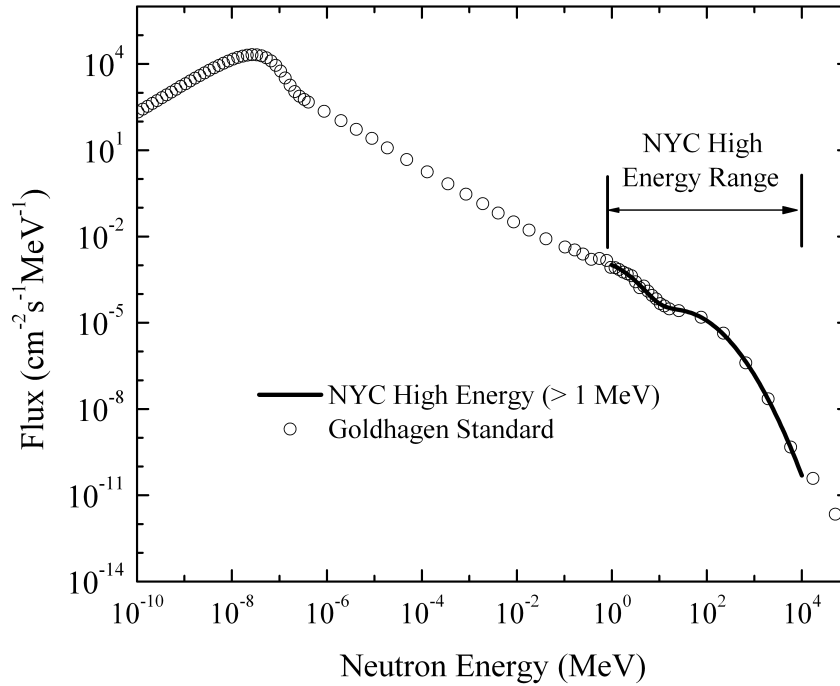

Figure 63: Full NYC neutron spectrum (Goldhagen) with *high-energy range* illustrated.

sections as well as irradiation at the ICE House facility. The calculated ICE House neutron FIT rate was 920 FIT/MBIT.

The highest fidelity method for estimating the high-energy neutron component of the terrestrial error rate by sampling the known neutron spectrum. This procedure was performed on the MRED SRAM model by selecting the sea-level NYC neutron spectrum shown in Figure 64 [64]. The beam direction was held normal to the device surface in the direction of the device. The initial positions of the particle were chosen randomly above the surface. The error rate from the high energy neutrons was calculated as 1240 FIT/MBIT. The combined results from all methods are shown in Figure 65. A summary of the trends is as follows:

1. The derived failure rate using the discrete experimental proton cross sections underpredicts the simulated spectrum of the high-energy NYC neutron rate by 35%.
2. The derived failure rate using the discrete experimental proton cross sections underpredicts the scaled, simulated spectrum of the ICE House error rate by 13%.

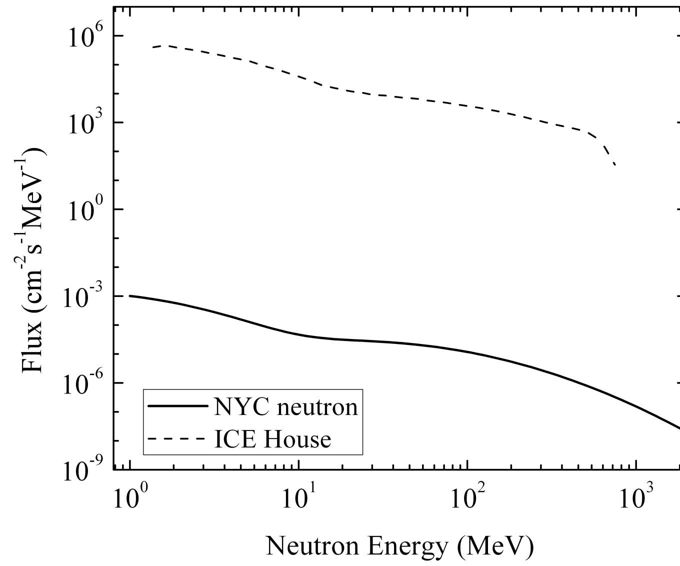

Figure 64: A comparison of the neutron flux at sea level and the ICE House neutron spectrum.

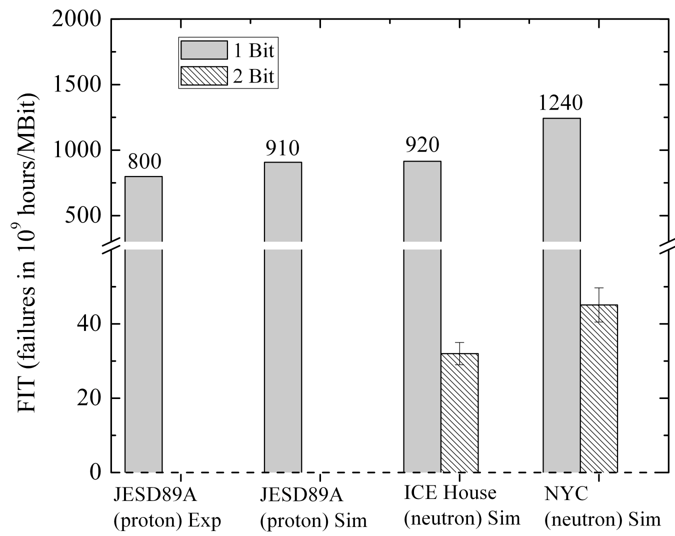

Figure 65: Calculated neutron FIT rates from experiment and simulation..

3. The simulated, discrete mono-energetic proton cross sections under-predict the full NYC spectrum error rate by 27%.
4. The JESD89A derived error rate from the simulated, discrete, mono-energetic protons is in good agreement with the ICE House spectrum simulation calculation.

Simulations indicate that test limitations (lack of low-energy data) introduced a 13% error in the calculated SER when applying JESD89A test and analysis methods to the experimental and simulated proton cross section curves. Furthermore, the evaluated accelerated test methods under-predict the true high-energy neutron SER (NYC) by 27% to 35%. The fidelity of the simulation approach is supported by the agreement between the simulated and measured proton cross sections.

Thermal Neutron Error Rate Calculation

As discussed in the Introduction, thermal neutrons represent a reliability concern for processes containing substantial quantities of ^{10}B by virtue of the $^{10}B(n,\alpha)^{7}Li$ capture and decay process. As shown in Figure 52, the SRAM evaluated in this chapter contains a BPSG planarization layer which exists in close proximity to the sensitive volumes previously described. Estimating the thermal neutron induced single event error rate is a necessary step in determining the total operational SER.

For simulation, the SRAM was exposed to 1×10^{9} normally incident mono-energetic neutrons at 26 meV using BPSG with ^{11}B isotopic purities of 80% (natural), 95%, and 99% in MRED. The standard physics list (Table 6) was invoked in MRED. Particles were randomized over the surface of the SRAM. For each incident neutron, the net collected charge in the sensitive volumes was tabulated in the usual fashion (as determined by the SV set shown in Figure 57). The cross section, $\sigma_{n_{th}}$, was calculated by (29) from the energy deposition histogram, performing a reverse integration and normalization in the usual manner, and identifying the sum of events whose mean charge exceeds Q_{coll}, and multiplying by the total irradiated surface area or randomization area, A. The cross sections

for the natural $^{10}B/^{11}B$ and purified ^{11}B cases as a function of collected charge are shown in Figure 66, without error bars for clarity. The corresponding thermal neutron soft error cross section is $6.15 \pm 0.05 \times 10^{-13}$ cm^2/bit where the error is from counting statistics only. The experimental value of $4.5 \pm 0.5 \times 10^{-13}$ cm^2/bit differs from the simulation result by approximately $35 \pm 15\%$.

$$\sigma\left(E_{coll}\right) = \frac{A \sum_{i(E>E_{coll})}^{\infty} N(E_i)}{\sum_{i=0}^{\infty} N(E_i)} \tag{29}$$

Given the cross section curve in Figure 66 and a typical atmospheric thermal neutron flux of 4 $cm^{-2}hr^{-1}$, the soft error rate is shown in Figure 67 for a range of collected charges. Also included in the plot is the effect on the SER of using 95% and 99% purified ^{11}B BPSG. For the natural boron case, the SER rate prediction is 2600 FIT/Mbit and purification to 95% and 99% ^{11}B reduces the SER to 700 and 150 FIT/Mbit, respectively, at V_{DD}=1.4 V. Increasing the supply voltage to 2.0 V reduces the SER to approximately 700 FIT/Mbit for the naturally occurring isotopic ratio. The simulation method described here produces results in good agreement (±30%) with experimental data for thermal neutron soft error cross sections and provides a direct method for predicting the SER given an terrestrial thermal neutron flux.

Simulating Alpha Sources

Alpha SEU simulations present a unique modeling challenge relative to the previously described environments. Alpha particles from radioactive decay have short ranges relative to high-energy and weakly interacting particles. The proposed solution is to model emission from within the TCAD object itself, using the radiation transport code to properly degrade the emission spectrum from thin and thick film sources. This approach differs from other environments where the radiation arrives from positions external to the CAD model. An alpha emitting film and SRAM model is illustrated in Figure 68 (note that the figure is for an americium source, but the same construction is used for thorium).

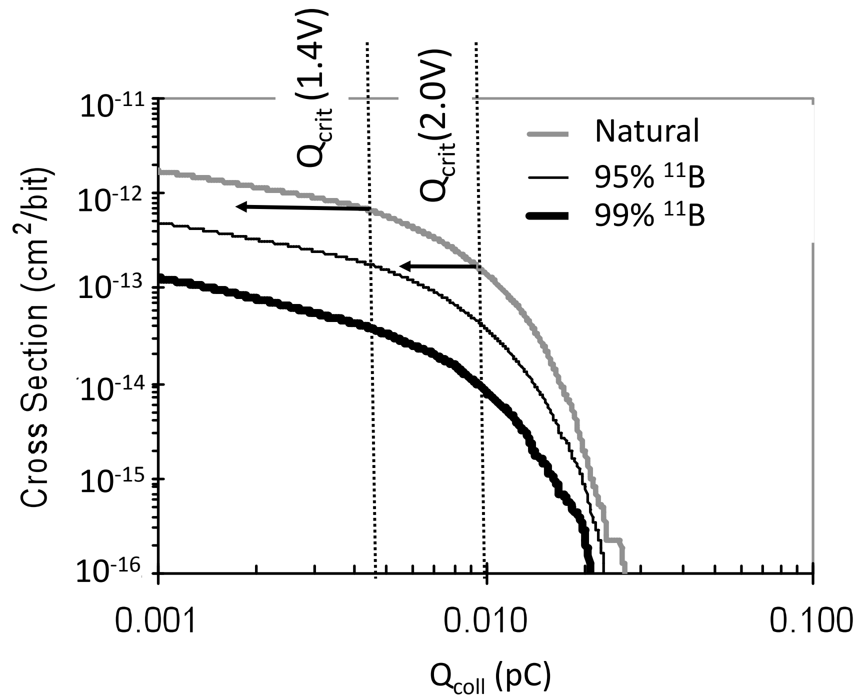

Figure 66: Thermal neutron cross section as a function of critical charge for the naturally occurring and purified compositions of $^{10}B/^{11}B$.

Alpha particles are emitted from within the device model itself, but in the experimental case, the separation distance between the source and DUT is an order of magnitude greater than the thicknesses of solid CAD model. Specifically, the experimental air-gap thickness used for determining the SEU cross section was 15 mm, but the single CAD device has dimensions on the order of 10s of μm. The high-aspect ratio (*long and thin*) this produces in the CAD model is unacceptable in that most emitted particles would simply exit the structure. The solution is to model a layer of air with the correct stoichiometry but at a density 1000x of air at 760 torr and 15 μm thick, as shown in Figure 68. For experimental cases other than 15 mm, the same CAD thickness of 15 μm is used, but the density of air is adjusted to mimic the effect of increased or decreased distance.

The scaling of the air-gap thickness introduces a difference in the admission angles (and thus energies) of alpha particles arriving at the active silicon surface between experiment

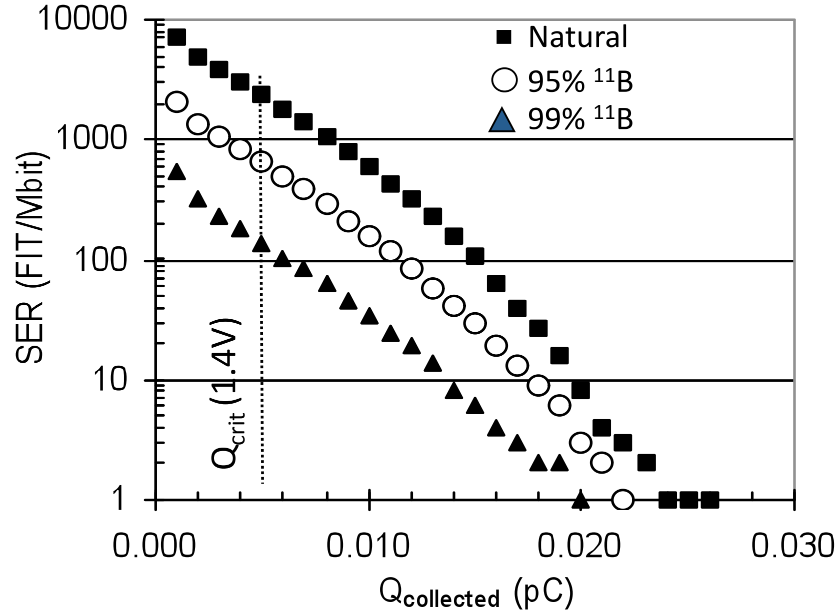

Figure 67: Predicted soft error rate as a function of Q_{crit}. The rates for 95% and 99% purified ^{11}B in BPSG are also shown.

and simulation. To overcome this, the 4 bit SRAM basic CAD model, with the air-gap and emission source is replicated 1024 times. Alpha particles are emitted from the source film (thick or thin) in the entire replicated array. However, only a subset of devices in the center of the array are monitored for SEU. This allows for accurate representation of slowing by alpha particles arriving at grazing incidence. Furthermore, a dosimetry volume is placed at the active silicon surface of the passivation layer of the CAD model which spans the extent of all SEU monitored cells, and is used to count alpha particle arrivals (regardless of whether or not SEU occurred). The 'dosimetry volume' determines the activity of the alpha emitting source as seen by the individual SRAM cells and the total number of particles counted in that region are used to calculate the source fluence. Thus, in simulation, the total number of events that are used in determining the SEU cross section are the number of hits to the 'dosimetry region', rather than the total number of particles emitted from the foil.

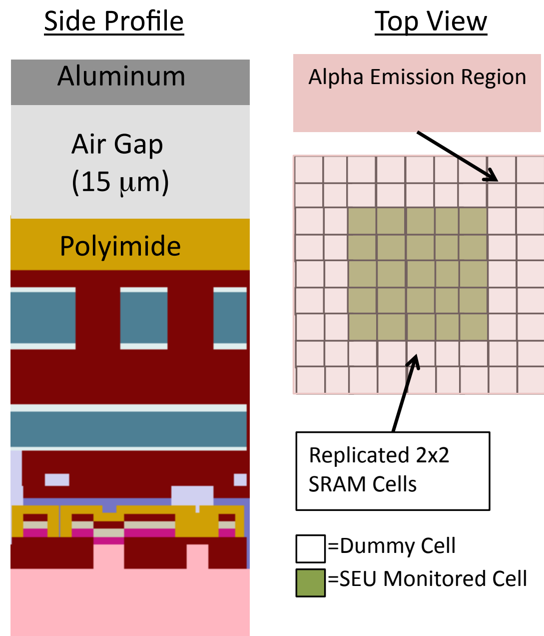

Figure 68: Side and Top Views of the SRAM solid model and emission locations as simulated in MRED (^{241}Am foil).

Americium Foil Source

The purpose of the americium foil simulations is to demonstrate that alpha SEU cross sections can be determined with MRED, using the heavy ion calibrated sensitive volume models, that are in agreement with SEU cross-section measurements for a thin foil source. The source, manufactured by Eckert & Ziegler, is made of ^{241}Am deposited on the surface of a thin aluminum foil 20 mm in diameter. The activity of the source was 300 nCi. This is $1.1 \times 10^4 \frac{decay}{s}$ for both top and bottom surfaces of the foil, and $5.5 \times 10^3 \frac{decay}{s}$ from one surface in the direction of the die. Uniformity of received dose (activity) at the die surface was improved by maintaining 15 mm of separation with the alpha source. Experimental measurements (of spectra and SEU rates) were performed by Scott Morrison[1].

MRED ^{241}Am thin film sources are modeled by creating a film of aluminum. 5.5 MeV alpha particles are emitted from the film. The emission position in the plane is random over

[1]At Medtronic, Inc.

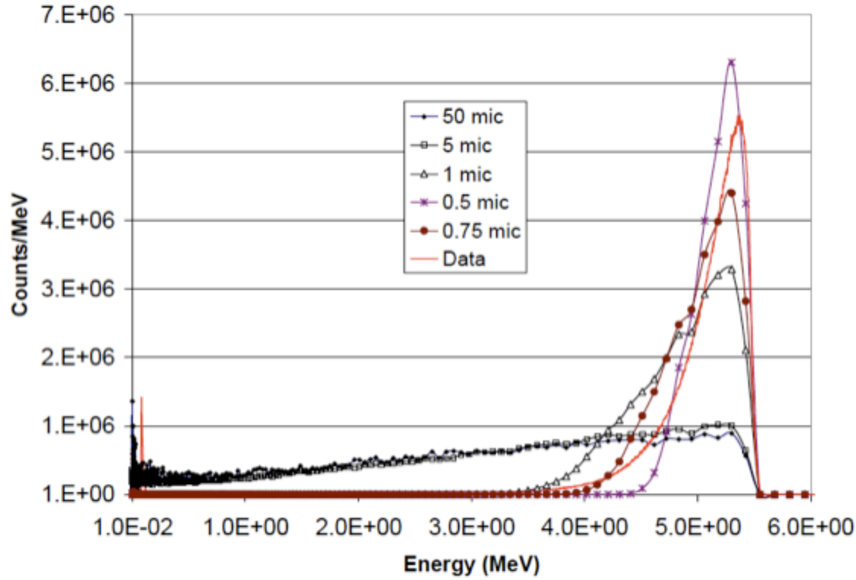

Figure 69: Series containing the simulation of ^{241}Am activity as a function of energy for a range of source depths and the actual source used in measurement.

the lateral extents of the foil, and the emission depth relative to the foil surface is randomly chosen (shown in the figure legend) between the surface and a fixed maximum depth, and the direction is random uniform over 4π. The experimental and simulated spectra for a series of maximum emission depths are shown in Figure 69. The MRED simulation and experimental measurements most strongly agree for maximum emission depths of 0.5 to 0.75 μm, which is consistent with the porous-foil manufacturing process as described by the foil supplier.

A series of experiments and simulations were performed to validate the proposed alpha-particle simulation methodology on the SRAM using the ^{241}Am source. SEU measurements were taken on the 4 MBit SRAM for source-to-DUT spacings of approximately 5, 10, and 15 mm in a bell jar at 760, 350, and ≈ 0.1 torr. MRED simulations were performed using the CAD model shown in Figure 68 and the sensitive volume parameters derived from circuit simulation, TCAD modeling, and heavy ion beam calibration. Alpha particles were randomly emitted from the aluminum film at the bottom (oriented as shown in the figure)

to a maximum depth of 0.6 μm.

The emission angle range ($\pm\theta_{max}$) in MRED is the maximum angle at which alpha particles may reach the die surface, as shown in Figure 70, determined from the geometry of the experimental setup. The hard limitation is necessary (in MRED) since the CAD model uses a 15 μm rather than a 15 mm air-gap. The 15 mm air-gap, in conjunction with the 6x6 mm die size and the 20 mm diameter foil limits the range of the angles of the incident alpha particles. Without imposing a hard limit on the emission angle, the MRED model would incorrectly include alpha particles arriving at grazing incidence.

A complicating factor in relating the source activity to the error rate of the SRAM is the capture efficiency (ξ) of the die surface as a function of foil distance, shown in the right-hand side of Figure 70. In short, a fraction of the emitted alpha particles reach the die, and one must know this efficiency to calculate the SEU rate as a function of source activity in MRED. Baumann, et al. discuss the issue in detail in [114]. For the purpose of this work, a separate Monte Carlo simulation was used to calculate the efficiency factor as the ratio of the number of emitted particles from the foil to the number of particles passing through the die surface using the dimensions of the experimental setup. The results are shown in Table 7.

The chip-level (4 MBit) SER in MRED is calculated according to (30), where N_{SEU} is the number of valid SEU, N_{DR} is the number of counts in the 'dosimetry region' (number of alpha particles striking the monitored SRAM bits), ξ is the efficiency defined in Table 7, A_S is the activity of the source, and S_{bit} is the number of bits contained within the 'dosimetry region'. The experimental and simulation results are shown in Figure 71 and shows excellent agreement between the methods over distance and ambient pressure.

$$SER_{sim} = \frac{N_{SEU}}{N_{DR}} \cdot \xi \cdot A_S \cdot \frac{4MBit}{S_{bit}} \qquad (30)$$

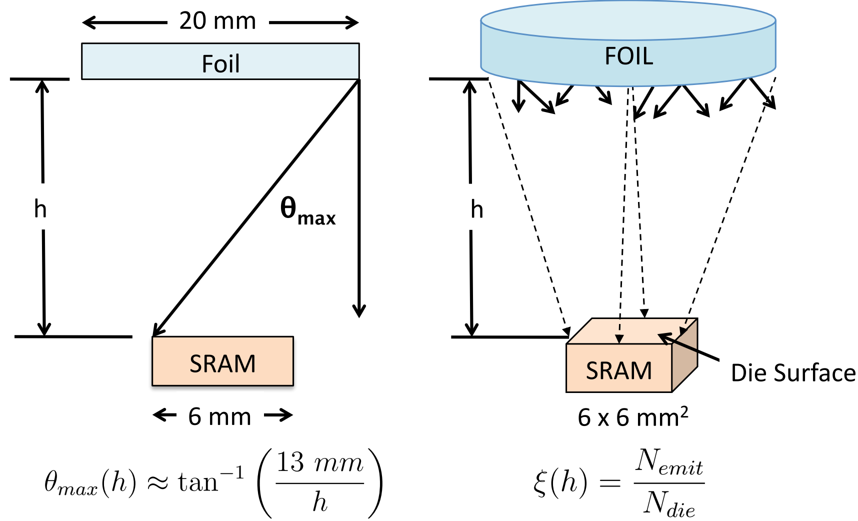

Figure 70: Graphical representation of the maximum emission angle (left) and capture efficiency calculations (right) for the MRED ^{241}Am alpha model.

Table 7: ^{241}Am Simulation Parameters

Spacing, h (mm)	θ_{max} (degrees)	ξ %
15	41	0.66
10	52	1.4
5	69	2.6

Thorium Thick Source

The simulation methodology presented in the previous section is now applied to a thick-film ^{232}Th source. While the emission randomization in space and angle was similar to that illustrated in Figure 68, the nature of the source presented an additional challenge with regards to properly defining the alpha emission energy and abundance. This is due to the fact that the thorium source is composed of solid thorium in secular equilibrium. Thus, the emission spectrum is not mono-energetic with some degradation due to the film thickness (as in the americium case), but rather, multi-spectral and degraded due to the presence of multiple emission energies from ^{232}Th daughter products.

The solution to the emission energy problem was to determine by defining an analytical

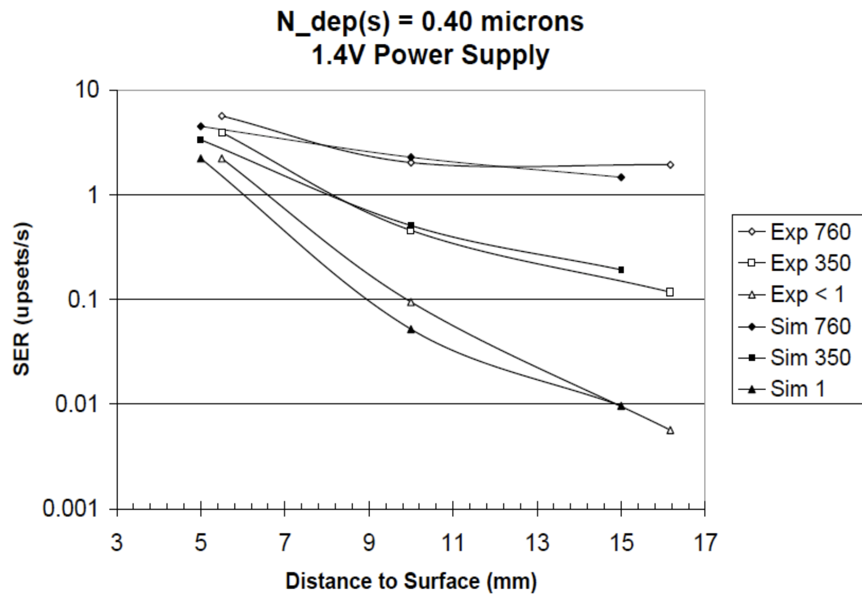

Figure 71: Soft error rate as a function of air gap thickness for the 300 nCi Am source on the 4 Mbit SRAM. Each series is for a given atmospheric pressure (in units of torr).

solution to the decay chain sequence using algebraic techniques described in [115], built upon knowledge of the decay sequence, daughter products and their lifetimes, and emission energies for each species [113]. Note that this approach produces a line spectrum, weighted by the abundance and activity of each product as a function of equilibration time. The resultant thick-film emission spectrum from the line spectrum generated at 50 years of equilibration time is shown in Figure 72. By 50 years, the source is predominantly in secular equilbrium. That is, its composition does not dramatically change per increase in time.

A comparison between simulation predictions and experimental measurements was performed for the ^{232}Th thick source. Unlike the Americium experiments, a polyimide degrader of varying thickness was placed between the source and the DUT and the cross-section was measured for each thickness. The results are shown in Figure 73. Note that both the experimental and simulated curves show good agreement in rate of cross section decrease per increase in polyimide thickness. The magnitudes are also in relatively good agreement,

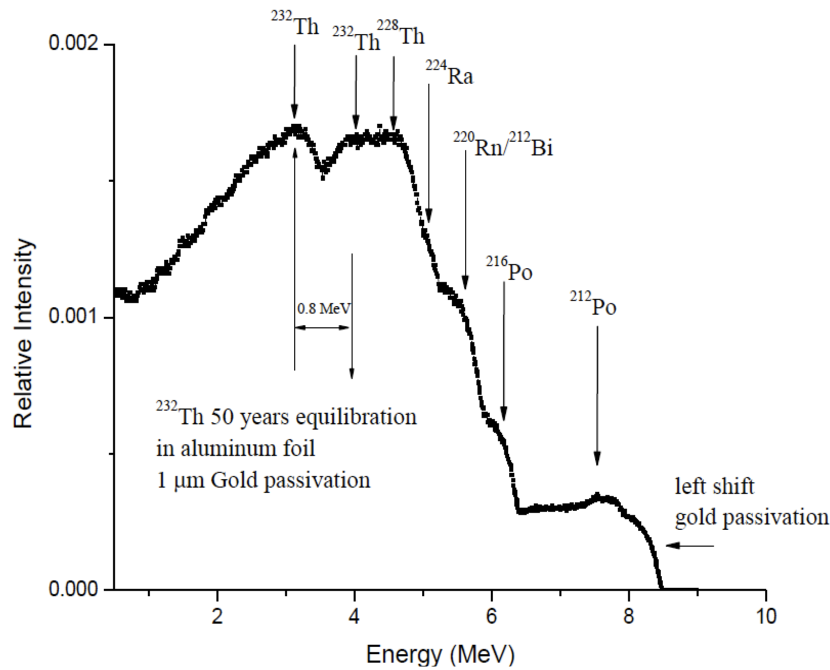

Figure 72: Simulated ^{232}Th source activity in secular equilibrium. The gold passivation is intended to capture degradation due to source or detector passivation materials. Peaks of the various ^{232}Th decay products are shown.

differing by less than 25% over the range of evaluated conditions.

The critical difference between the thorium and americium simulations lies in the energy distribution of the alpha particles and the measurement the activity, A_s, of the source. The thorium decay chain contains several β emission channels in the sub- 1 MeV range. While a 1 MeV cutoff was used in the 'dosimetry volume' to discard SEU and alpha counts in this range in accordance with the activity measurements performed by Medtronic, it was not specifically determined if sub 1 MeV alpha particles were causing SEU. In short, it was not immediately clear if the source of error was due to difference in the dosimetry performed using MRED and by experimental methods which resulted in error in the magnitude of the source activity.

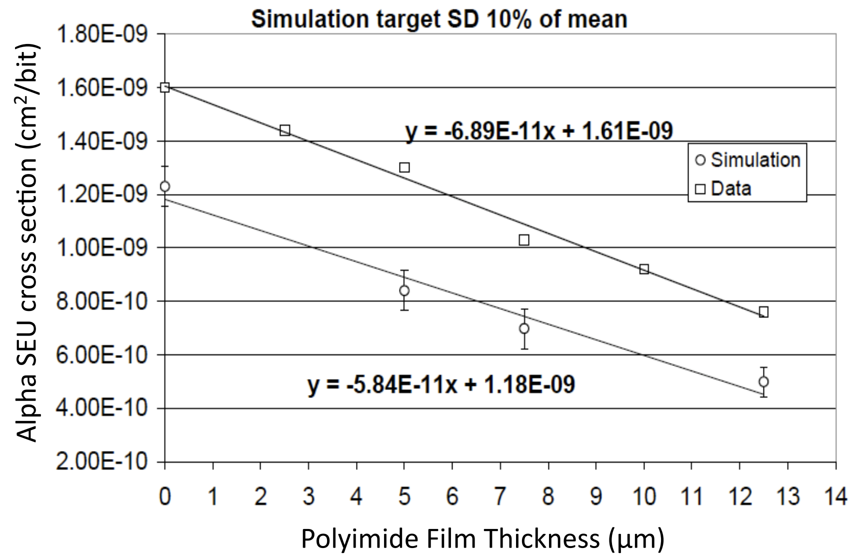

Figure 73: MRED simulated and experimentally measured alpha SEU cross-section as a function of polyimide film degrader film thickness on the SRAM. The source activity was calibrated to the vendors ^{232}Th thick source.

Conclusions

It has been demonstrated that a sensitive volume model can be used to accurately predict the SEU cross sections and error rates from high energy neutrons, thermal neutrons, protons, and alpha particles for an SRAM. The method of calibrating sensitive volume differs from that explored in Chapter II in that heavy ion SEU cross sections are used to determine the final extents of the sensitive volume dimensions and the circuit response (Q_{crit}) was determined by SPICE simulation. Calculation of collected charge is provided by the multiple sensitive volume model, but energy loss calculations require the use of physics based transport which in this study is provided by MRED. This unified approach to error rate prediction deviates from the traditional, independent methods discussed in Chapter I.

CHAPTER IV

SENSITIVE VOLUME GROUPS AND MULTI-NODE SEU MECHANISMS

Introduction

In this chapter, the SEU response of a hardened-by-design latch, fabricated in a 90 nm technology, is analyzed using multiple sensitive volume groups within MRED. Angular dependencies on the measured heavy ion SEU cross section along both axes were determined to be results of multiple-node charge collection processes. The ability of the multiple sensitive volume model to reproduce the complex features of the experimental data and its subsequent application to on-orbit soft error rate (SER) prediction is demonstrated.

Latch Design

The latch circuit design is that of a dual interlocked cell and a detailed discussion of its operation is contained in [116]. Ion strikes to a single node will not result in a SEU. However, the state can be corrupted if a single particle deposits sufficient energy to simultaneously perturb the potential of two sensitive nodes [53].

The 12-transistor SEU hardened latch is fabricated in a 90 nm CMOS epitaxial, 9 layer metal process. Schematic and annotated layout views of the circuit are shown in Figure 74. Spatial separation of sensitive node pairs reduces the probability of multiple-node effects such as charge sharing, especially between NMOS transistors, reducing the probability of SEU.

Experimental

Heavy ion broadbeam SEU experiments were performed by Xilinx, Inc. Ion beams of 10 MeV/u Xe (58.7 $MeVcm^2/mg$), Kr (31.2 $MeVcm^2/mg$), and Ar (9.7 $MeVcm^2/mg$) were used. Static SEU cross were measured at tilt angles between 0° and 75° and over

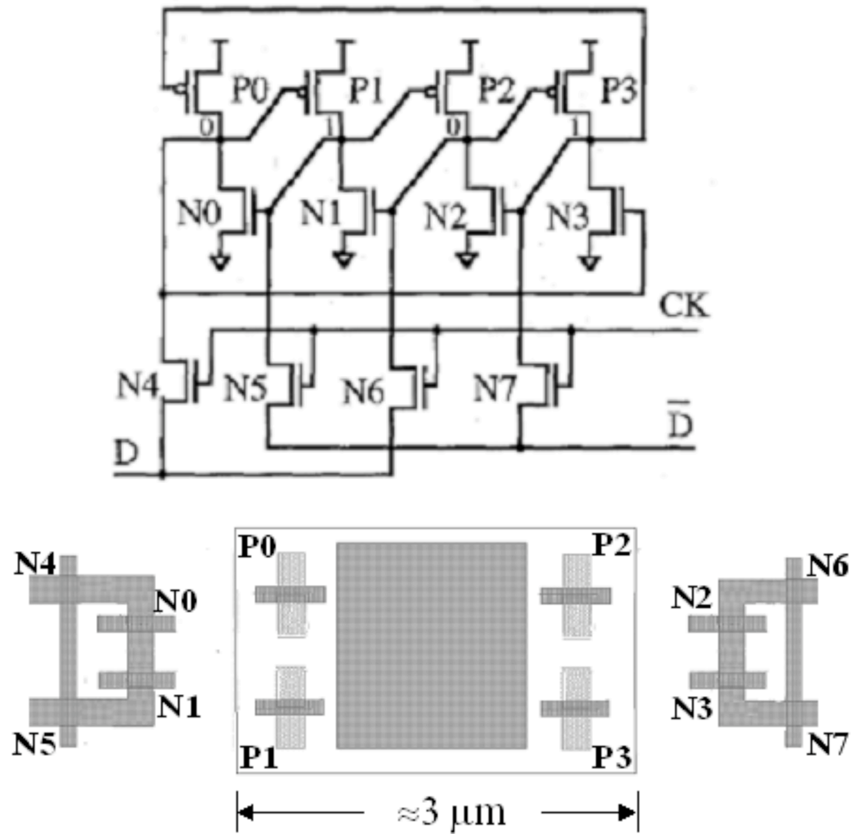

Figure 74: Schematic and Layout of DICE Latch.

a 180° range of roll angles. In this discussion, tilt refers to the angle between the device surface normal and the beam direction. Roll refers to the relative angle of the DUT about the axis of the beam direction (Figure 75). The devices were programmed in a checkerboard pattern (spatially alternating 1s and 0s).

The SEU cross sections are presented in Figure 76 as a function of effective LET in the customary manner. The data points represent the cross sections measured at regular intervals over 180° of roll, at tilt angles greater than 40°. For tilt angles less than 40°, the cross sections were vanishingly small.

It is worthwhile to note that the concept of effective LET itself is not valid in this case as the device SEU cross section is not uniquely defined at each tilt angle and primary species LET. In this case, there exists a span of two to four orders of magnitude in the measured

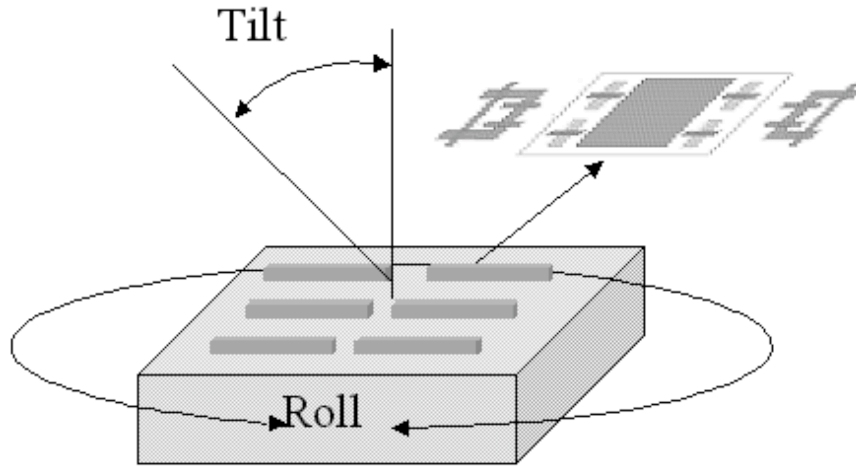

Figure 75: Orientation of the ion beam with respect to the DUT surface and related nomenclature.

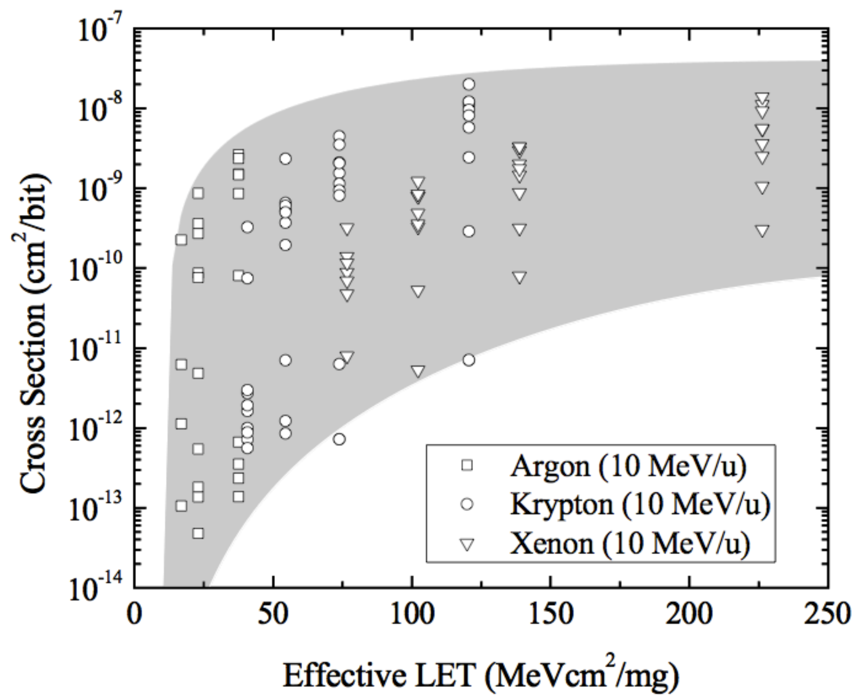

Figure 76: Compilation of heavy ion data from irradiation of the latch shown in the classical effective LET manner.

cross section for equal values of effective LET over the range of roll angles. The broad range of upset cross sections and the strong roll dependence on cross section are not consistent with the assumptions of the traditional rectangular parallelepiped (RPP) model.

SEU Analysis

SPICE: Circuit Simulation

SPICE analysis on the latch was performed for the purpose of identifying and quantifying the sensitive node or nodes and their respective critical charges. Single event charge collection was approximated using a double exponential current source. The peak amplitudes of the current sources were limited so that the potential of the evaluated node or nodes did not exceed the supply or ground rail. Charge was sunk or sourced from the drain of the off-state NMOS and PMOS transistors, respectively. The critical charge was defined as the minimum charge or combination of charges required to upset the circuit and was calculated by the current source or sources over time.

The circuit was found to be immune to upset when only a single node of the device was struck. However, a number of two-node combinations were found to produce an error. Sensitive pairs depended on the state of the device and the critical charge was not the same for different pairs. This is illustrated in Table 8, where for any struck transistor, Tx(A), the quantity of charge required on Tx(B) to cause an upset was less. Furthermore, the Tx(A) and Tx(B) Qcrit values did not commute for the N-P pairs (e.g., N0/P1 vs. P1/N0).

TCAD: Transistor and Cell Simulation

To validate that the SPICE conditions examined are physically justifiable from a charge transport perspective, two sets of three-dimensional mixed-mode TCAD simulations were performed to investigate simultaneous charge collection on the N0/N2 and the N0/P1 transistor pairs. TCAD simulations were performed by Brian Sierawski.

Table 8: Latch Sensitive Node Pairs and Critical Charge.

	T_x Pair Q_{crit}(fC) and Data State			
	D=0		D=1	
	Q_{crit} T_x(A)	Q_{crit} T_x(B)	Q_{crit} T_x(A)	Q_{crit} T_x(B)
N0/N2	6.3	2.5	N/A	N/A
P1/P3	13.9	2.5	N/A	N/A
N0/P1	4.4	1.7	N/A	N/A
N2/P3	3.2	1.8	N/A	N/A
N2/N0	2.5	6.3	N/A	N/A
P3/P1	2.5	13.9	N/A	N/A
P1/N0	2.0	5.5	N/A	N/A
P3/N2	1.5	5.5	N/A	N/A
N1/N3	N/A	N/A	6.3	2.5
P0/P2	N/A	N/A	13.9	2.5
N1/P0	N/A	N/A	4.4	1.7
P2/N3	N/A	N/A	3.2	1.8
N3/N1	N/A	N/A	2.5	6.3
P2/P0	N/A	N/A	2.5	13.9
P0/N1	N/A	N/A	2.0	5.5
N3/P2	N/A	N/A	1.5	5.5

Ion strikes were modeled using a constant LET vs. depth and a Gaussian radial profile with a characteristic length of 0.1 μm. An iterative process of varying the incident LET was used to determine the threshold for which upset occurred. Two possible upset mechanisms are considered in the following sections.

N-N Simultaneous Charge Collection

The latch design was intended to provide sufficient separation between the N-N sensitive pairs to eliminate single particle charge sharing mechanisms. However, a particle at a large tilt angle (grazing incidence) may pass in proximity to both transistors, resulting in some degree of collected charge on both of them.

Both transistors comprising the SEU-sensitive pair were simulated in three dimensions, while the remainder of the latch (minus access transistors) was modeled with compact circuit models. The separation of the sensitive pair was based on the physical design layout. The

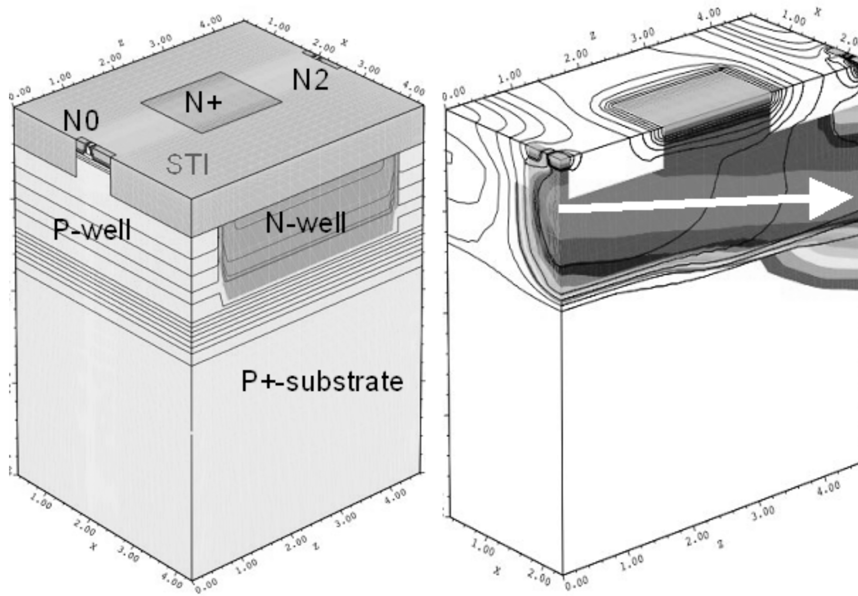

Figure 77: Depiction of the TCAD model containing the N0 and N2 transistors separated by the n-well (left). Charge diffusion from the track to both N0 and N2 causes upset (right).

single event strike was simulated at a tilt angle of 80°, entering near the drain diffusion of N0 and passing beneath N2 (Figure 77). The single event strike passes immediately beneath the drain of N0 in the direction of N2. Particle LETs between 5-10 $MeVcm^2/mg$ were found to be sufficient to upset the latch.

N-P Upset Mechanism

The possibility of inducing a SEU by simultaneously depressing the N0 drain and elevating the P1 drain node voltages from a single strike was examined. The N0-P1 sensitive node pair was simulated as a TCAD structure with appropriately distanced well taps and the remaining portion of the circuit solved as SPICE elements.

The results of TCAD simulation (Figure 78) show that a single particle corresponding to the 75° tilt, 150° roll heavy ion irradiation resulted in direct charge collection by the NMOS transistors with parasitic bipolar conduction in the off-state PMOS transistors due to n-well potential depression similar to that reported by [19]. The minimum LET particle

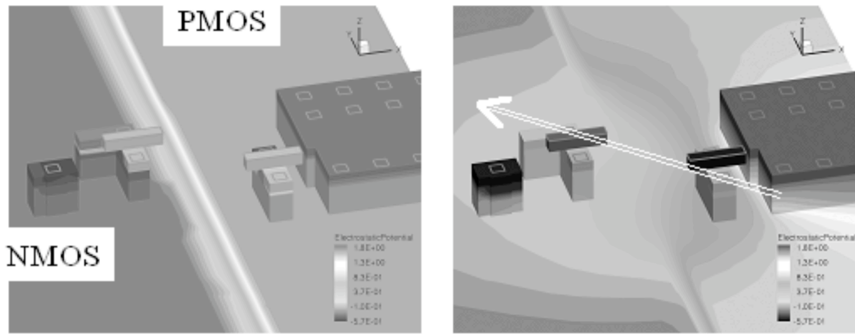

Figure 78: TCAD simulation showing electrostatic potential in the vicinity of the N0-P1 transistor pair before a heavy ion strike (left) and the N-well potential collapse after the strike (right).

found to cause an upset was approximately 2.5 $MeVcm^2/mg$).

MRED Base-Line Models and Configuration

DICE Latch Solid Model

A solid model of the latch was generated using PROCEM, a module contained in the *sde* tool, a product of Synopsys, Inc. Each process layer (polysilicon, metal-1, metal-2, etc.) was derived from the layout files and SEM cross sections and is shown in Figure 79. For this simulation, the solid model was replicated into a 5 x 5 bit array for the purpose of reducing possible edge effects as well as allowing the evaluation of cross sections on the programmed state of the device (e.g., all 1s, all 0s, checkerboard).

MRED SEU Conditions

The circuit operation and SEU mechanisms of the hardened latch explored in the previous sections demonstrate that a minimum of two critical charge conditions must be evaluated and satisfied to upset the circuit, where a total of four possible transistor combinations have 8 critical charge conditions for each logic state. For example, if a latch was programmed in a

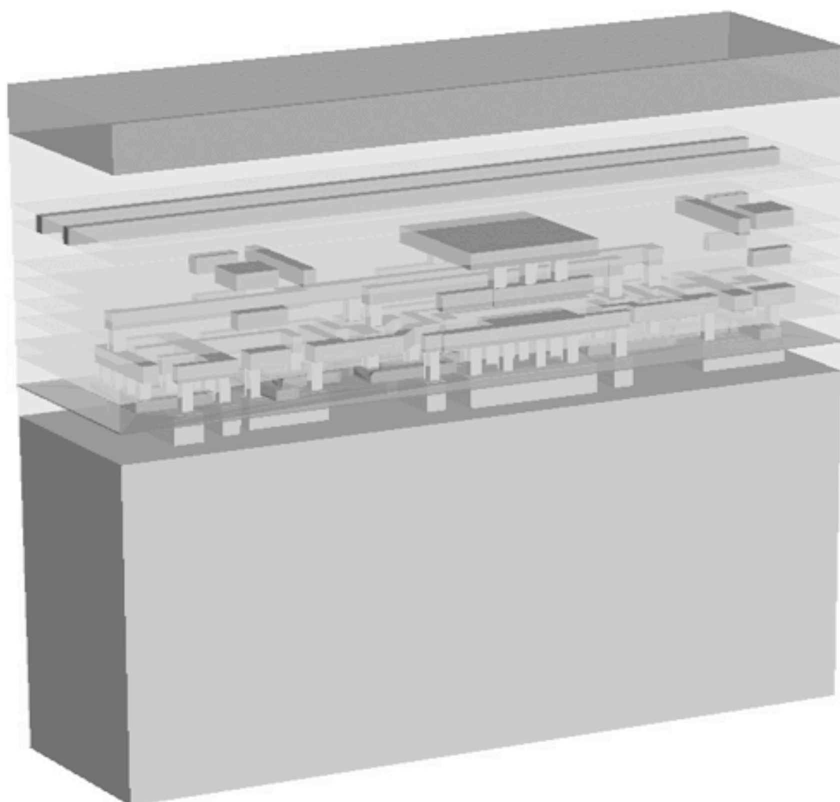

Figure 79: Solid model of a single latch. The oxide and interlayer-dielectric material has been made transparent to illustrate the metallization layers.

data state of 1, the simulator determined the collected charge of N0, N2, P1, and P3 following a radiation event. If any of the eight relevant combinations (Table 8) of critical charges were satisfied, an upset was counted. This is illustrated algorithmically in (31) where "$\cdot$" is the logical AND, and the conversion from energy to charge ($22.5MeV/pC$) is omitted for the sake of clarity. Eight evaluations were performed for each bit, with the specific pairs under evaluation dependent on the data state (logic 1 or logic 0). The solid model and the accompanying sensitive volume groups were placed in a 5x5 array. SEU evaluations within the arrayed structure were performed in such a way as to mimic a programmed checkerboard pattern (per heavy ion test conditions).

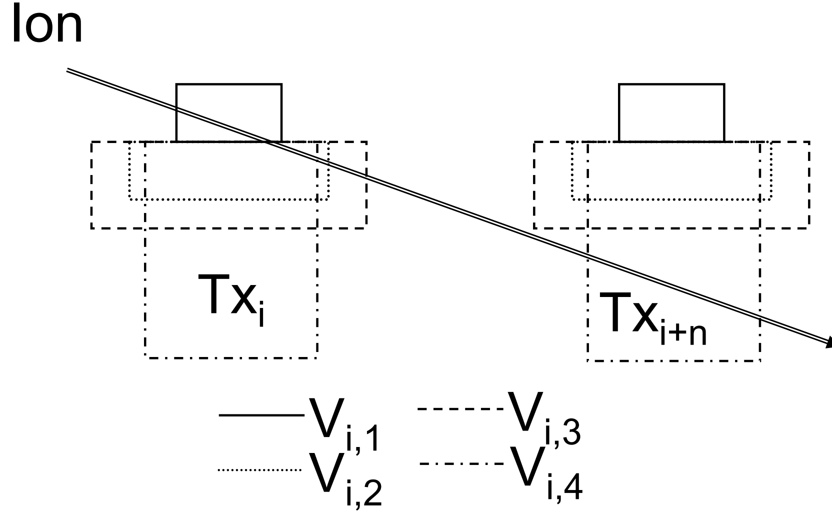

Figure 80: Conceptual 2-dimensional cross sectional drawing of two (multi-)sensitive volume groups.

$$SEU_{j,k} \equiv \left(\sum_{i=1}^{N} \alpha_{ij} E_{ij} \geq E_{crit,j} \right) \cdot \left(\sum_{i=1}^{N} \alpha_{ik} E_{ik} \geq E_{crit,k} \right) \tag{31}$$

Sensitive Volume Model

Multiple sensitive volumes were grouped together in such a way as to define the collected charge for a single transistor as described in Chapters II and III. The initial estimates of the geometry and efficiency of the substrate sensitive volumes were largely determined by physical boundaries within the device layout, such as well boundaries or adjacent transistors. The depth of the volumes corresponds to junction depths such as the n-well (PMOS) or the epitaxial peak implant depth (NMOS). Each transistor in the circuit was assigned a unique sensitive volume group. The composite sensitive volume groups were further replicated to match the degree of replication of the base TCAD object. These outermost volume in the substrate sensitive volume groups are shown in Figure 81.

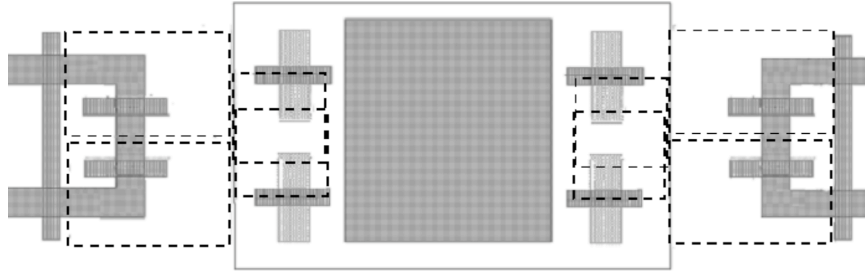

Figure 81: Final placement of the sensitive volume set for each transistor with respect to the circuit layout. The dashed lines represent the outer boundary of the sensitive volume set for a transistor.

Sensitive Volume Calibration

Calibration of the sensitive volume parameter set (final dimensions and efficiencies) was achieved by repeated comparison of simulation results to the experimental data. The complete simulation set involved calculating the cross section for approximately 100 different heavy ion beam conditions (roll, tilt, and ion species).

Figures 82-89 contain examples of the level of simulation fidelity achieved over a range of species, roll and tilt angles. Rapid calibration through multiple simulations over all beam conditions was made possible by the use of the Vanderbilt University Advanced Computing Center for Research & Education (ACCRE) VAMPIRE computing cluster [117].

The maximum NMOS and PMOS charge collection depths were determined to be 1.95 and 0.40 μm, respectively. The shallow tilt-angle cross sections were largely dominated by the N-P upset mechanism (close proximity, shallow collection depth) while at grazing incidence, the N-N mechanism was the most probable (large separation distance, deep charge collection depth).

At tilt angles at or below 40° the experimental cross sections were the smallest. This is also the region of the greatest discrepancy between the MRED model and experimental results. An example is shown in Figure 85 for krypton at 40°. The is likely due to the geometrical approximation of the sensitive volumes as rectangular regions as well as the

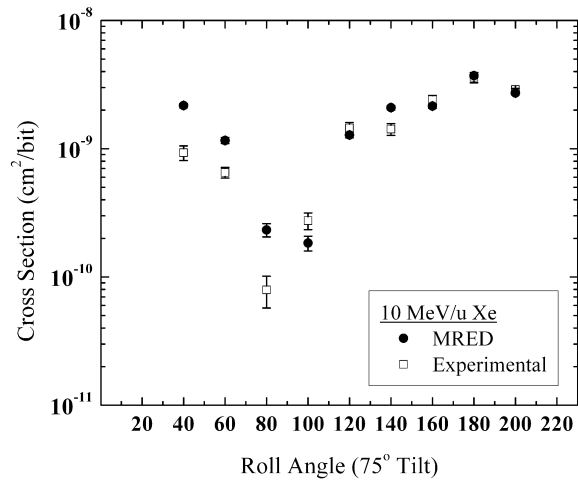

Figure 82: SEU cross sections for the 10 MeV/u xenon (58.7 $MeVcm^2/mg$) beam at 75° tilt as a function of roll angle.

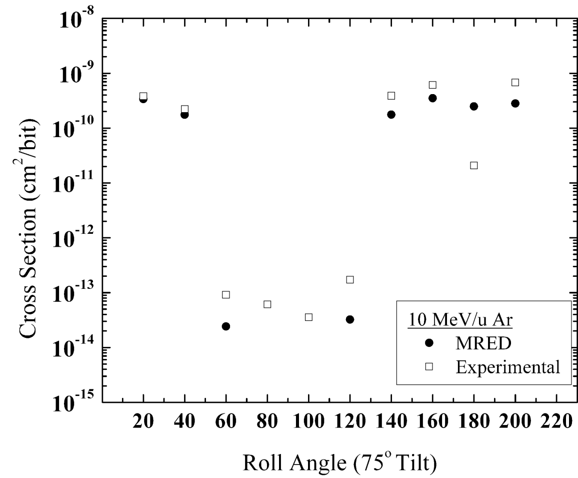

Figure 83: SEU cross sections for the 10 MeV/u argon (9.7 $MeVcm^2/mg$) beam at 75° tilt as a function of roll angle.

limitations associated with descritizing a spatially continuous physical process such as charge collection. Furthermore, the rate of decrease in cross section with decreasing tilt angle is at a maximum at 40°, which adds to the difficulty in calibrating cross sections at the threshold. From an engineering perspective, over-predicting cross sections at a relatively small number of angles can be viewed as being conservative, but reasonable, for the final

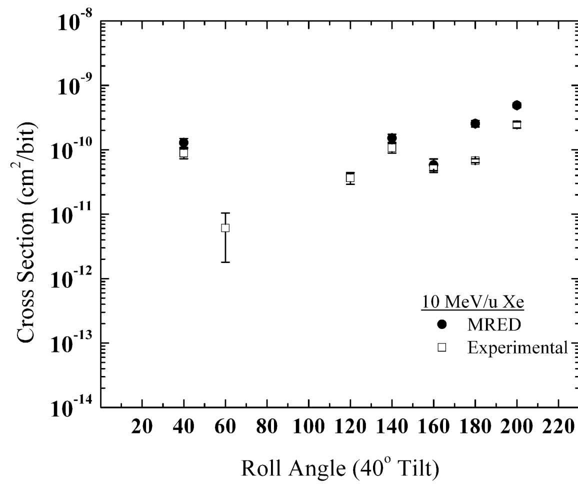

Figure 84: SEU cross sections for the 10 MeV/u xenon (58.7 $MeVcm^2/mg$) beam at 40° tilt as a function of roll angle.

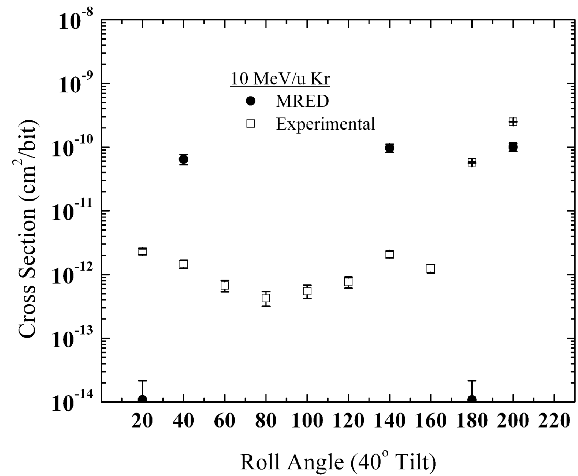

Figure 85: SEU cross sections for the 10 MeV/u krypton (31.2 $MeVcm^2/mg$) beam at 40° tilt as a function of roll angle. No SEU were recorded in MRED between 60° and 120°.

error rate prediction.

Heavy Ion Space Environment Rate Prediction

In this study, GEO/interplanetary spectra during solar minimum for atomic numbers from 1 to 92 were selected and transported through 100 mils (0.10 inches) of aluminum

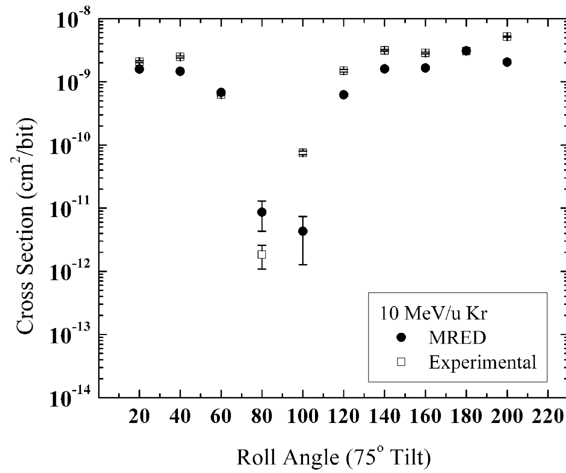

Figure 86: SEU cross sections for the 10 MeV/u krypton (31.2 $MeV cm^2/mg$) beam at 75° tilt as a function of roll angle.

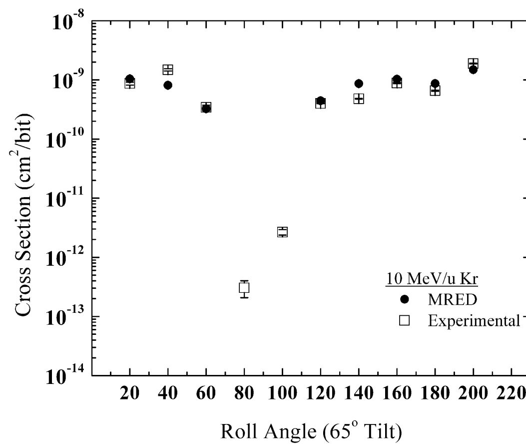

Figure 87: SEU cross sections for the 10 MeV/u krypton (31.2 $MeV cm^2/mg$) beam at 65° tilt as a function of roll angle.

using the CREME96 TRANS algorithm[31]. Each spectrum was evaluated separately in MRED to determine the contribution of each atomic species to the on-orbit SER.

The true energy spectrum for each atomic species is sampled and transported through the solid model (Figure 79) in a physical manner (e.g., screened coulomb scattering, hadronic

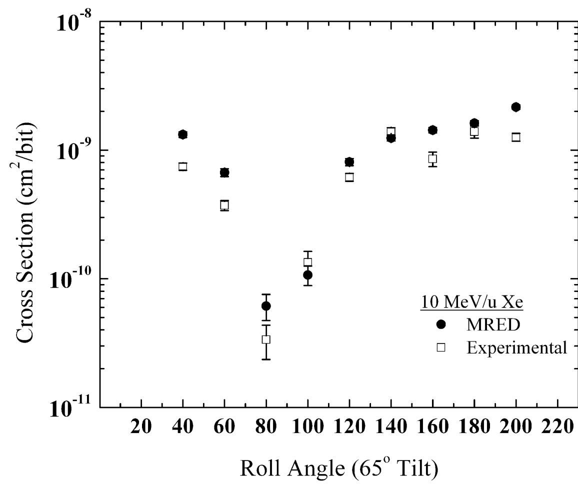

Figure 88: SEU cross sections for the 10 MeV/u xenon (58.7 $MeVcm^2/mg$) beam at 65° tilt as a function of roll angle.

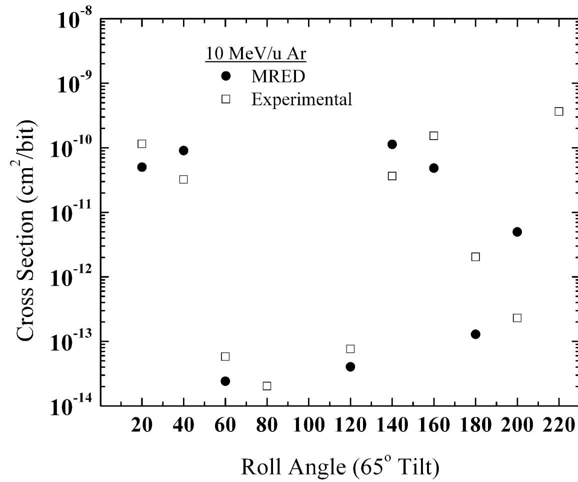

Figure 89: SEU cross sections for the 10 MeV/u argon (9.7 $MeVcm^2/mg$) beam at 65° tilt as a function of roll angle.

interactions, etc.). No path-length-style calculations are associated with this type of simulation. Particle trajectories were randomly selected to mimic the isotropic nature of the natural space environment.

The result of the rate prediction, divided into the absolute contribution from each species, is shown in Figure 90 for particles up to Z=65. The combined SEU rate is

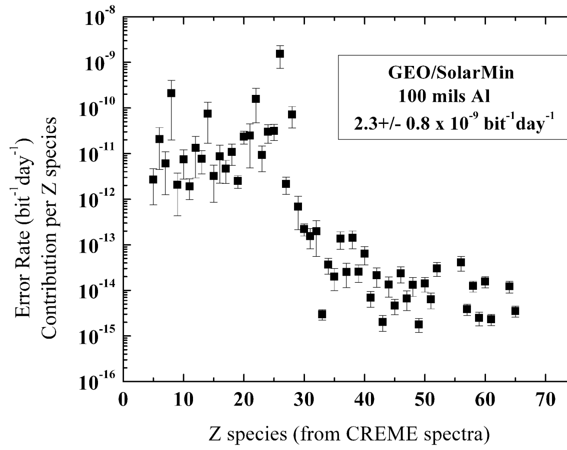

Figure 90: SEU rate of the latch for each species in the space environment.

$2.3 \pm 0.8 \times 10^{-9}$ $bit^{-1}day^{-1}$. The uncertainty is derived from counting statistics only and does not represent systematic errors in the model or spectra.

Conclusions

The level of complexity of the SEU response shown in Figure 76 indicates that the concept of effective LET has no reasonable physical interpretation for devices whose upset response is driven by multiple node upset mechanisms. SEU cross sections cannot be viewed as single critical charge and simple path length calculations in a single rectangular volume. Rather, one must consider the charge characteristics of multiple transistors and the probabilities of coincident charge collection dominating the SEU response. The agreement between the model and the experimental data for the hardened latch not only supports the proposed SEU mechanism and the simulation methodology, but also provides the maximum possible confidence in the final on-orbit soft error rate prediction.

Eight transistors were modeled with individual sensitive volume groups and 16 composite Q_{crit} analyses were performed per ion (8 sensitive pairs x 2 logic states). MRED was programmed to test each of the known upset mechanisms for a valid SEU condition, resulting in an algorithm that had two sets of eight Q comparisons (per Equation 31). It

is important to recognize that identifying the number of potential sensitive node pairs (or higher coincidence) grows in complexity, both from a circuit analysis and SEU algorithmic perspective, as the transistor count of the circuit increases. In the following chapter, a flip flop (containing two internal DICE latch elements) with over 60 transistors is analyzed where a circuit (SPICE) simulation is substituted for the direct node-by-node pair analyses used in this chapter.

CHAPTER V

INTEGRATION OF MONTE CARLO RADIATION TRANSPORT AND CIRCUIT LEVEL SIMULATORS

Introduction

The previous chapters demonstrate that Monte Carlo radiation transport codes combined with the multiple sensitive volume model can be used to predict SEU cross sections, terrestrial and space error rates for a range of circuits and environmental conditions. However, the level of complexity of the circuit can affect the fidelity of the simulation by virtue of the number of potential upset pathways. In the case of the SRAM, two transistors were found to be sensitive under a given logic condition. In the case of the DICE latch, multiple combinations of transistor nodes were involved in the sensitive volume calorimetry and the valid SEU logic evaluation, and the relevant combinations were also state dependent.

Although fixed end-point critical charges were used in the case of the DICE latch [54], Velazco, et al. demonstrated that critical charges for multiple node processes are not discrete values, but rather a continuum of values, resulting in a potentially infinite solution space of node combinations and critical charges [53]. Not all node combinations may be vulnerable and some may not be physically significant from a cross section or error rate perspective due to their physical spacing or location within the circuit. A full solution at the TCAD level for larger circuits (containing 10 or more transistors) is not yet numerically feasible for evaluating SEU errors for a single ion. For even the simplest of TCAD structures, calculating cross sections at each particle orientation and LET encountered in the space environment is prohibitively time consuming. Hybrid substrate models have been reported which reduce the simulation time and complexity and are possible candidates for integration in radiation transport codes [20]. Monte Carlo circuit simulation has been used to identify sensitive node pairs in analog to digital converters [118] containing a relatively large number

of transistors.

In this chapter, a technique for coupling the energy deposition in multiple transistors of multiple sensitive volumes to circuit level simulation is presented for two different implementations of a single-event hardened master-slave flip flop fabricated on a 90 nm process line. Data logging and post-processing capabilities are used to demonstrate the analytic capabilities of the simulation method in identifying and prioritizing SEU mechanisms at the layout and circuit level. An investigation of systematic uncertainties associated with simulation and data gathering is presented in addition to an examination of frequency effects on SEU hardness for the DICE flip-flops.

The SPICE Interface

The traditional approach to SEU analysis using circuit simulators exclusively involves the injection of a time dependent charge (current) onto circuit nodes. Comparison of the logic state of the circuit following the current transient (either immediately or after a number of clock cycles) to the correct state provides the investigator with an immediate determination of whether or not an SEU occurred. This methodology was used to determine the critical charge for the SRAM and DICE circuits presented in previous chapters. The approach taken for the multiple sensitive volume (and multiple sensitive volume group) method is to compare the energy deposited by an ion in one or multiple transistors to the critical charge or charges for the circuit under analysis, independent of time. To integrate the two methodologies requires a mechanism for translating the static, fixed charge from the Monte Carlo transport simulator, to a time dependent current pulse suitable for the circuit simulator.

Current Pulse Calculation

The current pulse profiles used in prior chapters were based upon the double-exponential formulation shown in (32). The SPICE current pulse for a given Q_{coll}, is divided into three

regions, where t is time, t_{d1} is the pulse delay time, t_{d2} is the onset of the pulse decay, τ_1 is the rise time, τ_2 is the decay time, and I_m is the peak current. The integral of all current over time must be equal to the total collected charge (33) where I_1 and I_2 are the current in the rise and fall regions of the current pulse, respectively, and Q_1 and Q_2 refer to the charge collected in those regions.

For times less than the t_{d1}, the node current is zero. The current then rises and saturates from t_{d1} to t_{d2} (depositing Q_1) and decays from t_{d2} to infinite time (depositing Q_2). It is assumed that positive charge is deposited on all struck PMOS drain nodes and positive charge is removed from NMOS drain nodes (Chapter II).

$$\begin{aligned} I(t) &= 0 && t < t_{d1} \\ I_1(t) &= I_m\left[1 - e^{-\frac{t-t_{d1}}{\tau_1}}\right] && t_{d1} \le t < t_{d2} \\ I_2(t) &= I_m e^{-\frac{t-t_{d2}}{\tau_2}} && t \ge t_{d2} \end{aligned} \tag{32}$$

$$Q_{coll} = \int_0^{\infty} I(t)\,dt = \int_{t_{d1}}^{t_{d2}} I_1(t)\,dt + \int_{t_{d2}}^{\infty} I_2(t)\,dt = Q_1 + Q_2 \tag{33}$$

In order to satisfy the conditions of (33) the parameters of (32) must be calculated for each Q_{coll}. The following properties of the transformation of Q_{coll} to $I(t)$ are required:

1) The current magnitude, I_m, should not exceed the drive capability of the complimentary transistor or transistors since it operates as the restorative element during single event recovery. For values of I_m below the drive current of the complimentary device, small variations in Q_{coll} will result in changes in I_m only in order to conserve Q_{coll}.

2) If Q_{coll} is deemed to be sufficiently high as to saturate I_m, conservation of charge will be achieved by extending the saturation time ($t_{o,d2} + \Delta t_1$) and the fall-time decay constant ($\tau_{o2} + \Delta t_2$).

The point at which I_m saturates is defined as the minimum collected charge, Q_{min}, and is calculated by (34) where τ_{o1}, τ_{o2}, and $t_{o,d2}$ represent the user specified minimum values of the rise time, fall time, and holding time, respectively. These parameters must be estimated

based upon the technology, or at a minimum, made sufficiently small to approximate a fast current pulse relative to the response time of the circuit. In this derivation, they represent the fastest possible response of the current pulse. The injection time, t_{d1}, is only relevant in the sense that it defines the start of the current pulse and can be defined to suite the point of injection during circuit operation (e.g. relative to the clock signal). The rise time, τ_{o1} is assumed constant for all Q_{coll}.

$$Q_{min} = \frac{V_{DD}}{R_{on}} \left[(\tau_{o1} + \tau_{o2}) + (t_{o,d2} - t_{d1}) - \tau_{o1} e^{-\frac{t_{o,d2} - t_{d1}}{\tau_{o1}}} \right] \tag{34}$$

$$I_m = \begin{cases} \frac{Q_{coll}}{\left(\tau_{o2} + \tau_{o1} + \left(t_{o,d2} - t_{d1}\right) - \tau_{o1} e^{-\frac{t_{o,d2} - t_{d1}}{\tau_{o1}}}\right)} & Q_{coll} < Q_{min} \\ \frac{V_{DD}}{R_{on}} & Q_{coll} \geq Q_{min} \end{cases} \tag{35}$$

Once the determination of Q_{min} and I_m have been made, τ_2 is calculated by (36), where f is the fraction of the Q_{coll} contained in Q_1, calculated by (37). f is specified by the user and can be approximated based upon knowledge of the technology, during calibration, or other suitable means. In general, the magnitudes of f and τ_2 are inversely related. f specifies the extent to which the collected charge is prompt relative to the event time, t_{d1}.

$$\tau_2 = \begin{cases} \tau_{o2} & Q_{coll} < Q_{min} \\ (1 - f) \frac{Q_{coll}}{I_m} & Q_{coll} \geq Q_{min} \end{cases} \tag{36}$$

$$f = \frac{Q_1}{Q_1 + Q_2} \tag{37}$$

The hold time, $t_{d2} - t_{d1}$, is calculated according to (38), where when $Q_{coll} \geq Q_{min}$, one must solve for χ in the transcendental equation given by (39).

$$t_{d2} - t_{d1} = \begin{cases} t_{0,d2} - t_{d1} & Q_{coll} < Q_{min} \\ \chi & Q_{coll} \geq Q_{min} \end{cases} \tag{38}$$

Table 9: Default Current Pulse Parameters.

Parameter	Value	Units
$t_{o,d2}$	10	pS
τ_{o1}	2	pS
τ_{o2}	5	pS
V_{DD}	0.9	V
R_{on}	1000	Ω
f	0.67	

$$\chi = \left(\frac{Q_{coll}}{I_m}\right) \cdot f + \tau_1 \left(1 - e^{-\frac{\chi}{\tau_1}}\right) \tag{39}$$

Technology Specific Example

The technology considered in this process has a 90 nm minimum feature size and the assumptions made for the default parameters are shown in Table 9 and are based upon TCAD simulations of the technology. For example, an R_{on} of 1000 Ω is based upon IV characteristics of the NMOS and PMOS devices. It represents an estimate of the average of the true on-state resistance for both device types under operating conditions and for the sizes (length and width) used in the circuit design.

$$I_m\ (\mu A) = \begin{cases} 59.2\ ns^{-1} \cdot Q_{coll} & Q_{coll} < 15.2\ fC \\ 900 & Q_{coll} \geq 15.2\ fC \end{cases} \tag{40}$$

A series of current pulses corresponding to collected charges from 2 fC to 250 fC is shown in Figure 91 with t_{d1}, the delay for the start of the current pulse, equal to 1 nS. For $Q_{coll} < 15\ fC$, the peak current is less than the saturating current of 900 μA and increases with increasing Q_{coll}. As the collected charge increases beyond 15 fC, the current pulse is stretched and its width increases linearly with increasing Q_{coll}.

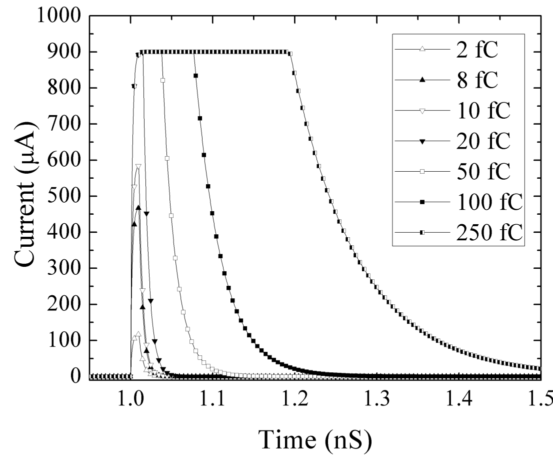

Figure 91: Double exponential current pulse for a series of Q_{coll}.

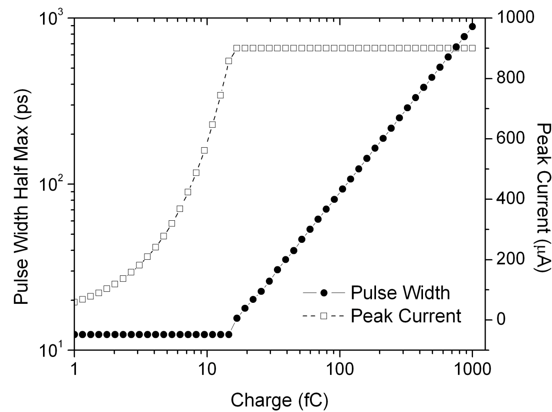

Figure 92: Pulse width and peak current as a function of Q_{coll}.

Python Interface

The SPICE interface is written in Python and manages the conversion of energy tables from the radiation transport simulator (MRED) to double exponential current pulses. It generates netlists with the appropriate current pulse parameters, executes the SPICE simulator, analyzes the resultant output for single event errors, and passes the results back to MRED. A commercial version of HSPICE was used to analyze the circuit response. Assistance in the development of the SEU enabled SPICE netlists was provided by Andrew

Sternberg [1]using techniques developed in [119].

Each particle event, defined as the passage of a single particle through a solid model containing the sensitive volume groups, could result in one, two, or many values of collected charge depending on the number of transistors struck during its passage. Thus, an event will refer to the array of collected charges, indexed by transistor name (the name provides a correlation between sensitive volume set and the netlist), to a single parent particle. The process is illustrated mathematically in (41), where $Q_{(coll),i,j}$ refers to the collected charge on the jth transistor in the model for the ith event. The summation is taken over all volumes, N_j in the jth sensitive volume group. The array, $Q_{(coll),j}$ is evaluated by SPICE for all i in the event buffer.

$$Q_{(coll)i,j}(pC) = \frac{pC}{22.5MeV} \sum_{k=1}^{N_j} \alpha_{j,k} E_{(dep)i,j,k}(MeV) \tag{41}$$

Once the event buffer is filled (typically a maximum of 50 events), MRED calculates the double exponential current pulse parameters (e.g., $\{I_m, \tau_2, t_{d1}, t_{d2}, ..\}_i$), halts simulation, and passes the table to the SPICE interface. Note that t_{d1} can be chosen to occur at a fixed time, as in the case of a purely static device, or over a random interval, such as the clock period of a dynamically operating circuit.

The SPICE interface automatically builds a netlist containing the calculated double exponential current sources from a template netlist. The interface determines current pulse direction (source or sink) based upon transistor type (N or P). In this study, the template contains two identical flip-flops as shown in Figure 93, but only accepts current pulses on nodes contained in FF1 during the *Irradiate* frame. For each event, a t_{d1} (32) is randomly chosen between 0 and $2T$, where 0 represents the start of the *Irradiate* frame and T is the clock period. The t_{d1} is the same for all current pulses associated with a single event. That is, the event is assumed to occur at a random time between (0,2T]. The output of the second

[1]Andrew Sternberg is with the Institute for Space and Defense Electronics

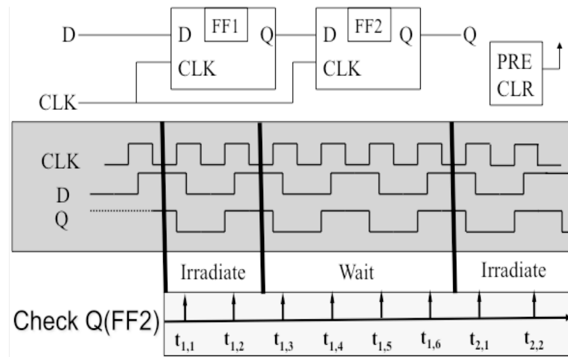

Figure 93: Diagram of the current pulse injection and upset monitoring sequence of the flip-flop circuit.

flip-flop, FF2, is monitored for errors at Q at regular intervals (clock state) during the *Wait* period. The second flip-flop provides a means for differentiating transient errors in Q(FF1) from latched errors, recognizing that under dynamic conditions, transients in Q(FF1) may be latched into FF2. The FF2 is not modeled in radiation transport and exists only in SPICE as a means for detecting SEU in FF1.

Alternating (logic 0 and logic 1) were clocked into the data line of FF1, D(FF1), during simulation to ensure that all possible combinations of external signal levels and internal flip-flop states were evaluated. Four full clock periods beyond the end of the *Irradiate* frame were evaluated to ensure that any possible SEU had propagated to the FF2 output, Q(FF2).

General Device Description and Test Conditions

Two separate designs of a radiation hardened, master-slave flip-flop containing 64 transistors, fabricated in a 90 nm bulk CMOS technology, are evaluated. A dual interlocked cell (DICE) design is used to provide SEU resistance through spatial redundancy of the datapath in each stage where a change in logic state occurs only if the states of the internal data-lines are in agreement [120] The circuit designs are identical, having changes only in the physical layout of the devices. The general structure, operation, and configuration for

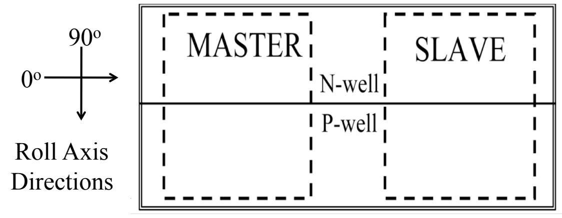

Figure 94: Block level drawing of DICE flip-flop.

heavy ion testing of the two flip-flops are identical. Unless otherwise specified, subsequent descriptions are applicable to both designs[1].

A block diagram of the flip-flop is shown in Figure 94. Flip-flops were placed on a test chip in single-file, shift register fashion. The shift registers were composed of 500 devices and placed at the die edge to minimize shadowing from the test fixture. Four chains were clocked simultaneously for a total of 2000 flip-flops. The output of each of the four shift register chains was simultaneously monitored such that temporally coincident errors between shift-register chains could be identified (Figure 95). addition, temporally coincident errors between shift register chains were identified in order to differentiate upsets due to transients in the external clock circuitry.

Heavy ion irradiation was performed at the Lawrence Berkeley National Laboratory. Ion species were argon, copper, xenon, neon, oxygen, boron, silicon, and krypton with linear energy transfers (LETs) ranging from 2.4 to 62.6 $MeVcm^2/mg$. Irradiation angles, identified with respect to the surface of the device, as shown in Figure 96, were measured from $0° \leq \theta \leq 80°$ and $0° \leq \phi \leq 180°$ with varying degrees of range and resolution, depending on DICE version number and heavy ion species. For the remainder of this work, θ will be referred to as the tilt axes and ϕ will be referred to as the roll axis, both taken with respect to the incoming particle and the device surface normal.

[1]Devices were fabricated by The Boeing Company, and heavy ion test data were supplied by Mark Baze and Ethan Cannon of Boeing.

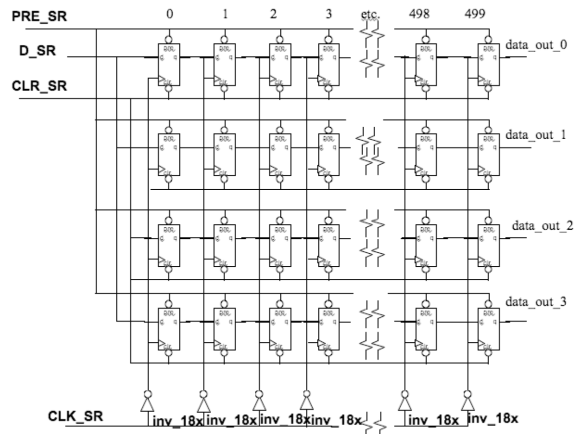

Figure 95: Schematic of the DICE flip-flop chains used during heavy ion irradiation.

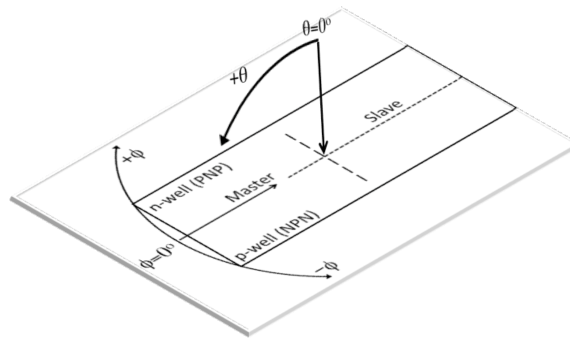

Figure 96: Orientation of heavy ion irradiation and simulation angles with respect to the devices' surface.

DICE Version 1

The dimensions of the Version 1 (V1) flip-flops are 31.2 μm and 3.6 μm along the 0° and 90° axes, respectively (Figure 94). The solid model through which the particles were transported is shown in Figure 97.

MRED Model and Calibration

The sensitive volume parameters that comprise the sensitive volume group for each transistor were varied in such a way as to visually minimize the difference between the

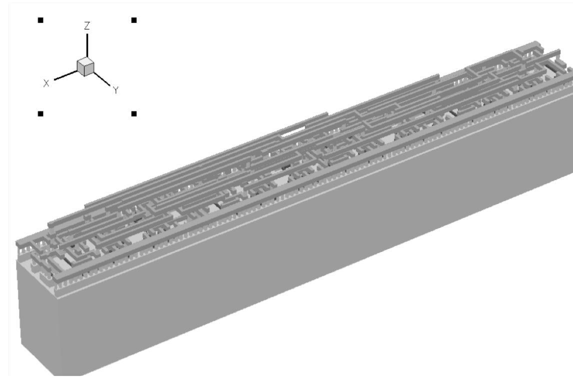

Figure 97: Solid model of the V1 flip-flop.

simulation and experiment cross sections as performed in Chapters III and IV. As such, a semi-empirical method of calibration was used. The calibration process proceeds as follows:

1. Assign a sensitive volume with unit efficiency ($\alpha = 1$) in the active regions of the transistors in the solid model. The volumes are located within the drain diffusion of each transistor.
2. Assign a sensitive volume of unit efficiency to each transistor that extends into the substrate to a depth approximately equal to the n-well depth (CMOS).
3. Perform heavy ion broadbeam simulations and evaluate the results.
4. Add additional volumes to each volume set in step 2 with less than unity efficiency, which generally extend deeper into the substrate and laterally outward from the volumes in (2) in a nested configuration. Sensitive volumes sets should be modified equally to reduce the parameter-space as well as to limit unintentionally biasing the sensitivity of a small set of transistors.
5. Adjust efficiencies, α, to shift cross sections, from threshold or otherwise, to match data.
6. Repeat step 3.

No parameters exceeded physically justifiable values. For example, the boundaries of the micro-volumes did not extend into SiO_2 and their depths were approximately equal to known junction depths. For the simulations described in this work, a maximum efficiency of 100% was used for the drain node region of the NMOS devices with a maximum collection depth of 1.5 μm at an efficiency of 5%. Likewise, the drain regions of the PMOS devices

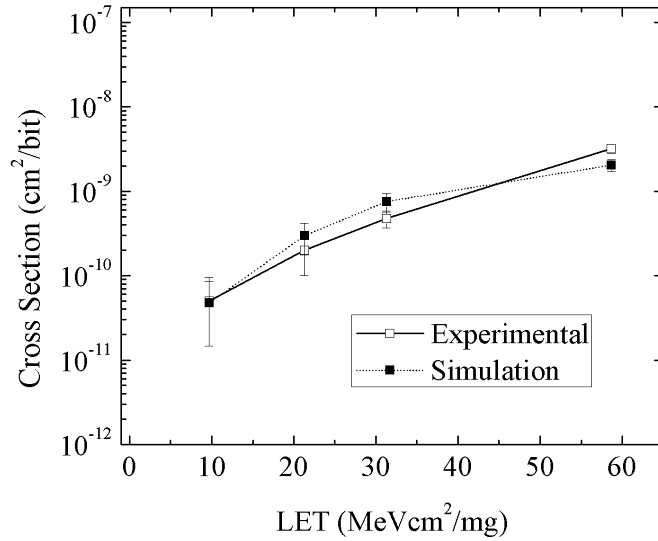

Figure 98: Experimental and simulated cross sections at normal incidence for the V1 flip-flop.

were limited to 70% collection efficiency and the maximum collection depth was 0.80 μm with an efficiency of 2%.

The cross section curve for the experimental and simulated broadbeam experiment at normal incidence is shown in Figure 98. Good agreement was achieved by extending lateral dimensions of the sensitive volumes to allow for overlap. In this manner, charge sharing between devices was factored into the simulation. This mechanism has previously been shown to play a role in soft errors for this technology [91]. No errors were found to occur below 10MeVcm^2/mg in either simulation or experiment.

Greater deviation is seen at the 60° tilt and 0° roll condition as shown in Figure 99. Although the saturation cross sections differ, the most likely impact on the calculated soft error rate is the apparent difference in threshold LET. Figure 100 contains the heavy ion data for irradiation at 90° of roll and 60° of tilt. The simulation model over-predicts the cross sections under these conditions. This is the only irradiation for which errors were shown to occur in either simulation or experiment below an LET of 10 $MeVcm^2/mg$. The *Analysis* section of this chapter discusses the impact of errors in calibration on the calculated

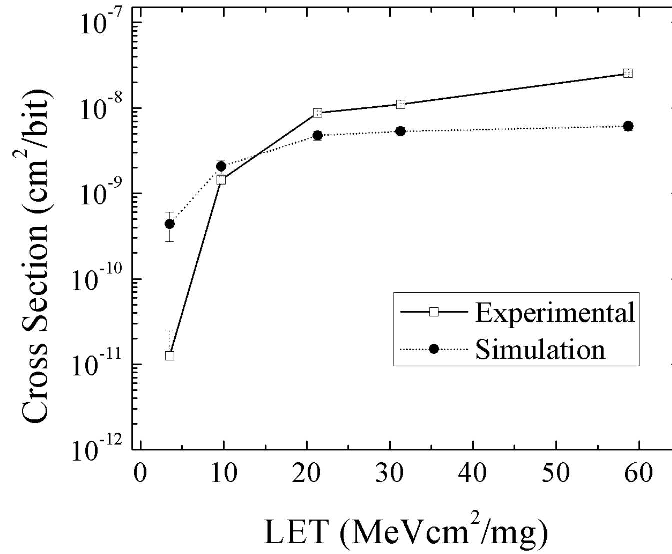

Figure 99: Experimental and simulated cross sections at 60° tilt and 0° roll for the V1 flip-flop.

soft error rate.

The extent to which the sensitive volume dataset for this flip-flop could be calibrated was limited by the experimental data set, which had only three irradiation angles (compared to the extensive data set over roll and tilt shown in Chapter IV). Thus, a priority was placed on capturing the trend of the cross section data in the calibration stage. Extensive adjustment of the sensitive volume parameters could not be justified without further experimental results. However, the good qualitative (trend) agreement as well as qualitative agreement at the largest values of SEU cross section was deemed adequate for analyzing the flip-flops SEU mechanisms and predicting the on-orbit SEU rate.

SEU Rate

The ultimate application of the coupled MRED and SPICE simulators is the prediction of error rates. Specifically, for this study the objective is to determine the on-orbit error rate under the Adams 90% worst-case conditions [121]. Although highly conservative in

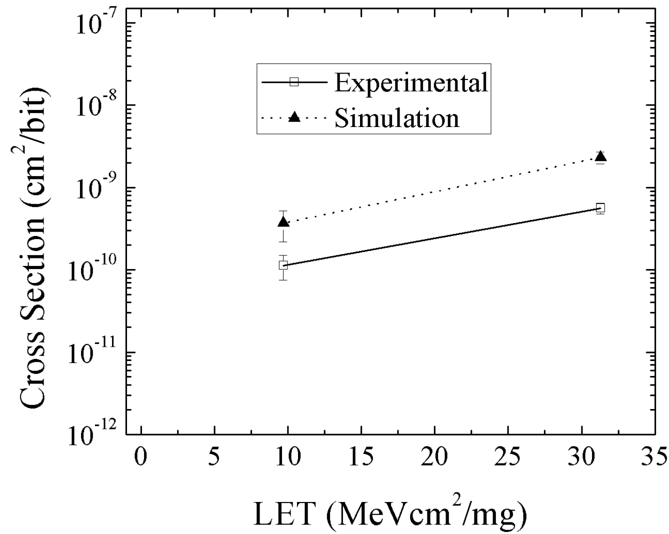

Figure 100: Experimental and simulated cross sections at 60° tilt and 90° roll for the V1 flip-flop.

its heavy ion flux levels, the environment is considered appropriate for some programs in which an absolute upper-bound on the on-orbit SER is required.

Computational requirements were 2400 CPU-hours distributed over 100 processors on the Vanderbilt Advanced Computing Center for Research and Education (ACCRE) computing cluster [117]. The calculation required 10^8 simulated particle events, resulting in over 12500 SPICE simulations. The simulation predicted a final calculated SEU rate of $1.9 \pm 0.1 \times 10^{-8}$ $e/b/d$. The uncertainty in the estimate is a single standard deviation and incorporates the counting error associated with Monte Carlo simulation. It is not a reflection of the systematic uncertainty in the method.

Figure 101 contains the integral LET spectrum for all species from Z=1 (H) to Z=92 (U). Although MRED does not calculate charge generation by path lengths and stopping power tables, the integral LET spectrum provides a useful representation of the environment. In performing the transport simulations, MRED samples from the differential flux spectra associated with the environment. The spectrum of each atomic species is passed to MRED, from Z=1 to Z=92, and the absolute contribution of each species to the on-orbit SEU rate

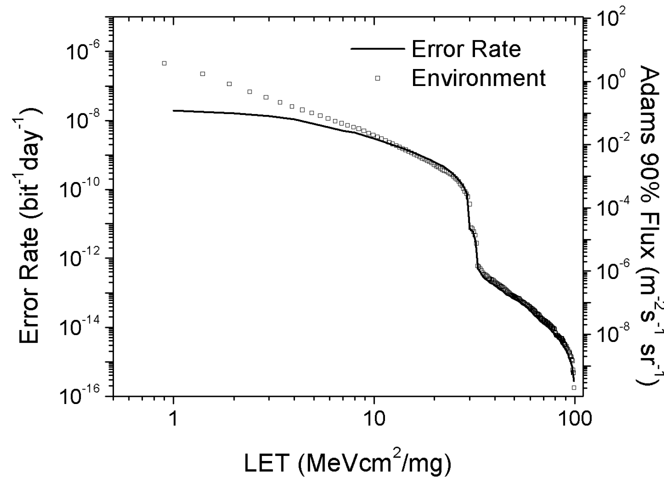

Figure 101: The integral LET spectrum for the Adams 90% environment (open squares) and the equivalent response plot of the V1 DICE flip-flop (solid line).

is determined.

Also included in Figure 101 is a comparison between the flux of particles as a function of LET and the contribution of those particles to the SEU rate. Above 10 $MeVcm^2/mg$ the integral flux and integral error rate track by a uniform scale factor. The divergence of the two curves below 10 $MeVcm^2/mg$ illustrates the decreased probability of low LET particles contributing to the SEU rate. The rate of change in the predicted SEU rate with decreasing LET is zero below 2 $MeVcm^2/mg$ per Figure 101, which can be viewed as an omni-directional threshold LET. The effect of the omni-directional threshold LET on the calculated SEU rate is discussed in greater detail in the *Sources of Uncertainty* section of this chapter.

The directional vectors of the heavy ions that resulted in SEUs were tracked and are plotted in Figure 102 and Figure 103 as a function of their contribution to the SEU rate. The scatter associated with Figures 102 and 103 is due to both simple counting statistics and the weighting scheme used in spectral sampling [110]. That is, the figures should not be viewed as frequency plots, rather weighted frequency plots. In Figure 102, the open triangles represent the simulator output as a function of tilt angle and indicate that a substantial

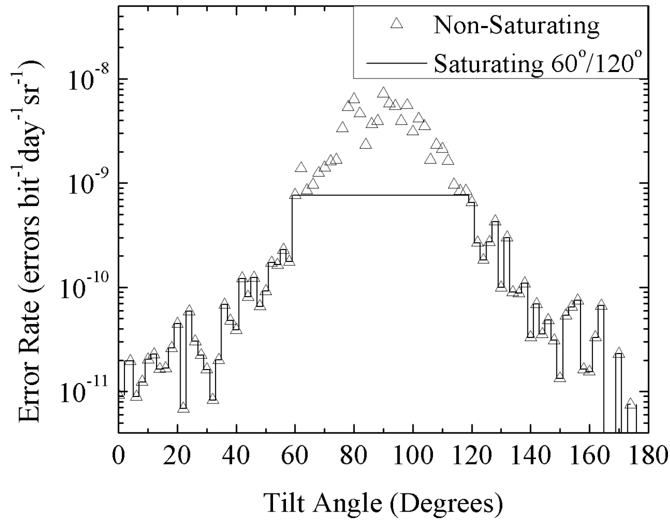

Figure 102: Solid-angle normalized error rate as a function of the ions tilt component from the on-orbit SEU rate calculation (open triangles) of the V1 flip-flop integrated over all roll angles

portion of the predicted errors occur outside of the range of calibration (between 60° and 120°). The solid line is discussed in the *Sources of Uncertainty* section of this chapter. Figure 103 indicates peaking for two distinct directions, labeled A and B in the figure. The circuit level cause of the peaks is discussed in the *Circuit Level Effects* subsection of the *Analysis* section. As in Figure 102, a significant portion of the overall SEU rate is predicted to occur outside of the region of heavy ion calibration.

Analysis

In the previous chapters, and in [54], it was demonstrated that groups of multiple sensitive volumes (one group per transistor) could be used to accurately model SEU cross sections for single and multiple node driven SEU mechanisms. In [54], extensive data sets over a large range of roll and tilt angles allowed for a detailed analysis of the interaction between multiple sensitive volume sets and consequently good quantitative agreement with

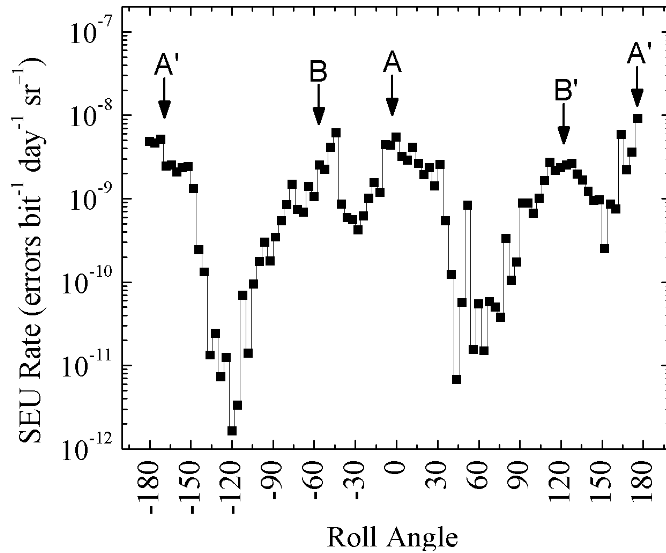

Figure 103: Solid-angle normalized error rate as a function of the ions roll component of the directional vector from the on-orbit SEU rate calculation of the V1 flip-flop integrated over all tilt angles

experimental data was achieved. Unlike [54], the analysis technique presented in this chapter incorporates SPICE, which eliminates a priori determination of critical charge values of the circuit under investigation. SPICE analysis on an event-by-event basis provides a mean to investigating, validating, and improving single event upset performance.

Identifying the cause of SEU in the particular circuit under consideration is critical for the purpose of improving subsequent layout and circuit design and is a substantial advantage of the method presented in this work over other techniques. As MRED tracks all information related to each event, it is possible to analyze the contribution of any transistor or combination of transistors to the final SEU cross section or SEU error rate. With the inclusion of SPICE, the simulation inherently provides a layout-to-schematic correlation useful for investigating the mechanisms of SEU.

As an example, post-processing of simulation data was performed to identify errors that resulted from coupling, either by coincidence or charge sharing, between NMOS devices, PMOS devices, and those events that resulted from coincident charge deposition in NMOS

Table 10: The error rate on the V1 flip-flop for three types of multi-node events.

Event Type	SEU Rate (e/b/d)
NMOS only	$4.8 \pm 0.8 \times 10^{-9}$
PMOS only	$4.5 \pm 0.4 \times 10^{-9}$
N and PMOS	$1.1 \pm 0.1 \times 10^{-8}$

and PMOS transistors. The contribution of each type is contained in Table 10. The overall error rate is shown to be almost equally dependant on mixed transistor type events (labeled N and PMOS) and those from NMOS and PMOS only.

An excerpt of the flip-flop layout is shown in Figure 104 with the circuit schematic of the master stage. The transistors shown in the layout are NMOS devices and the type of event is considered here as NMOS only. These types of events are found in the A and A' peaks of Figure 103. For this specific event, the ion passed through two sets of NMOS transistors (labeled 26-27,30-32). By inspection of the circuit schematic, it is clear that each set drives a different redundant data path and both N1 and N2 are simultaneously pulled low, causing the master stage to upset during clock-high conditions. Similar effects were observed over the entire device as illustrated in Figure 105. The frequency of events, as reflected in the SEU rate calculation, is due to the physical proximity of the nodes. An increase in separation of the devices will result in a decrease in the predicted SEU rate from this type of event. Although coincidence charge collection is possible for certain ion trajectories, an increase in spacing will reduce or eliminate charge sharing [91] and cause a decrease in the SEU rate.

Sources of Uncertainty and Systematic Error

The nature of Monte Carlo simulations as well as the circuit level response prediction by SPICE results in a single event error rate that is achieved via a non-analytical solution. Consequently, the SEU rate cannot be described as a function of the sensitive volume (and

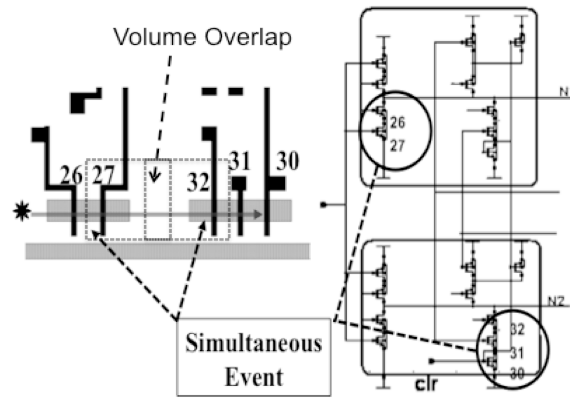

Figure 104: Schematic and layout views illustrating charge sharing between NMOS devices in the V1 flip-flop.

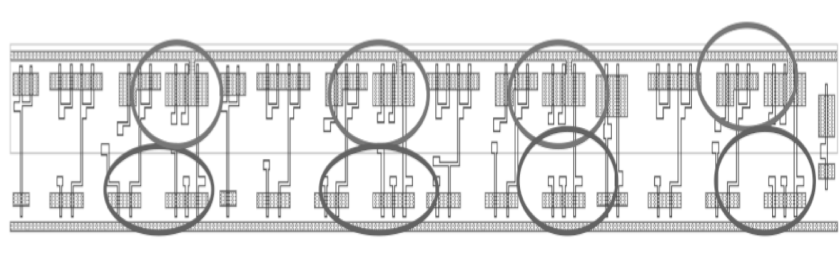

Figure 105: Layout view of the V1 flip-flop with the NMOS pair and PMOS pair sensitive regions circled.

other) parameters, and a systematic uncertainty in the method itself as a function of these parameters is not readily attainable.

As has been shown in previous sections, MRED simulations provide a comprehensive set of information pertinent to the analysis of each radiation evident. For example, the stopping power of ions can be calculated during run-time and logged. By inspection of Figure 99, the calibrated MRED model overpredicts the cross section at an LET of 3.5 $MeV cm^2/mg$ and subsequently is under-estimating the threshold LET. In Figure 101, the cumulative error rate contribution as a function of LET is shown against the environment. By rejecting events that occur below a given LET, the impact of inaccuracies of the model in predicting threshold LET (or the experimental data in improperly quantifying it) can be evaluated.

Table 11 contains the error rate for rejection of events for a hypothetical cutoff in LET of 5.0 and 9.5 $MeVcm^2/mg$, which results in a calculated error rate of $8.0 \pm 0.3 \times 10^{-9}$ and $3.2 \pm 0.1 \times 10^{-9}$ $e/b/d$, respectively. From the perspective of sensitive volume parameterization, the logical deduction is that the efficiency of a small volume or set of volumes is too high, or that for a given efficiency, their dimensions are too great. A rigorous treatment of impact of sensitive volume parameterization on the error rate would require slightly varying each parameter, would be unique to each simulation, and demand extremely long computational times using current hardware.

Experimental limitations, generally in the form of a sufficient number of roll and tilt angles to quantify a devices cross section completely, may also play a role in uncertainty in the calculated SEU rate. For example, the SEU rate over tilt angles shown in Figure 102 continues to increase beyond 60° and peaks at grazing incidence, beyond the angle for which experimental cross sections were measured. The solid line in Figure 102 represents an artificial limitation on the SEU rate in which its value is forced to saturate at the 60° tilt value. Under these conditions, the SEU rate was calculated to be $5.7 \pm 0.4 \times 10^{-9}$ $e/b/d$, a reduction of approximately 3.5 fold in the baseline SEU rate. Similarly, the off-axis peaking in the roll angle response shown in Figure 103 as peaks B and B' indicates a strong SEU response outside the range of data. A summary of the cutoff conditions are shown in Table 11. Unlike grazing incidence SEU cross section measurements, which are difficult to make due to ion range limitations at most test facilities, the off-axis roll rate warrants a broader heavy ion test and dataset to refine the SEU rate prediction.

DICE Version 2

Version 2 (V2) of the DICE flip-flop is operationally equivalent to Version 1. However, the device has been shrunk and specific transistors within the layout repositioned with respect to one another to maximize spacing of potentially SEU sensitive node pairs (NMOS). The Version 2 dimensions are 24.4 μm in width by 3.6 μm in height. The solid model of

Table 11: The baseline SEU rate and the effect of limiting the omnidirectional LET.

Condition	SEU Rate (e/b/d)
No Limits	$1.9 \pm 0.1 \times 10^{-8}$
LET_{cutoff}=5.0	$8.0 \pm 0.3 \times 10^{-9}$
LET_{cutoff}=9.5	$3.2 \pm 0.1 \times 10^{-9}$
60° tilt Saturation	$5.7 \pm 0.4 \times 10^{-9}$
LET_{cutoff}=5.0,60^0 tilt	$3.5 \pm 0.2 \times 10^{-9}$
LET_{cutoff}=9.5,60^0 tilt	$1.2 \pm 0.2 \times 10^{-9}$

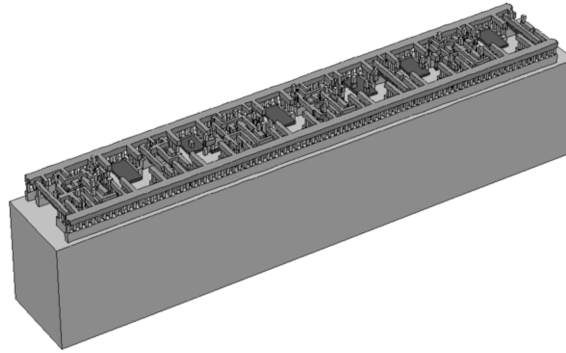

Figure 106: Selected layers from the solid model of the Version 2 DICE flip-flop.

the structure is shown in Figure 106. Note that only silicon, polysilicon, and metal layers up to metal 1 are shown for clarity, although the full structure was used in simulation.

MRED Model and Calibration

The MRED model development and calibration followed the process outlined in the V1 section. For all roll and tilt conditions, the SEU cross-sections decrease with decreasing LET, but are greater than 5×10^{-10} cm^2/bit at 2.4 $MeVcm^2/mg$ (shown in Figure 107). The best agreement between experimental data and simulations was achieved in the low LET regions.

By comparison, Figure 108 and Figure 109 contain plots of the cross section for copper

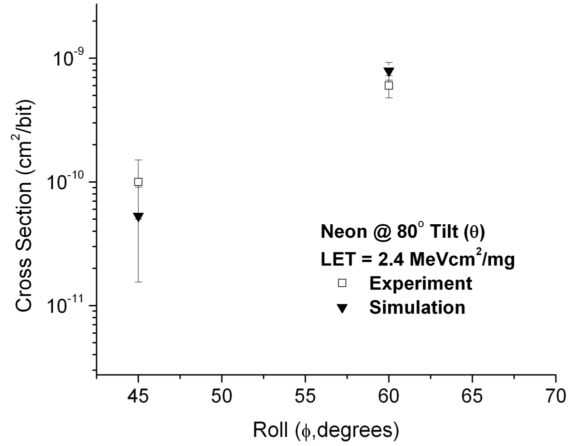

Figure 107: Neon at 80° tilt, plotted over roll.

(16.5 $MeVcm^2/mg$) at various roll and tilt angles. Agreement of the model with experimental data was not as good at higher LET, showing a tendency to over-predict cross sections at shallow tilt angles (Figure 109). Decreasing the charge collection efficiency parameters of the sensitive volumes resulted in an under-prediction of the SEU cross-sections of the 2.4 $MeVcm^2/mg$ species. Goodness of fit at the smaller LET was given preference, as it was assumed these would more accurately reflect SEU rate contributions in the natural environment due to their higher abundance. The systematic error that is introduced is present over all frequencies and relative comparisons between the two remain valid. The maximum SEU cross-section peaks occur for all species at angles of approximately 80° tilt and 60° roll (80/60).

An examination of the simulator output, as well as the device layout, indicated that simultaneous charge generation in PMOS and NMOS transistors in the sequential logic elements is the dominant contributor to the SEU vulnerability. The analyses and observed mechanism is consistent with charge-sharing and coincident multiple-node effects in DICE circuitry that have been previously reported [122], [19], [90], [91]. An investigation of the detailed mechanisms of SEU for this circuit by alternative methods is presented in [20], and is also consistent with the mechanism of SEU identified by MRED.

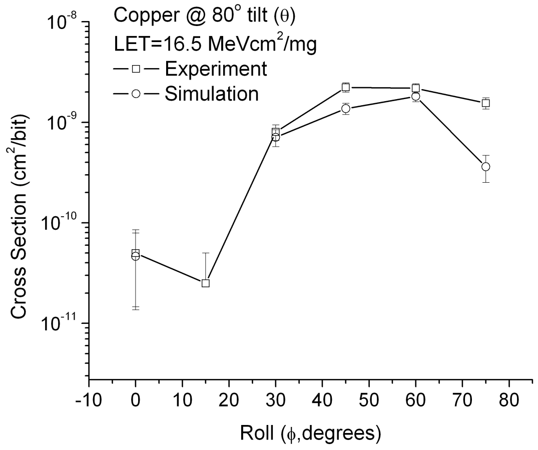

Figure 108: Experimental and simulated copper (16 $MeVcm^2/mg$) SEU cross-sections as a function of roll at a tilt angle of 80° at 100 kHz.

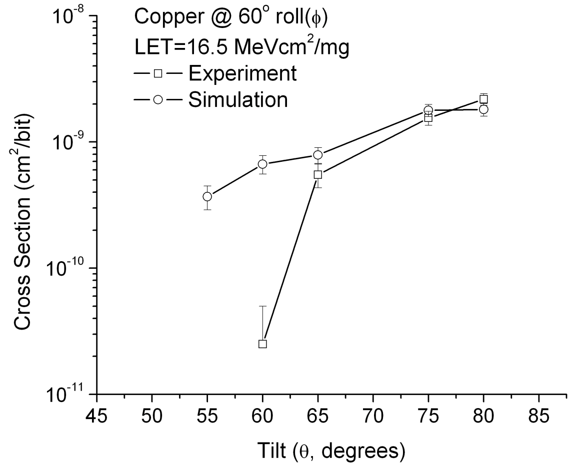

Figure 109: Experimental and simulated copper (16 $MeVcm^2/mg$) SEU cross-sections as a function of tilt at a roll angle of 60° (right) at 100 kHz.

SEU Rate

The effect of the strong directional dependence of the SEU cross section on the on-orbit rate prediction output is shown in Figure 110 and Figure 111. The highest probability of error is observed at large tilt angles ($> 60°$), which is consistent with the heavy ion cross-section data. Likewise, the SEU probability is highest at the $-60°$ and $120°$ roll angles,

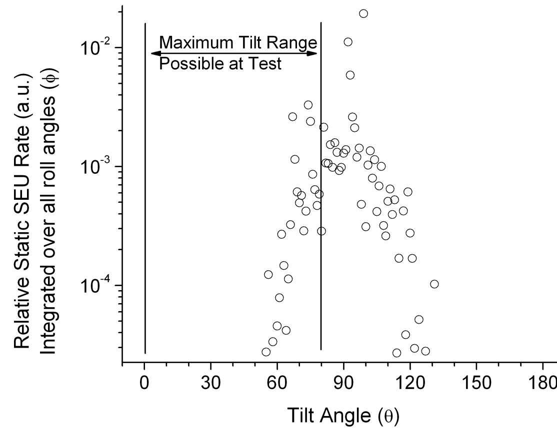

Figure 110: The relative error rate as a function of tilt for the flip-flop in the Adams 90% space environment at 100 kHz.

which corresponds to the axis of the SEU sensitive NMOS/PMOS transistor nodes. Note that the sign of the roll angle is opposite that of the heavy ion irradiations due to data logging differences between simulation types. From a layout standpoint, the locations of the errors are shown in Figure 112. The Version 2 design was constructed for the specific purpose of increasing the N-N sensitive node spacings identified in the Version 1 analysis. This solution did not, however, significantly alter the distance between N-P sensitive pairs, and the consequence of this is demonstrated by the marginal improvement in the predicted SEU rate between the Version 1 and Version 2 devices.

Analysis

The calibrated MRED model of the latch, discussed in previous sections, was used to study the frequency dependence of the SEU cross section. No experimental data were available to validate the sensitive volume models beyond 100 kHz. Consequently, the absolute cross sections and SEU rates alone should not be considered for their quantitative value, but rather the trends that are identified over clocking frequency.

For the frequency ranges simulated (< 1000 MHz), the static SEU cross sections around

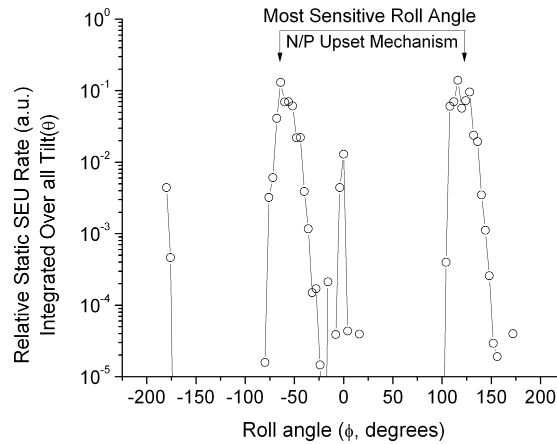

Figure 111: The relative error rate as a function of roll for the flip-flop in the Adams 90% space environment at 100 kHz.

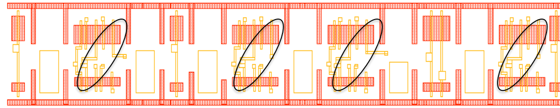

Figure 112: Locations of the dominant SEU rate directions and struck transistors in the Version 2 flip-flop.

the 80/60 orientation are the largest with respect to all other orientations of roll and tilt exposure. An example case is shown in Figure 113 for 7.5 $MeV cm^2/mg$ argon. The static SEU mechanisms (multiple-node, N-P coincidence) at tilt angles greater than 60° continue to dominate the SEU cross section relative to those at smaller angles.

No single-node charge collection induced errors were recorded by the simulator until 100 MHz. Single-node mechanisms (e.g., internal transients) became more probable with increasing frequency and were approximately 50% of the overall error rate by 1000 MHz. The fraction of errors from charge collection on a single node relative to the measured error rate as a function of frequency is shown in Figure 114. The calculation in Figure 114 accounts for those errors in which a single transistor was struck. It does not contain information for cases in which multiple devices were struck, but only one device within list

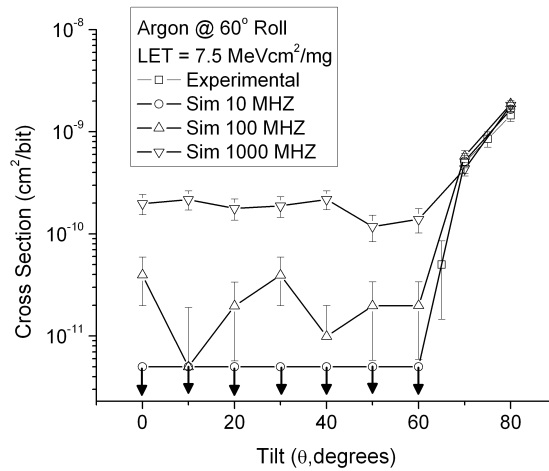

Figure 113: Experimental (100 kHz) SEU cross sections over tilt angle versus MRED predictions for Argon at 60° roll.

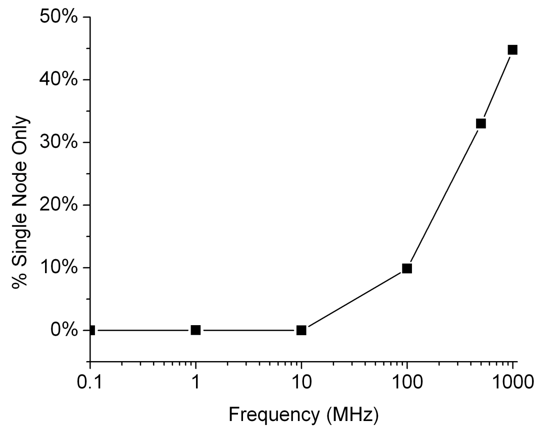

Figure 114: Percentage of errors from charge collection on a single transistor relative to the overall error rate as a function of frequency.

of simultaneously struck devices would have caused SEU.

Because single-node mechanisms are driven by direct charge collection on a single transistor, they are not as sensitive to the orientation of the beam, and are present over a greater range of tilt angles.

The combined effect on SEU rate in the space environment is illustrated in Figure 115,

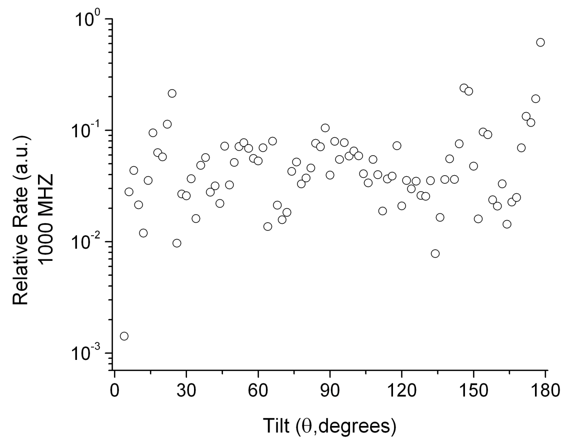

Figure 115: Scatter plot of the relative contribution of tilt angles to the SEU rate prediction at 1000 MHz, integrated over all roll conditions.

where little difference in sensitivity is observed over tilt angles. Recognize that Figure 115 is not a measurement of SEU cross-section alone. Rather, it is the combined effect of all species spanning the range of LET in the natural environment from an isotropic exposure. A direct comparison between broad-beam simulations over all LET and the space environment is difficult due to the presence of a continuum of LET values and the exponentially decreasing flux with increasing LET in the space environment. Competing mechanisms, related to pulse width, LET, and particle flux affect the SEU rate.

Classification of Static and Dynamic SEU

The relative contribution of static and dynamic SEU mechanisms are investigated in this section. The results are compared to SEU rates predicted by the standard IRPP model (CREME96 [31]). To reiterate, static and dynamic refer to the mechanism of SEU, not the condition of the device under test or simulation. For the device studied in this work, a static SEU is the corruption of the stored state of the device, by simultaneous multiple circuit node charge collection. It does not require a clock cycle to latch the error. Dynamic SEU are from the transient perturbation of an internal node, which, if occurring near a

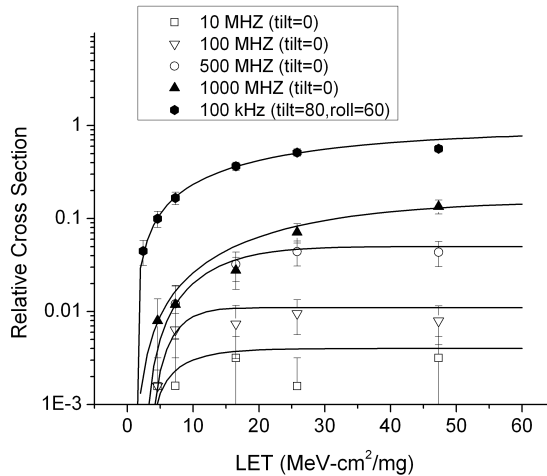

Figure 116: Simulated heavy ion relative SEU cross-section curves.

clock edge, may result in the storage and propagation of erroneous data.

The simulated heavy ion cross-sections for the ions discussed in the *MRED Model and Calibration* section are shown in Figure 116, with visually minimized Weibull fits for each frequency series at normal incidence only. No errors were predicted by simulation at normal incidence for 100 kHz. The data represented by the open markers are for a normally incident beam direction, at frequencies of 10, 100, 500, and 1000 MHz. The data are normalized to the worst-case cross-sections (tilt = 80°, roll = 60°) at various values of LET, which were insensitive to variations in the clock frequency up to 1 GHz. As discussed in previous sections, the 80/60 SEUs were static in nature, and sufficiently large as to dominate the SEU cross section of the less probable dynamic errors. Note that for the normally incident ions, simulations predict that the SEUs were due to transient corruption of an internal node, which was latched at the clock edge. These arose only from strikes to single circuit nodes. The SEU cross section trends at normal irradiation angles as a function of clocking frequency are in agreement with those reported in [123],[124].

The Adams 90% worst-case environment was imported into CREME96 and, in conjunction with the Weibull parameters from the curves of Figure 116, used to examine the

changes in the SEU rate as a function of clock frequency (Figure 117). Shown on the same curve are the MRED SEU rates and two boundaries labeled 100% admittance and 14% admittance. The line labeled 100% Admittance is the CREME96 prediction based on the tilt = 80°, roll = 60° rate cross-section curve alone, and the line labeled 14% Admittance represents the rate scaled by the fractional area of the unit sphere subtended by the angles of the dominant cross-sections as determined by Figure 110 and Figure 111, calculated using (42).

$$Fraction = \frac{1}{2\pi}\int_{30^\circ}^{90^\circ}\int_{65^\circ}^{115^\circ} \sin\theta d\theta d\phi \tag{42}$$

Simulation does not predict that the SEU rate will depend on frequency below 100 MHz. This region is dominated by errors in the sequential logic that are independent of the clock frequency and establish a base-line SEU rate that is in relatively good agreement with the scaled 100 kHz tilt = 80°, roll = 60° CREME96 prediction (14% Admittance). In this region, static SEU (mechanisms) establish the error rate.

As clock frequency increases, the SEU response becomes more isotropic as the dynamic SEU mechanisms play an increasingly significant role. Inspection of Figure 117 suggests that more traditional single-volume IRPP rate prediction method begins to approach the full physics-based rate prediction simulation for this case. This behavior is not unexpected, since RPP models are built upon the assumption of a response that is closer to isotropic (albeit cuboidal).

Conclusions

By incorporating both radiation transport and SPICE simulation tools into a single automated simulation flow it is possible to identify single event upset vulnerabilities from both a layout and circuit perspective with no user intervention during run time. The multiple sensitive volume model provides the investigator the ability to capture intra-transistor charge collection dynamics. The multiple sensitive volume group implemented in a suitable

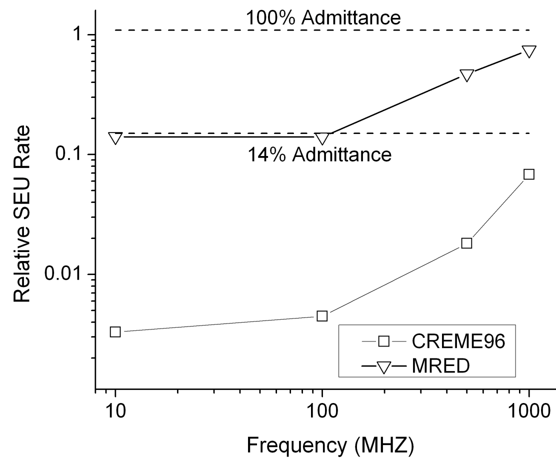

Figure 117: Relative error rates as a function of frequency for MRED simulations and CREME96 Weibull parameters, normalized to the static SEU rate estimate from the 80/60 data.

environment transport code, coupled with SPICE simulation provides both a determination of the environmental SEU rate as well as diagnostic information regarding the mechanism of SEU, the locations of SEU, and the propagation of errors within the circuit under analysis. The results are useful for guiding subsequent re-designs and identifying the effects of layout modifications on the SEU cross sections and SEU rate, as they directly relate the layout to the circuit performance. Furthermore, the simulations can be used to verify that the heavy ion test campaign used to calibrate the models was adequate for accurate prediction of SEU rates.

To reduce the overall rate, redesign of the integrated circuit is required to eliminate charge sharing between proximate NMOS devices, proximate PMOS devices, as well as the coincident charge collection between NMOS and PMOS transistors. An adequate range of tilt and roll angle heavy ion irradiations must be part of test plans when measuring SEU cross sections in single-node hardened circuitry to calibrate models accurately and predict on-orbit SEU rates, as well as identify all possible coupling mechanisms. In order to achieve significant changes in the on-orbit mean time between SEU, all possible coincident

mechanisms must be identified and addressed during layout, as demonstrated by the V1 and V2 DICE analyses.

In the V2 DICE, competition between static and dynamic SEU mechanisms that is dependent on device orientation, particle LET, and operating frequency was examined. Identifying the angular dependence of the SEU cross section within the frequency extremes of the component at a reduced set of orientations is not alone sufficient to determine the SEU rate, whether the frequency extremes are determined by mission requirements or as part of determining the datasheet performance of the component.

It was shown for the V2 DICE that within the range of frequencies examined, the baseline SEU rate is determined by the high-angle cross sections (for this class of device). In the range of intermediate frequencies, it is not accurate to assume that the relatively small cross sections observed over the typical tilt ranges ($< 60^\circ$) are sufficient for a proper rate prediction. This, however, does not appear to be a reasonable assumption based on the results presented in this work. For circuitry designed to be resistant to single-node effects, one should anticipate and account for such an outcome in the test planning phases.

CHAPTER VI

SOURCES OF UNCERTAINTY

In this work, examples of estimating charge collection by using the multiple sensitive volume model and relatively complex cases of estimating error rates in circuits operating dynamically with multiple sensitive volume groups were examined. In the case of the SRAM discussed in Chapter III, the unit cell was compact and the circuit response was readily characterized. That is, the memory element exist in one of two states, and in each state, two transistor nodes were sensitive. A broad scope of data were available and the modeled and measured responses for the environments were in good agreement, validating the multiple sensitive volume model for the component, the circuit response metric (Q_{crit}), and the physics transport. Conversely, the DICE flip-flop of Chapter V contained almost 10 times more transistors with the circuit level response dependent data and clock states (and transition edges) and a less well defined and experimentally characterized response that was determined to be based on both single and multiple node SEU mechanisms.

Regardless of the level of complexity of the model, potential sources of error in the predictions it makes should be identified and minimized, where possible. The analyses in this work are organized in such a way as to separate the processes of energy loss, charge transport, and circuit response. The physical transport processes that are used in conjunction with the size, placement, and efficiencies of the system volumes to define where and how much energy is deposited per radiation event. The linear weighted summation of energy deposited within them defines the collected charge. And ultimately, the quantity of collected charge at each circuit node is used to predict the circuit response (e.g., SEU cross section or error rate) to the environment. Each stage of the calculation introduces some measure of uncertainty in the predicated parameter.

Sources of uncertainty in modeled systems are often divided into two categories: Epistemic and Aleatory. Epistemic sources of uncertainty are defined as those that arise from a lack of knowledge of quantities or processes of the system or the environment. In this work, epistemic uncertainty arises from a model that is not properly calibrated or not calibrated within the range of the environment, such as the case of building a multiple sensitive volume model from limited heavy-ion irradiation angles which are ultimately used to predict an SEU rate in an isotropic environment. Failing to recognize and incorporate an SEU mechanism, such as a sensitive node pair in DICE circuitry, into the rate prediction model is another pertinent example of epistemic uncertainty.

Aleatory uncertainty results from variations in the physical system or the environment [125]. Examples include variability in the external environment, the logic state of the circuit, and the logic levels of the signals that interface the circuit to upstream and downstream logic. The aleatory uncertainty associated with the predicted SEU rate as a function of logic condition has been addressed in Chapter III through V by evaluating the the SEU response in fixed states (logic 1 or 0), checkerboard patterns in SRAM, and as a function of clocking frequency in the DICE flip-flop. In all cases, assumptions had to be made about the state of the circuit or memory array that were based on the most probable configuration of it. However, ultimately this type of uncertainty can only be reduced by knowing precisely the configuration of the device or devices in their ultimate application.

Epistemic and aleatory uncertainty may be introduced in the predicted parameter by terminating Monte Carlo simulations based on an arbitrarily large sampling of the simulated space or an arbitrarily small variance in the estimated mean (or rate of change in variance with increasing N). However, it is impossible to assign a value of uncertainty to an effect that is neither known nor measured. Therefore, the burden is on the investigator to recognize all the possible mechanisms that may lead to SEU and to verify that the mechanisms have been sampled in simulation. If a known SEU mechanism is not observed in the rate estimation, the investigator must fundamentally understand why the plausible outcome was

not observed and if the observation is consistent with physical reality. For example, if a two-node mechanism is known to potentially cause SEU, but is not observed in alpha simulations of energies in the realm of radioactive decay, then the investigator may recognize that the two sensitive nodes are farther apart than the maximum alpha range. Thus, the simulation result is physically reasonable. If, however, both the separation and sensitivity of the nodes is consistent with the expected range and stopping power, a more extensive sample count, sufficient to observe a statistically meaningful number of events, is warranted.

Consider the progression of a rate calculation shown in Figure 118, where the variance is reported in terms of the single standard deviation percent of the mean ($\sqrt{\sigma_\mu^2}/\mu$). The simulation, performed in MRT, is of a two-volume group containing a small volume (0.2 x 0.2 x 0.2 μm^3) of unity efficiency and a relatively large volume (5.0 x 5.0 x 5.0 μm^3) of 0.5% efficiency. The sensitive volume group has a Q_{crit} of 4 fC and the rate prediction is performed for the *GEO Solar Min* environment. The simulator was directed to report the mean and variance of the SEU rate during execution. Prior to approximately 8000 events, the estimate of the mean is below 5×10^{-12} day^{-1} and the trend in the percentage of the standard deviation with respect to the mean suggests that the simulation is converging. However, at approximately 8000 events a particle is observed to cause a SEU which drives both the event rate several orders of magnitude higher and the error in the mean close to unity. This type of progression is called the *lucky particle* problem and is most often evidenced by the periodic steps in the variance and the estimated mean, as shown in Figure 118.

The circumstances of the simulation represented in Figure 118 are contrived for the purpose of illustrating the *lucky particle* problem. However, they were contrived on the *a priori* knowledge of two correlated mechanisms that are common in the implementation of the multiple sensitive volume model. That is, the volumes that represent the active silicon region are of the highest efficiency, but often the smallest cross-section (projected surface area). In contrast, suitable substrate volume models have lateral extents that are commonly

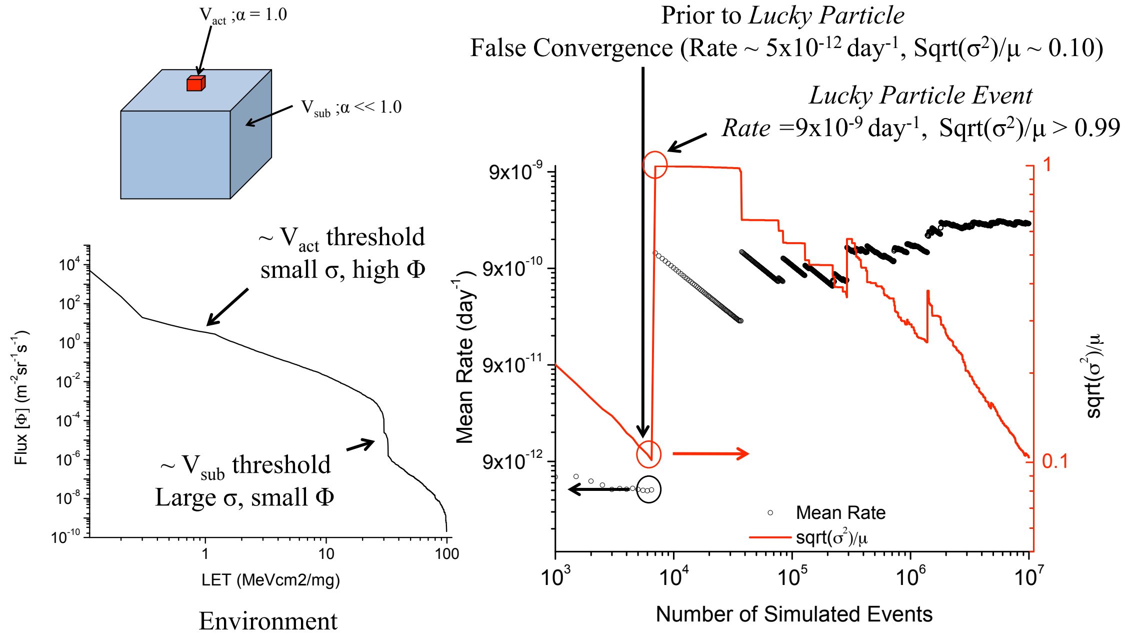

Figure 118: Example of the progression of the estimated rate with increasing samples in a Monte Carlo simulation.

on the order of a magnitude greater in each dimension than the active silicon volume. In the space environment, the particle flux decreases by at least a decade in abundance per decade increase in LET (Figure 118). Intuitively, one recognizes that the probability of striking the smaller volume is less, but the effect on the rate estimate is large relative to lower LET particles striking the outer-most substrate volume.

In Appendix A, it is shown that the total error rate can be decomposed into the sum of all mechanisms for Poisson processes. Therefore, a suitable approach to overcoming the spectral sampling error is to separate the error rate into discrete ranges of LET, per (43), and requiring that non-zero estimates of $\lambda(LET)$ be determined by the simulator prior to completion. The variance of the estimate is calculated in the usual manner as the square of the sum of the weights (44). A suitable data structure and event tracking algorithm must be used which preserves the correlation between the source particle LET and the accumulated weights and squares.

$$\lambda \approx \frac{1}{N}\left(\sum \lambda(0 \leq LET < 2) + \sum \lambda(2 \leq LET < 4) + ...\right) \tag{43}$$

$$Var[\lambda_{est}] = \frac{1}{N^2}\sum w^2_{|(0 \leq LET < 2)} + \frac{1}{N^2}\sum w^2_{|(2 \leq LET < 4)} + ... \tag{44}$$

In most applications, (43) is not practical. A more easily implemented approach is to determine the threshold LET, which is known based on the sensitive volume dimensions, efficiencies, and critical charge of the circuit divide the rate into two separate regions, such as that shown in (45), where LET_{th} is the threshold LET and 2 is chosen arbitrarily for the purpose of illustration. If it is known that LET_{th} exists in the environment being sampled, and that the abundance of particles is relatively high near threshold, then the simulation should be constructed to guarantee that a nonzero estimate of $\lambda(LET < 2 \cdot LET_{th})$ is achieved. Repeated simulations are often required to explore the boundaries of the two regions to yield the greatest confidence in the estimate of the system λ.

$$\lambda \approx \frac{1}{N}\left(\sum \lambda(LET < 2 \cdot LET_{th}) + \sum \lambda(LET > 2 \cdot LET_{th})\right) \tag{45}$$

In physics-based simulation, the environment is sampled by atomic number and energy rather than LET. There are orders of magnitude variation in particle abundance across both dimensions, Z and E. Careful consideration must be given to the number of samples taken from each particle spectrum, $\phi(E|z)$. If one knows the peak LET for all atomic numbers, then identifying the point at which SEU are expected as a function of Z is attainable. The estimated error rate can then be decomposed into $\lambda(Z)$, and the sampling adjusted to minimize the variance of the estimated λ for all species. The process is shown mathematically in (46). As in (43), (46) is not always practical. Greater efficiency, in terms of simulation time and confidence, may be achievable by considering unit increases in $\lambda(Z)$ within the range of $1 \leq Z \leq 26$, and $\lambda(Z > 26)$, as 26 is the atomic number of iron, after which the space environment spectral abundances decreases dramatically [1].

$$\lambda \approx \frac{1}{N}\left(\sum \lambda(Z=1) + \sum \lambda(Z=2) + \sum \lambda(Z=3)...\right) \tag{46}$$

In Chapter III, the uncertainty in the full-spectrum error rate calculation was mitigated by proton testing, and proton and mono-energetic neutron simulation, where the cross-section at low energies ($\approx 10\ MeV$) were determined and convolved with the natural environment to put an upper bound on the overall contribution to the full-spectrum rate. It was recognized that sub-10 MeV neutrons *could* cause SEU, and thus the sampling requirements were not based on the number of particles, but the number of SEU measured (and the corresponding variance) for particles in the sub-10 MeV range. This subtle, but critical difference in sampling requirements was enforced in all chapters. Re-stated, it is not the number of particles, but the number of SEU that result within the range of highest particle abundance, regardless of probability, that define confidence in the final estimated rate and variance in the estimation.

$$\lambda \approx \frac{1}{N}\left(\sum \lambda(1 < E < 10\ MeV) + \sum \lambda(10 \leq E < 20\ MeV)...\right) \tag{47}$$

In Chapter IV, the SEU mechanisms, from the circuit perspective, were clearly defined. That is, valid SEU occurred only when explicitly defined Q_{crit} coincidence criteria were met. The λ estimate was decomposed into discrete contributions from the defined coincidence requirements and variance criteria established for the separate components, shown in (48), where $TxA, B, C..$ is the identity of the transistor participating in the SEU. As in all analyses, confidence in the sensitive volume parameters, critical charges, and mechanisms was gained by calibration of the model to experimental data. Execution of the full-environment SEU rate prediction was reduced to guaranteeing that all modes of failure were sampled.

$$\lambda \approx \frac{1}{N}\left(\sum \lambda(TxA \cdot TxB) + \sum \lambda(TxB \cdot TxC) + \sum \lambda(TxA \cdot TxC)...\right) \tag{48}$$

In Chapter V, MRED-SPICE coupled simulation results were used to probe the sensitive node combinations of the DICE flip-flop. The process of calibrating the simulation results to heavy ion data, and the iterative process of predicting the error rate built the decomposition of the system error rate into separate mechanistic contributions and their respective thresholds. Systematic error was quantified by lack of experimental data outside of the range of calibration by investigating the failure rate from ions arriving over angle, as in (49). Epistemic sources of error were minimized repeated Monte Carlo simulations and inspection of the simulation output using (47), (48), and (46), following calibration to the heavy ion broadbeam data.

$$\lambda \approx \frac{1}{N}\left(\sum \lambda(90^\circ \geq \theta > 65^\circ) + \sum \lambda(65^\circ > \theta \geq 0^\circ)\right) \tag{49}$$

In summary, one must not assume that a total event count, N, or achieving a target variance of the estimated mean rate of the entire system is sufficient under any circumstances. An understanding of the SEU mechanisms of the circuit under investigation must exist prior to executing the calculation and calibration of the model to experimental data is required. Recognizing the range of applicability of the data against the contribution from mechanisms that occur outside of calibration must also be reported.

Defining the circumstances that distinguish between all processes which contribute to the estimated rate is arbitrary and exploitable for the purpose of gaining confidence in the accuracy of the estimation within the systematic uncertainty of the as-modeled system. One cannot know the number of distinguishable mechanisms by merely observing the final estimate of the rate integral. Further, what constitutes a unique mechanism from a simulation standpoint, is subjective, regardless of what is known *a priori* of the system's failure mechanisms.

CHAPTER VII

CONCLUSIONS

The multiple sensitive volume model is a novel approximation of the charge transport and collection processes associated with ionizing radiation. It was shown in Chapter II that multiple sensitive volumes could be constructed in such a way as to approximate the collected charge at commonly encountered device nodes (e.g., NMOS and PMOS transistors) as a function of ion strike parameters (e.g., direction, position, and LET). The method was shown to be extensible for multiple node charge collection from single ion strikes by the use of sensitive volume groups. When combined with layout (transistor placement) information it provides a relationship between the as-built silicon and the charge collected at all transistors affected by an ion or ions. In short, it is possible to generate a definite relationship between the charge generated in silicon to the charge collected at transistor contacts, which naturally integrates with commonly accepted techniques in circuit level SEU simulation.

The application the Monte Carlo method eliminates the computational burden imposed on the individual for determining analytic solutions to chord length distributions. This is especially beneficial for multi-node mechanisms which require solutions of coincident chord length distributions. The method does place the burden of recognizing all mechanisms of SEU on the investigator in order to properly estimate the desired parameters (e.g., SEU cross section and error rate) as discussed in Chapter VI.

As discussed in the introductory chapter, terrestrial environments present the investigator with particles whose energy loss mechanisms are more complex than that of the space environment. High energy and thermal neutrons undergo nuclear reactions which subsequently produce showers of charge particles that lead to SEU. Alpha particles result from nuclear decay of contaminant materials. They have ranges that are comparable to the

depth of the silicon BEOL and as such, their LET is highly variable in and around the active silicon region. Terrestrial SEU rate predictions involve the application of empirical and semi-empirical particle dependent models. In this work it was proposed and demonstrated that using Monte Carlo physics based transport in conjunction with the multiple sensitive volume model could address and unify the problem of terrestrial SEU rate prediction.

An analysis of terrestrial SEU mechanisms was performed on a full SRAM circuit in Chapter III. Analyses using SPICE and TCAD identified the location and approximate extents of the sensitive volumes. Critical charge was retained as the salient metric for defining valid SEU conditions at the circuit level. Calibration of the sensitive volume parameters to heavy ion data, rather than charge collection simulations alone, was used. It was shown that the calibrated sensitive volume model, when incorporated into physics based transport software, is applicable to predicting error rates across the spectrum of particles and energies encountered in the terrestrial environment, unifying the error rate calculation approach into a single simulation flow.

Multiple sensitive volume groups were extended to the problem of predicting SEU rates in DICE circuitry, where coincident charge collection (per ion) is required on two transistor nodes to cause SEU. As in the case of Chapter III, experimentally measured SEU cross sections were used to generate sensitive volume parameters. The combination of circuit analyses and calibration to experimental SEU cross sections was used to create a grouped sensitive volume model. The model was able to capture the LET and angular dependence of the SEU cross section for the part. In modeling the SEU response of circuitry with multiple node SEU requirements, multi-volume models must be applied as no manipulation of the traditional RPP, IRPP, or other RPP variants is suitable. Once a calibrated model is developed, a number of investigative avenues are available which may be exploited to improve the understanding of the relationship between the layout, circuit design, and error rate.

In Chapter V, the DICE latch architecture was extended to the case of a master-slave

flip-flop. Incorporation of SPICE simulation within the transport simulator provided a mechanism for investigating the circuit response directly from the radiation environment in a dynamic operating mode. By combining the transport and circuit simulation, it was shown that one could prioritize the sensitive parameters of both the environment (e.g., particle type, energy, and direction) and the circuit state (master-slave states, clock conditions, and frequency). Epistemic sources of uncertainty were examined at length to identify potential error arising from limited experimental calibration and the model's prediction. The sensitive volume group paradigm is a natural interface to external simulators since collected charge is analyzed on a per-transistor basis.

The multiple sensitive volume model and the Monte Carlo methods presented in this work present a significant evolution in the process of error rate prediction and modeling that was not possible with the classic single volume RPP model. Assumptions of continuous stopping power for particles in the environment are relaxed, as the local environment relative to the sensitive volumes becomes determined by physics based transport through the surrounding materials.

The flexibility the method affords introduces a significant number of possible sources of uncertainty in the final estimate. The parameters that are predicted in simulation only reflect those mechanisms that are included by the investigator, be they proper selection of physics models for transport or a complete and exhaustive set of coincident node critical charge requirements. As such, model predictions should be verified against experimental results, and predictions made outside of the calibration range should reflect the error that is introduced. The simulation method itself should be used for quantifying the probability of known mechanisms, which are determined by other simulation techniques (e.g., TCAD and SPICE) and experimental measurements (e.g., heavy ion broadbeam, neutron, proton, and microbeam measurements).

Appendix A

POISSON PROCESSES

The Poisson Distribution

The Poisson distribution is a discrete probability distribution function (*pdf*) that describes the probability of a given number of events occurring in a fixed period of time, when the mean is time independent. Poisson distributions are used to describe numerous random processes including SEU.

Poisson processes are *memoryless*, in which case the probability of future events is not affected by the occurrence of prior events. They are homogenous as long as the mean time between failure over the time interval for which the estimate is being calculated is static.

The probability of measuring k events, in the time interval $(\mathrm{t}, (\mathrm{t} + \Delta\mathrm{t})]$ is given by (50), where λ is the rate (as in, SEU), or the inverse of the mean time between failure (MTBF), and N is the cumulative number of events measured as a function of total time.

$$p\left[\left(N\left(t + \Delta t\right) - N\left(t\right)\right) = k\right] = \frac{e^{-\lambda \Delta t}\left(\lambda \Delta t\right)^{k}}{k!}; k = 0, 1, 2... \tag{50}$$

The total probability of no events being measured in the time interval (0,t], or alternatively, that the time of first arrival, $t_1 > t$, is given by (51).

$$P[t_1 > t] = e^{-\lambda t} \tag{51}$$

The probability density of the arrival of the first event occurring precisely at time, t_1, is given by (52). The expected value of t is the average time of first arrival or λ^{-1}, shown in (53).

$$p[t = t_1] = \lambda e^{-\lambda t} \tag{52}$$

$$\langle t \rangle = \int_0^\infty \lambda t e^{-\lambda t} = \frac{1}{\lambda} \tag{53}$$

The expected value of t^2 for the inter-arrival times of a Poisson process is given by (54).

$$\left\langle t^2 \right\rangle = \int_0^\infty \lambda t^2 e^{-\lambda t} = \frac{2}{\lambda^2} \tag{54}$$

The variance of t, $Var[t]$, is calculated by the difference of (54) and the square of (53) to give (55). The standard deviation is the the square root of the variance, which is $\frac{1}{\lambda}$ - the same value as the mean.

$$Var[t] = \left\langle t^2 \right\rangle - \langle t \rangle^2 = \frac{2}{\lambda^2} - \frac{1}{\lambda^2} = \frac{1}{\lambda^2} \tag{55}$$

Sum of Poisson Distributed Random Variables

If one considers the accumulation of random variables, X_i, their sum is also a random variable, Z, and is given simply by (56). Given the objective of recognizing the rate of failures induced by any number of failure mechanisms, one not only needs to know the sum of the random events (as in the accumulation of weights), but the probability distribution that arises in Z from their summation. In other words, what is the relationship between the statistical properties of X_i, such as the expected value and variance, and the same properties in Z that arises from the summation?

$$Z = \sum_{i=1}^{M} X_i \tag{56}$$

Consider the general case of the probability density function, $f_z(z)$, that arises from the sum of random variables, each with probability density functions, f_{x_i}. The resultant *pdf* can be calculated by the convolution of the respective probability density functions of X_i, shown in (57) [126].

$$f_z(z) = f_{x_1}(x) * f_{x_2}(x) * f_{x_3}(x)*, ..., f_{x_M}(x) \tag{57}$$

The convolution calculation can be greatly simplified by recognizing that the Fourier Transform of M convolutions is the product of the Fourier transform of each f_{x_i}, given by (58).

$$\mathcal{F}\left(\mathrm{f_z(z)}\right) = \mathcal{F}\left(\mathrm{f_{x_1}(x) * f_{x_2}(x)*, ..., f_{x_M}(x)}\right) = \prod_{\mathrm{i=1}}^{\mathrm{M}} \mathcal{F}(\mathrm{f_{x_i}(x)}) \tag{58}$$

In this derivation, the Fourier Transform is defined by (59), which is also the *characteristic function*, $\varphi_x(s)$, commonly used in statistical analyses. For the case of this derivation, the sign convention in the Fourier Transform is only relevant when performing the inverse transformation.

$$\mathcal{F}(\mathrm{f_x(x)})(\mathrm{s}) = \int_{-\infty}^{\infty} \mathrm{e^{isx} f(x) dx} \equiv \varphi_{\mathrm{x}}(\mathrm{s}) \tag{59}$$

Substituting (59) into (58) results in the expression for the probability density function of z, $f_z(z)$, given in (60).

$$f_z(z) = \mathcal{F}^{-1}\left(\prod_{\mathrm{i=1}}^{\mathrm{M}} \varphi_{\mathrm{x_i}}(\mathrm{s})\right) \tag{60}$$

Up until this point, no assumptions have been made about the *pdf* of each random variant, X_i. However, if it assumed that each random event is generated from a Poisson process having a unique λ, $\varphi_x(s)$ is calculated by (61), where the integral has been replaced by a summation over k, $k \in \{0, 1, 2, ..., \infty\}$.

$$\varphi_x(s) = \sum_{k=0}^{\infty} \frac{(\lambda t)^k}{k!} e^{-\lambda t} e^{isk} = e^{\lambda t\left(e^{is}-1\right)} \tag{61}$$

After substitution and algebraic manipulation, $\varphi_z(s)$, is reduced to the simplified form shown in (62). Note that λ_i have been collected and $\varphi_z(s)$ is otherwise identical to the *characteristic function* of the Poisson Distribution.

$$\varphi_z(s) = \prod_{i=1}^{M} \varphi_{x_i}(s) = e^{\left(\sum_{i=1}^{M} \lambda_i\right) t \left(e^{is}-1\right)} \tag{62}$$

By deduction (rather than rigorously performing the Fourier inversion), the *pdf* of $f_z(t)$, assuming that each random variant is Poisson distributed, is also Poisson distributed, and given by (63).

$$f_z(t;\lambda_1,\lambda_2,...,\lambda_M) = \mathcal{F}^{-1}\left(\varphi_{\mathrm{z}}(\mathrm{s})\right) = \frac{\left(\left(\sum_{\mathrm{i}=1}^{\mathrm{M}} \lambda_{\mathrm{i}}\right) \mathrm{t}\right)^{\mathrm{k}}}{\mathrm{k}!} \mathrm{e}^{-\left(\sum_{\mathrm{i}=1}^{\mathrm{M}} \lambda_{\mathrm{i}}\right) \mathrm{t}} \tag{63}$$

Likewise, the *pdf* of inter-arrival times is given by (64).

$$f_z(t;k=1,\lambda_1,\lambda_2,...,\lambda_M) = \left(\sum_{i=1}^{M} \lambda_i\right) e^{-\left(\sum_{i=1}^{M} \lambda_i\right) t} \tag{64}$$

The expected value, $\langle f_z \rangle$, is given by (65), which is the average time of arrival between events.

$$\langle f_z \rangle = \frac{1}{\sum_{i=1}^{M} \lambda_i} \tag{65}$$

The failure rate of the system, λ_{sys}, is thus the linear sum of each λ_i, (66). This results indicates that the overall system error rate is just the linear combination of error rates arising from, M, individual mechanisms.

$$\langle \lambda_{sys} \rangle = \sum_{i=1}^{M} \lambda_i \tag{66}$$

Experimentally, the measured the failure rate is given by (67), where N_u is the number of observed SEU, and t is the time period of exposure.

$$\lambda_{exp} = \frac{N_u}{t} \tag{67}$$

Given that the events are independent, the error rate is the arithmetic mean of the measured time intervals, Δt_i, which corresponds to the average of λ_i, shown in (68).

$$\lambda_{exp} = \frac{1}{N}\sum_{i=1}^{N}\frac{1}{\Delta t_i} = \frac{1}{N}\sum_{i=1}^{N}\lambda_i \tag{68}$$

Equation 66 demonstrates that regardless of the internal mechanisms that contribute to the error rate, as long as they are Poisson distributed, the measured failure rate is also Poisson distributed. The measured error rate, with or without knowledge of the internal mechanisms, is given by the average of all measurements (68).

Estimation

As mentioned in the previous section, the accumulation of N experimental (or simulation) measurements of the error rate can be viewed as the sum of N weighted λ, each of weight $\frac{1}{N}$. This is formally defined as the estimator for the mean error rate, which is also the maximum likelihood estimator of λ, given by (69).

$$\langle\lambda\rangle \approx \hat{\lambda} = \frac{1}{N}\sum_{i=1}^{N}\lambda_i \tag{69}$$

Depending on the level of knowledge of the system, one can describe (by mechanism) the total error rate as the sum of the average of all estimated rates, shown in (70), where N measurements of the system are evaluated over M mechanisms. Equation 70 is valid as long as the set M contains all possible failure modes.

$$\hat{\lambda}_{sys} = \sum_{i=1}^{M}\left(\frac{1}{N}\sum_{j=1}^{N}\lambda_{i,j}\right) \tag{70}$$

Equation 55 is the variance associated with the parent distribution. There is also a variance associated with the estimator of the mean. That is, the estimate of λ is made by counting the number of events over a time interval. if the mean of N observed events is N_{SEU}, then a suitable expression for an estimate of the $Var[N_{SEU}]$ is needed.

Consider scaling $Var[N_{SEU}]$ into an arbitrarily small time intervals of width Δt. This results in $\frac{t}{\Delta t}$ equally probable bins of $N_{\Delta t}$ counts. The sum of all $Var[N_{\Delta t_i}]$ is the total

variance, per (71).

$$Var[N_{seu}] = Var\left[N_{\Delta t_1} + N_{\Delta t_2} + ...\right] = \frac{t}{\Delta t} Var[N_{\Delta t}] \tag{71}$$

The expected number of events that one observes in Δt is given by (72), where it is assumed that Δt has been made sufficiently small that the probability of observing more than one event is also vanishingly small (that is, $\lambda << \Delta t^{-1}$). The expectation of the square of $N_{\Delta t}$ is calculated similarly and with the same assumptions (73).

$$\langle N_{\Delta t} \rangle = \sum_{i=1}^{\infty} i \cdot p(i) = 0 \cdot p(0) + 1 \cdot p(1) + 2 \cdot p(2) ... \approx p(1) \tag{72}$$

$$\left\langle N_{\Delta t}^2 \right\rangle = \sum_{i=1}^{\infty} i^2 \cdot p(i) = 0^2 \cdot p(0) + 1^2 \cdot p(1) + 2^2 \cdot p(2) ... \approx p(1) \tag{73}$$

The variance of $N_{\Delta t}$ is calculated in the usual manner and shown in (74), assuming that $p(1) >> p(1)^2$.

$$Var[N_{\Delta t}] \approx \left\langle N_{\Delta t}^2 \right\rangle - \langle N_{\Delta t} \rangle^2 \approx p(1) - p^2(1) \approx p(1) = \langle N_{\Delta t} \rangle \tag{74}$$

The $Var[N_u]$ is also $\langle N_u \rangle$, which is found by substituting (74) into (71) and simplifying, as shown in (75).

$$Var[N_u] \approx \frac{t}{\Delta t} \langle N_{\Delta t} \rangle = \left(\frac{t}{\Delta t} \right) \lambda \Delta t = \lambda t = \langle N_u \rangle \tag{75}$$

Therefore, when counting the number of SEU the reported number of events is given with the estimate of the mean and the square of the variance of its estimate, as shown in (76).

$$N_u = N_u \pm \sqrt{Var[N_u]} = N_u \pm \sqrt{N_u} \tag{76}$$

Reports of the estimates of λ, or the error rate as well as σ_{SEU} follow from (76) and are shown in (77) and (78), respectively. Note that Φ is the broadbeam flux (typically in $cm^{-2}s^{-1}$). If the total fluence, F, is reported, then (79) applies.

$$\hat{\lambda}_u = \frac{N_u}{t} \pm \frac{1}{t}\sqrt{N_u} \tag{77}$$

$$\hat{\sigma}_u = \frac{N_u}{\Phi t} \pm \frac{1}{\Phi t}\sqrt{N_u} \tag{78}$$

$$\hat{\sigma}_u = \frac{N_u}{F} \pm \frac{1}{F}\sqrt{N_u} \tag{79}$$

Appendix B

MONTE CARLO CALCULATIONS OF SEU CROSS SECTIONS AND ERROR RATES

SEU Cross Section and Rate Prediction

Weller, et al. [29], proposed a general single event rate calculation formula, shown in (80), where the total event rate, R_t is the sum of the events that originate from primary particles entering from the outside of the device or simulation boundaries, R_{ext}, and of particles that originate from within, R_{int}. Examples of external primary particles include heavy ions, neutrons, and protons. Internal particles are any species originating from radioactive decay. The total event rate is determined for a given time (t) and system configuration (ξ).

The calculation for R_{ext} is shown in (81). Each particle originates from the world surface, shown in Figure 119. That is to say, the particle's history always begins on the world surface. It may either terminate at another point on the surface, or stop at some point within it. The unit vector, $\hat{u}$, and the position vector, $\vec{x}$, describe each particles position and direction on the surface of the world (shown as a sphere for the sake of simplicity, though this assumption is not required). The *Heaviside function*, H, enforces the requirement that only particles in the direction of the interior of the world are considered (negative of the vector from

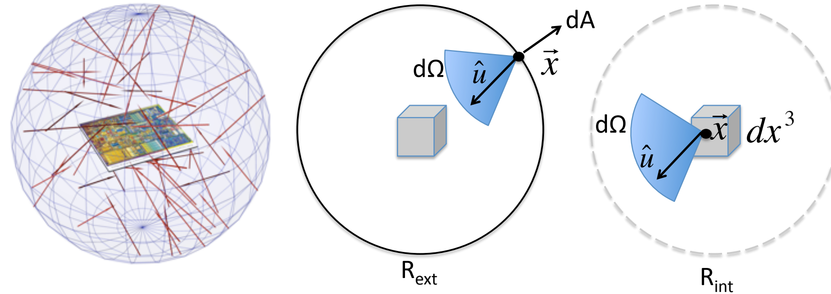

Figure 119: Concept of the world volumes (left) and parameters in the general rate equation (right).

the worlds origin to its surface). The differential particle flux, in addition to position and direction, is a function the particle type (z) and energy (E), which has a certain probability per unit time (P_e), of producing an effect (e.g., SEU) between all times in the past and the current time, t. ξ, represents the vector that describe the internal configuration of the system for the resultant P_e (e.g, clock state, node voltages, Q_{crit}, etc.). The integration is performed over each particle with energies, $E(z)$; position, $\vec{x}$ on the world surface, dA, and for all directions Ω at each $\vec{x}$. The process is repeated and the summation is taken over all species, z, in the environment.

The internal event rate, (82), retains the same properties as the external rate, however a new function, G, is introduced that describes the emission properties of the radiation source *within* the relevant volume, S. Particles are not restricted in their direction with respect to the world surface, so there is no requirement for the *Heaviside function*.

$$R_t\left(\xi,t\right) = R_{ext}\left(\xi,t\right) + R_{int}\left(\xi,t\right) \tag{80}$$

$$R_{ext}\left(\xi,t\right) = \sum_Z \int_E dE \int d\Omega \oint dA \left(-\hat{n}\left(\vec{x}\right)\cdot\vec{u}\right) \int_{-\infty}^{t} dt^{'}\,\Phi\left(z,E,\hat{u},\vec{x},t^{'}\right) p_e(z,E,\hat{u},\vec{x},t^{'};\xi,t) \tag{81}$$

$$R_{int}\left(\xi,t\right) = \sum_Z \int_E dE \int d\Omega \int_S dx^3 \int_{-\infty}^{t} dt^{'}\,G\left(z,E,\hat{u},\vec{x},t^{'}\right) p_e(z,E,\hat{u},\vec{x},t^{'};\xi,t) \tag{82}$$

Equations (80), (81), and (82) are valid for describing the process of predicting single event upset rates in an environment, including that of a test facility, depending on the correct integration ranges (e.g., Ω, S, E, and z). The effect description (in this case, an SEU) is entirely contained within p_e. Analytic solutions to the general rate equations are difficult, if not impossible, to determine in all but the simplest applications. It is for this reason that Monte Carlo integration techniques are applied to solving R_t by virtue of sampling over the integration domains and generating estimates of p_e during the course of

simulation. The process of Monte Carlo integration is described in the remainder of this Appendix.

Monte Carlo Integration

Monte Carlo integration is a powerful tool for determining integrals for complex functions. It overcomes the difficulty of generating analytic solutions for the processes described by them. In this work, Monte Carlo integration techniques are used to arrive to approximations of the failure rate as described by the integrals in (80) through (82). This section describes the basic process of Monte Carlo integration and the minimum set of randomization techniques necessary to simulate the radiation environment.

Consider the one-dimensional integral in (83) and the definition of the expectation value of a function, $\langle g(x) \rangle$ shown by (84).

$$I = \int f(x)\, dx \tag{83}$$

$$\langle g(x) \rangle = \frac{\int g(x) p(x) dx}{\int p(x) dx} \tag{84}$$

By defining $g(x)$ according to (85) and substituting the result into (84), one arrives at (86). Assuming $p(x)$ is normalized to unity (87), one finds that the definition of the integral given by (83) is the expected value of the ratio of $f(x)$ to $p(x)$, shown in (88).

$$g(x) \equiv \frac{f(x)}{p(x)} \tag{85}$$

$$\left\langle \frac{f(x)}{p(x)} \right\rangle = \frac{\int \left(\frac{f(x)}{p(x)} \right) p(x) dx}{\int p(x) dx} = \frac{\int f(x) dx}{\int p(x) dx} \tag{86}$$

$$\int p(x) dx = 1 \tag{87}$$

$$\left\langle \frac{f(x)}{p(x)} \right\rangle = \int \left(\frac{f(x)}{p(x)} \right) p(x)dx = \int f(x)dx \tag{88}$$

Equation 88 is not immediately useful for calculating I until one recognizes than an estimate of $\left\langle \frac{f(x)}{p(x)} \right\rangle$ can be formed by taking N samples of the random variable, X_i, over the integration domain, as shown in (89). Defining the *weight*, $w(X_i)$ according to (90), and substituting the result into (88) results in the expression for the Monte Carlo estimate, $\widetilde{I}$, of the analytic solution to I, shown by (91).

$$\left\langle \frac{f(x)}{p(x)} \right\rangle = \int f(x)dx \approx \frac{1}{N} \sum_{i=1}^{N} \frac{f(X_i)}{p(X_i)} \tag{89}$$

$$w(X_i) \equiv \frac{1}{p(X_i)} \tag{90}$$

$$I \approx \frac{1}{N} \sum_{i=1}^{N} w(X_i) f(X_i) \tag{91}$$

For k-dimensional integration of independent uncorrelated variables, (91) can be extended to (92). Where each function, f_j, is sampled at a unique point in its domain, $X_{i,j}$, multiplied by the corresponding *weight*, $w_j(X_{i,j})$, for the probability density function describing it. This result is the key aspect of the utility of Monte Carlo simulation as applied to rate predictions and the solution of the general rate equation presented in Chapter II.

$$\int dx_1 \int dx_2 ... \int dx_k f(x_1, x_2 ..., x_k) \approx \frac{1}{N} \sum_{i=1}^{N} f(X_{i,1}, X_{i,2} ..., X_{i,k}) \prod_{j=1}^{k} w_j(X_{i,j}) \tag{92}$$

The variance in the expected arrival times was previously determined to be $\frac{1}{\lambda^2}$. What remains to be calculated is the variance in the estimate of λ, where λ is determined by (92). Knowing that each evaluation of $f(\vec{X}_i)$ of the summation of (92) returns either a 1 or 0 the variance of the count is the same (per equation 75) must also be 1. Alternatively, one can recognize that no matter what small (δ) variability exists in X_i, the effect on $f(\vec{X}_i)$ is

limited to a unity transition. The resulting estimate of the variance in the calculated mean is given by (95), where $f(\vec{X}_i)$ selectively accumulates only those events that cause an error.

$$Var[f(\vec{X}_i)] = 1 \tag{93}$$

Given:

$$f(X_{poisson}) = \begin{cases} 1 & SEU \\ 0 & \overline{SEU} \end{cases} \tag{94}$$

$$\begin{aligned} Var[I] &\approx Var[\tfrac{1}{N}\textstyle\sum_{i=1}^{N} f(X_{i,1}, X_{i,2}..., X_{i,k}) \prod_{j=1}^{k} w_j(X_{i,j})] \\ &\approx \tfrac{1}{N^2}\textstyle\sum_{i=1}^{N} Var[f(X_{i,1}, X_{i,2}..., X_{i,k}) \prod_{j=1}^{k} w_j(X_{i,j})] \\ &\approx \tfrac{1}{N^2}\textstyle\sum_{i=1}^{N} f(X_{i,1}, X_{i,2}..., X_{i,k}) \prod_{j=1}^{k} w_j^2(X_{i,j}) \end{aligned} \tag{95}$$

Randomization Methods

In order to generate estimates of the integrals using Monte Carlo methods, one needs to determine suitable methods for the selection of the random variables contained within the integral.

Linear Sampling and Transformation of Variables

Consider the basic integral shown in (96). The selection of the independent random variable, X, is chosen randomly between $[a, b]$ and the probability associated with the selection is the inverse of the width of the domain per (97). The Integral than be approximated by randomly choosing N values of the random variable, X, over the domain, shown in (98).

$$\int_a^b f(x)dx \tag{96}$$

$$\frac{1}{w(x)} = p(x) = \begin{cases} \frac{1}{b-a} & x \in [a, b] \\ 0 & elsewhere \end{cases} \tag{97}$$

$$\int_a^b f(x)dx = \langle f(x)w(x)\rangle \approx \frac{b-a}{N}\sum_{i=1}^{N} f(X_i) \tag{98}$$

A convenient way to select X uniformly on the domain is by (99) on the interval $[0,1]$. Random selections on the interval $[0,1]$ are implemented in most programming languages. While not overly useful in this example, subsequent examples will strengthen the utility of the approach.

$$X(u) = a + (b-a) * u \quad u \in [0,1] \tag{99}$$

Note that one formally gets to (99) according to (100), where $X(u)$ is the quantile function generated by inversion of the cumulative density function of x. In this (and subsequent) examples, the inversion process is trivial, as the cumulative density function is monotonically increasing over the domain.

$$\begin{aligned} u(x) &= \frac{\int_a^x p(x)dx}{\int_a^b p(x)dx} \\ &= \frac{b-a}{b-a}\frac{x-a}{b-a} \\ &= \frac{x-a}{b-a} \end{aligned} \tag{100}$$

The *weight*, w, for all u, is simply $(b-a)$.

Transformation of the variables of integration is given by (101), where $\left|\widetilde{J}\right|$ is the determinant of the Jacobian matrix shown in (102).

$$\int_{x(u)} f(\vec{x})\, d\vec{x} = \int_u f(x(\vec{u}))\left|\widetilde{J}\right| d\vec{u} \tag{101}$$

$$\left|\widetilde{J}\right| = \begin{vmatrix} \frac{\partial x_1}{\partial u_1} & \frac{\partial x_1}{\partial u_2} & \cdots & \frac{\partial x_1}{\partial u_j} \\ \frac{\partial x_2}{\partial u_1} & \frac{\partial x_2}{\partial u_2} & \cdots & \frac{\partial x_2}{\partial u_j} \\ \cdots & \cdots & \cdots & \cdots \\ \frac{\partial x_i}{\partial u_1} & \frac{\partial x_i}{\partial u_2} & \cdots & \frac{\partial x_i}{\partial u_j} \end{vmatrix} \tag{102}$$

Transformation of the integral of $f(x)$ into the new domain $u \in [0,1]$ gives (103).

$$x(u) = a + (b-a)u$$
$$\frac{dx}{du} = b - a \tag{103}$$

$$\int_a^b f(x)dx = \int_0^1 f(x(u))\frac{dx}{du}du = (b-a)\int_0^1 f(x(u))du \tag{104}$$

The Monte Carlo approximation to the integral is now given by (105), where the constant weight has been pulled out of the summation.

$$(b-a)\int_0^1 f(x(u))du \approx \frac{b-a}{N}\sum_{i=1}^{N} f(x(U_i)) \tag{105}$$

Logarithmic Sampling

One may choose to select values of the independent variable, x, over [a,b] logarithmically. Such is the case when more sampling is desired closer to a, as in sampling LET spectra where a greater reduction in variance per sample can be achieved by increasing the probability of selecting an ion with lower LET. As will be shown, such biasing has an effect on the calculation of the *weight*, w.

$$u(x) = \frac{\int_{ln(a)}^{ln(x)} dx}{\int_{ln(a)}^{ln(b)} dx} = \frac{ln(\frac{x}{a})}{ln(\frac{b}{a})} \tag{106}$$

Solving for the inverse of u(x) gives (107).

$$x(u) = a\left(\frac{b}{a}\right)^u \tag{107}$$

The derivative with respect to u, also defined as the weight, $w(u)$, is given by (108).

$$\frac{dx}{du} = a\left(\frac{b}{a}\right)^u ln\left(\frac{b}{a}\right) \tag{108}$$

The final expression for the integral is given by (109), or more compactly, using the weighting notation, by (110). Note that unlike the uniform sampling on x, the logarithmic

sampling on x from the uniform sampling on u, produces a weight that is not constant, but a function of u. This gives more weight to larger u, or conversely, less weigh to smaller values of u. This is intuitively reasonable in that the sampling function produces a greater density of samples of x closer to a per (107)

$$a \cdot ln\left(\frac{b}{a}\right)\int_0^1 f(x(u))\left(\frac{b}{a}\right)^u du \approx \frac{a \cdot ln\left(\frac{b}{a}\right)}{N}\sum_{i=1}^{N}\left(\frac{b}{a}\right)^{U_i} f(x(U_i)) \tag{109}$$

$$I \approx \frac{1}{N}\sum_{i=1}^{N} f(x(U_i))w(U_i); w(u) = a\left(\frac{b}{a}\right)^u ln\left(\frac{b}{a}\right) \tag{110}$$

Picking Points on a the Interior of a Disk

The property of a broadbeam ion source, and the isotropic environment (once a direction is chosen), can be viewed as a uniform directional flux over the surface of an arbitrarily chosen disk. The radius of the disk can be defined in any number of ways, but the most common and convenient is that of one that entirely contains the target object(s). As such, in order to simulate both the broadbeam and isotropic environments, it is necessary to have a mechanism for picking points randomly on the surface of a disk, and evaluating the function of interest at those points. The equation for this operation is shown in (111), assuming that θ and r' are independent.

$$\int_0^{2\pi}\int_0^{r} f(r',\theta)r'dr'd\theta \tag{111}$$

$$\int_0^1\int_0^1 f\left(r'(u_1),\theta(u_2)\right) r'(u)\frac{dr'}{du_1}\frac{d\theta}{du_2}du_1du_2 \tag{112}$$

The transformation of θ proceeds in the usual way to give (113). The transformation of radial component requires greater attention, as the differential element is dependent on r', and is shown in (114), with the solution given by (115).

$$\begin{aligned} \theta(u) &= 2\pi \cdot u \quad u \in [0,1] \\ \tfrac{d\theta}{du} &= 2\pi \end{aligned} \tag{113}$$

$$u(r') = \frac{\int_0^{r'} r'dr'}{\int_0^{r} r'dr'} \tag{114}$$

$$\begin{aligned} r'(u) &= r\sqrt{u} \\ r'\tfrac{dr'}{du} &= \tfrac{1}{2}r\sqrt{u}ru^{-\frac{1}{2}} = \tfrac{1}{2}r^2 \end{aligned} \tag{115}$$

Equations 115 and (113) are substituted back into (111) to give the continuous solution in (116) and the Monte Carlo approximation in (117).

$$\int_0^1 \int_0^1 f\left(r'(u_1), \theta(u_2)\right) r'(u) \frac{dr'}{du_1} \frac{d\theta}{du_2} du_1 du_2 = \pi r^2 \int_0^1 \int_0^1 f\left(r'(u_1), \theta(u_2)\right) du_1 du_2 \tag{116}$$

$$I \approx \frac{\pi r^2}{N} \sum_{i=1}^{N} f\left(r'(U_i), \theta(U_i)\right) \tag{117}$$

Picking Points on the Surface of a Sphere

The directional component of the isotropic environments involves the uniform sampling of points on a sphere, and the direction is defined by the vector that joins the chosen point to the origin of the sphere. There is no radial element, as the purpose of the operation is simply to define the direction. The equation for the integral of a function over the surface a sphere is given by (118).

$$\int_0^{\pi} \int_0^{2\pi} f(\theta, \phi) sin(\theta) d\phi d\theta \tag{118}$$

As demonstrated previously, one wishes to achieve the transformation to the uniform random variant on $[0, 1]$, shown in (119).

$$\int_0^1 \int_0^1 f\left(\theta(u_1), \phi(u_2)\right) sin(\theta(u_1)) \frac{d\theta}{du_1} \frac{d\phi}{du_2} du_1 du_2 \tag{119}$$

The transformations for ϕ and θ are given by (120) and (121), respectively.

$$\begin{aligned} \phi(u_2) &= 2\pi u_2 \\ \tfrac{d\phi}{du_2} &= 2\pi \end{aligned} \tag{120}$$

$$\begin{aligned} \theta(u_1) &= cos^{-1}(1 - 2u_1) \\ sin(\theta)\tfrac{d\theta}{du_1} &= \tfrac{2sin\left(cos^{-1}(1-2u_1)\right)}{\sqrt{1-(1-2u_1)^2}} = 2 \end{aligned} \tag{121}$$

Substituting (120) and (121) into (119) produces the expression for the integral in (122). The Monte Carlo approximation is shown in (123).

$$\int_0^1 \int_0^1 f\left(\theta(u_1), \phi(u_2)\right) sin(\theta(u_1)) \frac{d\theta}{du_2} \frac{d\phi}{du_2} du_1 du_2 = 4\pi \int_0^1 \int_0^1 f\left(\theta(u_1), \phi(u_2)\right) du_1 du_2 \tag{122}$$

$$I \approx \frac{4\pi}{N} \sum_{i=1}^{N} f\left(\theta(U_{1,i}), \phi(U_{2,i})\right) \tag{123}$$

Monte Carlo Ray Tracing (MRT) Simulator

Introduction

The previous sections describe the basic procedures that form the basis of a Monte Carlo process and randomization techniques. The requirements of the randomization process determine the selection of the components that compound to describe the general expression for the SEU rate or SEU cross section. The general formula for the estimate of the integral and variance to be calculated by Monte Carlo simulation is shown in (124) and (125), where it is assumed that f returns 1 or 0. The objective is to find a suitable expression of f that captures the processes being investigated and translates them into a valid error condition

for the given state, $\vec{\xi}$ (configuration of the circuit, detectors, volumes, etc.). In this example, ξ is assumed to be constant, but in the general sense it can be a function of time or location.

$$I \approx \frac{1}{N}\sum_{i=1}^{N} f\left(x_1(U_{1,i}), x_2(U_{2,i}), ...x_k(U_{k,i}); \vec{\xi}\right)\prod_{j=1}^{k} w_j \tag{124}$$

$$Var[I] \approx \frac{1}{N^2}\sum_{i=1}^{N} f\left(x_1(U_{1,i}), x_2(U_{2,i}), ...x_k(U_{k,i}); \vec{\xi}\right)\prod_{j=1}^{k} w_j^2 \tag{125}$$

For the case of linear sampling from the differential LET spectrum, the rate equations takes the form of (126), where Φ is the differential particle flux at the selected LET, and LET_{max} and LET_{min} are the maximum and minimum ranges of LET in the spectrum. Note that the assumption is a linear sampling over the range of the LET (99). If the sampled spectrum is inverted (quartile function), (127) applies. Regardless of which sampling approach is chosen, a splined (inverted PDF) or interpolating look-up function must determine Φ from LET or *vice-versa*.

$$R \approx \frac{4\pi^2 r^2\left(LET_{max} - LET_{min}\right)}{N}\sum_{i=1}^{N} f\left(\vec{x}\left(\vec{U}_{pos,i}\right), LET(U_{LET,i}); \vec{\xi}\right)\Phi(LET(U_{LET,i})) \tag{126}$$

$$R \approx \frac{4\pi^2 r^2 \Phi_o}{N}\sum_{i=1}^{N} f\left(\vec{x}\left(\vec{U}_{pos,i}\right), LET(U_{LET,i}); \vec{\xi}\right) w_i(U_{LET,i}) \tag{127}$$

Where:

$$\Phi_o = \int_{LET_{min}}^{LET_{max}} \Phi(LET)d(LET)$$

In the case of a broadbeam simulation, there is no randomization over the unit sphere and only a fixed value of LET is assumed. The general equation for the uni-directional broadbeam case is shown in (128).

$$\sigma_{seu|LET} \approx \frac{2\pi r^2}{N}\sum_{i=1}^{N} f\left(\vec{x}\left(\vec{U}_{pos,i}\right); LET, \vec{\xi}\right) \tag{128}$$

A simple case of a single sensitive volume and Q_{crit} for the description of the event function, f, is shown in (129), where s is the chord length determined by suitable means through the volume for points P_1 and P_2 on the world surface (calculated from the initial position and direction on the disk and sphere).

$$f\left(\vec{P}_1, \vec{P}_2, LET\right) = \begin{cases} 1 & s(\vec{P}_1, \vec{P}_2) \cdot LET \geq Q_{crit} \\ 0 & s(\vec{P}_1, \vec{P}_2) \cdot LET < Q_{crit} \end{cases} \tag{129}$$

The remainder of the solution for both error rates and cross sections is one of describing $f\left(\vec{P}_1, \vec{P}_2, LET; \vec{\xi}\right)$.

Construction

The MRT software tool is one that is dedicated to testing for valid SEU conditions for a given sensitive volume and, if required, sensitive volume grouping, accumulating the weights of each evaluation, and reporting the final error rate or error cross section per (124), (126), and (128). MRT is not a physics-based transport tool. It's applicability is limited to the constant LET assumption; that is, the LET and trajectory of the particle does not vary over the course of the path through the sensitive volumes. It does not contain machinery for analyzing secondary particle production, such as elastic and inelastic proton or neutron reactions, thermal neutron capture, etc.

MRT can be configured to operate as a pure Python script, or for rapid analyses, a combination of Python and C^{++}. Collision detections and randomizations represent a large percentage of the total per-event run time, and C^{++} modules are preferred when large numbers of events, or configurations, are required. The mixed Python-C^{++} package was utilized in the optimizations of Chapter II.

The functional components of MRT are shown in Figure 120. The randomization components for the sphere, disk, and spectrum are identical to that discussed in Appendix B. For the isotropic case, all components of the *randomizer* (*Sphere*, *Disk*, and *Spectrum*) are

Table 12: Randomization Terms.

Symbol	Description	Expression	Weight
θ_s	Sphere	$cos^{-1}(1-2u)$	2
ϕ_s	Sphere	$2\pi u$	2π
θ_d	Disk	$2\pi u$	2π
r_d	Disk	$r\sqrt{u}$	$\frac{1}{2}r^2$
LET	Lin. Sample	$L_{min} + (L_{max} - L_{min})u$	$L_{max} - L_{min}$
LET	Log. Sample	$L_{min}\left(\frac{L_{max}}{L_{min}}\right)^u$	$L_{min}\left(\frac{L_{max}}{L_{min}}\right)^u ln\left(\frac{L_{max}}{L_{min}}\right)$

used. For a broadbeam simulation, the orientation angles are specified during the setup phase, and the *Sphere* and the *Spectrum* randomizers are not called. A summary of the calculations for the parameters of the Disk and Sphere, and their respective weights, are shown in Table 12. The *Spectrum Randomizer* maintains a database of spectra, the ability to parse differential spectra from CREME96, and interpolating functions.

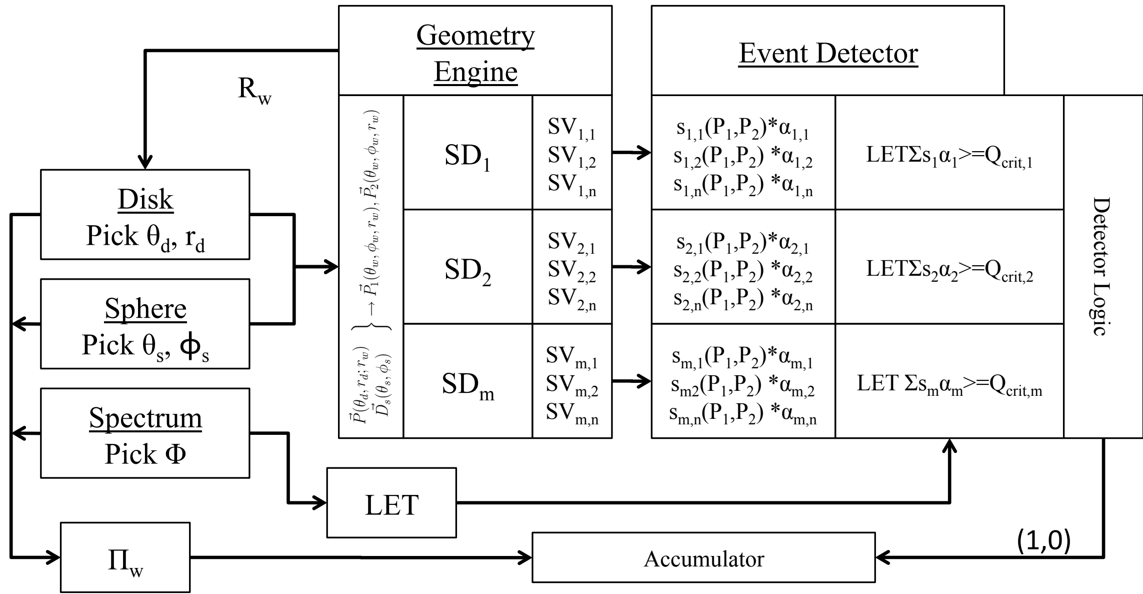

Figure 120: Design of the Monte Carlo Ray Tracing Program

The *Geometry Engine*, following setup of the sensitive volumes and detectors, calculates the maximum radius, R_w, of the sphere that entirely encompasses them, called the *world*

sphere. During run-time, the *Geometry Engine* translates the position, $\vec{P}$ and direction $\vec{D}$ vectors from the *Randomizer* into points, $\vec{P}_1$ and $\vec{P}_2$, which are located on the surface of the *world sphere*.

The *Geometry Engine* calculates the lengths of the segments, s, through each sensitive volume, SV, and weighs the lengths by the efficiency of the sensitive volumes, α. Detector weighting can also be employed. The segment length is defined as the distance between the two points of intersection of the ray segment on the surface of the sensitive volume being analyzed. Naturally, this value can be zero if the ray segment does not pass through the sensitive volume. The algorithms employed for calculating the intersection points of segments, planes, and the surfaces of closed volumes are geometrically straightforward and available on-line [127].

The product of the summation of all weighted chord lengths and LET is tested against the Q_{crit} requirement for that detector containing the group of multiple sensitive volumes, SD. The process is repeated for all detectors. The *Detector logic* has switches for material definitions (e.g., $0.01035\frac{pC}{\mu m \cdot LET}Si$). A valid SEU condition is determined if the *detector logic* requirements are satisfied. Note that the *detector logic* can be constructed in such a way to track the number of total detectors that upset (as in multiple bit upsets), logical *and* operation for coincidence requirements (DICE circuitry), or any other set of conditions that depend on the effect being investigated.

The main purpose of the *Accumulator* is to accumulate the sum of the product of the weights for all valid SEU conditions. The *Accumulator* also serves the purpose of the *Run manager*, which directs the simulator to repeat the analysis until termination requirements are satisfied. Generally, this is until N events have been simulated or a target variance is reached. The *Accumulator* can also be used to log event information, such as which detectors upset and at what LET.

Analysis Techniques

Two approaches to generating and post-processing results in both MRED and MRT were used in this research, *Histogram* and *Run-time* analyses. The former is a method for tracking the frequency and probability of net energy loss in any or all sensitive volumes as a function of energy. The latter is a more loosely defined concept that involves an interrupted per-particle analysis and data logging approach. The two are not inherently distinct methods, and neither precludes the use of the other. In actuality, one may think of *histograms* as merely one method of the *Run-time* approach, though the two are described as distinct methods in this document for clarity.

The *Run-time* approach, in some instances, bypasses the limitations that are associated with a purely *histogram* based approach. For this work, *Run-time* analysis has been used for logging valid SEU events in circumstances where the SEU conditions were determined by coincidence, as in Chapter IV, and when interfaces to external simulation tools were required, as in Chapter V. *Run-time* evaluation of data was used extensively in Chapter V to capture and analyze the angular and species dependence of SEU rates and cross sections. Information of this type is not contained in a histogram.

The Histogram: A Measure of the Event Probability

Histograms are a useful operation for investigating the frequency distribution of events in energy space for a given detector (or sensitive volume) configuration. They are constructed of a finite number of bins, distributed linearly or logarithmically, in energy space. The utility of the histogram is presented in this section following a definition with an example application.

The function described by (130) is called the *binning function*, for the ith bin of a histogram, where E^{-} and E^{+} are the upper and lower limits of the bin.

$$b_i(E; E_i^-, E_i^+) = \begin{cases} \frac{1}{\Delta E_i} & E \in \left[E_i^-, E_i^+\right) \\ 0 & elsewhere \end{cases} \quad (130)$$

The expectation value of the *binning function* is given by (131), where the index has been dropped for clarity and assuming that $P(E)$ is unity at the highest energy range (i.e., all energies are binned within some b_i). Equation 131 can be simplified to (132), where P(E) is the cumulative density function at E.

$$\langle b(E) \rangle = \int p(E) b(E) dE = \lim_{\epsilon \to 0} \frac{1}{\Delta E} \int_{E^-}^{E^+ - \epsilon} p(E) dE \quad (131)$$

$$\langle b(E) \rangle = \lim_{\epsilon \to 0} \frac{1}{\Delta E} \left[P(E^+ - \epsilon) - P(E^-) \right] = \frac{1}{\Delta E} \left[P(E^+) - P(E^-) \right] \quad (132)$$

Taking the limit of $\Delta E \to 0$ results in the probability of the event occurring at E^-, $p(E^-)$, which is also the probability $p(E)$, as shown in (133). Note that this useful result demonstrates that the *binning function* in the limit of vanishingly small bin widths reduces to a description of the probability of the event occurring at E.

$$\begin{aligned} \lim_{\Delta E \to 0} \langle b(E) \rangle &= \lim_{\Delta E \to 0} \tfrac{1}{\Delta E} \left[P\left(E^- + \Delta E\right) - P\left(E^-\right) \right] \\ &= P'\left(E^-\right) \\ &= p\left(E^-\right) = p(E) \end{aligned} \quad (133)$$

In the discrete case, the difference of the cumulative probabilities $(P_2 - P_1)$ occurring within the bin can be approximated by (134), where the summation is taken over j for N_t events, H is the *Heaviside function*, and w_j is the weight of the jth randomly sampled variable $\hat{E}_j$. The *Boxcar function*, Π, represents the difference of the two *Heaviside functions*. Note that the *Heaviside Function*, for adjacent bins (e.g., at the boundary of b_i and b_{i+1}), will divide w_i evenly between the two.

$$
\begin{aligned}
P_2(E) - P_1(E) &\approx \tfrac{1}{N_t} \textstyle\sum_{j=1}^{N_t} w_j \left[H\left(\hat{E}_j - E^-\right) - H\left(\hat{E}_j - E^+\right)\right] \\
&\approx \tfrac{1}{N_t} \textstyle\sum_{j=1}^{N_t} w_j \Pi_{E^-,E^+}\left(\hat{E}_j\right)
\end{aligned} \tag{134}
$$

Substituting the results of (134) into (132) results in the estimator, $\widetilde{p}_i$, for the *binning function* (130), in the ith bin, shown in (135).

$$
\langle b_i(E)\rangle \approx \widetilde{p}_i = \frac{1}{\Delta E_i N_t} \sum_{j=1}^{N_t} w_j \Pi_{E_i^-,E_i^+}\left(\hat{E}_j\right) \tag{135}
$$

The total histogram function over the range of valid bins (encompassing all energies or a predefined range of energies), is given by $\Upsilon(E)$, shown in (136). Again, the *Boxcar function* selectively picks the bin containing E. In the implementation shown, no explicit treatment is given to the bin edges. In (136), the function will return the average of the adjacent bins at values of E equal to the bin edge.

$$
\begin{aligned}
\Upsilon(E) &= \textstyle\sum_{i=1}^{N_{bins}} c_i(E)\widetilde{p}_i \\
c_i(E) &= \Pi_{E_i^-,E_i^+}(E)
\end{aligned} \tag{136}
$$

It has been shown that (136) provides an estimate of the probability that an event with fall within the range $[E^-, E^+)$ for that bin. Error rates and single event cross-sections are calculated from an estimate of the probability of the total number of events that meet or exceed a minimum conditions, such as $Q_{coll} \geq Q_{crit}$. Or, retaining the concept of minimum energy, $E_{dep} \geq E_c$ (where E_{dep} may or may not be scaled by the efficiency of the dosimeter described by α). Depending on the independent variable or variables (e.g., energy, time, etc..) that are not absorbed by the integration of the general rate equation, the histogram is the estimate of p_e shown in (81) and (82).

The cumulative probability for all events that exceed a critical energy, E_c, is expressed for the continuous case as shown in (137).

$$
P(E \geq E_c) = \int_{E_c}^{E_{max}} p(E)dE \tag{137}
$$

In the case of the histogram having discrete bins, the reverse integral is approximated by (138), where the mass within the bins, w_i with an index corresponding to $E = E_c$ to the maximum energy, E_{max}, are summed and multiplied by their width, ΔE.

$$\widetilde{P}(E \geq E_c) = \sum_{i=i(E_c)}^{i(E_{max})} w_i \Delta E_i \tag{138}$$

For the case of tracking energy loss in a single multiple volume group, the histogram is the preferred approach in MRED. However, if a simulation has multiple Q_{crit} conditions, or coincidence requirements between multiple sensitive volume groups, the construction of the histogram logic, and analyses of histogram results, can be unnecessarily challenging, as coincidence is currently not preserved between histogram groups.

Example Histogram

In the Chapter I, the probability distribution of chord lengths through a rectangular volume was introduced. While the solutions employed in the RPP model are analytic, it is also possible to estimate them by Monte Carlo methods. For example, MRT simulation tool simulates the isotropic environment and calculates the length of rays through any number of sensitive volumes. The length of those rays in the volume are converted to energy (assuming a single value of linear energy transfer) and used to generate histograms according to the procedures previously described.

For this example, a particle of LET = 1.0 $MeV cm^2/mg$ in an isotropic environment is simulated. The RPP dimensions are 5 x 10 x 15 μm^3. 5000 samples were generated and their weights were accumulated in 100 bins spanning the range of 0 to 5 MeV. The analytic solutions derived by Bendel [30] were also calculated for the same RPP dimensions. In order to directly compare the calculations of Bendel and the Monte Carlo simulation, only those events that struck the RPP surface were tabulated in the total event count, N_t. This is necessary because the Bendel calculation assumes all particles hit the RPP surface, whereas the Monte Carlo simulation launches particles from a sphere (world volume) containing the

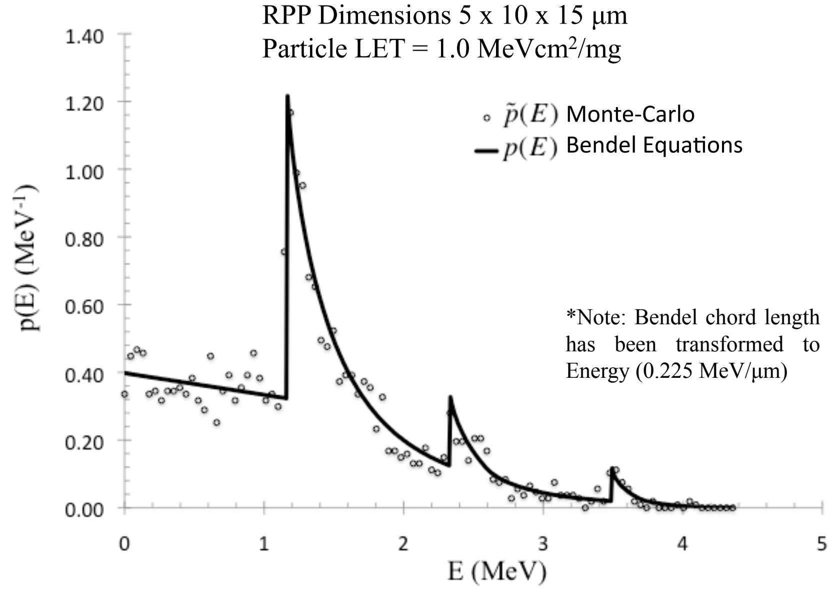

Figure 121: Continuous and Monte Carlo sampled energy probability distributions in an RPP of 5 x 10 x 15 μm^3.

RPP, per (82).

The results of the MRT simulation, presented as a normalized histogram of the accumulated weights is shown in Figure 121. Note for the large bin count with respect to the number of samples produces significant scatter about the analytic solution. The reverse integrated histogram is shown in Figure 122. By visual inspection, the reverse integrated probabilities between the Monte Carlo calculation show significantly less scatter.

Recognize that the histogram provides the discretized description of the probability terms in (81) and/or (82). The calculation of the error rate is simply the integration of $p_{hist}(E)dE$, or the summation of $p_i \Delta E_i$, from the critical energy (bin) to the maximum energy (bin). The units of p_e may be in s^{-1} or $Area^{-1}$, depending on the integration domain (e.g., error rate or cross section).

The histogram provides a mechanism for generating a probability distribution function for SEU as a function of energy or energies within sensitive volume regions. It is not vital to derive a histogram for all applications, such as those in which only the final error rate is

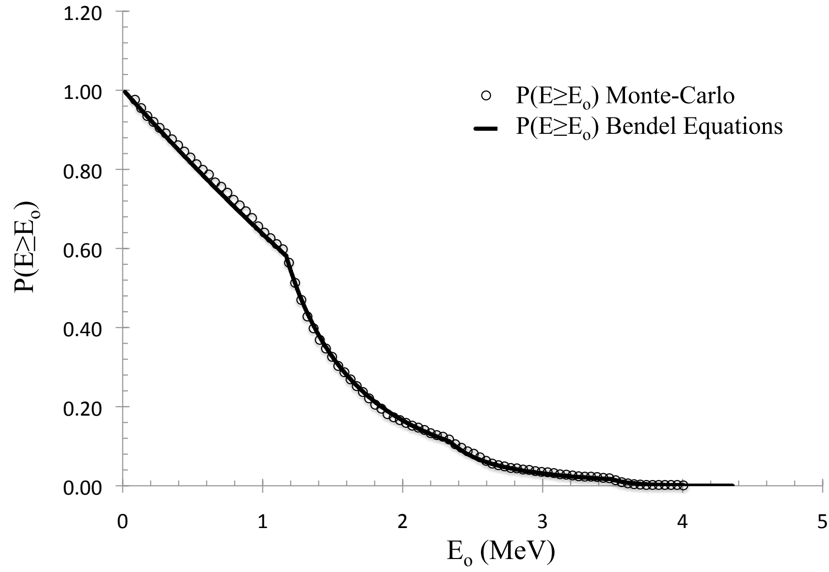

Figure 122: Continuous and Monte Carlo sampled reverse integrated probabilities.

needed.

Run-Time Analysis

The difficulty associated with predicting SEU rates, cross sections, and analyzing details of the events that led to them by use of histogram method alone warranted the construction of an event call-back routine in MRED (and the construction of MRT entirely around the concept of the run-manager as the interface to the user). In *Run-time* analysis, which in the case of MRED is the call-back routine, the transport machinery is halted following each completed particle event simulation. The state of the system and the results from the particle event (energy deposition vector, parent physics process, etc.) are made available to the user for processing.

Within the call-back routine of MRED the user is allowed to perform the analyses that determine a valid event condition. In this work, the call-back routine is constructed in a manner that is conceptually identical to that of the *Event Detector* within MRT (Figure 120). It performs the linear weighted summation that defines the multiple sensitive volume

model for each sensitive volume group (a native option available in MRED Version 9, not used in this work). The logical functions and comparisons that define the valid SEU condition for any volume, sets of volumes, or volume groups are performed within the call-back. The weight and variance of the event is tracked as a global variable. Logging of event details (parent process, event number, secondary species, physics processes, etc.) are based upon user requirements and the sophistication of the means by which the analyses are done is limited only by the user. Upon the completion of the analysis, control is returned to the MRED core and the simulation proceeds. Naturally, the interrupt driven approach consumes more time per event.

Aside from the added flexibility that the *Run-Time* approach affords, it also provides a mechanism for identifying convergence of the estimated result (cross-section or error rate) during processing, where convergence is defined as the condition of $SEURate_{est} \rightarrow SEURate_{true}$, to within some degree of uncertainty. In this work, internal upset mechanisms were tracked using the interrupt driven (*run time*) methods to ensure that all known internal mechanisms were sampled to minimize uncertainty in the final estimated SEU rate.

REFERENCES

[1] J. L. Barth, "Modeling space radiation environments," in *1997 IEEE NSREC Short Course, Section I*, 1997.

[2] J. F. Ziegler and W. A. Lanford, "Effect of Cosmic Rays on Computer Memories," *Science*, vol. 206, no. 4420, pp. 776–788, 1979.

[3] E. Normand, "Single event upset at ground level," *Nuclear Science, IEEE Transactions on*, vol. 43, no. 6, pp. 2742–2750, Dec 1996.

[4] M. E. Porter, J. D. Wilkinson, K. Walsh, B. D. Sierawski, K. M. Warren, R. A. Reed, and G. Vizkelethy, "Soft error reliability improvements for implantable medical devices," in *Reliability Physics Symposium, 2008. IRPS 2008. IEEE International*, May 2008, pp. 488–491.

[5] S. Gladstone, *The Effects of Nuclear Weapons, Revised Edition.* US Atomic Energy Commission, April 1962.

[6] D. J. Lawrence, R. C. Elphic, T. H. Prettyman, and R. C. Wiens, "Effects of an rtg power source on neutron spectroscopy measurements on the martian surface," *Lunar and Planetary Sciences*, vol. 34, pp. 1763–1764, 2003.

[7] T. C. May and M. H. Woods, "Alpha-particle-induced soft errors in dynamic memories," *Electron Devices, IEEE Transactions on*, vol. 26, no. 1, pp. 2–9, Jan 1979.

[8] D. Binder, E. C. Smith, and A. B. Holman, "Satellite anomalies from galactic cosmic rays," *Nuclear Science, IEEE Transactions on*, vol. 22, no. 6, pp. 2675–2680, Dec. 1975.

[9] E. L. Petersen, "Single-event analysis and prediction," in *1997 IEEE NSREC Short Course, Section III*, 1997.

[10] G. C. Messenger and M. S. Ash, *Single Event Phenomena.* Chapman and Hall Publishing, 1997.

[11] J. F. Ziegler, "Stopping of energetic light ions in elemental matter," *Journal of Applied Physics*, vol. 85, no. 3, pp. 1249–1272, 1999.

[12] R. C. Alig and S. Bloom, "Electron-hole-pair creation energies in semiconductors," *Phys. Rev. Lett.*, vol. 35, no. 22, pp. 1522–1525, Dec 1975.

[13] K. M. Warren, "The influence of soi-mosfet geometry on predicted single event cross sections," MS, Vanderbilt University, May 1999.

[14] R. S. Muller and T. I. Kamins, *Device Electronics for Integrated Circuits*, 2nd ed. John Wiley and Sons, 1986.

[15] F. B. McLean and T. R. Oldham, "Charge funneling in n- and p-type si substrates," *Nuclear Science, IEEE Transactions on*, vol. 29, no. 6, pp. 2017–2023, Dec. 1982.

[16] J. D. Patterson and L. D. Edmonds, "Modeling the contribution of diffusion to device-upset cross sections," *Nuclear Science, IEEE Transactions on*, vol. 49, no. 6, pp. 3067–3074, Dec 2002.

[17] R. L. Woodruff and P. J. Rudeck, "Three-dimensional numerical simulation of single event upset of an sram cell," *Nuclear Science, IEEE Transactions on*, vol. 40, no. 6, pp. 1795–1803, Dec 1993.

[18] C. Detcheverry, C. Dachs, E. Lorfevre, C. Sudre, G. Bruguier, J. Palau, J. Gasiot, and R. Ecoffet, "Seu critical charge and sensitive area in a submicron cmos technology," *Nuclear Science, IEEE Transactions on*, vol. 44, no. 6, pp. 2266–2273, Dec 1997.

[19] B. D. Olson, D. R. Ball, K. M. Warren, L. W. Massengill, N. F. Haddad, S. E. Doyle, and D. McMorrow, "Simultaneous single event charge sharing and parasitic bipolar conduction in a highly-scaled sram design," *Nuclear Science, IEEE Transactions on*, vol. 52, no. 6, pp. 2132–2136, Dec. 2005.

[20] M. P. Baze, B. W. Hughlock, J. J. Wert, J. Tostenrude, L. W. Massengill, O. A. Amusan, R. D. Lacoe, K. Lilja, and M. T. Johnson, "Angular dependence of single event sensitivity in hardened flip/flop designs," *Nuclear Science, IEEE Transactions on*, vol. 55, no. 6, pp. 3295–3301, Dec. 2008.

[21] D. Giot, P. Roche, G. Gasiot, and R. Harboe-Sorensen, "Multiple-bit upset analysis in 90 nm srams: Heavy ions testing and 3d simulations," *Nuclear Science, IEEE Transactions on*, vol. 54, no. 4, pp. 904–911, Aug. 2007.

[22] D. R. Ball, K. M. Warren, R. A. Weller, R. A. Reed, A. Kobayashi, J. A. Pellish, M. H. Mendenhall, C. L. Howe, L. W. Massengill, R. D. Schrimpf, and N. F. Haddad, "Simulating nuclear events in a tcad model of a high-density seu hardened sram technology," *Nuclear Science, IEEE Transactions on*, vol. 53, no. 4, pp. 1794–1798, Aug. 2006.

[23] W. L. Bendel and E. Petersen, "Proton upsets in orbit," *Nuclear Science, IEEE Transactions on*, vol. 30, no. 6, pp. 4481–4485, Dec. 1983.

[24] E. L. Petersen, "Single-event analysis and prediction," in *2008 IEEE NSREC Short Course, Section III*, 2008.

[25] E. L. Petersen, J. C. Pickel, E. C. Smith, P. J. Rudeck, and J. R. Letaw, "Geometrical factors in see rate calculations," *Nuclear Science, IEEE Transactions on*, vol. 40, no. 6, pp. 1888–1909, Dec 1993.

[26] J. H. Adams, R. Silberberg, and C. H. Tsao, *Cosmic Ray Effects on Microelectronics; Part I: The Near-Earth Particle Environment.* NRL Memorandum Report 4506, Aug 1981.

[27] L. W. Connell, P. J. McDaniel, A. K. Prinja, and F. W. Sexton, "Modeling the heavy ion upset cross section," *Nuclear Science, IEEE Transactions on*, vol. 42, no. 2, pp. 73–82, Apr 1995.

[28] P. E. Dodd and F. W. Sexton, "Critical charge concepts for cmos srams," *Nuclear Science, IEEE Transactions on*, vol. 42, no. 6, pp. 1764–1771, Dec 1995.

[29] R. A. Weller, R. D. Schrimpf, R. A. Reed, M. H. Mendenhall, K. M. Warren, B. D. Sierawski, and L. W. Massengill, "Monte carlo simulation of single event effects," in *2009 RADECS Short Course*, 2009.

[30] W. L. Bendel, *Length Distribution of Chords Through a Rectangular Volume.* NRL Memorandum Report 5369, Jul 1984.

[31] A. J. Tylka, J. Adams, J. H., P. R. Boberg, B. Brownstein, W. F. Dietrich, E. O. Flueckiger, E. L. Petersen, M. A. Shea, D. F. Smart, and E. C. Smith, "Creme96: A revision of the cosmic ray effects on micro-electronics code," *Nuclear Science, IEEE Transactions on*, vol. 44, no. 6, pp. 2150–2160, Dec 1997.

[32] http://tdvg10.phy.bnl.gov.

[33] http://cyclotron.tamu.edu.

[34] E. L. Petersen, J. C. Pickel, J. Adams, J. H., and E. C. Smith, "Rate prediction for single event effects-a critique," *Nuclear Science, IEEE Transactions on*, vol. 39, no. 6, pp. 1577–1599, Dec 1992.

[35] C. Hu, "Alpha-particle-induced field and enhanced collection of carriers," *Electron Device Letters, IEEE*, vol. 3, no. 2, pp. 31–34, Feb 1982.

[36] K. W. Golke, "Determination of funnel length from cross section versus let measurements," *Nuclear Science, IEEE Transactions on*, vol. 40, no. 6, pp. 1910–1917, Dec 1993.

[37] A. Akkerman and J. Barak, "Ion-track structure and its effects in small size volumes of silicon," *Nuclear Science, IEEE Transactions on*, vol. 49, no. 6, pp. 3022–3031, Dec 2002.

[38] P. E. Dodd, O. Musseau, M. R. Shaneyfelt, F. W. Sexton, C. D'hose, G. L. Hash, M. Martinez, R. A. Loemker, J. L. Leray, and P. S. Winokur, "Impact of ion energy on single-event upset," *Nuclear Science, IEEE Transactions on*, vol. 45, no. 6, pp. 2483–2491, Dec 1998.

[39] M. A. Xapsos, "Applicability of let to single events in microelectronic structures," *Nuclear Science, IEEE Transactions on*, vol. 39, no. 6, pp. 1613–1621, Dec 1992.

[40] O. Fageeha, J. Howard, and R. C. Block, "Distribution of radial energy deposition around the track of energetic charged particles in silicon," *Journal of Applied Physics*, vol. 75, no. 5, pp. 2317–2321, 1994.

[41] L. W. Connell, F. W. Sexton, P. J. McDaniel, and A. K. Prinja, "Modeling the heavy ion cross-section for single event upset with track structure effects: the hic-up-ts model," *Nuclear Science, IEEE Transactions on*, vol. 43, no. 6, pp. 2814–2819, Dec 1996.

[42] J. C. Pickel, *Modeling for Single Event Error Rate Prediction.* DNA-TR-317, 1984.

[43] D. Binder, "Analytic seu rate calculation compared to space data," *Nuclear Science, IEEE Transactions on*, vol. 35, no. 6, pp. 1570–1572, Dec 1988.

[44] A. J. Tylka, W. F. Dietrich, P. R. Boberg, E. C. Smith, and J. Adams, J. H., "Single event upsets caused by solar energetic heavy ions," *Nuclear Science, IEEE Transactions on*, vol. 43, no. 6, pp. 2758–2766, Dec 1996.

[45] C. I. Underwood, R. Ecoffet, S. Duzefier, and D. Faguere, "Observations of single-event upset and multiple-bit upset in non-hardened high-density srams in the topex/poseidon orbit," in *IEEE NSREC Radiation Effects Data Workshop*, 1999.

[46] W. J. Stapor, P. T. McDonald, A. R. Knudson, A. B. Campbell, and B. G. Glagola, "Charge collection in silicon for ions of different energy but same linear energy transfer (let)," *Nuclear Science, IEEE Transactions on*, vol. 35, no. 6, pp. 1585–1590, Dec 1988.

[47] R. Koga, S. H. Crain, W. R. Crain, K. B. Crawford, and S. J. Hansel, "Comparative seu sensitivities to relativistic heavy ions," *Nuclear Science, IEEE Transactions on*, vol. 45, no. 6, pp. 2475–2482, Dec 1998.

[48] K. M. Warren, R. A. Weller, M. H. Mendenhall, R. A. Reed, D. R. Ball, C. L. Howe, B. D. Olson, M. L. Alles, L. W. Massengill, R. D. Schrimpf, N. F. Haddad, S. E. Doyle, D. McMorrow, J. S. Melinger, and W. T. Lotshaw, "The contribution of nuclear reactions to heavy ion single event upset cross-section measurements in a high-density seu hardened sram," *Nuclear Science, IEEE Transactions on*, vol. 52, no. 6, pp. 2125–2131, Dec. 2005.

[49] A. S. Kobayashi, D. R. Ball, K. M. Warren, R. A. Reed, N. F. Haddad, M. H. Mendenhall, R. D. Schrimpf, and R. A. Weller, "The effect of metallization layers on single event susceptibility," *Nuclear Science, IEEE Transactions on*, vol. 52, no. 6, pp. 2189–2193, Dec. 2005.

[50] D. McMorrow, W. T. Lotshaw, J. S. Melinger, S. Buchner, J. D. Davis, R. K. Lawrence, J. H. Bowman, R. D. Brown, D. Carlton, J. Pena, J. Vasquez, N. F. Haddad, K. M. Warren, and L. W. Massengill, "Single-event upset in flip-chip sram induced by through-wafer, two-photon absorption," *Nuclear Science, IEEE Transactions on*, vol. 52, no. 6, pp. 2421–2425, Dec. 2005.

[51] K. M. Warren, R. A. Weller, B. D. Sierawski, R. A. Reed, M. H. Mendenhall, R. D. Schrimpf, L. W. Massengill, M. E. Porter, J. D. Wilkinson, K. A. LaBel, and J. H. Adams, "Application of radsafe to model the single event upset response of a 0.25 μ m cmos sram," *Nuclear Science, IEEE Transactions on*, vol. 54, no. 4, pp. 898–903, Aug. 2007.

[52] Y. Boulghassoul, L. W. Massengill, A. L. Sternberg, R. L. Pease, S. Buchner, J. W. Howard, D. McMorrow, M. W. Savage, and C. Poivey, "Circuit modeling of the lm124 operational amplifier for analog single-event transient analysis," *Nuclear Science, IEEE Transactions on*, vol. 49, no. 6, pp. 3090–3096, Dec 2002.

[53] R. Velazco, T. Calin, M. Nicolaidis, S. C. Moss, S. LaLumondiere, V. Tran, and R. Koga, "Seu-hardened storage cell validation using a pulsed laser," *Nuclear Science, IEEE Transactions on*, vol. 43, no. 6, pp. 2843–2848, Dec 1996.

[54] K. M. Warren, B. D. Sierawski, R. A. Reed, R. A. Weller, C. Carmichael, A. Lesea, M. H. Mendenhall, P. E. Dodd, R. D. Schrimpf, L. W. Massengill, T. Hoang, H. Wan, J. L. De Jong, R. Padovani, and J. J. Fabula, "Monte-carlo based on-orbit single event upset rate prediction for a radiation hardened by design latch," *Nuclear Science, IEEE Transactions on*, vol. 54, no. 6, pp. 2419–2425, Dec. 2007.

[55] A. Campbell, S. Buchner, E. L. Petersen, B. Blake, J. Mazur, and C. Dyer, "Seu measurements and predictions on mptb for a large energetic solar particle event," *Nuclear Science, IEEE Transactions on*, vol. 49, no. 3, pp. 1340–1344, Jun 2002.

[56] H. B. Barber, T. Bowen, D. A. Delise, E. W. Jenkins, J. J. Jones, R. M. Kalbach, and A. E. Pifer, "Predictions and measurements of mass spectra of the charged nucleonic component of cosmic rays at mountain altitude," *Phys. Rev. D*, vol. 22, no. 11, pp. 2667–2687, Dec 1980.

[57] W. J. Stapor, J. P. Meyers, J. B. Langworthy, and E. L. Petersen, "Two parameter bendel model calculations for predicting proton induced upset [ics]," *Nuclear Science, IEEE Transactions on*, vol. 37, no. 6, pp. 1966–1973, Dec 1990.

[58] P. M. O'Neill, G. D. Badhwar, and W. X. Culpepper, "Internuclear cascade-evaporation model for let spectra of 200 mev protons used for parts testing," *Nuclear Science, IEEE Transactions on*, vol. 45, no. 6, pp. 2467–2474, Dec 1998.

[59] D. M. Hiemstra and E. W. Blackmore, "Let spectra of proton energy levels from 50 to 500 mev and their effectiveness for single event effects characterization of microelectronics," *Nuclear Science, IEEE Transactions on*, vol. 50, no. 6, pp. 2245–2250, Dec. 2003.

[60] P. J. McNulty, G. E. Farrell, and W. P. Tucker, "Proton-induced nuclear reactions in silicon," *Nuclear Science, IEEE Transactions on*, vol. 28, no. 6, pp. 4007–4012, Dec. 1981.

[61] R. A. Reed, P. W. Marshall, H. S. Kim, P. J. McNulty, B. Fodness, T. A. Jordan, R. Reedy, C. Tabbert, M. Liu, W. Heikkila, S. Buchner, R. Ladbury, and K. A. LaBel, "Evidence for angular effects in proton-induced single-event upsets," *Nuclear Science, IEEE Transactions on*, vol. 49, no. 6, pp. 3038–3044, Dec 2002.

[62] Geant4 Collaboration, S. Agostinelli, J. Allison, K. Amako, J. Apostolakis, H. Araujo, P. Arce, M. Asai, D. Axen, S. Banerjee, G. Barrand, F. Behner, L. Bellagamba, J. Boudreau, L. Broglia, A. Brunengo, H. Burkhardt, S. Chauvie, J. Chuma, R. Chytracek, G. Cooperman, G. Cosmo, P. Degtyarenko, A. dell'Acqua, G. Depaola, D. Dietrich, R. Enami, A. Feliciello, C. Ferguson, H. Fesefeldt, G. Folger, F. Foppiano, A. Forti, S. Garelli, S. Giani, R. Giannitrapani, D. Gibin, J. J. Gómez Cadenas, I. González, G. Gracia Abril, G. Greeniaus, W. Greiner, V. Grichine, A. Grossheim, S. Guatelli, P. Gumplinger, R. Hamatsu, K. Hashimoto, H. Hasui, A. Heikkinen, A. Howard, V. Ivanchenko, A. Johnson, F. W. Jones, J. Kallenbach, N. Kanaya, M. Kawabata, Y. Kawabata, M. Kawaguti, S. Kelner, P. Kent, A. Kimura, T. Kodama, R. Kokoulin, M. Kossov, H. Kurashige, E. Lamanna, T. Lampén, V. Lara, V. Lefebure, F. Lei, M. Liendl, W. Lockman, F. Longo, S. Magni, M. Maire, E. Medernach, K. Minamimoto, P. Mora de Freitas, Y. Morita, K. Murakami, M. Nagamatu, R. Nartallo, P. Nieminen, T. Nishimura, K. Ohtsubo, M. Okamura, S. O'Neale,

Y. Oohata, K. Paech, J. Perl, A. Pfeiffer, M. G. Pia, F. Ranjard, A. Rybin, S. Sadilov, E. di Salvo, G. Santin, T. Sasaki, N. Savvas, Y. Sawada, S. Scherer, S. Sei, V. Sirotenko, D. Smith, N. Starkov, H. Stoecker, J. Sulkimo, M. Takahata, S. Tanaka, E. Tcherniaev, E. Safai Tehrani, M. Tropeano, P. Truscott, H. Uno, L. Urban, P. Urban, M. Verderi, A. Walkden, W. Wander, H. Weber, J. P. Wellisch, T. Wenaus, D. C. Williams, D. Wright, T. Yamada, H. Yoshida, and D. Zschiesche, "Geant4-a simulation toolkit," *Nuclear Instruments and Methods in Physics Research A*, vol. 506, pp. 250–303, Jul 2003.

[63] J. F. Ziegler, "Terrestrial cosmic rays," *IBM J. Res. Develop.*, vol. 40, no. 1, p. 19, Jan 1996.

[64] JEDEC and Standards, "Measurement and reporting of alpha particles and terrestrial cosmic ray-induced soft errors in semiconductor devices," *JEDEC Solid State Technology Association*, Aug 2001.

[65] C. A. Gossett, B. W. Hughlock, M. Katoozi, G. S. LaRue, and S. A. Wender, "Single event phenomena in atmospheric neutron environments," *Nuclear Science, IEEE Transactions on*, vol. 40, no. 6, pp. 1845–1852, Dec 1993.

[66] K. M. Warren, B. D. Sierawski, R. A. Reed, M. E. Porter, M. H. Mendenhall, R. D. Schrimpf, and L. W. Massengill, "Predicting neutron induced soft error rates: Evaluation of accelerated ground based test methods," in *Proceedings of the 2008 International Reliability and physics Symposium*, April 2008.

[67] A. Lesea, S. Drimer, J. J. Fabula, C. Carmichael, and P. Alfke, "The rosetta experiment: atmospheric soft error rate testing in differing technology fpgas," *Device and Materials Reliability, IEEE Transactions on*, vol. 5, no. 3, pp. 317–328, Sept. 2005.

[68] G. Folger, V. Ivanchenko, and J. Wellisch, "The binary cascade," *Eur. Physic. J.*, vol. 21, pp. 407–417, 2004.

[69] D. Lambert, J. Baggio, G. Hubert, P. Paillet, S. Girard, V. Ferlet-Cavrois, O. Flament, F. Saigne, J. Boch, B. Sagnes, N. Buard, and T. Carriere, "Analysis of quasi-monoenergetic neutron seu cross sections for terrestrial applications," in *Radiation and Its Effects on Components and Systems, 2005. RADECS 2005. 8th European Conference on*, Sept. 2005, pp. LN5–1–LN5–6.

[70] J. Wilkinson, private Correspondence in Regards to the Revision of the JEDEC JESD89 Standard.

[71] B. D. Sierawski, J. A. Pellish, R. A. Reed, R. D. Schrimpf, K. M. Warren, R. A. Weller, M. H. Mendenhall, J. D. Black, A. D. Tipton, M. A. Xapsos, R. C. Baumann, X. Deng, M. J. Campola, M. R. Friendlich, H. S. Kim, A. M. Phan, and C. M. Seidleck, "Impact of low-energy proton induced upsets on test methods and rate predictions," *Nuclear Science, IEEE Transactions on*, vol. 56, no. 6, pp. 3085–3092, Dec. 2009.

[72] R. C. Baumann, "Soft errors in advanced semiconductor devices-part i: the three radiation sources," *Device and Materials Reliability, IEEE Transactions on*, vol. 1, no. 1, pp. 17–22, Mar 2001.

[73] E. Normand, K. Vranish, A. Sheets, M. Stitt, and R. Kim, "Quantifying the double-sided neutron seu threat, from low energy (thermal) and high energy (¿ 10 mev) neutrons," *Nuclear Science, IEEE Transactions on*, vol. 53, no. 6, pp. 3587–3595, Dec. 2006.

[74] M. Olmos, R. Gaillard, A. Van Overberghe, J. Beaucour, S. Wen, and S. Chung, "Investigation of thermal neutron induced soft error rates in commercial srams with 0.35 um to 90 nm technologies," in *Reliability Physics Symposium Proceedings, 2006. 44th Annual., IEEE International*, March 2006, pp. 212–216.

[75] D. Suryanarayana, T. Y. Wu, and J. Varcoe, "Encapsulants used in flip-chip packages," in *Electronic Components and Technology Conference, 1993. Proceedings., 43rd*, Jun 1993, pp. 193–198.

[76] S. Levine, "Alpha emission measurements of lids and solder preforms on semiconductor packages," *Components, Hybrids, and Manufacturing Technology, IEEE Transactions on*, vol. 2, no. 4, pp. 391–395, Dec 1979.

[77] T. Karnik and P. Hazucha, "Characterization of soft errors caused by single event upsets in cmos processes," *Dependable and Secure Computing, IEEE Transactions on*, vol. 1, no. 2, pp. 128–143, April-June 2004.

[78] J. Wilkinson and S. Hareland, "A cautionary tale of soft errors induced by sram packaging materials," *Device and Materials Reliability, IEEE Transactions on*, vol. 5, no. 3, pp. 428–433, Sept. 2005.

[79] M. K. Gong, D. W. Kim, C. Y. Lee, D. S. Choi, and D.-G. Kang, "Modeling alpha-particle-induced accelerated soft error rate in semiconductor memory," *Electron Devices, IEEE Transactions on*, vol. 50, no. 7, pp. 1652–1657, July 2003.

[80] H. Shin, "Modeling of alpha-particle-induced soft error rate in dram," *Electron Devices, IEEE Transactions on*, vol. 46, no. 9, pp. 1850–1857, Sep 1999.

[81] http://www.nndc.bnl.gov/databases/datases.html#structuredecay, the National Nuclear Data Center Nuclear Structure and Decay Databases.

[82] M. W. Roberson, "Soft error rates in solder bumped packaging," in *Advanced Packaging Materials, 1998. Proceedings. 1998 4th International Symposium on*, Mar 1998, pp. 111–116.

[83] S. K. Kang, J. Horkans, P. C. Andricacos, R. A. Carruthers, J. Cotte, M. Datta, P. Gruber, J. Harper, K. Kwietniak, C. Sambucetti, L. Shi, G. Brouillette, and D. Danovitch, "Pb-free solder alloys for flip chip applications," in *Electronic Components and Technology Conference, 1999. 1999 Proceedings. 49th*, 1999, pp. 283–288.

[84] A. Johnston, "Scaling and technology issues for soft error rates," in *Proceedings of the 4th Annual Research Conference on Reliability, Stanford University*, Oct 2000.

[85] L. W. Massengill, M. L. Alles, S. E. Kerns, and K. L. Jones, "Effects of process parameter distributions and ion strike locations on seu cross-section data [cmos srams]," *Nuclear Science, IEEE Transactions on*, vol. 40, no. 6, pp. 1804–1811, Dec 1993.

[86] K. M. Warren, L. W. Massengill, R. D. Schrimpf, and H. Barnaby, "Analysis of the influence of mos device geometry on predicted seu cross sections," *Nuclear Science, IEEE Transactions on*, vol. 46, no. 6, pp. 1363–1369, Dec 1999.

[87] K. M. Horn, B. L. Doyle, and F. W. Sexton, "Nuclear microprobe imaging of single-event upsets," *Nuclear Science, IEEE Transactions on*, vol. 39, no. 1, pp. 7–12, Feb 1992.

[88] S. Buchner, J. Langworthy, W. J. Stapor, A. B. Campbell, and S. Rivet, "Implications of the spatial dependence of the single-event-upset threshold in srams measured with a pulsed laser," *Nuclear Science, IEEE Transactions on*, vol. 41, no. 6, pp. 2195–2202, Dec 1994.

[89] F. W. Sexton, J. S. Fu, R. A. Kohler, and R. Koga, "Seu characterization of a hardened cmos 64k and 256k sram," *Nuclear Science, IEEE Transactions on*, vol. 36, no. 6, pp. 2311–2317, Dec 1989.

[90] O. A. Amusan, A. F. Witulski, L. W. Massengill, B. L. Bhuva, P. R. Fleming, M. L. Alles, A. L. Sternberg, J. D. Black, and R. D. Schrimpf, "Charge collection and charge sharing in a 130 nm cmos technology," *Nuclear Science, IEEE Transactions on*, vol. 53, no. 6, pp. 3253–3258, Dec. 2006.

[91] O. A. Amusan, L. W. Massengill, M. P. Baze, B. L. Bhuva, A. F. Witulski, S. Das-Gupta, A. L. Sternberg, P. R. Fleming, C. C. Heath, and M. L. Alles, "Directional sensitivity of single event upsets in 90 nm cmos due to charge sharing," *Nuclear Science, IEEE Transactions on*, vol. 54, no. 6, pp. 2584–2589, Dec. 2007.

[92] L. Edmonds, *SEU Rate Estimates for Devices Exhibiting Dual-Node susceptibility.* JPL Internal Memorandum, 2007.

[93] D. E. Fulkerson, D. K. Nelson, and R. M. Carlson, "Boxes: An engineering methodology for calculating soft error rates in soi integrated circuits," *Nuclear Science, IEEE Transactions on*, vol. 53, no. 6, pp. 3329–3335, Dec. 2006.

[94] D. Falguere and S. Petit, "A statistical method to extract mbu without scrambling information," *Nuclear Science, IEEE Transactions on*, vol. 54, no. 4, pp. 920–923, Aug. 2007.

[95] Y. Tosaka and S. Satoh, "Simulation of multiple-bit soft errors induced by cosmic ray neutrons in drams," in *Simulation of Semiconductor Processes and Devices, 2000. SISPAD 2000. 2000 International Conference on*, 2000, pp. 265–268.

[96] R. Naseer and J. Draper, "Parallel double error correcting code design to mitigate multi-bit upsets in srams," in *Solid-State Circuits Conference, 2008. ESSCIRC 2008. 34th European*, Sept. 2008, pp. 222–225.

[97] Y. Kawakami, M. Hane, H. Nakamura, T. Yamada, and K. Kumagai, "Investigation of soft error rate including multi-bit upsets in advanced sram using neutron irradiation test and 3d mixed-mode device simulation," in *Electron Devices Meeting, 2004. IEDM Technical Digest. IEEE International*, Dec. 2004, pp. 945–948.

[98] R. A. Reed, M. A. Carts, P. W. Marshall, C. J. Marshall, O. Musseau, P. J. McNulty, D. R. Roth, S. Buchner, J. Melinger, and T. Corbiere, "Heavy ion and proton-induced single event multiple upset," *Nuclear Science, IEEE Transactions on*, vol. 44, no. 6, pp. 2224–2229, Dec 1997.

[99] S. Buchner, A. B. Campbell, T. Meehan, K. A. Clark, D. McMorrow, C. Dyer, C. Sanderson, C. Comber, and S. Kuboyama, "Investigation of single-ion multiple-bit upsets in memories on board a space experiment," in *Radiation and Its Effects on Components and Systems, 1999. RADECS 99. 1999 Fifth European Conference on*, 1999, pp. 558–564.

[100] N. Rollins, M. J. Wirthlin, M. Caffrey, and P. Graham, "Evaluating tmr techniques in the presence of single event upsets," in *Military and Aerospace Programmable Logic Devices (MAPLD) Conference Proceedings*, 2003.

[101] D. Radaelli, H. Puchner, S. Wong, and S. Daniel, "Investigation of multi-bit upsets in a 150 nm technology sram device," *Nuclear Science, IEEE Transactions on*, vol. 52, no. 6, pp. 2433–2437, Dec. 2005.

[102] R. C. Martin, N. M. Ghoniem, Y. Song, and J. S. Cable, "The size effect of ion charge tracks on single event multiple-bit upset," *Nuclear Science, IEEE Transactions on*, vol. 34, no. 6, pp. 1305–1309, Dec. 1987.

[103] L. Edmonds, "A distribution function for double-bit upsets," *Nuclear Science, IEEE Transactions on*, vol. 36, no. 2, pp. 1344–1346, Apr 1989.

[104] T. D. Loveless, L. W. Massengill, B. L. Bhuva, W. T. Holman, R. A. Reed, D. McMorrow, J. S. Melinger, and P. Jenkins, "A single-event-hardened phase-locked loop fabricated in 130 nm cmos," *Nuclear Science, IEEE Transactions on*, vol. 54, no. 6, pp. 2012–2020, Dec. 2007.

[105] M. P. Baze, S. Buchner, W. G. Bartholet, and T. A. Dao, "An seu analysis approach for error propagation in digital vlsi cmos asics," *Nuclear Science, IEEE Transactions on*, vol. 42, no. 6, pp. 1863–1869, Dec 1995.

[106] L. W. Massengill, M. S. Reza, B. L. Bhuva, and T. L. Turflinger, "Single-event upset cross-section modeling in combinational cmos logic circuits," *Journal of Radiation Effects, Research, and Engineering*, vol. 16, no. 1, Dec 1998.

[107] L. W. Massengill, A. E. Baranski, D. O. Van Nort, J. Meng, and B. L. Bhuva, "Analysis of single-event effects in combinational logic-simulation of the am2901 bitslice processor," *Nuclear Science, IEEE Transactions on*, vol. 47, no. 6, pp. 2609–2615, Dec 2000.

[108] G. Asadi, S. G. Miremadi, H. R. Zarandi, and A. Ejlali, "Fault injection into sram-based fpgas for the analysis of seu effects," in *Field-Programmable Technology (FPT), 2003. Proceedings. 2003 IEEE International Conference on*, Dec. 2003, pp. 428–430.

[109] S. Rezgui, G. M. Swift, R. Velazco, and F. F. Farmanesh, "Validation of an seu simulation technique for a complex processor: Powerpc7400," *Nuclear Science, IEEE Transactions on*, vol. 49, no. 6, pp. 3156–3162, Dec 2002.

[110] R. A. Reed, R. A. Weller, M. H. Mendenhall, J. M. Lauenstein, K. M. Warren, J. A. Pellish, R. D. Schrimpf, B. D. Sierawski, L. W. Massengill, P. E. Dodd, M. R. Shaneyfelt, J. A. Felix, J. R. Schwank, N. F. Haddad, R. K. Lawrence, J. H. Bowman, and R. Conde, "Impact of ion energy and species on single event effects analysis," *Nuclear Science, IEEE Transactions on*, vol. 54, no. 6, pp. 2312–2321, Dec. 2007.

[111] J. M. Sisterson, J. B. Flanz, and J. E. Burns, "A new proton irradiation facility at the northeast proton therapy center," in *Radiation Effects Data Workshop*, 1999, pp. 123–127.

[112] D. Lambert, J. Baggio, G. Hubert, P. Paillet, S. Girard, V. Ferlet-Cavrois, O. Flament, F. Saigne, J. Boch, B. Sagnes, N. Buard, and T. Carriere, "Analysis of quasi-monoenergetic neutron and proton seu cross sections for terrestrial applications," *Nuclear Science, IEEE Transactions on*, vol. 53, no. 4, pp. 1890–1896, Aug. 2006.

[113] http://www.nndc.bnl.gov/exfor/endf00.jsp.

[114] R. C. Baumann and D. Radaelli, "Determination of geometry and absorption effects and their impact on the accuracy of alpha particle soft error rate extrapolations," *IEEE Transactions on Nuclear Science*, vol. 54, pp. 2141–2148, Dec 2007.

[115] L. Moral and A. Pacheco, "Algebraic approach to the radioactive decay equations," *American Journal of Physics*, vol. 71, pp. 684–686, Jul 2003.

[116] T. Calin, M. Nicolaidis, and R. Velazco, "Upset hardened memory design for submicron cmos technology," *Nuclear Science, IEEE Transactions on*, vol. 43, no. 6, pp. 2874–2878, Dec 1996.

[117] http://www.accre.vanderbilt.edu.

[118] A. L. Sternberg, L. W. Massengill, M. Hale, and B. Blalock, "Single-event sensitivity and hardening of a pipelined analog-to-digital converter," *Nuclear Science, IEEE Transactions on*, vol. 53, no. 6, pp. 3532–3538, Dec. 2006.

[119] A. L. Sternberg, "Single-event response and hardening techniques for high-performance pipelined analog-to-digital converters," PhD, Vanderbilt University, 2006.

[120] M. P. Baze, J. C. Killens, R. A. Paup, and W. P. Snapp, "Seu hardening techniques for retargetable scalable sub-micron digital circuits and libraries," in *21st SEE Symposium in Manhattan Beach, Ca*, 2002.

[121] J. H. Adams, *Cosmic Ray Effects on MicroElectronics.* NRL Memorandum Report 5901 Part IV, Aug 1986.

[122] K. M. Warren, A. L. Sternberg, R. A. Weller, M. P. Baze, L. W. Massengill, R. A. Reed, M. H. Mendenhall, and R. D. Schrimpf, "Integrating circuit level simulation and monte-carlo radiation transport code for single event upset analysis in seu hardened circuitry," *Nuclear Science, IEEE Transactions on*, vol. 55, no. 6, pp. 2886–2894, Dec. 2008.

[123] J. Benedetto, P. Eaton, K. Avery, D. Mavis, M. Gadlage, T. Turflinger, P. Dodd, and G. Vizkelethyd, "Heavy ion-induced digital single-event transients in deep submicron processes," *Nuclear Science, IEEE Transactions on*, vol. 51, no. 6, pp. 3480–3485, Dec. 2004.

[124] B. Narasimham, B. L. Bhuva, R. D. Schrimpf, L. W. Massengill, M. J. Gadlage, O. A. Amusan, W. T. Holman, A. F. Witulski, W. H. Robinson, J. D. Black, J. M. Benedetto, and P. H. Eaton, "Characterization of digital single event transient pulse-widths in 130-nm and 90-nm cmos technologies," *Nuclear Science, IEEE Transactions on*, vol. 54, no. 6, pp. 2506–2511, Dec. 2007.

[125] W. L. Oberkampf, "Uncertainty quantification using evidence theory," in *Advanced Simulation and Computing Workshop Error Estimation, Uncertainty Quantification, And Reliability in Numerical Simulations*, Aug 2005.

[126] H. Stark and J. W. Woods, *Probability, random processes, and estimation theory for engineers.* Upper Saddle River, NJ, USA: Prentice-Hall, Inc., 1986.

[127] http://local.wasp.uwa.edu.au/ pbourke/geometry/.